HIGHLY EFFICIENT PEROVSKITE MATERIALS FOR HYDROGEN PRODUCTION THROUGH WATER SPLITTING

Thesis Submitted for the Award of the Degree of

DOCTOR OF PHILOSOPHY

in

Chemistry

By

Amika

Registration Number: 41900676

Supervised By:

Dr. Deepak Kumar

Department of Chemistry

Assistant Professor

Co- Supervised By:

Dr. Rajesh Sharma

Department of Physics

Assistant Professor

LOVELY PROFESSIONAL UNIVERSITY, PUNJAB

2023

DECLARATION

I, hereby declared that the presented work in the thesis entitled "Highly Efficient Perovskite Materials for Hydrogen production through Water splitting" in fulfillment of degree of **Doctor of Philosophy (Ph.D.)** is outcome of research work carried out by me under the supervision of Dr. Deepak Kumar, working as assistant professor, in the Department of Chemistry Lovely Professional University, Punjab, India. In keeping with general practice of reporting scientific observations, due acknowledgements have been made whenever work described here has been based on findings of other investigator. This work has not been submitted in part or full to any other University or Institute for the award of any degree.

(Signature of scholar)

Name of scholar: Amika

Registration number: 41900676

Department: Chemistry

Lovely Professional University

Punjab, India.

CERTIFICATE

This is to certify that the work reported in the Ph.D. thesis entitled "Highly Efficient Perovskite Materials for Hydrogen production through Water splitting" submitted in fulfillment of the requirement for the award of degree of **Doctor of Philosophy (Ph.D.)** in the Department of Chemistry, is a research work carried out by Amika, 41900676, is bonafide record of her original work carried out under my supervision and that no part of thesis has been submitted for any other degree, diploma or equivalence course.

(Signature of Supervisor)

Name: Dr. Deepak Kumar

Designation: Assistant Professor

Department: Chemistry

University: LPU, Punjab.

(Signature of Co-Supervisor)

Name: Dr. Rajesh Sharma

Designation: Assistant Professor

Department: Physics

University: MNS govt college (CBLU) Bhiwani.

Abstract

This thesis entitled “HIGHLY EFFICIENT PEROVSKITE MATERIALS FOR HYDROGEN PRODUCTION THROUGH WATER SPLITTING” is concerned with the synthesis and various characterization techniques for nanostructured pure and doped bismuth titanate perovskite materials for photo-driven water splitting reactions. This thesis has been divided into five chapters including sub chapters which are as follows:

Chapter 1 is introductory chapter based on causes of energy crisis and need of renewable energy considering solar fuels as superior source because of abundant supply of solar energy. A brief overview of use of fossil fuels and their adverse environmental impacts has been discussed. Various renewable sources along with their power conversion efficiencies are shown. Hydrogen has been regarded as a viable energy source because of having high energy capacity and eco-friendly. This chapter includes hydrogen as a renewable energy source and also highlighted the status of hydrogen as revolutionary, alternative and clean energy source for various applications. This chapter provides insight on perovskites materials to be used as photocatalyst in water splitting reactions. A brief history of perovskites, with their general structure and classification has also been discussed. This chapter also outlines the synthetic techniques, properties and applications of perovskites with emphasis on their photocatalytic applications for water splitting. A detailed discussion of various synthetic procedures including hydrothermal, sol-gel, co-precipitation, solid state technique and chemical-vapour deposition method.

Chapter 2 reports water splitting reactions with a detailed discussion on photocatalytic water splitting mechanism and comparison with natural photosynthesis. Also explained the other methods of hydrogen generation like thermolysis, radiolysis and electrocatalysis. Basic mechanism of photocatalysis and requirements of photocatalytic properties for a semiconductor has been undertaken in this chapter. Presently, various photocatalyst are studied having water splitting abilities. Titanates are represented as effective photocatalysts for breakdown of water to produce hydrogen. Numerous strategies such as elemental doping, catalysts loading and heterojunction development, were discussed briefly. The development of type 1 and type 2 heterojunction between semiconductors has also been presented. Further, this chapter also reflected the factors including crystallinity, surface area, particle size and band gap, which

affects the photocatalytic performance of nanomaterials. The effect of catalyst dosage on water splitting reactions has also been discussed. This chapter deliberates previous studies on hydrogen generation efficiency of various photocatalytic materials and their advantages as superior photocatalyst. This chapter also includes the scope and objectives of this research work.

Chapter 3 presents characterization techniques used for analysis of the synthesized samples, procedures of chemical synthesis for growth of nanostructured bismuth titanates ($Bi_4Ti_3O_{12}$), CdS/BT, PbS/BT and their composites with graphene oxide). A brief discussion of characterization techniques including XRD, FTIR, DRS-UV, EPR, FESEM and HRTEM spectroscopy has also been presented. The hydrothermal growth of nanoparticles is presented here and the setup for photocatalytic reaction along with reaction conditions are discussed.

Chapter 4.1 is on photocatalytic water splitting performance of Bismuth titanate nanoparticles. A simple, low-cost precursor free and consisting of a single step, synthetic technique has been presented for synthesis of bismuth titanate (BT) perovskite nanomaterials under surfactant free conditions. A brief history of nature of bismuth titanate as photocatalyst has also been discussed. All the chemicals essential for synthesis have also been expounded. This chapter emphasizes on the powdered XRD method for endorsement of crystal structure and morphology of synthesized nanomaterials was confirmed by FESEM study. The functionalization of effect of sacrificial agents on hydrogen production efficiency of $Bi_4Ti_3O_{12}$ are discussed and procedure for photocatalytic reaction along with mechanistic aspects are presented.

Chapter 4.2 is on photocatalytic water splitting behavior of CdS doped bismuth titanates. This chapter also reflects the method for incorporation of different concentrations (0.1%, 0.3% and 0.6% w/w) of Cadmium sulfide nanoparticles into the lattice site of Bismuth titanate for a cocatalyst free hydrogen generation via photocatalytic experiments. The effect of CdS doping on crystallite size and morphological features of Bismuth titanates has also been represented in this chapter. The functionalization of photochemical reactor having Xenon lamp is discussed to check the photocatalytic performance of nanoparticles for hydrogen generation in presence of different scavengers. All the characterization practices including XRD, FTIR, UV and FESEM utilized for various investigations has given in this chapter. The role of methanol as a scavenger is discussed and bar diagram showing comparative results for hydrogen production in presence of various scavengers has also been depicted.

Chapter 4.3 This chapter imitates the scheme for insertion of different concentrations (0.1%, 0.3% and 0.6% w/w) of Lead sulfide nanoparticles into the lattice site of bismuth titanate for hydrogen generation via water splitting reactions. A brief discussion of structural properties investigated by XRD, unit cell parameters, atomic radii and unit cell volume has been presented. The effect of addition of various amounts of PbS on crystallite size has also been discussed. The UV absorption graphs of pristine and PbS doped samples are represented as well as Tauc plots representing band gap values have been deliberated. This chapter also represents the hydrogen evolution rates of different photocatalysts in presence of EDTA acting as sacrificial agent and the comparison of hydrogen production efficiency of 0.6% PbS doped bismuth titanate samples in presence of methanol, TEOA and EDTA has been explained.

Chapter 4.4 focuses on the incorporation of graphene oxide into CdS and PbS doped bismuth titanate samples. This chapter represents the modified hummers method for synthesis of graphene oxide. Further, reflects the incorporation of graphene oxide into PbS and CdS doped samples of bismuth titanates. The photocatalytic efficiencies of GO composites have been tested through water splitting experiments carried out in photoreactor cell are demonstrated in this chapter. The effect of GO doping on band edge potentials has also been depicted. This chapter also illustrates the electron trapping mechanism of graphene oxide.

Chapter 5 presents summary and forthcoming work on the basis of performance of various perovskite catalytic materials and also emphasized on the key findings. This chapter shows the comparative analysis results of band gaps and hydrogen evolution efficiency of various samples synthesized during the current research work.

In this research work, the primary objective is to develop photocatalyst, showing energy conversion efficiency for water splitting, through doping and nanocomposites synthesis.

Acknowledgements

I thank God for giving me the strength to not discourage during hard times.

I am thankful to my supervisor, Dr. Deepak Kumar for his supreme guidance, expertise and insight throughout the entire work. Throughout the ups and downs, he remained focused and determined, two characteristics which have definitely rubbed off on me. He will remain a lifelong mentor and friend. I would also like to thank my co-supervisor, Dr. Rajesh Sharma, for many valuable discussions, for being very supportive in difficult times, for being my mentor, for sharing with me his valuable knowledge, for his continuous support and suggestions. I would like to extend special thanks to Dr. Ajit Sharma for his guidance, I couldn't have done it without you.

I am grateful to my husband Mr. Inderjeet Singh for his motivation, endless support and faith in me. I could not be more blessed for having you in my life. To my father-in-law Mr. Bhup Singh and mother-in-law Mrs. Ratni Devi for always being there for me and for being the best mother-in-law I could have had. Eternally grateful to you.

A very special thanks to my son Yashveer Gahlawat and my lovely daughter Tiyanshi Gahlawat, you both have made me stronger, better, and more fulfilled that I could have ever imagined. You both have sacrificed a lot during my research work. I love you to the moon and back.

Thanks to my Mother Mrs. Sunita Devi and Father Sh. Naphe Singh and to my brother Mr. Atul Sangwan and sister Aruna. Thanks for your never-ending encouragement.

To my friend Dr. Jyoti Sheoran, who was there throughout the good and bad times - I couldn't have done it without you. Thank you for your friendship, for offering me advice and supporting me through this entire process.

To my grandma who is with me from heaven and whom I will always remember with love and carry in my heart.

Contents

List of Tables

List of figures

List of abbreviations

BT	Bismuth titanate
BTNPs	Bismuth titanate nanoparticles
XRD	X-ray Diffraction Spectroscopy
FTIR	Fourier Transform Infrared Spectroscopy
DRS UV-Vis	Diffuse Reflectance UV-Visible Spectroscopy
FESEM	Field Emission Scanning Electron Microscopy
XPS	X-ray Photoelectron Spectroscopy
EPR	Electron Paramagnetic Resonance
HR-TEM	High Resolution Transmission Electron Microscopy
VB	Valence Band
CB	Conduction Band
mL	Millimeter
Min.	Minute
W	Watt
NPs	Nanoparticles
BTP	Bismuth titanate perovskites
TW	Terawatt
GW	Gigawatt
MJ/Kg	Megajoule/Kilogram
EJ	Exajoule

CHAPTER 1

INTRODUCTION

1.1 Global energy outlook

The deterioration of environment and energy issues are on the rise, mainly because of modern civilization's rapid growth and tremendous fossil fuel consumption. The widespread consumption of fossil fuels subsidizes to both global climate change and energy problems. Furthermore, decline in fossil fuels is irreversible, necessitating the development of sustainable green sources. These two together represent a significant threat to the advancement of human civilization (Fig. 1.1). As a result, both environmental preservation and energy use are highly valued in our universe. Fuels such as coal, natural gas and crude oil account for 79.90% of our energy production, while biomass, wind, tidal, solar, and geothermal energy contribute to the remaining 20%[1].

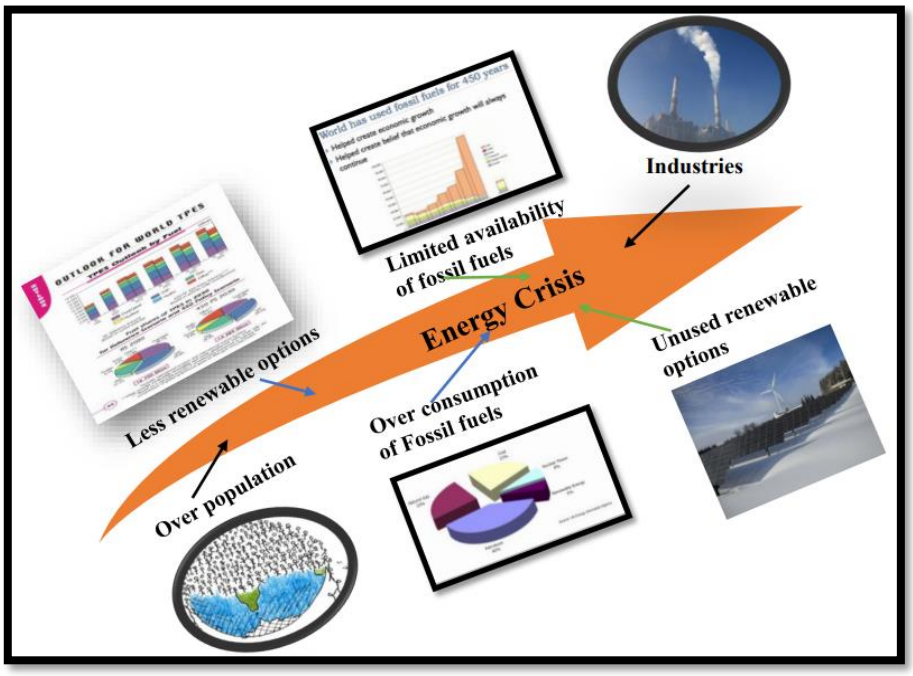

Fig 1.1 The reasons of energy crisis.

The general secretary of United Nations Ban Ki-moon said that we can no longer burn our means to opulence. Under mission the ‘Sustainable Energy for All’ they advocated to enhance the rate of inexhaustible energy production to about 30%. The social and commercial development can be

accessed by facilitating reliable and affordable energy to society but still there are challenges to give facilities of even electricity to 7 billion people.

Even though the energy supply is in a huge amount in some regions yet there are challenges. Presently, out of 15 TW of power consumption annually, around 85% energy that is we are consuming for everyday activities, for transport, agriculture and industries etc. is currently dependent on fossil fuels however, their exhaustion is resulting in environmental challenges. Today the ideal sources of fuel are coal, oil and natural gas having high energy density and easy transportation makes them suitable to fulfill the energy demands. However, these sources are getting depleted day by day and are also causing environmental pollution by releasing greenhouse gases on burning. In near future, the energy demand will increase around 58%, as the population approach to 9 billion[2]. Even the current consumption rate is also high and the reserves for coal, oil and natural gas will be depleted in around 150 to 400 years, 40 to 85 years and 60 to 165 years respectively.

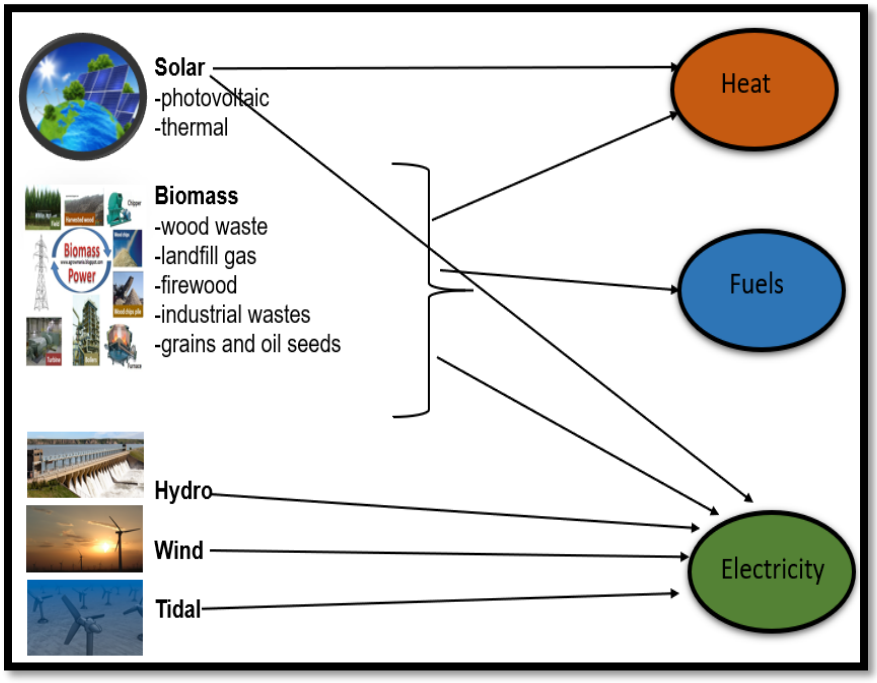

Fig 1.2 Sources of renewable energy.

The adverse environmental impacts on the environment, driven on by the combustion of carbon-based fossil fuels, specifically carbon dioxide pollutants, are of escalating concern. Renewable

energy is increasing popularity, despite predictions that we will continue to depend on fossil fuels contributing to about 78% of energy in 2045.

For the first time ever, in year 2013, the power of novel sustainable electricity initiatives surpassed that of previously established fossil fuel establishments, with 142 GW of inexhaustible electricity capacity built versus 140 GW of fossil fuel plants. Additionally, there is growing community demand on corporations and politicians to adopt green energy sources and stop funding industries that profit from oil, gas, and coal. 253 entities, including colleges, religious organizations, charity foundations, and governmental bodies, had divested from fossil fuel firms as of July 2015, for a total worth of over $61 billion.

The ongoing consumption of carbon-based fuels has exacerbated air quality issues in technologically advanced cities to levels above authorized health limits, leading to a variety of pollution-related disorders. In addition, novel innovations in technology are required to cut back on projected increases in worldwide emissions of carbon, which are expected to range near about 10.2 billion tones by 2025. Assumed the aforementioned, international civic acknowledges the need for renewable sources of energy, even though ensuring that individuals have a sustainable existence.

So, there is a strong need for sources of continuous energy that could satisfy the future energy demands without causing environmental pollution and also should be cost effective. The whole world countries are pledged to change the way of energy generation to accomplish the need of rising energy[3]. In the direction of resolving the problem of energy crisis and environmental issues in world, renewable production of energy is necessary. Gasoline and additional liquid gases (as fuels) as well as hydroelectricity, solar power, geothermal energy and ocean power are examples of clean energy sources**.**

Countries like China, India, the United States, Brazil, Nigeria, Indonesia, and Canada are currently employing renewable energy to combat environmental issues and meet growing energy needs. Figure 1.3 shows the rise of wind and solar energy specifically in Canada during the past few years. 18.3% of Canada's overall energy output, according to natural resources Canada, is derived from renewable sources.

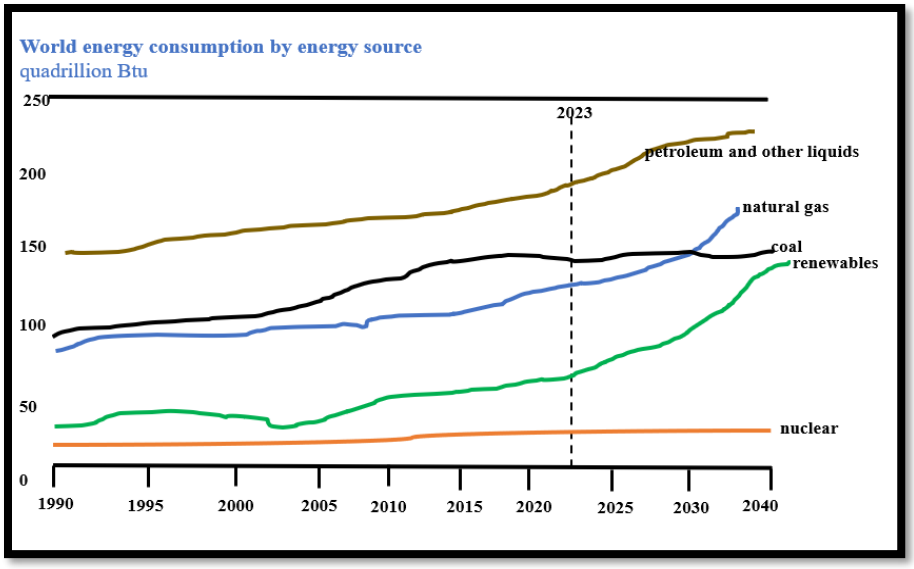

Fig 1.3 Consumption of energy in world by 2040.

Petroleum and other carbon-based fuels are castoff to afford the world's energy requirements. However, in order to produce renewable energy utilizing clean energy carriers from alternative technologies, as a consequence of the degradation of fossil-based fuels and their greenhouse gas emissions, is required. An appealing and sustainable energy source that can substitute fossil fuels is hydrogen (H_2). Because H_2 is a fuel that is more abundant in nature, pure, and efficient. It is also lightweight and portable[4]. Additionally, the use of H_2 as an energy intermediary helps to equilibrium the imbalance in distribution and requirement between the production of energy and other sectors.

There are numerous advantages of hydrogen fuel (as has been depicted in fig 1.4) including:

- Hydrogen energy offers more appealing qualities because of its non-toxic nature.
- The heat of ignition for hydrogen is 34.18 $kcalg^{-1}$, that is three times superior as compared to heat of combustion for petroleum.
- Transferring energy in hydrogen form is significantly simpler and can be transferred up to long distances because it simply creates steam and liquid water after combustion and cost-effective as compared to transferring electricity over high-voltage grid lines.

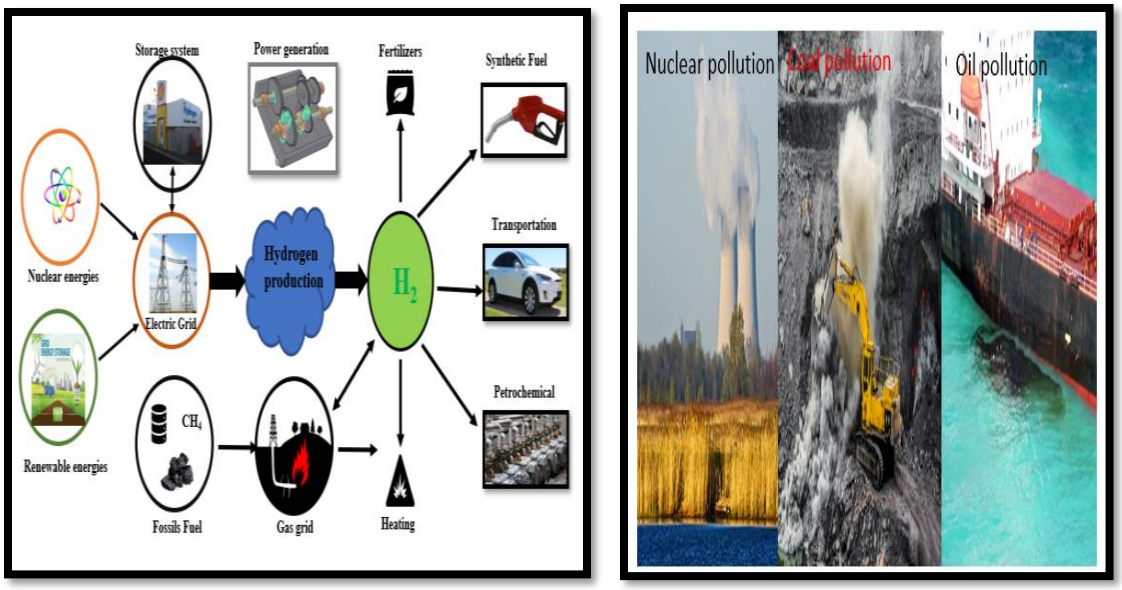

Fig 1.4 Importance of hydrogen energy.

Hydrogen has the following unique features:

(i) energy conversion efficiency is good.

(ii) can be generated from water splitting process with no emission of pollutants.

(iii) various storage options are available (e.g. can be stored in liquid form as well as in gaseous form or can also be absorbed in metal hydrides).

(iv) can be transported across extensive distances.

(v) can be converted into a numerous fuel by means of diverse procedures.

Additionally, the environment's lack of oxygen also has a negative impact. The survival of the creatures depends heavily on this. The oxidation of water to oxygen has long been an issue in the realm of sustainable energy[5].

1.1.1 Renewable causes of energy

Globally, the percentage of inexhaustible energy bases in our primary energy supply and in the electricity, we consume is currently at 13.2% and 22%, respectively; however, by the year 2040, this percentage is expected to expand by a factor of three, indicating the coming age of the renewable energy sector.

Conversely, despite conventional sources including natural gas, coal, and petroleum, sustainable energy techniques have capability to be used on a broad level. Most of countries in world have

access to a variety of resources and each country in the globe have at least one energy source that is abundant and renewable.

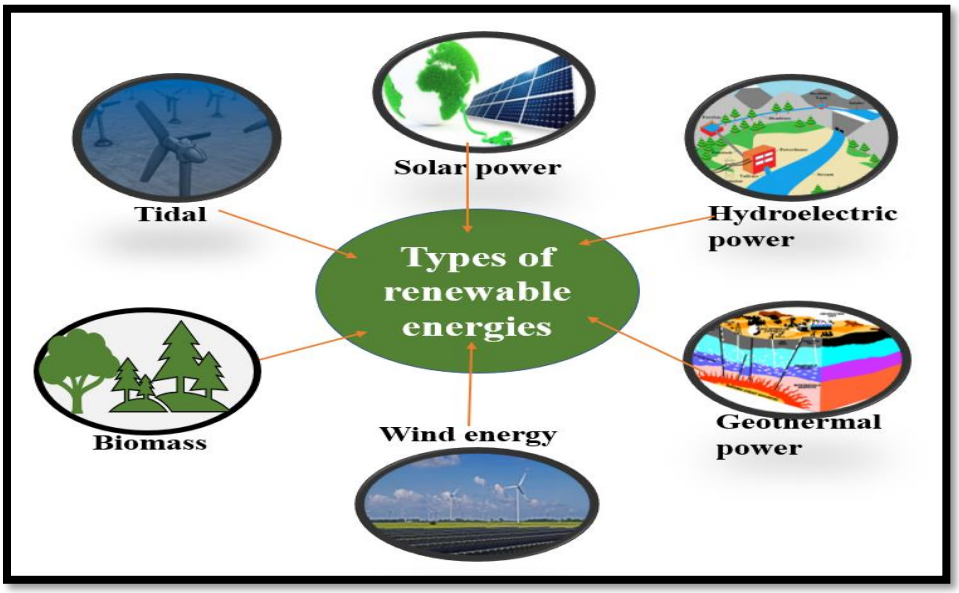

Fig 1.5 Types of renewable energy sources.

Depending on whether the resource is accessible, each and every forthcoming infrastructure of energy will possibly count on diverse technologies. Table 1.1 Illustrates the predictable power generation proficiencies of some renewable foundations of energy.

Through various approaches, primary energy sources including wind, biomass, and sunlight may be utilized to produce renewable energy as has been illustrated in figure 1.5. The US Department of Energy estimates that the steam reforming of natural gas produces 400 billion cubic meters of hydrogen annually throughout the world.

Fortunately, unlike conventional sources like natural gas, coal and petroleum, technologies for renewable energy production possess the ability to be employed on a broad scale because of worldwide diversity of resources. There is minimum one environmentally friendly source of energy in every nation, and most of nations have diverse resources.

Depending on whether resource is prevalent locally, the future infrastructure of energy will probably depend on diverse technologies. According to one prediction, the Middle East would generate more than 50% of its electricity from solar technology by 2040, but the European union,

which experiences weaker solar radiation, will rely more on other energy sources like wind power. With 125,000 TW of insolation hitting the surface of earth annually, renewable energy from sunlight has the highest capacity of the currently available renewable sources to satisfy our future energy needs.

Table 1.1 Renewable energy sources[5].

Type of renewable energy	**Power (TW)**	**Energy source**	**Advantages**	**Disadvantages**
Hydroelectric power	1-2	Can be produced by using mechanical energy of flowing water	High reliability	Initial cost is high
Solar power	>20	Energy conversion from sunlight into electricity	Low maintenance cost and reliable	Expensive solar panel
Wind energy	4	Kinetic energy of wind is transformed into mechanical power	Unlimited wind availability	Costly maintenance, fluctuations in wind
Biomass	10	Organic materials can be turned into fuel	Use of raw materials	Limited resources available
Geothermal power	12	Trap heat and steam from underground to generate electricity	Continuous operation	Limited access to geothermal locations

Researchers have recently started looking into additional sparkling and pollution free energy routes that could be alternative of fossil fuels in relation to the inexhaustible sources of energy listed in Table 1.1. The hydrogen is furthermost prevalent element in the world and can be derived from a varied array of feedstocks[6,7]. In addition to being plentiful, hydrogen has a prominent calorific value (143 MJ/kg) and produces no pollutants. The only result of burning of hydrogen with airborne oxygen gas is water. The above factors are tremendously beneficial for hydrogen as a sustainable fuel, however there are issues with storage and transportation[8].

In addition to reforming, water electrolysis is another method for hydrogen manufacturing. In water electrolysis, there emerges a substantial need for energy during water splitting. The energy

required can be provided in the form of electrical power and generated by using hydroelectric power. As a result, the entire process can be regarded as an unfeasible alternative, when fossil fuels are used. Water electrolysis also presents problems with its efficiency, maintenance costs, and robustness[9].

For hydrogen gas synthesis, water splitting in presence of solar light is a favorable tactic because both solar light and water are renewable. But, broad scale implementation of this scheme is inhibited due to the less efficiency and high cost of photoreactor set-ups. Of the existing inexhaustible energy sources, conversion of energy from sun light is the most upcoming solution to this growing issue of renewable production of energy thereby dropping the use of carbon-based fuels. The energy from sun light is predominantly attractive because of its richness, easy availability and cleanliness. If nearly 1 % of sun light energy could be used, it would sufficiently fulfill the demand of energy at existing consumption rate of energy. In one year, 3,850,000 EJ of solar light is captivated by earth's surface while, the current energy dissipation is only near about 474 EJ per year. So, using the solar power efficiently enough clean, renewable and long-lasting energy will be present [10]. Amongst numerous approaches of solar energy alteration, much consideration has been paid to photocatalytic water splitting because of its promising implication in gaining directly clean and sustainable energy containing hydrogen.

1.1.2 Solar Fuels

In the future years, solar energy will become a key component of the global energy mix as a result of the lowering cost of photovoltaic technology and the requirement to limit emissions of greenhouse gases. It is anticipated that by the year 2050, solar energy will have overtaken fossil fuels, wind, hydropower, and nuclear power to become the single most important source of electricity. Managing the fluctuating availability of solar power, both on a daily and seasonal basis, will become increasingly difficult for the power grid as per the proportion of sun light energy in overall energy blend continues to rise. This will be true in both the summer and winter months. Storage technologies on a massive scale are need to be put into place in order for solar energy to contribute significantly to our overall power supply. Presently, pumped-hydroelectrical facilities accounts for nearly 99% of the energy storage capacity around the world (an entire of 127 GW output), despite their restricted geographical dispersion.

The technique of transforming sunlight energy into fuel by employing man-made components has been the focus of significant investigation in current years. This process is known as "artificial photosynthesis," and it has been given this name. In Brazil, sugar cane is utilized as an alternative for making ethanol, which can be used as biofuel, have made use of photosynthesis as a means of their economic development. However, because of the relatively less proficiency of producing biomass energy from sun light, the manufacturing of biofuels can only take place in countries that have huge amounts of arable land[11]. Nanomaterials that utilize solar light to produce the renewable fuels have been synthesized as an alternative and has shown a great deal of potential.

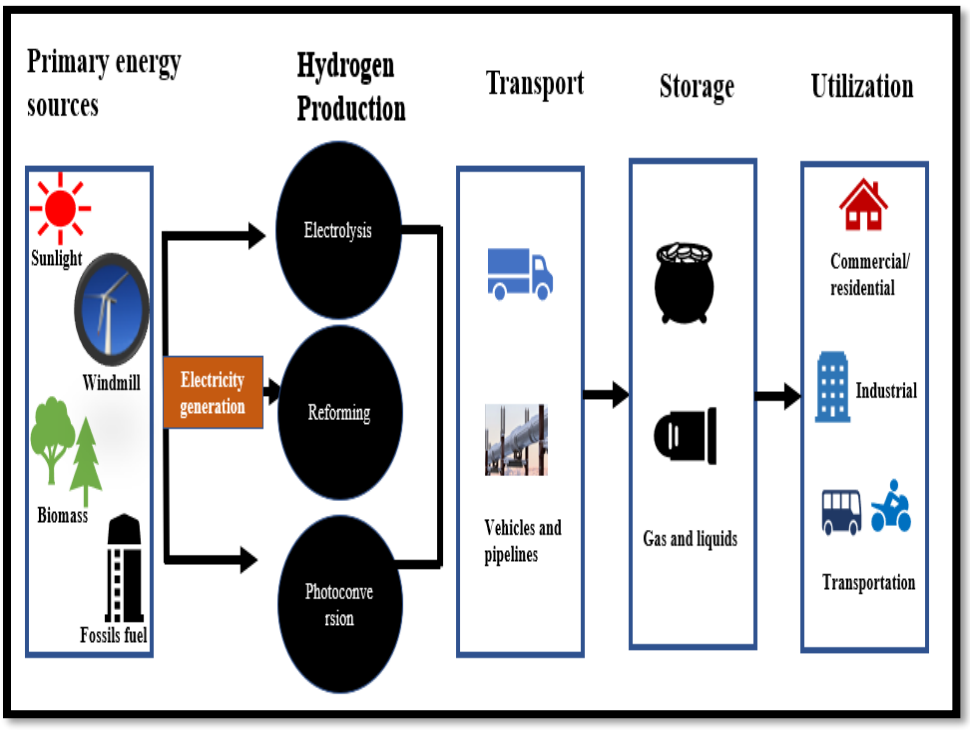

Fig 1.6 Hydrogen production technologies and primary energy sources.

These bio-inspired techniques are referred to as artificial photosynthesis, and they have shown significant promise as an alternative. The intention of man-made photosynthesis is to recreate primary processes that occur during natural photosynthesis. These processes include charge creation and separation, light gathering, and catalysis. Because of their ability to collect sun photons through the movement of electron from its low-lying VB to high energy CB, photocatalytic materials are frequently chosen for use as simple artificial photocatalytic materials. The valence and conduction bands of photocatalysts are designed to be electrically isolated from

one another, which creates the energy necessary to facilitate chemical reactions on the surfaces of these materials or at the outermost layer of cocatalyst.

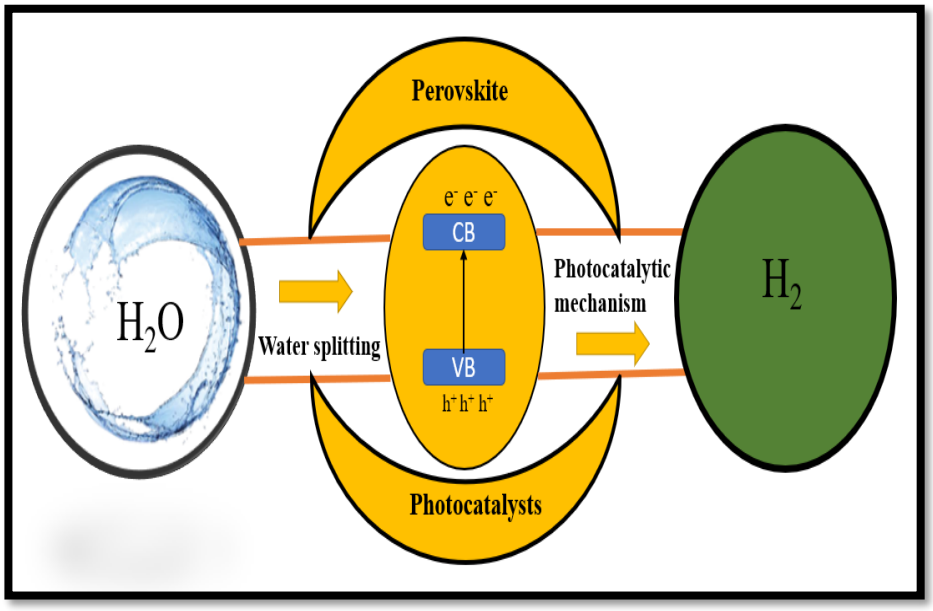

Fig 1.7 Fundamental mechanism for hydrogen production by water splitting[12].

On contrary, the photo-driven water splitting reactions to generate hydrogen gas, has been stated to have device efficiencies of maximum 18%. This method not only provides a route to an adaptable fuel source, but also an essential industrial commodity. As a result of the fact that the Haber-Bosch process, which uses hydrogen in industrial production, utilizes 3-6% of world's gasoline source and near about 2.1% of world's overall energy stream, generation of hydrogen from renewable sources has a significant bearing on the state of the world today. At the moment, fossil fuels are responsible for the production of 96% of hydrogen, that is why photovoltaic water splitting is such an appealing option for producing sustainable hydrogen. In order to be put to use as a source of energy, hydrogen can be transformed into electricity through the use of fuel cell technology. As a result, one can conceptualize a renewable energy infrastructure that is supported by sunlight, water, and electricity. Regrettably, the generation of electricity fails to efficiently mitigate the utilization of fossil fuels attributed to transportation sector, constituting approximately forty percent of the overall fossil fuel consumption [13]. Hydrogen has a higher gravimetric density than petrol (120 MJ/ kg), although it has a far lesser volumetric density (only 8 MJ/ L) than petrol does, which results in hydrogen having a lower energy density relative to its volume. Converting

hydrogen into liquid hydrocarbon fuels using recognized chemical processes is one solution of problem; nevertheless, this method is still related with the emission of CO_2 into the environment. The creation and implementation of innovative hydrogen storage techniques will be essential in the event that hydrogen itself is to be utilized in the transportation industry as a fuel. Both physically and chemically, by the creation of chemical bonds those can be found in hydrides of metal, hydrogen can be held. Some examples of physically stored hydrogen are high pressure or cryogenic storage tanks. In prototype hydrogen-powered cars, the primary method of hydrogen storage that has been utilized up until this point has been physical storage.

The Fuel Cell Electrochemical Technology programme of United States Division of Energy has demonstrated vehicles based on hydrogen fuel that have proficiency of travelling 255 miles on a tank having 4 kg of hydrogen fuel. These vehicles are highly effective as the petrol automobiles that are currently on the market.

1.2 Perovskites as photocatalytic material

Perovskite photocatalysts have demonstrated their capacity for water splitting among various developed photocatalysts. Perovskite's can be employed as a new strategy for photo catalysis of water because of having suitable band gap additionally, ferroelectric and piezoelectric properties of perovskites are also helpful in enhancing photo catalytic abilities for solar water splitting.

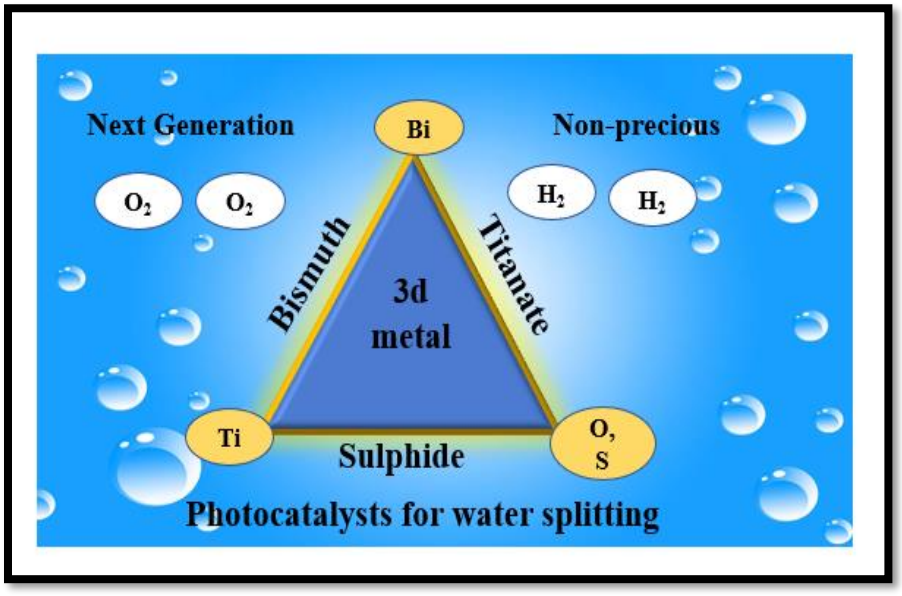

Fig 1.8 Perovskites as photocatalytic materials.

Perovskites based materials are of great interest in the study of photocatalysis and have fascinated widespread consideration in photocatalysis because of structure simplicity and flexibility of composition.

1.2.1 General introduction of Perovskites

In the year 1839, Gustav Rose worked on calcium titanium oxide ($CaTiO_3$), later termed as perovskite materials, situated in Russia (Ural Mountains). Perovskite's name was derived from calcium titanium oxide and was identified by Count Lev Aleksevich Von Perovski (a Russian mineralogist ,1792-1856) [14]. All materials with equivalent crystal structure to that of calcium titanium oxide, that is ABX_3, are termed Perovskites. General formula of perovskites is ABX_3 having two different sized cations (A and B) and anion (X). Where, usually X is oxygen nevertheless other large ions like halides, sulfides and nitrides can also be present. A and B = cations of unlike sizes (generally size of A is greater than B). X = anion making bond to individually A and B. X = normally oxygen or halides, sulfides, nitrides. Generally, perovskites are categorized into four forms.

(a) Normal perovskite having general formula ABO_3 ($BaTiO_3$).

(b) Layered perovskite having general formula A_2BO_4 (K_2NiO_4).

(c)Double perovskite having general formula $A_2BB^{|}O_6$ (Ba_2TiRuO_6).

(d)Triple perovskites $A_2A^{|}B_2B^{|}O_9$ ($La_2SrCo_2FeO_9$).

But perovskites are stable in ABO_3 type structure. B cation is slightly smaller than A site cation. Co-ordination number of B atom is 6 and A has 12-fold co-ordination number.

In perovskites unit cell, octahedral arrangement is formed by B cations with X-anions results in formation of BX_6 while "A" cations reside in cub-octahedral site along with X-anions and forms AX_{12}. The perovskites family encompasses a wide range of oxide arrangements, especially oxides of transition metal that possess the fundamental formula of ABO_3. In this framework, oxygen anions surround the A^{2+} cation and occupies corner position of the cubic lattice at coordinates (0,0,0). B^{4+} - occupies the body centered position ($^1/_2$, ½, ½). Perovskites can be synthesized in powdered form or as thin films.

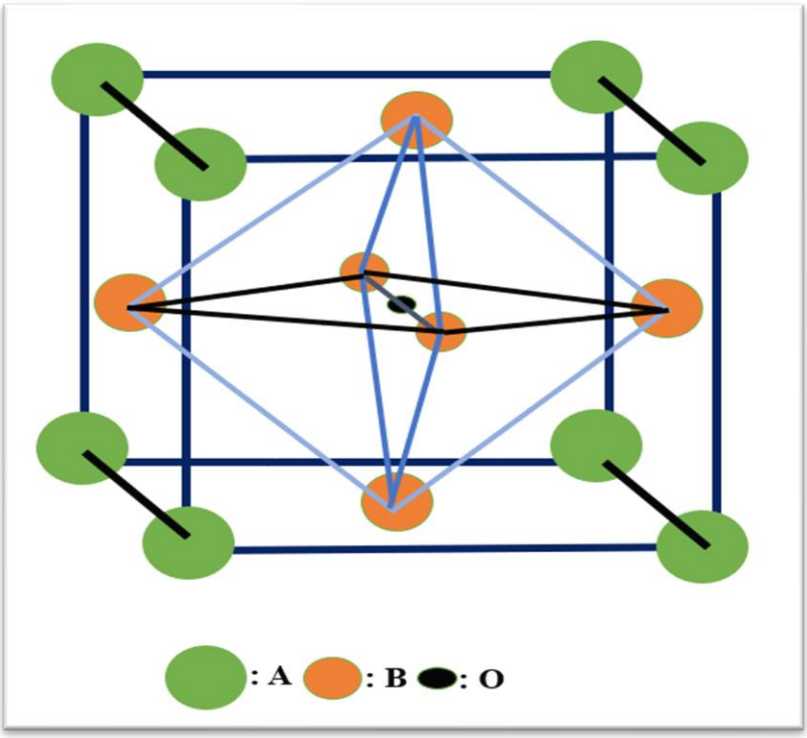

Fig 1.9 General structure of perovskite.

Composition and symmetry of perovskite materials may be changed by replacement at A and B locations which has a significant influence on band positions as well as affects the photocatalytic and photovoltaic properties of perovskites. Furthermore, the structure and band gap of perovskites are affected by doping of X site. Victor Moritz Goldschmidt acquaint with the term tolerance factor represented by term "t" as a means to evaluate the consistency of perovskites, by means of the empirical correlation between the ionic radii of elements (A, O and B)[15].

This relationship holds valid for pertinent ionic radii only at ambient temperature. The mathematical value of tolerance factor could be determined by:

$$t = (r_A + r_{O)} / [2^{1/2} (r_B + r_{O)}]$$

wherever, rA= ionic radius of cation A (which is larger than B), rB = ionic radius of cation B (which is smaller) whereas the radius of oxygen anion (O^{2-}) has been represented by rO.

The tolerance factor offers insight into the optimal selection of cations (A and B) for synthesis of a perovskite material with desirable properties. Distorted perovskite materials refer to those

materials that exhibit crystalline arrangements along with the cubic arrangement. Various cations can be accommodated by A and B locations. If distinction is done in cations site, then, variation in tolerance factor also occurs. Cubic perovskite's structure can be altered to non-cubic distorted structure, by changing the tolerance factor. To attain stability in a perovskite structure, it is essential for the tolerance factor to fall within the specified range of 0.88 to 1.09. A perovskite mineral that possesses the tolerance factor nearly equal to unity (t = 1), is considered to be an ideal perovskite structure. For values of t less than 1, perovskite materials exhibit a rhombohedral or monoclinic structure, whereas for values of t greater than 1, they display a tetragonal or orthorhombic structure. The deviation of the BO_6 octahedral from its ideal configuration in the perovskite system results in distortion, leading to alterations or improvements in the volume of the unit cell. Therefore, tolerance factor serves as a means for assessing the extent of distortion existing in perovskite crystals.

The optimal cubic arrangement of perovskites may lead to the development of various forms such as orthorhombic, rhombohedral, hexagonal, and tetragonal, due to occurrence of some changes in the crystal structure. The basic requirements for generation of a stable perovskite material are specified as[16]:

1. Radii: Primarily the ionic radii of cations of A- and B-locations should exceed 0.90 Å and 0.51 Å, correspondingly, secondly the range of tolerance factor should be within 0.88 to 1.09.

2. Electro-neutrality: The total sum charges of cations of A and B sites essentially to be comparable to the charge at anion site i.e. O^- (oxygen). An appropriate charge dispersal is to be accomplished in the forms of $A^{3+}B^{3+}O_3$ or $A^{4+}B^{2+}O_3$.

Generally, perovskites are classified into organic and inorganic perovskites. Metal organic halides are of great interest because of easy manufacturing, they have advantage that these can be produced at low temperature, although damages from moisture. In contrast, inorganic perovskite materials can be prepared at high temperature, but they are more sustainable in atmosphere. Current years have perceived an extremely great attention towards perovskite-based photocatalytic materials. Depending on the temperature conditions perovskite materials can exists in different phases. Perovskites exhibits stable orthorhombic phase (γ) below 100 K temperature. Further, the orthorhombic phase can be altered to tetragonal phase (β) by increasing the temperature to 160 K,

Once the temperature was further elevated to 330 K, stable cubic phase (α) replaces the tetragonal phase [17].

In recent years, a variety of perovskites including titanates, ferrites, tantalates, and vanadate's, have been documented in the scientific literature for their potential use in photocatalytic reactions. Especially, titanate-based perovskites have attracted significant attention owing to their outstanding photostability, resistance against corrosion in aqueous environments, and notable electronic and constitutional features. The materials exhibit reliable photocatalytic performance and exhibit stability when confronted with visible light irradiation[18].

1.3 Properties of perovskites

Due to their distinctive chemical nature, perovskite materials display a variety of intriguing characteristics, considering non-stoichiometry of anions as well as cations, electronic mixed valence states and distorted cationic configuration.

Due to non-stoichiometry of both cations and anions of A&B sites, perovskites have multi-functional properties. Many distinguished properties including; Dielectric characteristics, Optical properties, Ferroelectric, Superconductivity, Piezoelectricity, Multiferroicity and Catalytic activity are shown by perovskite materials by partial substitution of cations with transition metals.

1.3.1 Dielectric properties

Dielectrics are the materials with high electrical resistivities or we can say that the materials having long persistence time of electrostatic field. It displayed a significant resistance to electric current, when subjected to direct current voltage. For engineering and electronic industry, dielectric materials are of great significance as electro-ceramics. Titanium and niobium-based semiconductors such as $BaTiO_3$ and $KNbO_3$ showed a good dielectric constant. $BaTiO_3$ is also a good material used for capacitors. It showed that with change in temperature crystallographic dimensions also changed due to distortion of TiO_6 octahedron. There is a very large spontaneous polarization due to coupling of distorted octahedrons, giving rise to a large dielectric constant[19].

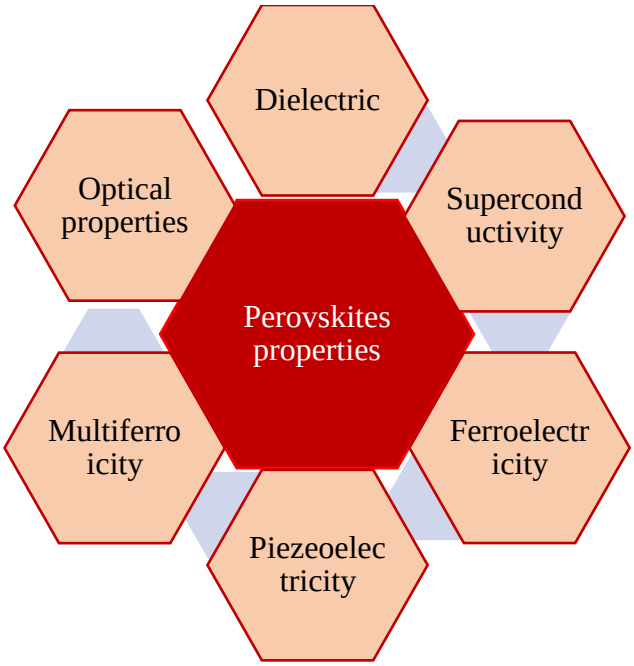

Fig 1.10 Different properties of perovskites.

The dielectric constant of a substance can be obtained by dividing the permittivity of material by permittivity of free space. $PbZrO_3$, $PbTiO_3$, BNT, BKT are examples of perovskites that have adequate values of dielectric constant. The dielectric constant for barium titanate is near about 1600 at standard conditions of temperature but a sharp increase to 6000 at 120^0C temperature. Noteworthy changes in dielectric properties takes place at both the curie temperature 120^0C and 5^0C because these are transition temperature where crystal structure of barium titanate deviates from rhombic to tetragonal and further to cubic arrangement[20].

1.3.2 Superconductivity

A variety of perovskites, when cooled underneath a definite temperature, displays the occurrence of precisely zero electrical resistance and undergo exclusion of magnetic flux fields, this process is known as superconductivity. The oxide perovskites provide a good structural framework for the existence of superconductivity. Perovskites having copper are high temperature superconductors. Sweedler et al. investigated super conductivity in sodium, potassium, ruthenium and cesium tungsten bronze. Superconductivity transitions were observed in three samples of reduced strontium titanate at 0.25K and 0.28K respectively. High temperature superconductors such as $YBa_2Cu_3O_7$, $Bi_2Sr_2Ca_2Cu_3O_{10}$ depicts a critical temperature range of superconducting transition

of around130-155K. $YBa_2Cu_3O_7$ has a critical temperature of 90K, well above liquid nitrogen's 77K temperature. $Bi_2Sr_2Ca_2Cu_3O_{10}$ has a critical temperature of 105K. DuPont et. al. firstly synthesized $Ba(Pb, Bi)O_3$ superconductors in 1973 and determined to have a Tc of 13 K.

1.3.3 Ferroelectricity

Whenever specific materials are exposed to external electric field, it leads to generation of abrupt electric polarization and this phenomenon is known as ferroelectricity**.** During World War II, ferroelectricity was discovered in barium titanate and other perovskites-based materials. It was seen that the ferroelectric materials have about twice dielectric constant as compared to ordinary dielectric. The discrete structural changes taking place at phase transitions, results in induction of ferroelectricity in materials[21]

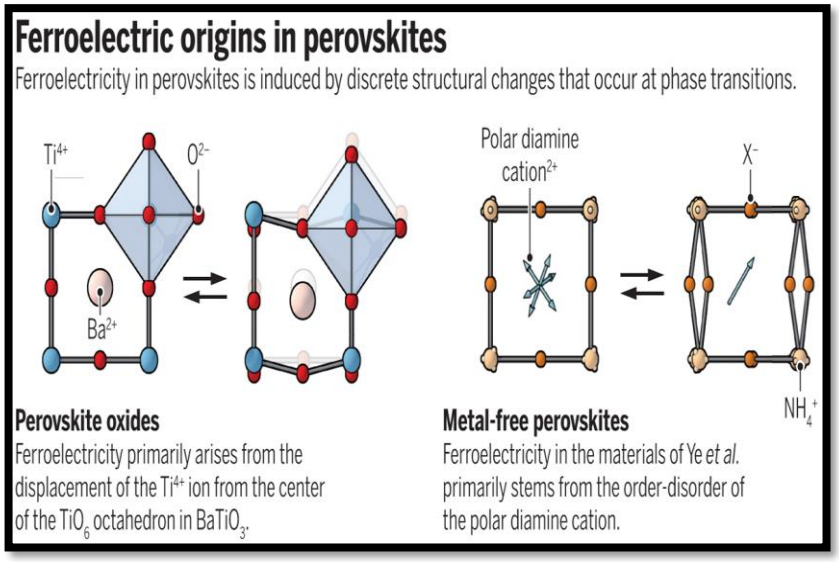

Fig 1.11 Ferroelectricity in Barium titanium oxide.

Example: ferroelectricity mainly arises from dislocation of Ti^{4+} ion from the center of TiO_6 octahedron in $BaTiO_3$. The widely recognized ferroelectric substance is $BaTiO_3$ having apparent dielectric constant of over ~2000. At ambient temperature and absence of external magnetic field, its crystals have no overall polarization, despite the alignment of dipoles in adjacent unit cells takes place. The unprompted polarization is caused by the arrangement of Ba^{2+}, Ti^{4+} and O^{2-} ions throughout the unit cell. Above 120^0C barium titanate is a cubic crystal. If crystal is allowed to cool, below the curie temperature (120^0C), shift in position of Ti^{4+} ion takes place to one side of body center. There is also a movement of neighboring anions (oxygen). At room temperature, the crystal undergoes a transformation from cubic arrangement to tetragonal phase[22].

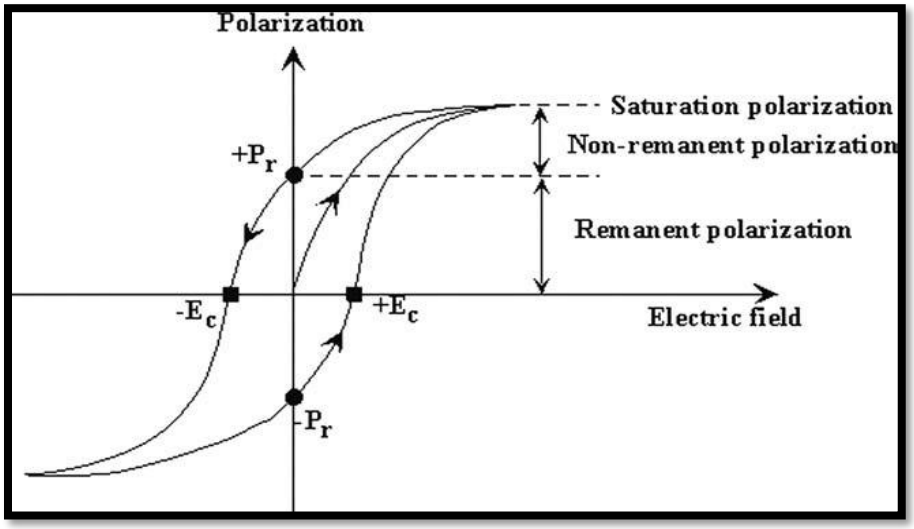

Fig 1.12 Hysteresis loop for a ferroelectric substance[23].

When electric field was applied, the domains get aligned in direction of field and this phenomenon has been studied by hysteresis loop. The unprompted polarization of perovskites entails the extrapolation of linear component of curve to the point where electric field tends to be zero.

Ferroelectric aspects assist in the manufacturing of sensors, capacitors and memory devices. Ferroelectric substances exhibit the feature of non-linearity, which is effectively used by tunable capacitors to alter the capacitance. Memory devices can benefit from the ferroelectric materials' hysteresis during spontaneous polarization.

1.3.4 Piezoelectricity

When mechanical stress was applied on certain substances, they have the capacity to produce an electric charge and this effect was revealed by Pierre Curie and Jacques Curie in 1995. It was found that when mechanical stress was applied on certain crystals, results in appearance of electric polarization with degree of polarization and it was noticed that the electric polarization was directly proportional to applied strain. The occurrence of inverse polarization effect was studied by Curie and observed that some specific materials get deformed when exposed to electric field.

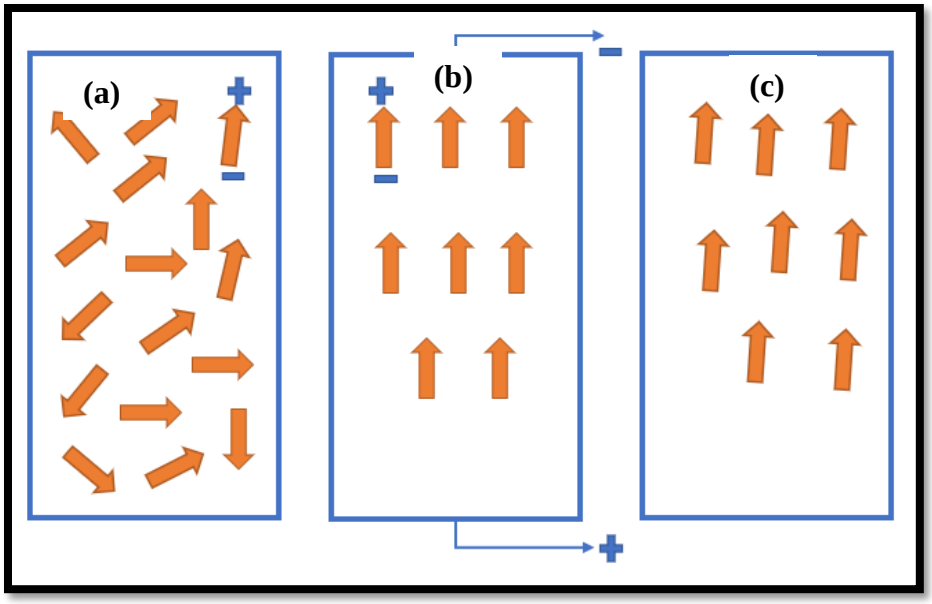

Fig 1.13 Piezoelectric ceramic polarization (a) random arrangement of polar domains before polarization (b) polarization in presence of DC electric effect (C) remanent polarization upon removal of electric field.

This property is shown by barium titanate, lead zirconate titanate, Lithium Niobate etc. In ferroelectric materials, electric dipoles align themselves by interaction with one another, while in piezoelectric substances there is need of some external force to align the dipoles. As a result, all ferroelectric materials behave as piezoelectric, but the reverse is not true. In addition to the previously discussed crystals, PZT is another significantly studied piezoelectric material. These materials have a crystal arrangement of tetragonal or rhombohedral which is closely similar to cubic.

These are polycrystalline ferroelectric materials. They are represented by the generic formula $A^{2+}B^{4+}O_3^{2-}$, where A depicts for a large metal cation (i.e., tetravalent), such as Ti, Zr etc. and B represents a divalent metal ion, like Ba and Pb.

Piezoelectric ceramics are the synthetic piezoelectric materials with perovskite arrangement depicting general formula A^{2+} B^{4+} O^{2-3}. Quartz (a mineral), cane sugar, collagen (a fiber), the mineral topaz, rochelle salt and tendon, acts as the naturally occurring piezoelectric materials. The piezoelectric property of perovskite materials has various scientific applications in lighters, sensors, microphones and high voltage power source.

Table 1.2 Piezoelectric coefficient of perovskites at room temperature[24].

Material	d_{33} (pmV^{-1})
BNT	15
$KNbO_3$	10.8
$LiNbO_3$	25
$NaNbO_3$	4
$BaTiO_3$	31.1
PZT (lead zirconate titanate)	117
PLZT(lead lanthanum zirconate titanate)	545
$BiFeO_3$	53
$BaSrTiO_3$	365
$BiNaTiO_3$	64

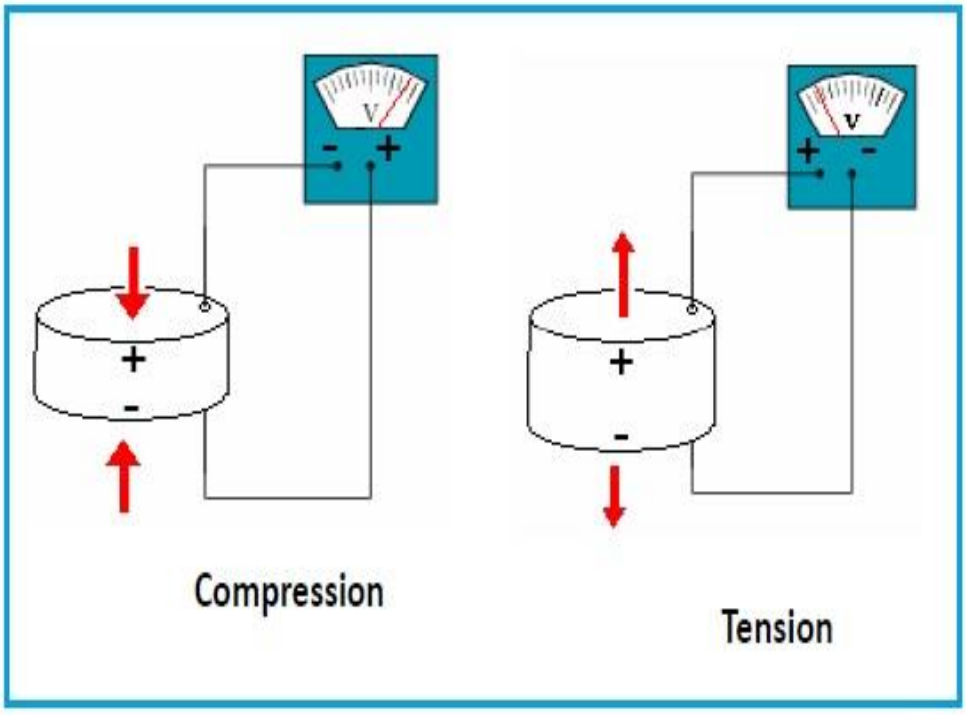

Fig 1.14 Schematic diagram showing Piezoelectric and reverse piezoelectric effect[24].

1.3.5 Multiferroicity

Multiferroics is a group of materials having synchronized ferroelectric, ferromagnetic and ferro-elastic assembling. In 1994 H. Schmid used the term multiferroic. In a single-phase material, there is a co-existence of magnetic and ferroelectric polarization, due to which multiferroics have prodigious scientific importance. The presence of asymmetry point groups facilitates an unexpected polarization that allowed the concurrent generation of natural ferroelectric and ferromagnetic moments. Fig 1.15 illustrates the multiferroic materials having consistent properties.

These materials have the unique property of concurrent employment of magnetization and polarization states, due to which these are significantly used for storage devices and sensors.

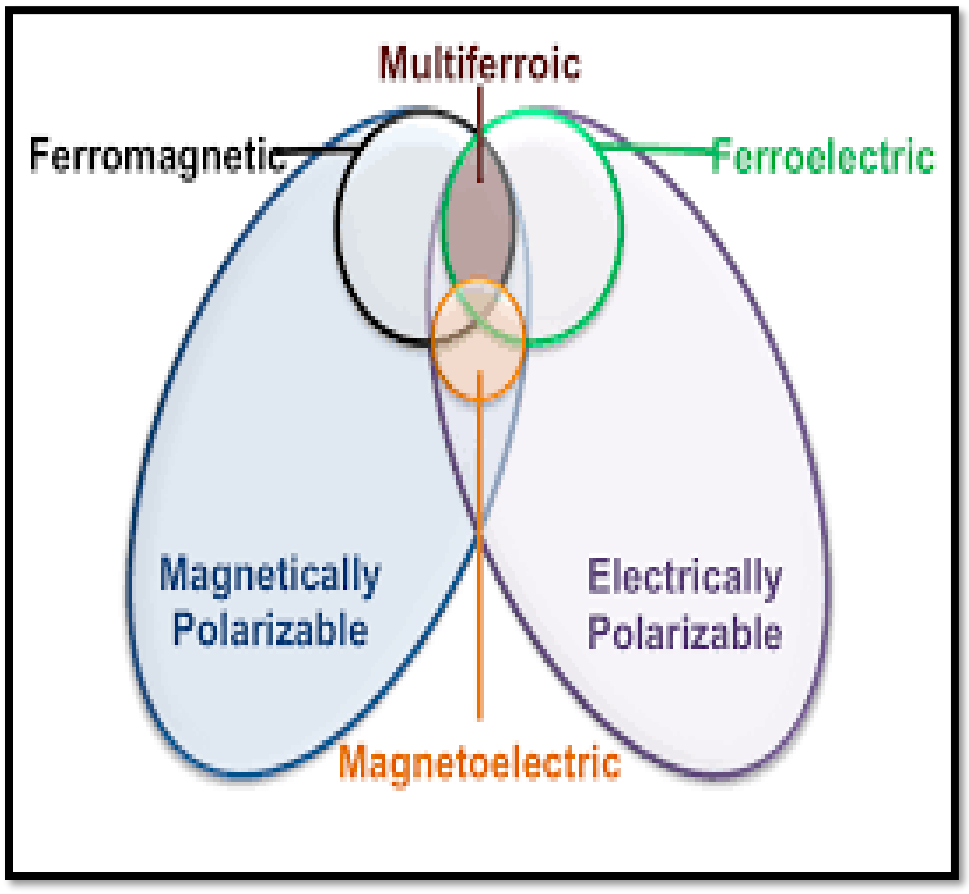

Fig.1.15 Magnetism in multiferroic materials[25].

1.3.6 Optical properties

Perovskite materials have arisen as an adequate group of substances showing outstanding optical and photoluminescence characteristics. It showed that single domain crystals of $BaTiO_3$ have good optical properties at various temperature. At 20^0C to 90^0C nearly a constant refractive index value of 2.4 was studied with a maximum value of 2.46 at 120^0C. It was found that single crystal of $BaTiO_3$ having 0.25mm thickness transmit from 0.5µ to 6µ. The optical properties of strontium titanate single crystal were studied with optical coefficient ranging between 0.20µ to 17µ with 310 dielectric constants. It was reported that the absorption characteristics of calcium titanate are analogous to those of $SrTiO_3$ crystals except the absorptions which exhibits a shift towards shorter wavelength.

$BaTiO_3$ and $SrTiO_3$ acts as efficient components for elevated temperature IR detectors, while $SrTiO_3$ is considered to be an outstanding material to be applied in infrared detectors[26].

Table 1.3 Properties of some perovskites along with applications.

Materials	**Properties**	**Applications**
$BaTiO_3$	Dielectric	Capacitor, sensor
(Ba, Sr) TiO_3	Pyroelectric	Pyrodetector
$PbTiO_3$	Pyroelectric, piezoelectric	Pyrodetector
Pb (Zr, Ti) O_3	Dielectric Pyroelectric Piezoelectric Electro-optic	Nonvolatile memory, Pyrodetector Surface acoustic wave device
$(Pb,La)(Zr,Ti)O_3$	Pyroelectric Electro-optic	Pyrodetector Optical memory display

1.3.7 Catalytic activity

Perovskites have been employed as a catalytic agent in numerous reactions because of excellent catalytic activity and high chemical stability. The high surface reactivity to reduce the oxygen or the abundance of oxygen vacancies, both are associated to the high catalytic activity of perovskites. Perovskites shown higher activity for direct decomposition of NO at high temperature ($2NO \longrightarrow N_2 + O_2$) and the elevated activity is attributed to the occurrence of oxygen deficit environment and removal of oxygen, present on surface, in the form of product. Perovskites established a significant impact as a superior catalyst. These perform as a very desirable photocatalyst in process of water splitting thereby producing hydrogen gas[27].

1.4 Synthesis of Perovskites

There are many different techniques that can be used to synthesize perovskites; however, they can mainly be splitted into two primary kinds:

(A) Bottom-up approach

(B) Top-down approach

1.4.1 Bottom-up approach

When the required precursors are put together in, they go through a controlled chemical reaction that results in synthesis of nanomaterials and the process is known as bottom-up method. Examples of bottom-up methods include the hydrothermal, sol-gel approach, chemical Vapour deposition method, microwave synthesis, and colloidal process, among others. This method offers improved control over particle shape, purity, quantity, quality and particle size[28].

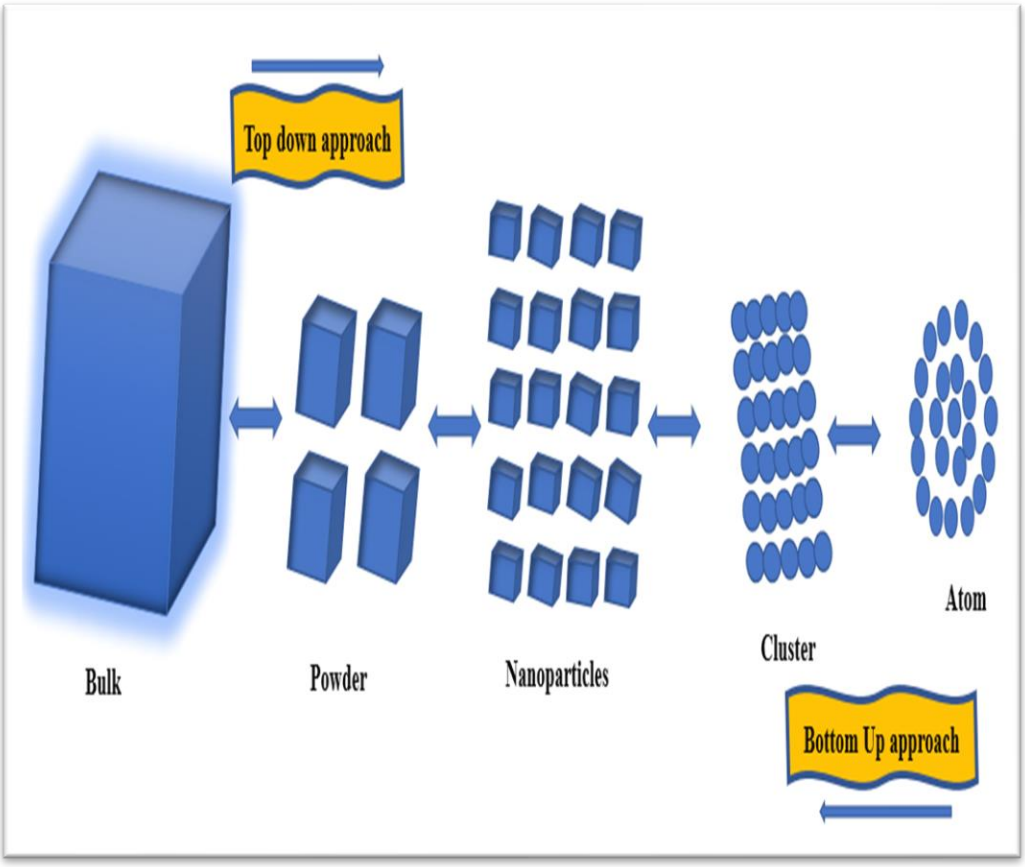

Fig 1.16 Representation of top-down and bottom-up schemes for nanoparticles preparation.

- Hydrothermal approach
- Sol-gel
- Co-precipitation technique
- Microwave synthesis
- Chemical vapour deposition method

1.4.1.1 Hydrothermal method

A low-cost approach known as the hydrothermal process uses a stainless-steel chamber known as autoclave for heating the aqueous solution of an insoluble salt. It is the most appropriate process regarding energy efficiency, cost effective and environmental sustainability. Nanocrystals of innumerable shapes such as cubic shaped, star shaped, nanowires, nanosheets, nanospheres and nanotubes can be produced by putting the aqueous solution of insoluble salts in autoclave and as the temperature rises precipitation occurs resulting in synthesis of nanocrystals.

For instance, Ao Xia. And his co-workers produced Bismuth titanate compound by making use of hydrothermal scheme. According to data, crystal development can be promoted by raising the temperature of reaction or extending the time duration. The SEM data demonstrate that with increasing reaction time, morphological structure of as-prepared nanomaterials alters from spherical to polyhedron with irregular shape. The compound exhibits a band edge gap of 2.76 eV, as seen via UV-vis DRS. Additionally, it was noticed that the diffraction peak intensity rise, as the reaction temperature raise, suggesting that increase in temperature is advantageous for facilitating the development of BTFO crystals. The quantity of BTFO crystals is infrequent and insufficient for testing when the reactions temperature is below 150ºC. As a result, the reaction temperature has an impact on BTFO crystal productivity besides to growth.

The impact of temperature on size of particles and morphology of Barium titanate nanocrystals has also been reported by Huei-Jyh Chen**.** The obtained powders by hydrothermal method had small crystal-like morphology with an agglomeration at 85ºC while at 130ºC, large (130nm) and nearly monodispersed nanoparticles were obtained. The effect of numerous Ti precursors on the properties of $BaTiO_3$ was examined. The study revealed that, particle size of Ti precursor greatly affects the size and shape of barium titanate nanomaterials.

When $BaTiO_3$ was synthesized utilizing anatase TiO_2 (Merck) as a precursor, it had the highest particle size after being produced at 120°C for 24 hours. When $Ti(OH)_4$ was employed as the precursor, the size of particles was about 0.1µm having a porous structure[29].

Similarly, Giovanna Canu et. al. investigated the significant developments on hydrothermal formation of strontium titanates perovskite. The key benefit of this solution-mediated precipitation technique is the ability to effectively control particle size, and morphology by adjusting physical as well as chemical parameters like temperature, concentration, pH, solvent composition, and the use of various precursors.

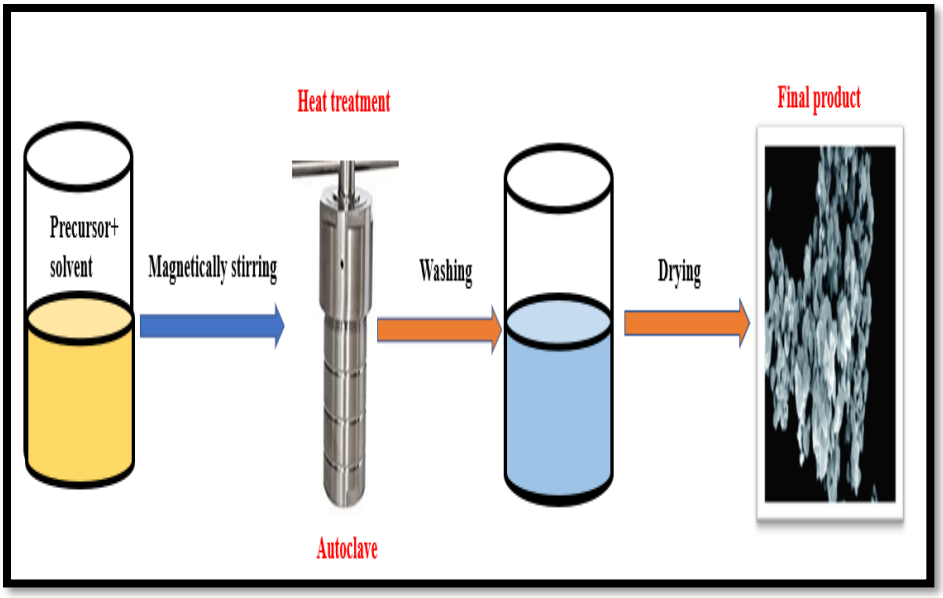

Fig. 1.17 Represents the hydrothermal technique of nanoparticles synthesis.

Particularly, the type and morphology of titanium precursor play a considerable role in hydrothermal crystallization since $SrTiO_3$ is frequently formed on the surface of precursor. The growth and nucleation of perovskite crystals, as well as dissolution of the precursor, are all related together over relatively short distances, and the solid/liquid interfaces play a role in this coupling. Thereby, the rate-controlling process, the nuclei surface density and the precursor/perovskite crystallographic matching all have an impact on the shape and morphology of strontium titanate nanomaterials. The formation of mesocrystals takes place by orientated accumulation of initial nanocrystals followed by Sr-Ti (amorphous gel-like precursors) crystallization in absence of crystalline surface[30].

1.4.1.2 Sol-gel method

A contemporary process to synthesize different perovskite oxides is the so-called sol-gel procedure. It is widely-known method for synthesis of uniform and nano range particles depicting high surface area. Numerous reaction parameters involving pH, solvent, temperature, catalyst and agitation, affects the morphological features of nanoparticles. It has been employed as a most appropriate method for synthesis of aluminates and titanates. Although, because of the formation of stable precursor, it is problematic to regulate the conformation of complicated oxides.

For example, L. V. Yafarova et. al. exploited sol-gel approach and synthesized an ultrafine perovskite powder of $GdFe_{1-x}Co_xO_3$ (where the value of x can be 0; 0.2; 0.5; 0.8; 1) having a grain

size of 40 to100 nm. The findings of XRD analysis of $GdFeO_3$ illustrates that, the oxide of Gd can be prepared by using citrate-nitrate sol-gel technique and there is no need of extra annealing. Single phase compounds having compositions of $GdFe_{1-x}Co_xO_3$ (where x = 0.2, 0.5, 0.8, and 1) could be generated via calcining the sample at 800°C up to two hours.

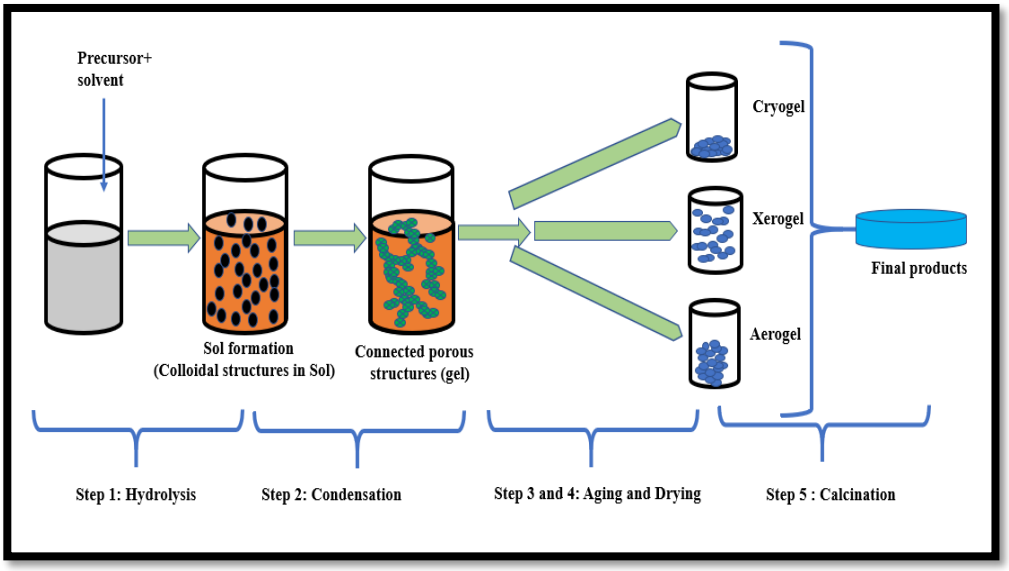

Fig 1.18 Sol-gel method for synthesis of nanoparticles.

Thermal analysis and XRD phase evaluation demonstrated that low-temperature conditions produce samples with porous surface. As a result, effective catalysts for the production of synthesis gas, based on solid solutions $GdFe_{1-x}Co_xO_3$ were developed using the sol-gel method [31].

Using a simple sol-gel and electrospinning process, consistent frameworks of strontium titanate ceramic fibers were created by J. H. Roque-Ruiz et. al. providing a different method for creating fibrillar membranes out of ceramics. Strontium nitrate and titanium tetraisopropoxyde were combined together to prepare two sol-gel solutions, which were then mixed and homogenized with a solution of polyvinylpyrrolidone which is polymeric in nature. The ceramic precursors produced green fibers with a diameter ranging from 140-180 nm. The shape of fiber was maintained at 1000°C, with a mean diameter of 103.39nm. Thermal investigation revealed that, at 800°C tetragonal titanium oxide phase changes to perovskite structure and this is known as the transition temperature. The precursor concentration had an impact on the shape and stability of the samples because higher concentrated solutions produced homogeneous and smooth fibers. Infrared and

Raman spectroscopy were used to identify the strontium titanate of the perovskite structure's distinctive bands. Tetragonal TiO_2 reduced and pure, crystalline strontium titanate was seen at 1200°C [32].

1.4.1.3 Co-precipitation

The coprecipitation technique involves mixing of more than two salts of water-soluble metal ions, often those that are divalent and trivalent. The soluble salts are primarily present in them as trivalent metal ions. These water-soluble salts go through a process and are reduced to create at least one precipitated water-insoluble salt. This approach usually results in particles with less crystalline character.

The nanostructured $HoFeO_3$ perovskites were synthesized by Co-precipitation of Fe^{3+} and Ho^{3+} ions in presence of ethanol, tailed through temperature treatment and this study was revealed by Anh Tien Nguyen and his research group. In lithium-ion batteries, $HoFeO_3$ acting as anode material demonstrated superior electroanalytical qualities including better capacity retention as well as Coulombic efficiency, good cyclability, less transfer of charges, high diffusion coefficient of Li^+, and superior rate.

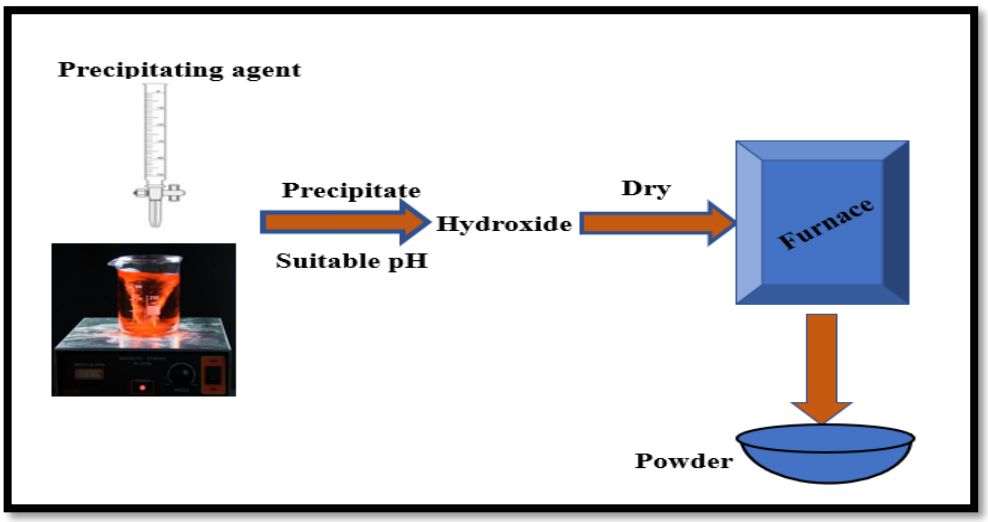

Fig 1.19 Co-precipitation method for preparation of nanoparticles.

At current density of 10 A/g (which is very high) provides the charge capacity of 299 mAh/g while afterwards 120 cycles at a reversible capacity, 437 mAh g^{-1} of charge capacity was shown at 0.1 A g^{-1} current density. The kinetics of the reaction was improved by higher

electrode/electrolyte interface and shorter diffusion length of Li-ion provided by nanosized materials [33].

M.A. Gadyal et. al. successfully produced Barium titanate nanoparticles via co-precipitation method. 0.1M Titanium tetrachloride ($TiCl_4$) and 0.1M $Bacl_2.2H_2O$ solutions were prepared in aqueous solution. XRD study reveals the crystalline nature of nanoparticles with tetragonal morphology, having particle size of 20.76nm. Similarly, another study was performed by S. Akbar et. al., $CaCO_3$, titanium dioxide and NaOH were utilized as the starting ingredients in a co-precipitation technique to create calcium titanate ($CaTiO_3$) powders with a perovskite structure. The impact of calcination temperature on morphology, phase development, and particle size distribution of suggested powders was examined. The dried gels were calcined at wide temperature range of 500°C, 600°C, and 700°C., The average size of the crystallite of $CaTiO_3$ calcined powder was 39 nm at 500°C, 36 nm at 600°C while 26 nm at 700°C. The size of crystallites reduced as the calcination temperature increased [34].

1.4.1.4 Microwave synthesis

Due to its unique characteristics, including quick reaction times, environmental friendliness, and energy efficiency, the microwave method has attracted attention for the synthesis of nanomaterials. To increase synthetic productivity, this method is typically combined with other techniques like hydrothermal, combustion, and sol-gel.

Another study performed by Upendra et. al. synthesized the Bismuth ferrite nanoparticles by simple microwave method results in production of typical nano cubes ranged in size from 50 to 200 nm. HR-TEM and a specified region electron diffraction pattern both verified that nano cubes are single-crystalline. Rhombohedral crystalline phase showing R3c space group was visible in X-ray diffraction pattern. The high-resolution TEM micrographs indicates that $BiFeO_3$ crystal have interplanar distances of d012= 0.397 nm and d006= 0.231 nm. $BiFeO_3$ cubes' capacity for photoinduced oxidation suggests that, it might be a valuable substance for photoelectrode and photocatalytic processes [35].

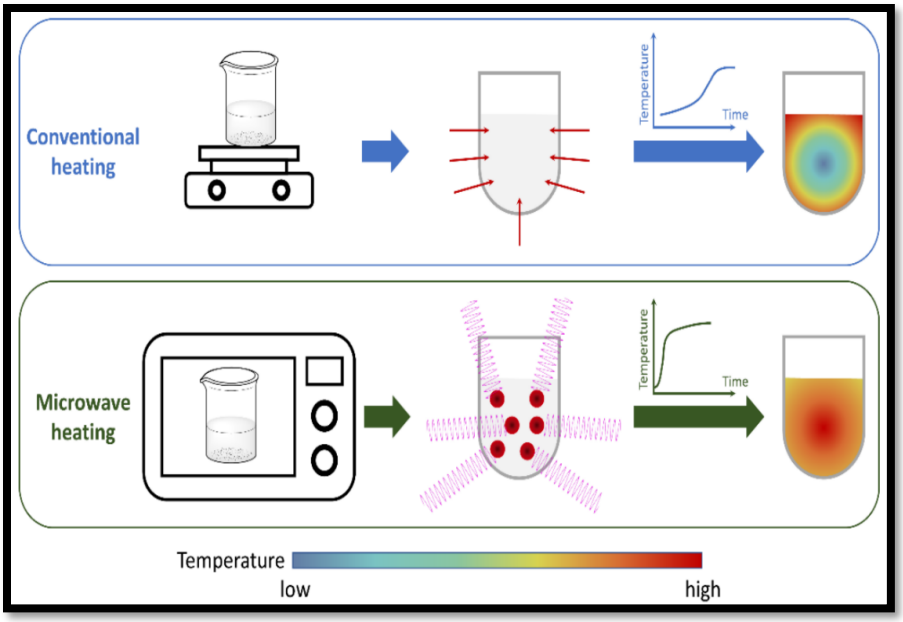

Fig. 1.20 Microwave synthesis of nanoparticles [36].

Mesoporous calcium titanate nanomaterials were produced by employing an easy single-source precursor method via microwave process and this study was done by Ravinder Pal et. al. According to Rietveld refinement, the phase, crystallite size and lattice strain enlarged as calcination temperature raised while the lattice parameters remained quite constant. Furthermore, nano powder produced using a microwave rather than an electric furnace had greater porosity. Additionally, compared to nano powder made in an electric furnace, the mean diameter of the capillary holes in nano powder made in a microwave was 25% larger. In conclusion, heating settings mainly impacted the calcium titanate nano powders' volume% of porosity, pore size distribution, and nanoparticle size distribution [37].

1.4.1.5 Chemical vapour deposition (CVD)

Apart from these techniques' CVD method has also been utilized for preparation of perovskites. For fabricating high quality perovskites, chemical Vapour deposition technique with excellent efficiency, better controllability and repeatability has been viewed as a cost-effective pathway. The properties like stability, structure, design of materials etc. of perovskites materials can be improved by synthesis from CVD technology. General steps for chemical Vapour deposition method: -Substrate should be pre-processed, after pre-processing of substrate, coating of TiO_2 layer on substrate, carry out spin coating, device drying.

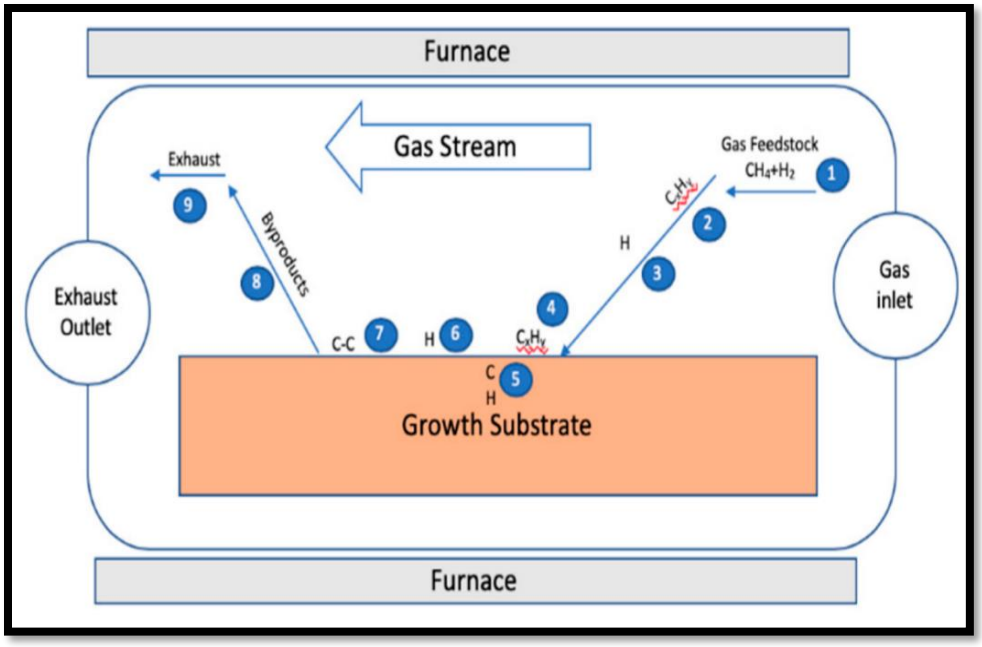

Fig 1.21 Chemical vapour deposition method for nanoparticles synthesis [38].

Xia Liu et al. synthesized photovoltaic films by various CVD technologies: atmospheric pressure and low-pressure CVD (APCVD and LPCVD) scheme were adopted for manufacturing high quality film materials of $CH_3NH_3PbI_3$ with large area. The conversion efficiency for sun light can reach up to 12.1% [39].

1.4.2 Top-down approach

- **Ball-milling**
- **Sputtering**

Atoms are broken down from larger solids into smaller pieces using this technique. Typical examples of a top-down strategy for synthesis of materials in nano range include mechanical grinding, also known as mechanical attrition, ball milling, sputtering and leaching. However, the most significant drawback of using this method is that it results in the breakdown of the nanomaterial's crystallographic structure, which leads to an imperfection of the surface structure.

1.4.2.1 Ball milling

This technique is also known as ceramic method because it has been utilized for synthesis of a wide range of ceramic materials. Raw constituents are required in form of carbonates or oxides. During this technique, at normal conditions of temperature, no chemical reaction takes place in

between raw components. While, when heated at elevated temperature range of 700 to 1500°C, the reaction proceeds at an extensive degree. Danks et. al. implemented the mechanical ball milling approach together with crushing, hand mixing, ball refining and fire of preparatory materials several times**.** For instance, the raw materials in oxides or carbonates forms are crushed, mixed manually, ball milled, and calcined at high temperatures.

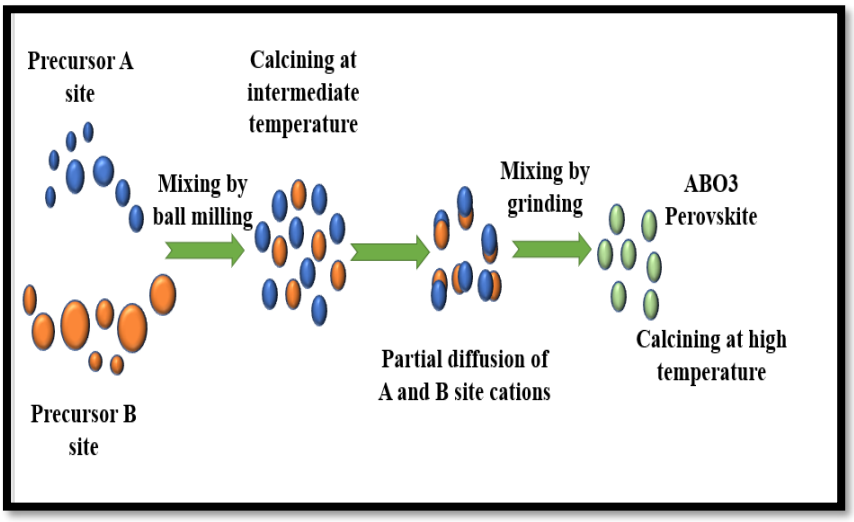

Fig 1.22 Steps in solid-state processing of ABO_3 perovskites.

1.4.2.2 Sputtering

A recently invented ecologically conscious technique, for preparation of metal oxide nanoparticles (NPs) is called sputter deposition on a less volatile liquid matrix. The combination of the sputter deposition and potential of the liquid matrix to control the development of particles, makes this technique tremendously advantageous. The size of particles, content, morphological features, and crystal structure of nanoparticle's can be controlled over an extensive range by controlling the synthesis constraints. For example, Morales et.al. applied radio frequency (RF) magnetron sputtering in an Ar/O_2 combination resulted in deposition of extremely textured and insulating thin films of $Li_zLa_{2/3+-y}TiO_3$ on MgO substrates for the first time.

These films contained lithium incorporated into their structural makeup. Rutherford backscattering spectroscopic analysis and nuclear reaction investigation were both utilized in order to ascertain the films' chemical make-ups.

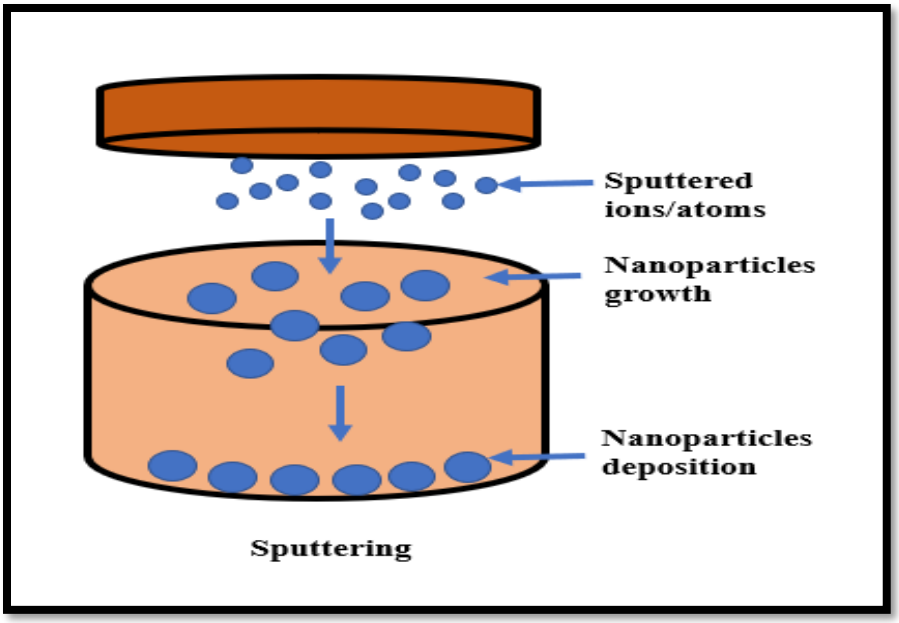

Fig 1.23 Synthesis of nanoparticles by sputtering.

The relationship of hetero-epitaxy is always the primary textural component that is always attained; however, several other textural components can generally be produced; these textural components are dependent on the composite materials of films and the conditions under which they were deposited [33].

1.5 Applications of Perovskites

Perovskites shows a variety of properties, forms a large number of compounds, have stable structure and shows structural diversity due to replacement of A and B site cations thus, acting as attractive nanomaterial for several practical applications. Perovskite oxides acts as better catalysts than other transition metals and precious metal oxides. Perovskites shows a variety of properties like superconductivity, dielectric behavior, ferroelectricity due to which they became precious for various applications such as: gas sensors, glucose sensors, adsorption of pollutants, capacitors, Photovoltaic cells, photoelectrochemical (PEC) cells, recording applications, Spintronics strategies, Laser applications, delivery of drugs, Catalysts in chemical industry.

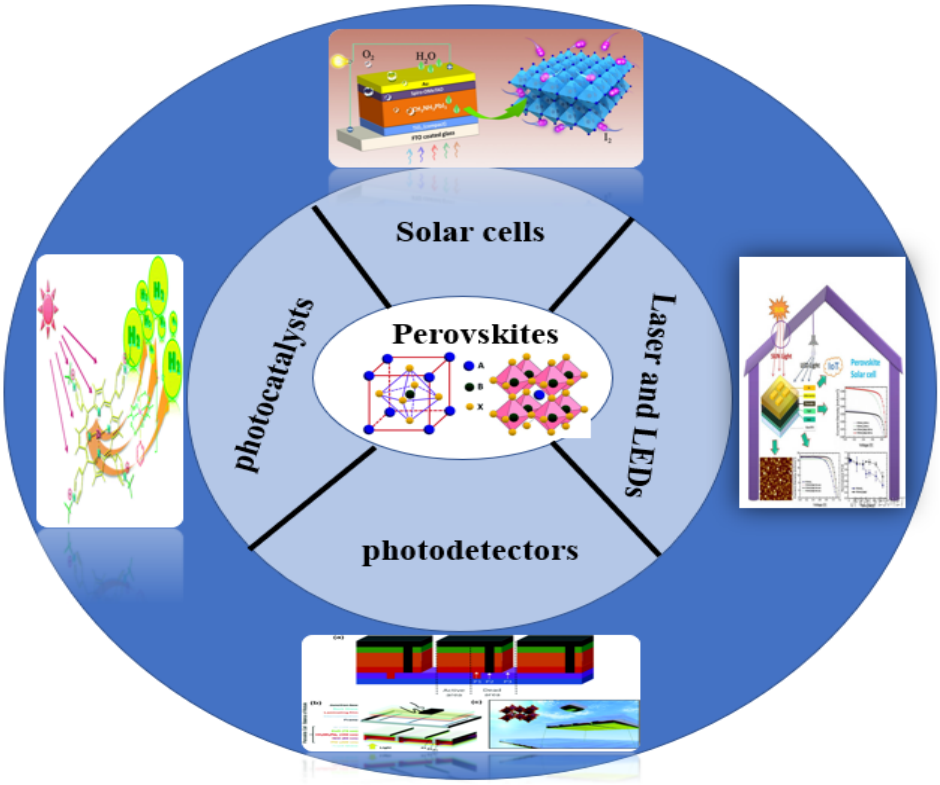

Fig 1.24 Applications of perovskites in different fields.

Currently, they have been utilized in monitoring and control of gaseous pollutants for air quality, electrochemical sensing of alcohols, also acts as glucose sensor, gas sensors, H_2O_2 sensitivity, exceptional reproducibility, exclusive long-term stability and neurotransmitters displaying decent selectivity, etc. Additionally, numerous perovskite oxides have been considered and showing worthy applications for growth of anodic catalysts used in fuel cells exhibiting superior catalytic activity. Some details of the applications are reviewed in the following.

1.5.1 Solar cells

In a short time period, perovskite based solar cells have attained considerable attention because of rapid progress by improvement in their solar cell efficiencies from 5.6% to 19.8%. Although, due to uncertainty of perovskite constituents in moist environment, the stability of these perovskites for long period is a big challenge. It was reviewed that the 2D perovskites were highly resistant against moisture as compared to 3D perovskites, thereby 3D perovskites got substantial consideration in previous years. The rapid progress in perovskite efficiencies have been shown in table 5. Solid-state methylammonium lead halide ($CH_3NH_3PbX_3$, X=Br, I) hybrid-based

perovskite solar cells garnered a lot of interest. This particular variety of solar cells exhibited useful characteristics, such as an efficiency of conversion of near about 20% and also cost-effective. These 3D organohalide perovskites demonstrated outstanding intrinsic characteristics for photovoltaic applications. Some of these properties include admirable stability, narrow band gap value (1.55 eV), high coefficient of absorption and this investigation was executed by Nada and his co-group[40].

Table 1.4 Distinctive performance of 2D perovskite solar cells[40].

Materials	**PCE (%)**	**Open voltage (V)**	**Short current density (mA cm^{-2})**	**Filled factor (%)**	**Stability**
$BA_2MA_3Pb_4I_{13}$	12.52	1.01	16.76	74.13	Null degradation up-to 2250 h with encapsulation under AM1.5G illumination
$PEI_2MA_6Pb_7I_{22}$	10.81	11.1	13.12	65	5% degradation after 500 h operation
$PEA_2MA_{59}Pb_{60}I_{181}$	15.36	1.09	19.12	73.7	88.7% degradation afterwards 60 days storage in a little humid environment
$PEA_2MA_3Pb_1I_{13}$	12.1	1.16	14.7	71	50% degradation after 1month storage in 45% humidity air
$PEA_2MA_2Pb_3I_{10}$	4.73	1.18	6.72	60	-
$BA_2MA_2Pb_3I_{10}$	4.02	0.929	9.42	46	-
$MAPbI_3$	14.6	1.025	18.84	75.4	>10,000 h showing no degradation beneath operation

It was observed that the effectiveness of Sn-based solar cells can be heightened by mixed 2D-3D perovskites. The activity of 3D tin perovskite based solar cells was enhanced by mixing of small quantity of layered tin perovskite thus inducing the higher crystallinity and also exhibits a precise orientation of 3D $FASnI_3$ and this study was conducted by Shao et al. Thus, the solar cell performance was improved by improving crystallinity and distinct orientation of crystals, acting as the primitive basis in enhancement of solar cell activity. However, in comparison to $MAPbI_3$ the energy alteration proficiency of fabricated solar cells is still low. The research and progress enterprises are being sponsored by the Department of Energy Solar Energy Technologies Office

(SETO) United States (U.S.) and trying to boost the efficiency as well as lifespan of hybrid perovskite solar cells with decreasing the manufacturing cost. But still now researchers are facing a number of challenges before the perovskite solar cells become a competitive commercial technology.

1.5.2 Photocatalysts

In recent years, perovskites have been employed as a promising photocatalytic material for generation of H_2 via water breakdown. For treatment of waste water, advanced oxidation process (AOPs) is the effective and most reliable technology. During water treatment perovskites are employed for the exclusion of organic pollutants, which comprises the production and usage of hydroxyl radicals (acting as oxidant), moreover initiating other chemical responses for destruction of organic pollutants. Photocatalysis is the process of excitation of electron from VB to CB of semiconductor by absorption of sufficient amount of energy.

On semiconductors surface, oxidation and reduction chemical reactions take place due to generation of electrons. Numerous photo-catalysts have been developed for hydrogen gas synthesis from water, such as TiO_2, ZnO, WO_3 were prominent semiconductors for generation of hydrogen but these were suitable only under UV light with a significantly broad value of band gap. The most often used photocatalyst is TiO_2 with reasonable cost and exceptionally immense efficiency for oxidation. Although, hydrogen production efficiency is still not so high due to quick recombination of photogenerated (i.e.electron-hole) pairs and less captivation in visible region of light.

Yahya et. al. studied $LaFeO_3$ for photocatalytic applications and found that it is a significant material in photocatalytic area. The narrow band of 1.86-2.36eV, environmentally friendliness and high stability of $LaFeO_3$ makes it a prominent semiconductor for water splitting and thus gained a lot of attention in photocatalytic field. Similarly, Zeynep Balta et. al. revealed $LaMnO_3$ (LMO) perovskite crystals exhibited good photocatalytic water splitting property. After integration with boron nitride quantum dots (BNQDs), a diminished recombination rate as well as a quicker migration of photogenerated carriers were attained. Likewise, the LMO@BNQDs catalyst confirmed hydrogen evolution of 146.78 mol/g, which was considerably high than the hydrogen production of LMO sample (89 mol/g)[41].

Various techniques were used to expand the catalytic activity of semiconductors like as doping with other metals thus improving surface areas and enhancing the charge transfer, developing heterojunction and light captivation. For illustration, porous lanthanum-titanium $La_2Ti_2O_7$ based perovskite materials were produced by Zhang W. et. al. in 2019 and they used Cetyltrimethylammonium ammonium bromide (CATB) as a reagent by adopting sol-gel scheme. The study of synthesized materials was performed on azophloxin dye. The researchers noticed that the specific surface area and crystalline arrangement of Lanthanum based titanate materials were strongly affected by the presence of CTAB. The UV-Vis analysis showed that after 180 min illumination of $La_2Ti_2O_7$, performed the reaction with 4 g of CTAB, nearby 95% of dye was degraded by generation of maximum number of hydroxyl radicals. The photocatalytic degradation efficiency declines from first to fifth cycle (100% to 91%) which was attributed due to loss of $La_2Ti_2O_7$ powder.

In 2020, Guan et.al. noticed that, the ternary composite of $LaFeO_3$ and Au nanoparticles on Cu_2O surface, are suitable photocatalytic materials for degradation of rhodamine B, furthermore the ternary composite shows better photocatalytic performance than bare $LaFeO_3$ and Cu_2O by conquering the mixing of electron-hole pairs. In one more investigation, $LaTiO_3$ particles were incorporated by Ag nanoparticles and tested for degradation of pesticides in waste water and the morphological analysis revealed an improvement in surface texture showing enhancement in light absorption in comparison to bare $LaTiO_3$. UV-Visible analysis revealed that 100% degradation of atrazine (a pollutant) takes place in 40 min of irradiation time [42].

Table 1.5 Perovskites as photocatalyst for waste water treatment [43].

Perovskite	**Co-catalyst**	**Pollutant**	**Time**	**% Removal**
$LaMno_3$	CTAB	Methylene Violet	315min.	95%
$LaTiO_3$	Ag	Atrazine	40 min	100%
$SrTiO_3$	rGO	Rhodamine B	40 min	94.5%
$LaMnO_3$	Ca	Methylene Blue	360 min	73%
$La_2Ti_2O_7$	CTAB	Azophloxine	180 min	65%

1.5.3 Laser and LED

In 1998, for the first time lasing in layered $(C_6H_{13}NH_3)PbI_4$ polycrystalline films behaving as perovskite materials was observed by T. Kondo and group. Successively, in 2014 G. Xing et. al. revealed that methylammonium based lead halide perovskite ($MAPbX_3$, where X can be Cl, Br, and I) thin films have good optoelectronic properties to perform laser applications. Several optical response structures like lasers Fabry–Pérot cavities (FPC), distributed feedback (DFB) gratings and whispering gallery cavities (WGM) were demonstrated by researchers for use of optically pumped lasers. It was reported that perovskite lasers (DFB CW) at 100 K are useful because of the distinctive optical and electronic properties including low defect density, large absorption coefficient and higher charge carrier mobility suitable for electrically pumped lasers.

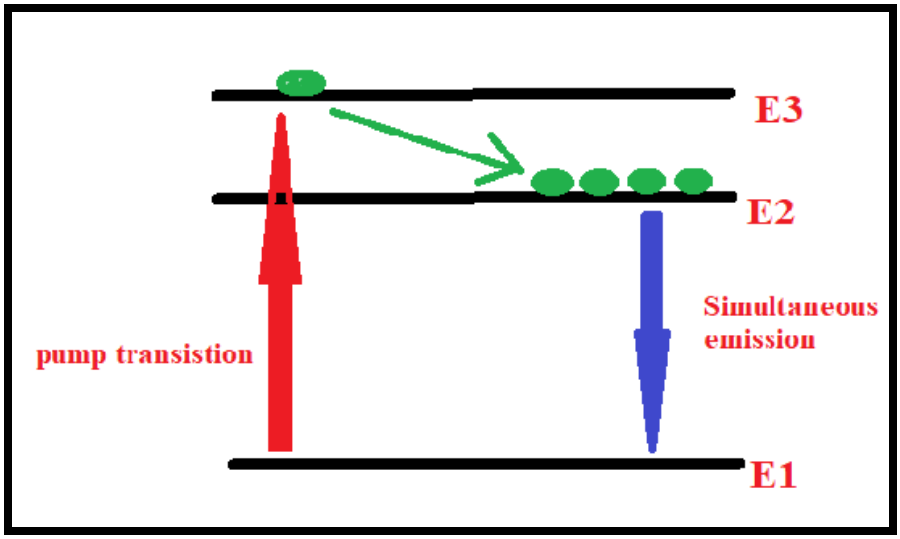

Fig 1.25 Representing three level system.

When optical pumping was performed, electrons from low level valence band (E1) gets excited to high energy conduction band (E3) thereafter these electrons lessen to the conduction band (E2) resulting in recombination with holes present in valence band. A very high intense excitation density has been achieved when half of electrons from E1 gets excited to E3 subsequently relaxing to E2 resulting in a high lasing threshold.

Many researchers observed that 2D perovskites have gained attention due to their better working efficiency in LED devices at ambient conditions of temperature although external quantum

efficiency was not much better. The strong light emission was observed in deep blue LEDs created on $2PbBr_4$ nanoplates and this work was analyzed by Liang and his group. The 0.04% of external quantum efficiency (EQE) was observed with a narrow FWHM of 14nm. Dimethylformamide was used as solvent via Vapour annealing resulting in enhanced EQE due to alteration of polycrystalline PEA_2PbBr_4 films into single-crystal nanoplates as shown in figure 1.25[44].

1.5.4 Photodetectors

Metal halide lead perovskites are suitable semiconductors to act as photodetectors showing extinct characteristics like high absorption coefficient and excellent charge carrier mobility.

Table 1.6 Photodetection ability of different perovskites[45].

Materials	Bias Voltage (V)	Light Wavelength (nm)	Responsivity (AW^{-1})
$MAPbI_3$ microplate	5	488	7
Monolayered$MAPbI_3$ sheet	1	405	22
$MAPbI_3$ nanosheets	5	532	12
$CsPbBr_3$ nanosheets films	10	517	0.65
$CsPbBr_3$ nanoplatelet	15	442	34

Furthermore, remarkable photo sensing properties were shown by 2D inorganic perovskites. Song et. al. revealed that $CsPbBr_3$ materials showed good stability and remarkable flexibility. They developed ultra-thin sheets of 1 to 3 layers and flexible photodetectors were fabricated on polyethylene terephthalate (PET) substrates. Thin films based on $CsPbBr_3$ has been spread on indium tin oxide acting as electrode, by adopting centrifugal casting method. When 10 V bias voltage was applied, 0.65 AW^{-1} responsivity was observed at 517nm. The ultra-fast photo response was exhibited by photodetectors with rise time of 19ms and the observed decay time was 25ms. The photodetectors showed a low responsivity which might be due to small lateral size of the synthesized nanosheets.

1.6 Water splitting

Over 70% of total earth's area has been occupied with water, making it a desirable and different energy supply when it is recycled back into nature. By producing hydrogen, it is possible to generate energy without using liquid or fossil fuels. The earliest and most abundant element in nature is hydrogen, which is also the simplest element in the periodic chart. It has a high energy storage capacity of near about 119 kJ/g and a very high heat of combustion of 34.19 kcal/g. Given its large capacity for storing energy, it might be burned as fuel to provide energy for the desired mechanical processes. Except for water electrolysis, the industrial processes for producing hydrogen from coal gasification, steam methane reforming, and water electrolysis all yield CO_2 or other byproducts that contribute to the "greenhouse effect." Hydrogen produces water Vapour when it burns as fuel or oxidizes. As a result, it might be utilized as clean fuel. Water splitting reaction is the breakdown of water into its atomic components, that are hydrogen and oxygen, using energy sources such as electricity, photons, and heat. It takes some energy to carry out this reaction because it is thermodynamically uphill. This involves a slow reaction kinetics multi-electron transfer mechanism.

Scientists have been looking for a method to fragment water to synthesize hydrogen, since the 1950s. Water splitting is an "uphill" endergonic progression in terms of thermodynamics. This reaction, which has a standard redox potential of 1.23 eV and having a Gibbs free energy of +237.2 $kJmol^{-1}$, is not spontaneous at ambient temperature and pressure.

Both solar energy and water are present abundantly on earth's surface and renewable. So, these both sources can be employed for energy generation. Water can be splitted by making use of solar power in presence of photocatalyst resulting in production of fuel known as solar hydrogen which can be utilized in fuel cells. Though, the transportation of hydrogen is not so easy due to its high flammability but in comparison to electricity transportation of hydrogen by pipelines is more efficient, which can be of great importance in near future[46].

Currently, the application of solar energy in photocatalysis and photovoltaic cells has fascinated substantial and growing attention.

1.6.1 Types of water splitting reaction:

The following categories could be explored based on sources of energy methods[47](Figure 2.1):

(1) **Electrocatalytic:** In this technique, an electrochemical cell's electrode is subjected to a set potential window in order to break the activation energy barrier and separate water into hydrogen and oxygen.

(2) **Photocatalytic:** This entails the employing of a source of illumination that can generate photons and are able to overcome the energy gap required to facilitate the production of hydrogen from water.

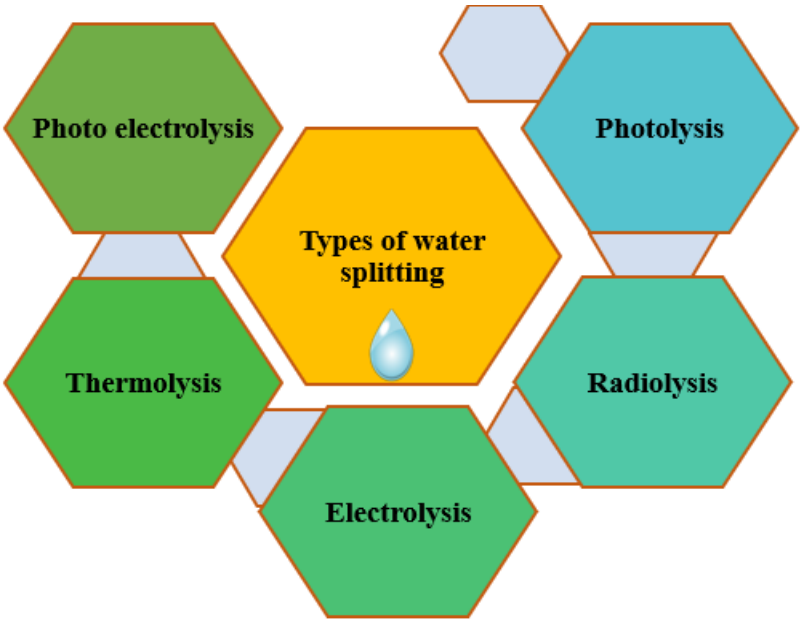

Fig 1.26 Types of water splitting reactions.

(3) **Photo electrocatalytic:** It is also known as artificial photosynthesis. In this method, solar light has been used for splitting of water by using photoelectrochemical cell.

(4**) Thermolysis:** If the splitting of water takes place at elevated temperatures the process is known as decomposition of water by thermocatalysis. At high temperature thermal decomposition of water can be performed by solar concentrators and catalysts.

(5) **Radiolysis:** In this method radioactive irradiation is utilized for breakdown of H_2O molecule into its components, i.e., hydrogen as well as oxygen, called radiolysis.

Amongst several technologies of solar power conversion into more usable forms of energy, considerable interest has been paid to water splitting by photocatalyst for its potential significance in producing clean and high energy in form of hydrogen directly from water [48]. In photocatalysis, water molecules are splitted by suitable photocatalysts in presence of light. Consequently, two step processes i.e. H_2 and O_2 progression, are involved in water splitting reactions. The photocatalytic splitting of water is most beneficial due to following reasons:

- Because both solar energy and water are renewable.
- Size flexibility and purity of hydrogen.
- No carbon-dioxide emission takes place.
- High sun light to hydrogen conversion efficiency.

In this method, there is requirement of a good photocatalyst having suitable band gap of 1.8ev to 3.5ev for better absorption of light in visible spectrum.

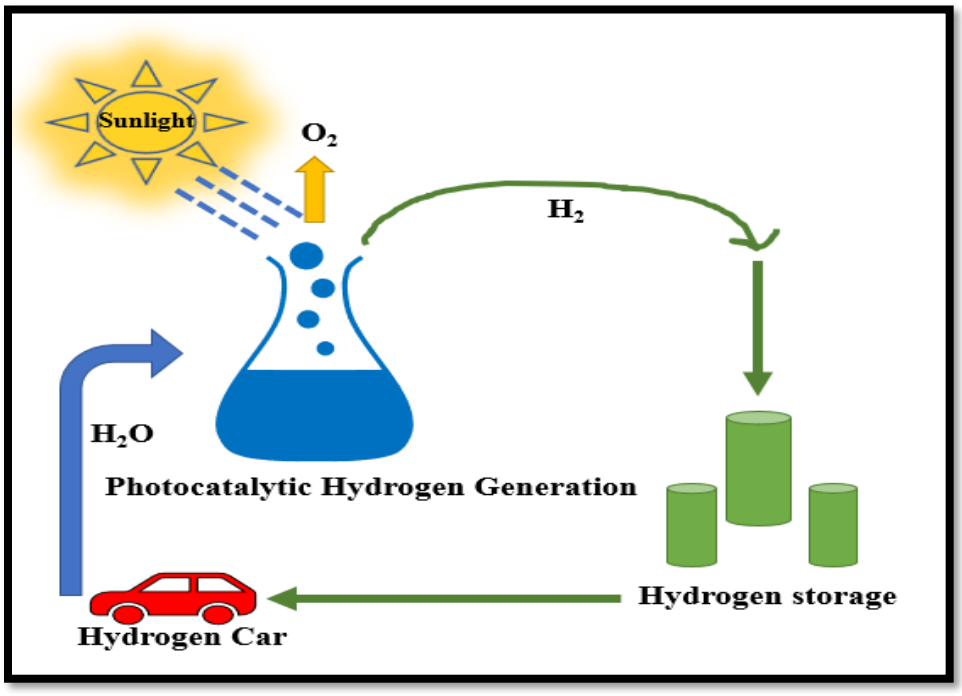

Fig 1.27 Hydrogen production presence of sunlight and its use.

1.6.2 Photocatalytic splitting of water and its theory

In 1972, Honda and Fujishima discovered the solar water breakdown by using crystalline TiO_2 as photoanode while Pt acts as cathode. Generally, semiconductor compounds are used as heterogenous photocatalysts because these are present in diverse phase with reactants throughout photocatalysis reaction.

Usually, the progression of photolysis is carried out by two approaches: (i) Photo electrolysis by utilizing PEC cells (ii) through photolysis employing powdered photocatalysts like TiO_2, $PbTiO_3$, $CdTiO_3$ etc.

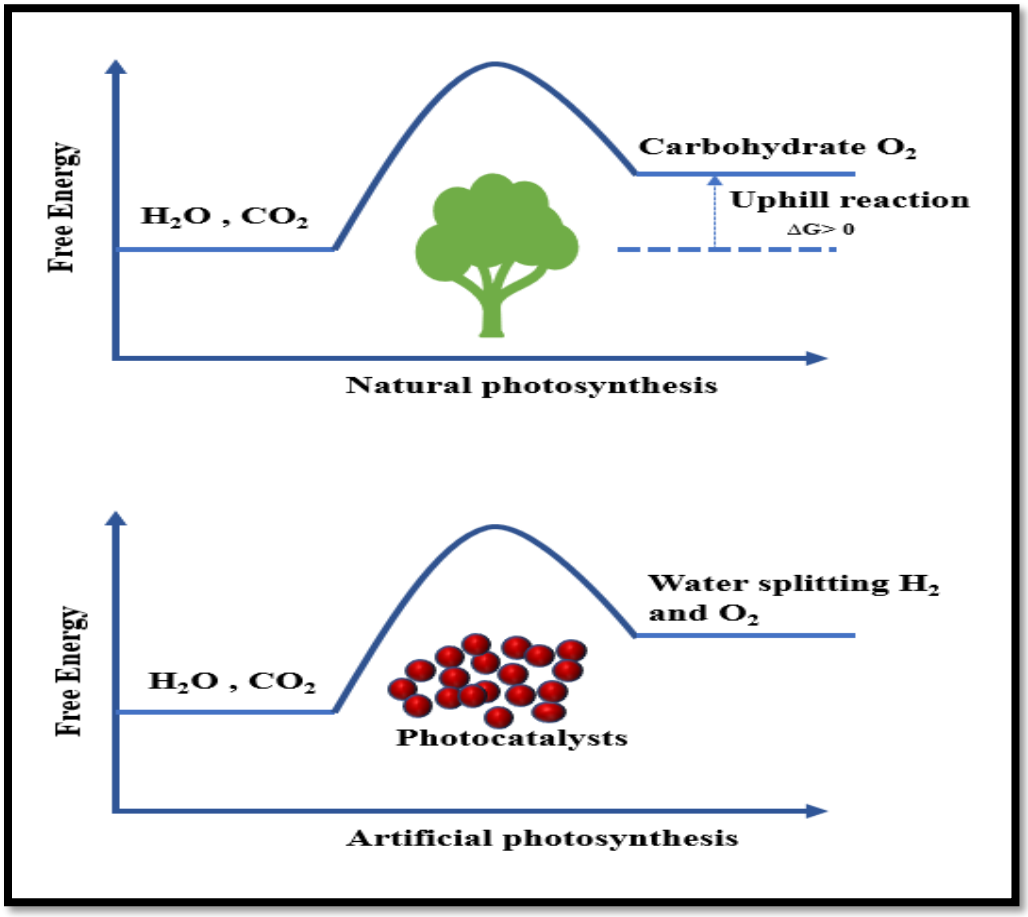

Fig 1.28 Process of natural and artificial photosynthesis.

In order to produce fuel from carbon dioxide and water, sustainable artificial photosynthesis technologies have been developed mimicking the natural photosynthetic process and known as

artificial photosynthesis. Figure 1.28 depicts a graphical representation of a hypothetical production and utilization facility of hydrogen [49].

1.6.3 Basic reaction mechanism

The electrons from low lying valence band can be promoted to conduction band, only when the energy of incident light is larger than the band gap of material, which accelerates the separation of electrons and holes. Thereby, resulting in release of H_2 and O_2 by directly reacting with water molecules.

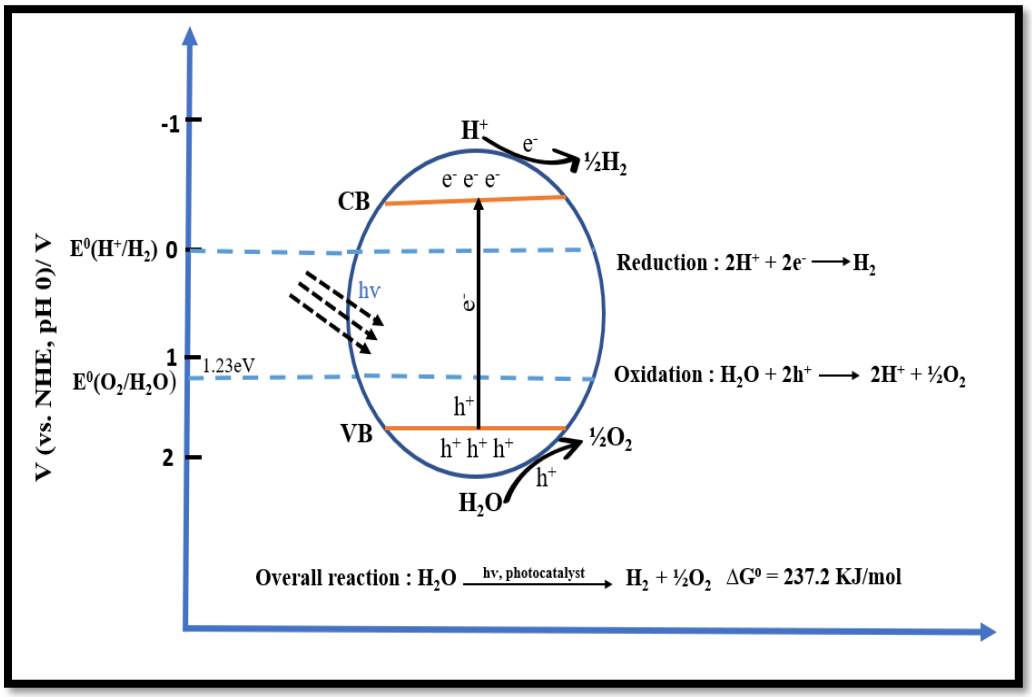

Fig 1.29 Basic mechanism of water splitting reaction.

The significant facts for water splitting are-

- Narrow band gap
- Potential of conduction band
- Valence band.

Most of the proposed methods for producing hydrogen are costly and exhibit low effectiveness when used on big scale. It has been suggested that significant advancements could be made using

biological schemes (plants, algae, and bacteria) or catalysts (semiconductors), while these technologies are least researched.

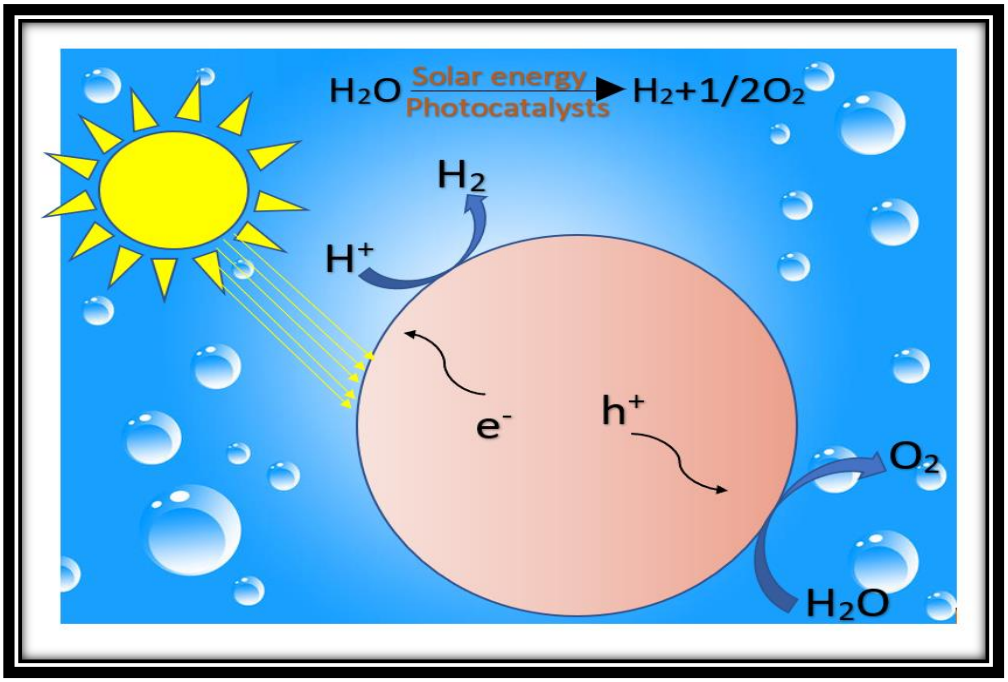

Fig 1.30 Photocatalysis reaction under sunlight.

Photocatalysts or photoactivated semiconductors deals with the substrate (water) to speed up the reaction and create photoproducts (H_2 and O_2). Sunlight radiation can be used to activate photons. However, chemical equilibrium might prevent this reaction from happening. To enable the photocatalytic reaction to undergo and produce the desired photogenerated products, such as hydrogen, photocatalysts are needed[49].

$$2H_2O + 2e^- \longrightarrow H_2 + 2OH^- \qquad E_O = 0.00V$$

$$2OH^- \longrightarrow 1/2O_2\,(g) + H_2O + 2e^- \qquad E = 1.23V$$

In conclusion, three (3) essential elements must be present for water splitting to form hydrogen:

I. A semiconductor (photocatalyst);
II. a light source
III. Water

The incident photons must have energy larger than band gap of photo catalyst. The required band gap for water splitting is 1.23eV. Photoelectrochemical (PEC) splitting technique by employing photo electrode is the greatest way for water splitting in presence of sun light. Numerous PEC cells

have been produced for solar splitting of water with adequate band edge potential as well as overall good stability. Visible light region is the main component of light spectrum, therefore prime goal of water splitting in presence of sun light, is to develop photo catalyst with effective visible light response.

1.7 Photocatalysts

Numerous photo-catalysts have been developed for hydrogen manufacturing from water in presence of sun light, such as TiO_2, ZnO, WO_3, $SrTiO_3$, $PbTiO_3$, $NbTiO_3$ etc. but there is a problem with these photocatalysts is that not showing good absorption of light in visible region therefore having low conversion efficiency of solar light. Furthermore, these have limited solar to hydrogen conversion efficiency because of having broad band gap, quick recombination of charges, and poor absorption of visible light. Particularly, water splitting is enabled by specific oxide materials with electrical configurations of d^0 or d^{10}.

The above said photocatalysts were thought to be efficient semiconductors for synthesizing hydrogen but these were suitable only under UV light. Researchers are trying to enterprise appropriate photocatalyst which functions under visible light and fulfill the requirements of tunable band gaps and excellent charge separation [50]. To successfully accomplish the photocatalytic reaction, semiconductors must fulfill the following criteria:

- A band gap above 1.23 eV for photocatalytic water splitting to be thermodynamically advantageous.
- The band gap energy positions should be $E_{cb} > E_{red}$ and $E_{vb} > E_{ox}$, respectively, greater than the electrolyte's redox potential.

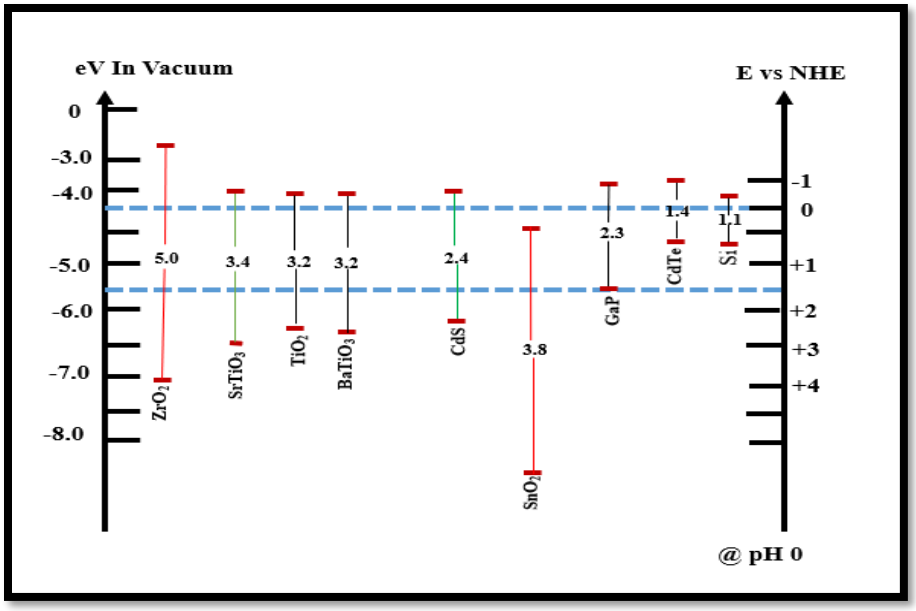

Fig 1.31 Band gap of photocatalysts suitable for water splitting reactions.

- ❖ The mobility of charge carriers should be sufficiently high to migrate on photocatalysts surface.
- ❖ The photocatalyst must be stable under illumination and undergo less charge carrier recombination.

1.8 Strategies to develop efficient photocatalysts

For photocatalysis, numerous perovskite materials are active in UV region owing to their wide band gaps, while others are visible light active because of their narrow band gaps. Just 4–6% of the solar spectrum accounts for UV radiation, whereas visible light spectrum covers contributes for around 43% of total solar radiations. For this reason, researchers are eager to produce materials whose absorption begins in the visible part of solar spectrum. Several techniques were established over the recent years to generate and produce effective visible light photocatalysts. The most popular approaches are:

1. Element doping
2. Catalyst loading
3. Surface modification technique
4. Band gap engineering of photocatalyst

5. Heterojunction formation

1.8.1 Element doping

Doping involves replacement of cation or anion with other elements. Band structure can be affected by doping and due to introduction of new forbidden band level; band gap decreases. The effect of Rh doping on $SrTiO_3$ was studied by Peichuan Shen et. al. and noticed the photocatalytic activity for hydrogen evolution. Three samples were prepared by polymerizable complex method having different concentrations of Rh (0, 1 and 5mol%). It was observed that doping of up-to 5mol% of Rh cations did not introduce impurities. Only a small structural change occurs due to similar ionic radii of Rh^{4+} (60.5pm) and Ti^{4+} (60pm). Results were compared for three photocatalysts with different loading concentration. $SrTiO_3$: Rh (1mol%) had the highest hydrogen evolution rate prepared by polymerizable complex method [51]. Similarly, He Yu Jiajia et. al. successfully synthesized Cr; B co-doped- $SrTiO_3$ by adopting hydrothermal method.

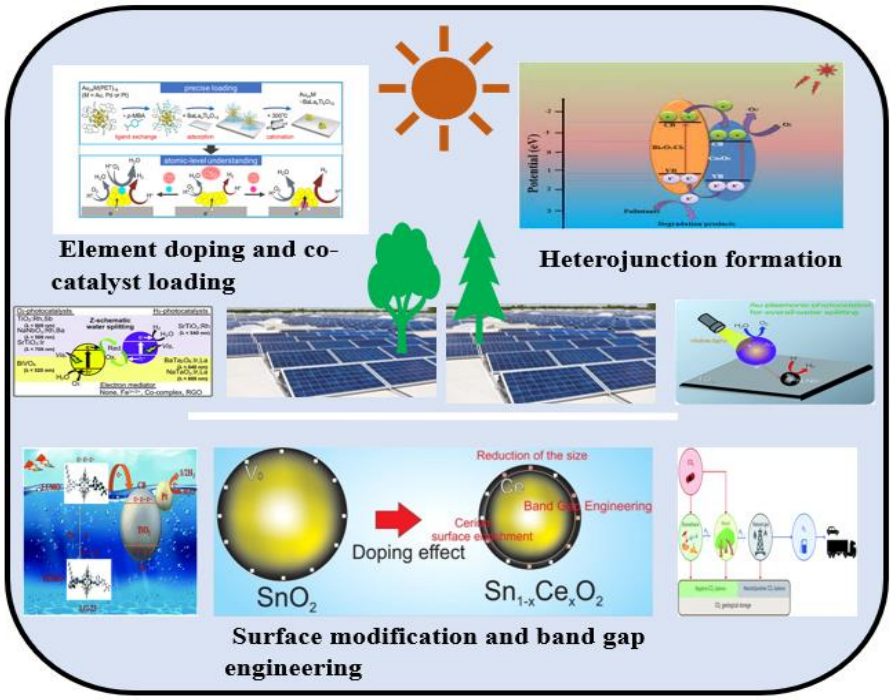

Fig 1.32 Various strategies for development of efficient photocatalysts.

Characterization results showed that Cr, B co-doped- $SrTiO_3$ had a smaller band gap of 2.07ev as compared to Cr doped $SrTiO_3$, which is due to strong interaction of Cr 3d with B 2p levels leading to stronger visible light absorption. The photocatalytic activity of both samples (Cr, B co-doped-

$SrTiO_3$ and Cr doped $SrTiO_3$) was compared. It was observed that hydrogen evolution rate of Cr, B co-doped- $SrTiO_3$ was higher (15.4µmol/h) as compared to Cr doped $SrTiO_3$ (9.3µmol/h). The higher activity of Cr, B co-doped- $SrTiO_3$ is due to its smaller band [52].

Cr-Ta: $SrTiO_3$ co-doped materials were synthesized by spray pyrolysis method. Photocatalytic activity was measured for hydrogen evolution under visible light. The powder was dispersed in 20vol% aqueous methanol solution forming a concentration of 5g/l. Xe lamp of 300W was used as a light source with a wavelength of 415nm. Results were compared by taking different concentration of dopants i.e., Cr/Ta-0.2 mol% and 0.4 mol%. Doping of Cr and Ta ions was done into the crystal lattice of $SrTiO_3$, replacing 2 ions of Ti^{4+} by Cr^{3+} and Ta^{5+} ions due to similar ionic radii. When 0.2 mol% of dopant was used hydrogen evolution rate was higher as compared to 4.0 mol% dopant. If polymeric additives were used as precursor solution in place of aqueous solution, better results were obtained having higher hydrogen production rate.

Table 1.7 Performance of titanate -based perovskites obtained by doping.

S.no.	Material	Synthesis method	H_2 evolution rate	Ref
1.	Rh: $SrTiO_3$	Polymerizable complex	47µmolh^{-1}	[74]
2.	Cr: $SrTiO_3$	Hydrothermal	9.3µmol$g^{-1}h^{-1}$	[79]
3.	Cr-Ta: $SrTiO_3$	Spray pyrolysis	211.4µmol $g^{-1}h^{-1}$	[79]
4.	Au-Al: $SrTiO_3$	Solid-State	347µmol$g^{-1}h^{-1}$	[80]

Dilara et. al. prepared Au/Al – $SrTiO_3$ by solid-state method to test the visible light splitting activity. First of all, Au/$SrTiO_3$ was prepared via solid state reaction. Homogeneous deposition precipitation method was used for Au loading. Three different solutions of methanol (10%), ethanol (20%) and isopropyl alcohol (30%) were taken to investigate the effects of Au and Al doping. The performance of methanol and isopropyl alcohol was found to be better than ethanol. For methanol 0.25% Au and 1% Al loading was beneficial. While for isopropyl alcohol 0.5% loading of Au and 1.5% loading of Al was advantageous. Hydrogen production rate by Au/Al –

$SrTiO_3$ was found to be higher due to increase in band energy of $SrTiO_3$ by Al doping. Al was found to be loaded as 30-40 nm particles by SEM [53].

1.8.2 Catalyst loading

Metals or oxides of other materials acting as cocatalysts, were loaded on perovskites to prevent the electron-hole recombination. Catalyst loading does not change the perovskite's structure. Loading occurs only on the surface of perovskite as a dispersion of nanoparticles. For example, Duc Nguyen et. al. loaded Cu on $SrTiO_3$ via photo-deposition method. $Cu/SrTiO_3$ showed higher photocatalytic activity for hydrogen evolution. Metallic copper was homogeneously loaded on surface of $SrTiO_3$. The efficient separation of electron-hole pairs was responsible for higher hydrogen production showing that metallic copper is an effective alternative to Pt as a co-catalyst. Cu acts a good co-catalyst because of low cost and chemical stability. Rate of hydrogen evolution of 0.5wt% $Cu/SrTiO_3$ was efficient to enhance the photocatalytic activity.

Similarly, P. Ilanchezhiyan et. al. described the synthesis of Neodymium (Nd) based perovskite ($Nd_{1-x}Co_xFeO_3$) nanostructures via hydrothermal method. In order to observe better photocatalytic and PEC processes, Co doping showed an enhanced absorbance concluded in the visible region. Here, the E_g of $Co/NdFeO_3$ (NCFO) decreased from 2.18 eV of $NdFeO_3$ (NFO) to 2.05 eV (visualised by alteration in the band edge). The improved photocatalytic splitting of water in NCFO upon successful addition of Co may also be associated to enhanced solar to hydrogen conversion proficiency. By preventing recombination of electron-holes, this characteristic enhances the process of transfer of charge with the nearby O_2 molecules, hence strengthening the photocatalytic process. The photocurrent density measured by the NFO at 0.83V was 0.8 A/cm^2 while NCFO photoelectrodes at 0.66 V shows 105 A/cm^2 of photocurrent density.

Rh was used as a co-catalyst for $SrTiO_3$ by Tarek Alammar. Co-catalyst was loaded with 0.025wt%. Rate of H_2 evolution was found to be enhanced due to increase in surface activity. Photo-deposition method was used for loading [54]. Su et. al. prepared multijunction $SrTiO_3/TiO_2$ nanotube. They doped TiO_2 by hydrothermal method. Due to different redox potential of materials, enhancement in visible light response takes place. A special band formed in depleted region caused by TiO_2 nanotubes.

Table 1.8 Co-catalyst loading on H_2 production rate.

S.NO	Material	Synthesis method	H_2 production rate	Ref
1.	Cu: $SrTiO_3$	Sol-gel and photo-deposition	395µmolh^{-1}	[81]
2.	Rh: $CaTiO_3$	Ultrasonic/photo-deposition	888 µmolh^{-1}	[81]
3.	TiO_2/$SrTiO_3$	Hydrothermal	3513 µmol$h^{-1}g^{-1}$	[82]
6.	La/$NaTaO_3$	Sol- gel	26940 µmol$h^{-1}g^{-1}$	[82]
7.	$NaTaO_3$/Ta_2O_5	Electrospinning, Sol-gel	1579 µmol$h^{-1}g^{-}$	[82]
8.	Ba doped $SrTiO_3$/ CdS	Solvothermal	1816.8µmol$h^{-1}g^{-1}$	[82]
9.	AgCl/Ag/ $CaTiO_3$	Hydrothermal / chemical deposition	226.5 µmol$h^{-1}g^{-1}$	[82]

Recombination of photogenerated e^- - hole pairs was prevented due to formation of a conduction band that can accept excited electrons from valence band of $SrTiO_3$. The Pt coating amount of multijunction photocatalyst was 5wt% while 0.2wt% of $SrTiO_3$/TiO_2 nanotube was taken. The excessive amount of catalyst can prevent the light from reaching the photocatalyst thus, reducing the hydrogen evolution rate. However, taking a very low amount of catalyst can also reduce the hydrogen evolution rate because of less separation of electrons and holes [55].

In contrast to their high visible light absorption, perovskite oxynitrides frequently have an inadequate photocatalytic ability under typical conditions. In example, $SrTaO_2N$ exhibits self-oxidative decompositions even when shielded by a hole scavenger. Therefore, Shunhang Wei and his co-workers created Sr_2TaO_3N, by incorporating SrO as a catalyst to the crystal structure of $SrTaO_2N$. Calculations using diffuse reflectance data and the Kulbelka-Munk transformation imply that Sr_2TaO_3N displays a band gap value of 1.97 eV, which is almost 0.2 eV less than $SrTaO_2N$ [56].

1.8.3 Surface modification

Surface modification is also an efficient technique for modification of perovskites. Photocatalytic reaction happens only at surface of semiconductor material. A larger surface area will enhance the photocatalytic performance of semiconductor. Therefore, the material surface area has gained more attention. Nanomaterial fabrication technique is an efficient process to increase the surface area. The photocatalytic activity of $MgTiO_3$ nanoparticles with $MgTiO_3$ nanofibers was compared by Wang et. al. They reported that $MgTiO_3$ nanofibers have excellent photocatalytic performance. The increase in hydrogen evolution rate is due to high surface area, purity of phase and high conduction band potential. Due to 1D structure and large specific area $MgTiO_3$ nanofibers facilitates separation of photoinduced charge carriers. Guo et. al. synthesized $ZnO/SrTiO_3$ nanorod arrays. By use of two types of materials, visible light absorption increases. Powdered form thin film perovskites show better efficiency then thin film perovskites.

Similarly, Sara Kawrani et. al. evaluated the addition of copper oxide on surface of calcium copper titanate, for photocatalytic applications. It was reported that, due to its remarkable structure, which includes a visible light absorbance constituent (CuO), $CaCu_3Ti_4O_{12}$ (CCTO) is used as a photocatalyst which is functional in visible light. Further, the surface locations were modified by means of different quantities of graphene oxide (GO). In comparison to the pristine phase of CCTO, CCTO produced with 3% of GO demonstrated 50% enhanced (2.9μmol/h) photocurrent generation and hydrogen production rates[57].

Table 1.9 Hydrogen production rate of doped perovskites.

S.NO.	Material	Synthesis method	H_2 production rate	Ref
1.	$ZnO/SrTiO_3$ nanoarrays	Hydrothermal	7.53 mA cm^{-2}	[83]
2.	$SrTiO_3/TiO_2$ nanotubes	Hydrothermal	3513 mmol g^{-1} h^{-1}	[82]
3.	$NiTiO_3/TiO_2$ nanotubes	Hydrothermal	680 mmol g^{-1} h^{-1}	[84]

Gao et. al. demonstrated the Zirconium doping on $CaTiO_3$ photocatalyst to alter the surface assemblies from smooth to characteristics nano steps arrangement. Such nano steps assembly, efficiently enhances the segregation of photo-induced charge carriers, subsequently results in enhanced photocatalytic ability. It has highly susceptible active sites along with larger surface area, oxygen vacancies as well as excellent reduction ability. BET surface area of $CaTi_{1-x}Zr_xO_3$ (x=0) is $16m^2/g$ while for x=0.21 is $21m^2/g$ which is greater than that of pristine sample. After the Zr element was added, the system's hydrogen evolution efficiency dramatically increased. When the Zr content was 9% atomic, H_2 evolution rate peaked at 679 $\mu molh^{-1}g^{-1}$.

Wei Liu and his co-workers, used an easy chemical bath approach to enhance the stability of perovskites solar cells (PSCs) after building optimized layers of CdS on TiO_2 nanorods (NAs) at ambient temperature conditions. Compared to 15.93% of pure TiO_2 NAs-based cells, the PSCs relied on TiO_2/CdS core-shell achieves greater power alteration efficiency up-to 17.71%. Principally, after optimized alteration of Cadmium sulfide (CdS) layer without encapsulation, there is a noticeable enhancement in the stability of the PSCs. Further, surface modification on TiO_2 NAs is also a potential tactic to expand the functioning and stability of PSCs. Without CdS shells, TiO_2 NAs have a smooth surface. Uniform CdS shells were incorporated on TiO_2 surface, indicates successful surface amendment [58].

1.8.4 Band gap engineering

The band gap alteration of broad band gap semiconductors is an effective approach to produce visible light active nanomaterials. The VB of an oxide semiconductor is primarily produced from 2p orbital of oxygen atoms, while CB comprises lower vacant molecular orbitals of metal cations. A semiconductor (having broad band gap) can be doped with appropriate foreign elements to create an active photocatalyst for visible light. When a metal cation was doped on semiconductor, it results in creation of impurity energy level in the semiconductors forbidden band thereby reducing the band gap. Depending on the type of dopant used, the impurity energy levels that are created can act as either donor or acceptor level and further it is crucial to optimize the type and quantity of doping components.

In order to entirely absorb solar radiation, band gap engineering entails changing a UV-active photocatalytic material into a visible light active photocatalyst. There are two ways to do it: (i)

doping of cation (ii) doping of anion in semiconductor lattice. Doping has frequently been utilized to increase the visible-light effectiveness of UV-active materials (photocatalysts).

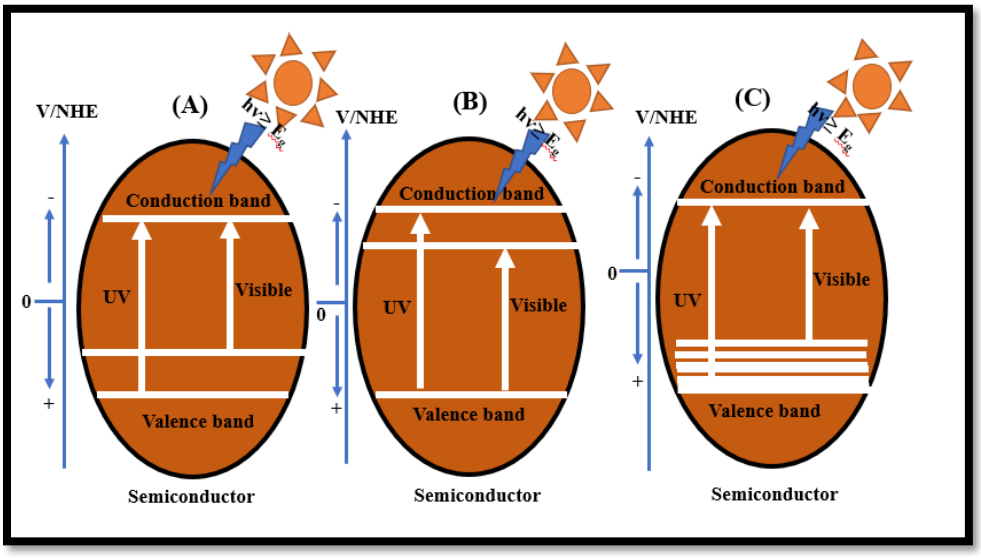

Fig 1.33 (A) and (B) reducing the band gap of a wide band gap semiconductor by cation doping, (C) anion doping.

The band edge potential of semiconductor may be reduced through the partial substitution of oxygen atoms within the semiconductor framework with appropriate non-metallic ions (e.g., C, N, S) resulting in upshift of VB edge of the semiconductor. In contrast to process of metallic ion doping, non-metal ion-based doping has been observed to generate a significantly lower quantity of recombination centers, thereby exhibiting greater efficacy in the field of photocatalysis. Numerous literary works have been published demonstrating the achievement of improved photocatalytic performance through anion doping, which narrows the band edge potential. The researchers Nishijima et al. have developed a photocatalyst consisting of S-doped TiO_2 and demonstrated its superior efficiency in hydrogen evolution when compared to TiO_2 without doping. Analogously, there have been documented instances of improved photocatalytic hydrogen production in systems such as N/TiO_2, S-N co-doped TiO_2 and Ca-N co-doped $LaTiO_3$.

To expand the photocatalytic retort of semiconductors towards visible light, transition metals like Sb, Cr, Zn and carbon can be employed as dopants[59].

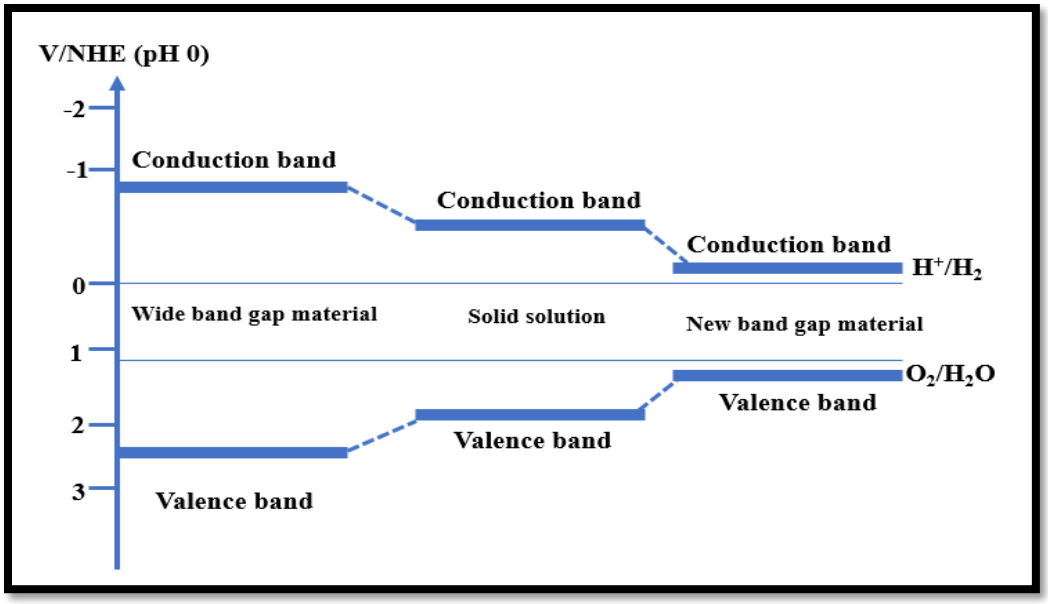

Fig 1.34 Development of narrow band gap semiconductor from broad band gap material.

For example, Chengduo Wang et. al. performed the band gap alteration of $SrTiO_3$ photocatalytic material via molybdenum and nitrogen co-doping. The pristine $SrTiO_3$ has a band potential of 3.27eV showing absorption in UV region while Mo doped material has 2.89eV band gap and further the gap was reduced to 2.07 by N doping, which is perfect band edge position for visible light absorption [60].

Fan et. al. checked the photocatalytic tendency of tantalum nitride for H_2 production applications. It was discovered that using Na_2SO_4 as the electrolyte and by setting up a heterojunction between IrO_2 acting as a cocatalyst and Ta_3N_5, significantly increased the photocurrent by more than three times. However, self-photooxidation caused the Ta_3N_5 photoelectrode to deteriorate when exposed to light. Using an alkaline electrolyte and a Co_3O_4 nanoparticle water oxidation cocatalyst, the stability of the Ta_3N_5 photoelectrode was greatly increased [61].

1.8.5 Heterojunction formation

An efficient technique with potential applications in water purification and the production of renewable energy is the facile synthesis of heterostructure photocatalysts with collaborative photoelectron migration. To better comprehend the approach for heterostructures, the photocatalysts are reviewed. The heterojunction, which results in band alignments, is the development of interface amongst two distinct semiconductors with irregular band structures. For

instance, Xiang et. al. developed a heterostructure junction between CdS and $SrTiO_3$ to boost the hydrogen evolution reaction. CdS/$SrTiO_3$ nanodots were created using an easy chemical bath deposition (CBD) technique at ambient temperature (25ºC). Owing to the development of well-defined heterostructures, the as-prepared nanohybrids not only increase the light absorption as well as dramatically slow down the charge recombination, with an H_2 evolution rate of 1322 µmol $g^{-1}h^{-1}$, which was found to be 2.8 and 12.1 times advanced than pure CdS and $SrTiO_3$ correspondingly. The heterostructure CdS doped $SrTiO_3$ exhibits superior photocatalytic activity.

Likewise, Morteza Kolaei et. al. reported a heterojunction formation at the boundary, between sodium titanate (NTO) nanorods and cadmium sulfide nanoparticles. Owing to the effective separation of charge and high migration rate of charge carriers, this connection led to a considerable increase in photocurrent density. Additionally, the integrated NTO/CdS photoanodes exhibits excellent stability. The determined photocurrent density was found in the NTO/CdS electrode with photocurrent efficiency of 2.37 mA/cm^2 at 1 V vs RHE while, NTO shows only the around 0.066 mA/cm^2 photocurrent density which is very less as compared to NTO/CdS heterojunction.

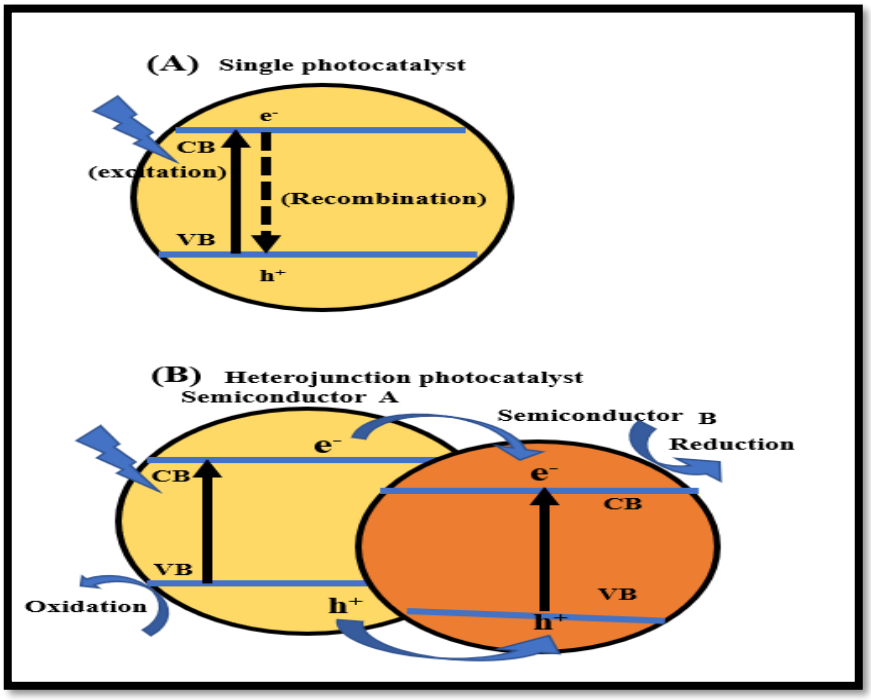

Fig 1.35 (A) Single photocatalyst showing electron hole recombination (B) separation of electron-hole on heterojunction photocatalyst.

The incident photon to current efficiency (ICPE) value for pure NTO between 295 and 375 nm is only about 1%. Due to its optical absorption edge, NTO's IPCE value decreases until it is zero at longer wavelengths. Deposition of CdS results in a noticeable increase in the IPCE value of NTO/CdS owing to improved light capture and the creation of type II heterojunction, which improves PEC activity of photoanode. The IPCE rate for NTO/CdS at 295 nm is around 36% higher than that of pristine NTO [62].

Ternary multi-heterojunction between CdS/$Bi_{20}TiO_{32}$/$Bi_4Ti_3O_{12}$ (CdSxBTC) photocatalysts was established by hydrothermally depositing the CdS nanoparticles (15–25 nm) on $Bi_{20}TiO_{32}$/$Bi_4Ti_3O_{12}$ (BTC) nanostructures. The analysis of ternary composites demonstrated improved optical absorbance, rapid electron transfer, and an extended life time of excited state. The composite materials produced 1890 µmol/g of H_2 per hour with the apparent conversion efficiency of 19%. For strong radical production capability, Z-scheme electron migration process (a synergistic Type-I bridged) was responsible and this study was described by Krishnendu Das et. al.[63].

A simple microwave-assisted approach was used by Dan Luo et. al. to exfoliate multilayer $HSr_2Nb_3O_{10}$ (a perovskite) nanosheets (HSNO-ns) successfully in two hours. Then, the heterojunction setup between HSNO-ns/CdS was done, by adapting hydrothermal method. By varying the amount of CdS, PC performance of different nano-composites was prudently tested and examined. The results displayed that the deposition of CdS nanoparticles on HSNO-ns greatly boosted the degree of hydrogen evolution**.** underneath visible light illumination (420 nm), the PC efficiency was approximately 8.38 and 330 times more intense to that of pure CdS and HSNO-ns, correspondingly [64].

Guigoz et. al. specified that $LaFeO_3$ was sputtered by employing magnetron sputtering technique and after that incorporated in graphitic carbon nitride (g-C_3N_4) layer for photoelectrochemical (PEC) water splitting reactions. In steady states, g-C_3N_4 yields 5.5 µmol$h^{-1}cm^{-2}$ of hydrogen while $LaFeO_3$ and $LaFeO_3$/g-C_3N_4 produces 6.2 and 10.8 µmol h^{-1} cm^{-2} of hydrogen, correspondingly**.** Heterojunction formation between g-C_3N_4 and $LaFeO_3$ thin film consequences in an upsurge of 74% rate of H_2 synthesis [65].

1.9 Factors affecting photocatalytic efficiency of photocatalysts

Numerous operational factors that control the photocatalytic splitting of water have a noteworthy impact on the rates of hydrogen production and effectiveness of the photocatalytic system. The importance of operational parameter has been discussed in numerous studies.

1.9.1 Crystallinity

Crystalline materials that exhibit a high degree of order are demonstrating superior performance in comparison to their amorphous counterparts. The crystalline TiO_2 nanotubes showed superior photocurrent properties over amorphous TiO_2 nanotube. The crystalline nature of amorphous TiO_2 nanotube can be induced through exposure to 300°C temperature. This study examines the photodegradation capacity of TiO_2 nanotubes in both amorphous and annealed states, with a focus on comparing the two.

The utilization of highly organized TiO_2 nanotubes has been observed to result in an enhanced production of hydrogen through PEC water splitting. According to a study, it was noticed that anodic TiO_2 nanotubes (with a high degree of order) exhibited 2.2 times greater photocurrent density than regular TiO_2 nanotubes. Additionally, these nanotubes possess favorable charge transfer properties, as their electrolytes can come into direct contact with the tube's extensive internal surface area. The relationship between crystallinity and photocurrent efficiency is influenced by structural properties. Specifically, an increase in crystallinity results in a decrease in density defects and location for electron-hole recombination [66].

1.9.2 Surface area, particle size and morphology of photocatalyst

The surface morphological features, encompassing parameters like particle size and surface area, holds significant importance in context of PC hydrogen production. The reaction rate is determined by the, quantity of photons that are in proximity of photocatalyst, indicating that reaction solely occurs within absorbed segment of photocatalyst.

The larger surface area of a photocatalyst results in an increased quantity of active sites thereby adsorbing a greater number of water molecules, thereby facilitating hydrogen evolution reaction (HER). Additionally, it enables the provision of elevated adsorption sites to enhance the efficiency of co-catalyst adsorption. For example, the specific surface area of $Bi_4Ti_3O_{12}$/ $Bi_{12}TiO_{20}$ (S1) and $Bi_4Ti_3O_{12}/Bi_2O_3$ (S2) was determined by BET and this study was reported by Pirgholi Givi et. al.

Table 1.10 Effect of morphologies of various photocatalysts on hydrogen production [67].

Photocatalysts	Light source	Hydrogen production rate (μmol/g/h)
1. $NaNbO_3$ Particles	1000 W (Xe)	1255
2. $NaNbO_3$ nanowires	400 W (Hg)	13,500
3. $NaNbO_3$ nanocubes	400 W (Hg)	48,000
4. $SnNb_2O_6$ nanoplates	300 W (Xe)	18.4
5. $SnNb_2O_6$ nanosheets	300 W (Xe)	264

It was investigated that S1 has 0.652[cm^3 (STP)g^{-1}] surface area of which is lesser than that of S2 sample (1.494 cm^3 (STP)g^{-1}). Therefore, sample S2 shows better photocatalytic performance because of larger surface area having more active sites.

1.9.3 Effect of light intensity

Probability of electron excitation is positively correlated with the intensity of light. The excitation of electrons in semiconductors necessitates exposure to ultraviolet irradiation of a short wavelength range, typically between 250 and 350 nanometers. The majority of solar radiation falls within the visible light range of 400 nm to 650 nm, while the near-ultraviolet range constitutes only a minor portion. According to the literature, the process of water splitting does not occur spontaneously under such circumstances.

Table 1.11 Sources of light in photocatalytic water splitting [68].

Photocatalyst	Light source	Wavelength
Pt, Cr, Ta on TiO2	Visible light	>420
Pt-TiO2	Xe	320-400
Rh-La-SrTiO3	300W Xe	>420
Au-TiO2	Visible light	>420

Enhancements to the process of water splitting are necessary to attain superior efficiencies in the utilization of sunlight. Table 1.11 displays the new photocatalysts that are currently under consideration for this purpose. Additionally, novel photoreactors have been designed to uniformly irradiate a significant surface area of the catalyst and prevent any occurrences of internal or external diffusion transport phenomena. The process involves the selection of a suitable light source that can facilitate the creation of electron-hole pairs. Various types of visible lamps have been utilized for water splitting, including the 150W Xe arc, a 300W Xe cut-off filter and solar simulated radiation apparatus equipped with 300W and 15W Hg lamps.

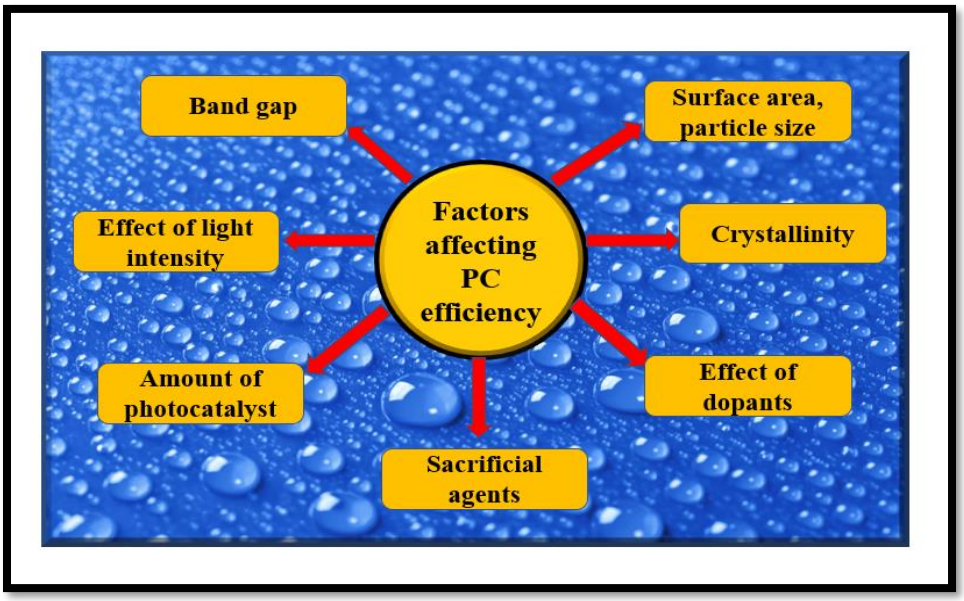

Fig 1.36 Factors affecting photocatalytic efficiency.

1.9.4 Band gap

The band edge potential of photocatalyst is key characteristics affecting PC reactions and can be determined from the difference among top position of VB and bottom of CB. The material must then display metallic conductivity with the precise band gap. The band gap can be narrowed by fine tailoring, which is the key benefit of nanomaterials. Thereby, assistance in the wide range of light absorption in solar spectrum. The precise band gap is 1.6–2.3 eV and charge carrier mobility is higher in this range of band gap.

Kudo's group discovered that $ZnNb_2O_6$ (showing band gap of 4.0eV) with d^{10} and d^0 metal ions was extremely effective for photocatalytic water splitting. Thereafter, other techniques for creating

nanostructured $ZnNb_2O_6$ with enhanced photocatalytic activity had been established. The SSR method was employed to incorporate vanadium into $ZnNb_2O_6$, leading to the formation of $Zn(Nb_{1-x}V_x)_2O_6$ solid solutions depicting reduced band gap of around 2.5 eV. The resulting solution demonstrated excellent photocatalytic activity for O_2 generation under illumination ($\lambda > 420$ nm) in presence of RuO_2 as co-catalyst [69].

To analyze the hydrogen production in presence of visible light, Jishu and his group synthesized $CdSe/SrTiO_3$ nanocomposites (having average diameter of 114.5 nm) depicting good photocatalytic proficiency. The band gap energy (E_g) of $SrTiO_3$ was 2.67eV, for $CdSe/SrTiO_3$-1 2.15eV, $CdSe/SrTiO_3$-2 (2.0eV) and $CdSe/SrTiO_3$-3 showed 1.0eV which were calculated from Tauc plot. When CdSe was added to $SrTiO_3$, a shift in absorption edge was observed, thus boosting the ability to absorb visible light. By utilizing $CdSe/SrTiO_3$-3 as a photocatalyst, the maximal H_2 efficiency was found to be 3350.53 µmol in 8 hours [70].

1.9.5 Amount of photocatalyst

In general, as catalyst dosage is increased, there is a rise in the quantity of photocatalytic splitting of water. This is because extra active sites on the surface of photocatalyst were exposed, which absorbs additional number of photons and generate high number of OH• radicals and holes.

Vijay Kanhal et. al. examined the effect of amount of Fe loading on Bismuth titanates (BT) for photocatalytic applications. It was reported that by Fe loading on BT the band gap decreases by 0.4eV i.e. from 2.8 (for pure BT) to 2.4 eV for Fe/BT. When 250 mg of catalyst was taken, it results in 58% reduction of gas evolution while 200 mg catalyst reduces the production rate of H_2 gas by 27%. This finding suggests that with a catalyst weight of above than 150 mg, the light scattering effect become prominent and may have a negative influence by reducing the number of absorbed photons [71].

Wang et al. performed an investigation on the doping content of Zr in $LaCoO_3$ and noticed that the reoxidation extent was better in the sample with 30% Zr doping contrasted to those with 100% or 50% Zr doping. In the current realm of thermochemical applications of perovskite materials, the materil $LaCo_{0.7}Zr_{0.3}O_3$ has been recognized as an intrugining substance for CO production.

Noteworthy, it produced an average carbon monoxide of 1066.6 mol/g, which was an impressive performance[72].

1.9.6 Sacrificial agents

The recombination of electro-hole couples results in lower efficiency for photocatalytic hydrogen generation. Improved hydrogen efficiencies can be achieved by using electron donors to act as sacrificial agents and stop the aforementioned recombination. Methanol, triethanolamine, ethanol, acids, and inorganic chemicals are examples of common sacrificial agents. The most studied sacrificial agents, methanol and ethanol, have remarkable quantum efficiencies. Since these offers easy electron donor. Specified that ethanol can be readily manufactured by fermentation reaction from renewable biomass, making it accessible and affordable, using ethanol as a sacrificial agent is desirable. Because of the indirect hydroxyl radical oxidation, it works well when used in small amounts.

Table 1.12 Hydrogen production efficiency of various photocatalysts [73].

Photocatalyst	**Light source**	**Sacrificial agent**	**Hydrogen evolution ($\mu molh^{-1} g^{-1}$)**
TiO_2	300W Xe lamp	10% Methanol by vol.	3200
$MoSe_2$ /TiO_2	Xe arc lamp	10% methanol by vol.	4.9
BCN-TiO_2	300W xenon lamp with a UV-cutoff filter ($\lambda \geq 420$ nm)	20% by vol. triethanolamine	68.54
ZnS@g-C_3N_4 /TiO_2	300W Xe lamp ($\lambda > 400$ nm)	10% vol. triethanolamine	422
Cr-doped $Bi_4Ti_3O_{12}$	300W Xe lamp	7 vol % of methanol, $\lambda > 420$ nm	116.75

Bhawna and her co-researchers deliberated the effect of numerous scavengers on hydrogen production efficiency of N doped SnO_2 nanoparticles. In order to easily introduce N into SnO_2 framework, one-step synthetic technique (solution-based) was used. The water splitting experiment was performed by utilizing a photochemical reactor consisting of a 250W Xe lamp and the reaction was carried out with methanol, EDTA and TEOA scavengers. The experimental results were utilized to evaluate the hydrogen gas evolution activity of N/SnO_2. It was examined that the above prepared nanoparticles result in evolution of maximum hydrogen gas in proximity of methanol, yielding 168.9 $\mu mol^{-1}g$. The sequence of scavengers for hydrogen gas production employing N/SnO_2 nanoparticles is Methanol>EDTA and TEOA [74].

1.9.7 Effect of dopants

The impurities incorporated in the photocatalysts, to boost up the photocatalytic productivity, are termed as doping agents. Dopants alter the bandgap of photocatalysts by introducing new impurity energy positions thus traps electrons, additionally enhancing the number of active locations for adsorption of molecules. Furthermore, the incorporation of additional energy levels supports in charge carrier's separation.

The outcome of Ag doping on TiO_2 was conveyed by Devipriya et. al. and checked the efficiency of Ag/TiO_2 to that of pristine TiO_2 for PC water splitting reactions. To determine an appropriate concentration for effective photon absorption, the impact of 1.5g of Ag concentration on TiO_2 and response extent on water splitting action, was investigated. At all catalyst concentrations, the overall H_2 generation awoke approximately linearly with reaction time. The photocatalyst concentration of 20 mg L^{-1} resulted in a maximum photocatalytic activity of 470 $\mu mol\ g^{-1}\ h^{-1}$, in a sacrificial agent free environment. Excessive catalyst loading may prevent the absorption of radiation and, in some circumstances, may encourage recombination of e/h pairs. The highest ever recorded yield of hydrogen (23.5 $mmolg^{-1}h^{-1}$) was noticed over 1.5Ag doped TiO_2 showing quantum yield of 19%. The development of Ti-Ag-O phase and presence of oxygen vacancies are key causes of the increased photocatalytic activity [75].

A two-step based Solvo-thermal method was employed by Ankireddy et al. and synthesized CdS-nanoparticles decorated with g-C_3N_4 and further, doped with Fe_3O_4 nano-cube catalyst, referred to as g-CNCSF. The above-prepared composites demonstrated outstanding efficiency and stability

due to the development of interfacial coordination between g-C3N4 and CdS nanoparticles, which subsequently promotes the bandgap-dependent interfacial transfer of charges. Through photoelectrochemical (PEC) water splitting, it accelerated H_2 evolution produced by splitting of water. By calcining melamine and extracted onion leaf extract at 450°C in a N_2 environment, g-C_3N_4 was produced. After calcining the sample on 450°C under N_2, a CdS based Fe_3O_4 catalyst was generated by, hydrothermally incorporating CdS nanoparticles into layers of Fe_3O_4. The PEC analysis described that, the current density of the g-CNCSF catalyst was 2.5 times greater (0.023 $mAcm^{-2}$) than gC3N4@CdS while, 6.25 times more than that of binary hybrid CdS@Fe_3O_4.

Similarly, Pushkal Sharma et. al. described the effect of different dopants (Fe, V Ga and Rh) on hydrogen production yield of $SrTiO_3$. Among all the doped samples of $SrTiO_3$, 1% Rh doped $SrTiO_3$ was discovered to have the maximum water dissociation efficiency. Which was explained according to first principle DFT calculations. It was noticed that a new dopant energy level was created a little bit above the VB and threshold excitation energy is a little lower in Rh doped sample. Subsequent on excitation, the empty dopant states can serve as an electron recombination center in CB. Because Rh dopant states are so close to VB, they can quickly refill their electron supply by absorbing thermal vibrations of the crystal or low energy photons [76].

1.10 Scope of the research work

From the literature it has been found that a number of studies have been conducted over photocatalytic perovskite materials for their use in water breakdown for hydrogen gas evolution under illumination of solar light. But till date no perovskite material has been synthesized depicting excellent stability, high proficiency, efficient technique and also cost effective, for hydrogen production. It was noted from the literature that the above discussed perovskite materials have low efficiency in visible light and have wide band gaps. In this research work the prepared perovskite materials are such that they are active in visible light, have narrow band gap and showed excellent effectiveness for hydrogen gas production under solar light illumination.

1.11 Objectives of the proposed work

1. Synthesis of Bismuth (Bi) and Cadmium sulfide (CdS) and Lead (II) sulfide (PbS) co-nanocomplex titanate perovskites using hydrothermal process to enhance visible light driven photo-catalysis.
2. Bi/CdS/PbS co-nanocomplex titanate perovskite embedded with graphene oxide (GO) to improve the photo-metal oxide dispersion and enhance solar catalysis process.
3. Hydrogen production using efficient photocatalytic system under solar irradiation.
4. Characteristic analysis of novel photo-catalytic system for renewable energy production.
5. Hydrogen production and characteristic co-comparative studies of co-nanocomplex titanate perovskite materials.

References

(1) Amin, M.; Shah, H. H.; Fareed, A. G.; Khan, W. U.; Chung, E.; Zia, A.; Rahman Farooqi, Z. U.; Lee, C. Hydrogen Production through Renewable and Non-Renewable Energy Processes and Their Impact on Climate Change. Int J Hydrogen Energy 2022, 47 (77), 33112–33134. https://doi.org/https://doi.org/10.1016/j.ijhydene.2022.07.172.

(2) Amika; Sharma, R.; Sharma, A.; Chandrani, A.; Singh, J.; Kumar, D. Role of Titanate-Based Perovskites in Solar Water Splitting: An Overview. J Phys Conf Ser 2022, 2267 (1), 012016. https://doi.org/10.1088/1742-6596/2267/1/012016.

(3) Lee, S.; Jang, G. Y.; Kim, J. K.; Park, J. H. Solar-Harvesting Lead Halide Perovskite for Artificial Photosynthesis. Journal of Energy Chemistry 2021, 62, (26). https://doi.org/https://doi.org/10.1016/j.jechem.2021.02.025.

(4) Rohloff, M.; Anke, B.; Zhang, S.; Gernert, U.; Scheu, C.; Lerch, M.; Fischer, A. Mo-Doped $BiVO_4$ Thin Films – High Photoelectrochemical Water Splitting Performance Achieved by a Tailored Structure and Morphology. Sustain Energy Fuels 2017, 1 (8), 1830–1846. https://doi.org/10.1039/C7SE00301C.

(5) Campos, J.; Csontos, C.; Munkácsy, B. Electricity Scenarios for Hungary: Possible Role of Wind and Solar Resources in the Energy Transition. Energy 2023, 278, 127971. https://doi.org/https://doi.org/10.1016/j.energy.2023.127971.

(6) Kumar, A.; Kumar, K.; Kaushik, N.; Sharma, S.; Mishra, S. Renewable Energy in India: Current Status and Future Potentials. Renewable and Sustainable Energy Reviews 2010, 14 (8), 2434–2442. https://doi.org/https://doi.org/10.1016/j.rser.2010.04.003.

(7) Jacobson, M.; Delucchi, M. Providing All Global Energy with Wind, Water, and Solar Power, Part I: Technologies, Energy Resources, Quantities and Areas of Infrastructure, and Materials. Energy Policy 2011, 39, 1154–1169. https://doi.org/10.1016/j.enpol.2010.11.040.

(8) Lovins, L. H. The Triumph of Solar in the Energy Race. Journal of Fundamentals of Renewable Energy and Applications 2015, 05. https://doi.org/10.4172/2090-4541.1000187.

(9) Ghasemian, S.; Faridzad, A.; Abbaszadeh, P.; Taklif, A.; Ghasemi, A.; Hafezi, R. An Overview of Global Energy Scenarios by 2040: Identifying the Driving Forces Using Cross-Impact Analysis Method. International Journal of Environmental Science and Technology 2020. https://doi.org/10.1007/s13762-020-02738-5.

(10) Steinfeld, A. Solar Thermochemical Production of Hydrogen - A Review. Solar Energy 2005, 78, 603–615. https://doi.org/10.1016/j.solener.2003.12.012.

(11) Licht, S.; Wang, B.; Mukerji, S.; Soga, T.; Umeno, M.; Tributsch, H. Over 18% Solar Energy Conversion to Generation of Hydrogen Fuel; Theory and Experiment for Efficient Solar Water Splitting. Int J Hydrogen Energy 2001, 26, 653–659. https://doi.org/10.1016/S0360-3199(00)00133-6.

(12) Hoang, A. T.; Pandey, A.; Chen, W.-H.; Ahmed, S. F.; Nižetić, S.; Ng, K. H.; Said, Z.; Duong, X. Q.; Ağbulut, Ü.; Hadiyanto, H.; Nguyen, X. P. Hydrogen Production by Water Splitting with Support of Metal and Carbon-Based Photocatalysts. ACS Sustain Chem Eng 2023, 11 (4), 1221–1252. https://doi.org/10.1021/acssuschemeng.2c05226.

(13) Tachibana, Y.; Vayssieres, L.; Durrant, J. Artificial Photosynthesis for Solar Water Splitting. Nat Photonics 2012, 6, 511–518. https://doi.org/10.1038/nphoton.2012.175.

(14) Bin Adnan, M. A.; Arifin, K.; Minggu, L. J.; Kassim, M. B. Titanate-Based Perovskites for Photochemical and Photoelectrochemical Water Splitting Applications: A Review. Int J Hydrogen Energy 2018, 43 (52), 23209–23220. https://doi.org/10.1016/J.IJHYDENE.2018.10.173.

(15) Assirey, E. Perovskite Synthesis, Properties and Their Related Biochemical and Industrial Application. Saudi Pharmaceutical Journal 2019, 27. https://doi.org/10.1016/j.jsps.2019.05.003.

(16) Shi, Z.; Jayatissa, A. H. Perovskites-Based Solar Cells: A Review of Recent Progress, Materials and Processing Methods. Materials. 2018. https://doi.org/10.3390/ma11050729.

(17) Bischak, C. G.; Hetherington, C. L.; Wu, H.; Aloni, S.; Ogletree, D. F.; Limmer, D. T.; Ginsberg, N. S. Origin of Reversible Photoinduced Phase Separation in Hybrid Perovskites. Nano Lett 2017, 17 (2), 1028–1033. https://doi.org/10.1021/acs.nanolett.6b04453.

(18) Zhang, G.; Liu, G.; Wang, L.; Irvine, J. T. S. Inorganic Perovskite Photocatalysts for Solar Energy Utilization. Chem Soc Rev 2016, 45 (21), 5951–5984. https://doi.org/10.1039/C5CS00769K.

(19) Bhatti, H. S.; Hussain, S. T.; Khan, F. A.; Hussain, S. Synthesis and Induced Multiferroicity of Perovskite $PbTiO_3$; A Review. Appl Surf Sci 2016, 367, 291–306. https://doi.org/https://doi.org/10.1016/j.apsusc.2016.01.164.

(20) Xiao, Z.; Ren, Z.; Liu, Z.; Wei, X.; Xu, G.; Liu, Y.; Li, X.; Shen, G.; Han, G. Single-Crystal Nanofibers of Zr-Doped New Structured $PbTiO_3$: Hydrothermal Synthesis, Characterization and Phase Transformation. J Mater Chem 2011, 21 (11), 3562–3564. https://doi.org/10.1039/C0JM04212A.

(21) Cohen, R. E. Origin of Ferroelectricity in Perovskite Oxides. Nature 1992, 358 (6382), 136–138. https://doi.org/10.1038/358136a0.

(22) Röhm, H.; Leonhard, T.; Schulz, A.; Wagner, S.; Hoffmann, M.; Colsmann, A. Ferroelectric Properties of Perovskite Thin Films and Their Implications for Solar Energy Conversion. Advanced Materials 2019, 31. https://doi.org/10.1002/adma.201806661.

(23) Izyumskaya, N.; Alivov, Y.; Cho, S.-J.; Morkoç, H.; Lee, H.; Kang, Y.-S. Processing, Structure, Properties, and Applications of PZT Thin Films. Critical Reviews in Solid State and Materials Sciences - 2007, 32, 111–202. https://doi.org/10.1080/10408430701707347.

(24) Damjanovic, D. Piezoelectric Properties of Perovskite Ferroelectrics: Unsolved Problems and Future Research. Annales de Chimie Science des Matériaux 2001, 26 (1), 99–106.

(25) Ramesh, R.; Spaldin, N. Multiferroics: Progress and Prospects in Thin Films. Nat Mater 2007, 6, 21–29. https://doi.org/10.1038/nmat1805.

(26) Sun, D.; Li, D.; Zhu, Z.; Xiao, J.; Tao, Z.; Liu, W. Photoluminescence Properties of Europium and Titanium Co-Doped $BaZrO_3$ Phosphors Powders Synthesized by the Solid-State Reaction Method. Opt Mater (Amst) 2012, 34, 1890–1896. https://doi.org/10.1016/j.optmat.2012.05.024.

(27) Nishihata, Y.; Mizuki, J.; Tanaka, H.; Uenishi, M.; Kimura, M. Self-Regeneration of Palladium-Perovskite Catalysts in Modem Automobiles. Journal of Physics and Chemistry of Solids 2005, 66, 274–282. https://doi.org/10.1016/j.jpcs.2004.06.090.

(28) Astruc, D.; Lu, F.; Ruiz Aranzaes, J. Nanoparticles as Recyclable Catalysts: The Frontier Between Homogeneous and Heterogeneous Catalysis. Angew Chem Int Ed Engl 2006, 44, 7852–7872. https://doi.org/10.1002/anie.200500766.

(29) Chen, H.-J.; Chen, Y.-W. Hydrothermal Synthesis of Barium Titanate. Industrial & Engineering Chemistry Research 2003, 42. https://doi.org/10.1021/ie010796q.

(30) Canu, G.; Buscaglia, V. Hydrothermal Synthesis of Strontium Titanate: Thermodynamic Considerations, Morphology Control and Crystallisation Mechanisms. CrystEngComm 2017, 19 (28), 3867–3891. https://doi.org/10.1039/C7CE00834A.

(31) Yafarova, L.; Chislova, I.; Zvereva, I.; Kryuchkova, T.; Kost, V.; Sheshko, T. Sol–Gel Synthesis and Investigation of Catalysts on the Basis of Perovskite-Type Oxides $GdMO_3$ (M = Fe, Co). J Solgel Sci Technol 2019, 92, 264–272. https://doi.org/10.1007/s10971-019-05013-3.

(32) Roque-Ruiz, J.; Meraz-Angel, J.; Farias, R.; Meléndez-Lira, M.; Reyes-López, S. Sol-Gel Synthesis of Strontium Titanate Nanofibers by Electrospinning. Journal of Ceramic Science and Technology 2019, 10, 29–38. https://doi.org/10.4416/JCST2018-00072.

(33) Nguyen, M. T.; Deng, L.; Yonezawa, T. Control of Nanoparticles Synthesized via Vacuum Sputter Deposition onto Liquids: A Review. Soft Matter 2022, 18 (1), 19–47. https://doi.org/10.1039/D1SM01002F.

(34) Hosseini, S. Preparation and Characterization of Calcium Titanate Nanoparticles with the Aid of Different Acids and Study of Their Photocatalytic Properties. Journal of Materials Science: Materials in Electronics 2017, 28, 1–6. https://doi.org/10.1007/s10854-016-5976-1.

(35) Joshi, U.; Jang, J.; Borse, P.; Lee, J. S. Microwave Synthesis of Single-Crystalline Perovskite $BiFeO_3$ Nanocubes for Photoelectrode and Photocatalytic Applications. Appl Phys Lett 2008, 92, 242106–242109. https://doi.org/10.1063/1.2946486.

(36) Gabano, E.; Ravera, M. Microwave-Assisted Synthesis: Can Transition Metal Complexes Take Advantage of This “ Green” Method. Molecules. 2022. https://doi.org/10.3390/molecules27134249.

(37) Singh, R. P. Conventional and Microwave Synthesis of Mesoporous Calcium Titanate Nanopowders: A Comparative Study. J Solgel Sci Technol 2018, 88 (3), 574–583. https://doi.org/10.1007/s10971-018-4860-2.

(38) Saeed, M.; Alshammari, Y.; Majeed, S. A.; Al-Nasrallah, E. Chemical Vapour Deposition of Graphene—Synthesis, Characterisation, and Applications: A Review. Molecules. 2020. https://doi.org/10.3390/molecules25173856.

(39) Luo, P.; Zhou, S.; Xia, W.; Cheng, J.; Xu, C.; Lu, Y.-W. Chemical Vapor Deposition of Perovskites for Photovoltaic Application. Adv Mater Interfaces 2017, 4, 1600970. https://doi.org/10.1002/admi.201600970.

(40) Atta, N. F.; Galal, A.; El-Ads, E. H. Perovskite Nanomaterials – Synthesis, Characterization, and Applications; Pan, L., Zhu, G., Eds.; IntechOpen: Rijeka, 2016; p Ch. 4. https://doi.org/10.5772/61280.

(41) Balta, Z.; Bilgin Simsek, E. Boosted Photocatalytic Hydrogen Production and Photo-Fenton Degradation of Ciprofloxacin Antibiotic over Spherical $LaMnO_3$ Perovskites Assembled Boron Nitride Quantum Dots. Int J Hydrogen Energy 2023, 48. https://doi.org/10.1016/j.ijhydene.2023.03.382.

(42) Guan, S.; Li, R.; Sun, X.; Yang, H. Construction of Novel Ternary Au/$LaFeO_3$ /Cu_2O Composite Photocatalysts for RhB Degradation via Photo-Fenton Catalysis. Materials Technology 2020, 36, 1–13. https://doi.org/10.1080/10667857.2020.1782062.

(43) Kumar, P.; Chand, P.; Singh, V. La^{3+} Substituted $BiFeO_3$-a Proficient Nano Ferrite Photo-Catalyst under the Application of Visible Light. Chem Phys Lett 2020, 754, 137715. https://doi.org/10.1016/j.cplett.2020.137715.

(44) Ha, S.-T.; Su, R.; Xing, J.; Zhang, Q.; Xiong, Q. Metal Halide Perovskite Nanomaterials: Synthesis and Applications. Chem Sci 2017, 8 (4), 2522–2536. https://doi.org/10.1039/C6SC04474C.

(45) Song, J.; Xu, L.; Li, J.; Xue, J.; Dong, Y.; Li, X.; Zeng, H. Monolayer and Few-Layer All-Inorganic Perovskites as a New Family of Two-Dimensional Semiconductors for Printable Optoelectronic Devices. Adv Mater 2016, 28. https://doi.org/10.1002/adma.201600225.

(46) Fajrina, N.; Tahir, M. A Critical Review in Strategies to Improve Photocatalytic Water Splitting towards Hydrogen Production. Int J Hydrogen Energy 2019, 44 (2), 540–577. https://doi.org/https://doi.org/10.1016/j.ijhydene.2018.10.200.

(47) Ahmad, H.; Kamarudin, S. K.; Jeffery Minggu, L.; Kassim, M. Hydrogen from Photo-Catalytic Water Splitting Process: A Review. Renewable and Sustainable Energy Reviews 2015, 43, 599–610. https://doi.org/10.1016/j.rser.2014.10.101.

(48) Matsuoka, M.; Kitano, M.; Takeuchi, M.; Tsujimaru, K.; Anpo, M.; Thomas, J. Photocatalysis for New Energy Production: Recent Advances in Photocatalytic Water Splitting Reactions for Hydrogen Production. Catal Today 2007, 122, 51–61. https://doi.org/10.1016/j.cattod.2007.01.042.

(49) Ye, S.; Ding, C.; Chen, R.; Fan, F.; Fu, P.; Yin, H.; Wang, X.; Wang, Z.; Du, P.; Li, C. Mimicking the Key Functions of Photosystem II in Artificial Photosynthesis for Photoelectrocatalytic Water Splitting. J Am Chem Soc 2018, 140 (9), 3250–3256. https://doi.org/10.1021/jacs.7b10662.

(50) Khan, M. M.; Adil, S. F.; Al-Mayouf, A. Metal Oxides as Photocatalysts. Journal of Saudi Chem Society 2015, 19 (5), 462–464. https://doi.org/https://doi.org/10.1016/j.jscs.2015.04.003.

(51) Ziati, M.; Bekkioui, N.; Ez-Zahraouy, H. Ruddlesden-Popper Compound Sr_2TiO_4 Doped with Chalcogens for Optoelectronic Applications: Insights from First- Principle Calculations. Chem Phys 2021, 548, 111221. https://doi.org/https://doi.org/10.1016/j.chemphys.2021.111221.

(52) Yu, H.; Wang, J.; Yan, S.; Yu, T.; Zou, Z. Elements Doping to Expand the Light Response of $SrTiO_3$. Journal of Photochemistry and Photobiology A: Chem 2014, 275, 65–71. https://doi.org/10.1016/j.jphotochem.2013.10.014.

(53) Saadetnejad, D.; Yıldırım, R. Photocatalytic Hydrogen Production by Water Splitting over Au/Al-$SrTiO_3$. Int J Hydrogen Energy 2018, 43 (2), 1116–1122. https://doi.org/https://doi.org/10.1016/j.ijhydene.2017.10.154.

(54) Alammar, T.; Hamm, I.; Wark, M.; Mudring, A.-V. Low-Temperature Route to Metal Titanate Perovskite Nanoparticles for Photocatalytic Applications. Appl Catal B 2015, 178, 20–28. https://doi.org/https://doi.org/10.1016/j.apcatb.2014.11.010.

(55) Roque-Ruiz, J. H.; Meraz-Angel, J.; Farias, R.; Meléndez-Lira, M.; Reyes-López, S. Y. Sol-Gel Synthesis of Strontium Titanate Nanofibers by Electrospinning. Journal of Ceramic Science and Technology 2019, 10 (1), 29–38. https://doi.org/10.4416/JCST2018-00072.

(56) Wei, S.; Xu, X. Boosting Photocatalytic Water Oxidation Reactions over Strontium Tantalum Oxynitride by Structural Laminations. Appl Catal B 2018, 228, 10–18. https://doi.org/https://doi.org/10.1016/j.apcatb.2018.01.071.

(57) Kawrani, S.; Boulos, M.; Bekheet, M. F.; Viter, R.; Nada, A. A.; Riedel, W.; Roualdes, S.; Cornu, D.; Bechelany, M. Segregation of Copper Oxide on Calcium Copper Titanate Surface Induced by Graphene Oxide for Water Splitting Applications. Appl Surf Sci 2020, 516 (February), 146051. https://doi.org/10.1016/j.apsusc.2020.146051.

(58) Li, X.; Dai, S.-M.; Zhu, P.; Deng, L.-L.; Xie, S.-Y.; Cui, Q.; Chen, H.; Wang, N.; Lin, H. Efficient Perovskite Solar Cells Depending on TiO_2 Nanorod Arrays. ACS Appl Mater Interfaces 2016, 8 (33), 21358–21365. https://doi.org/10.1021/acsami.6b05971.

(59) Nishijima, K.; Kamai, T.; Murakami, N.; Tsubota, T.; Ohno, T. Photocatalytic Hydrogen or Oxygen Evolution from Water over S- or N-Doped TiO_2 under Visible Light. International Journal of Photoenergy 2008, 2008, 173943. https://doi.org/10.1155/2008/173943.

(60) Wang, C.; Qiu, H.; Inoue, T.; Yao, Q. Band Gap Engineering of $SrTiO_3$ for Water Splitting under Visible Light Irradiation. Int J Hydrogen Energy 2014, 39, 12507–12514. https://doi.org/10.1016/j.ijhydene.2014.06.059.

(61) Fu, J.; Zeyu, F.; Nakabayashi, M.; Ju, H.; Pastukhova, N.; Yequan, X.; Feng, C.; Shibata, N.; Domen, K.; Li, Y. Interface Engineering of Ta_3N_5 Thin Film Photoanode for Highly Efficient Photoelectrochemical Water Splitting. Nat Commun 2022, 13, 729. https://doi.org/10.1038/s41467-022-28415-4.

(62) Kolaei, M.; Tayebi, M.; Masoumi, Z.; Tayyebi, A.; Lee, B.-K. Decoration of CdS Nanoparticles on Dense and Multi-Edge Sodium Titanate Nanorods to Form a Highly Efficient and Stable Photoanode with Great Enhancement in PEC Performance. Environ Sci Nano 2021, 8 (6), 1667–1679. https://doi.org/10.1039/D1EN00221J.

(63) Das, K.; Bariki, R.; Majhi, D.; Mishra, A.; Das, K. K.; Dhiman, R.; Mishra, B. G. Facile Synthesis and Application of $CdS/Bi_{20}TiO_{32}/Bi_4Ti_3O_{12}$ Ternary Heterostructure: A Synergistic Multi-Heterojunction Photocatalyst for Enhanced Endosulfan Degradation and Hydrogen Evolution Reaction. Applied catalysis B: 2022, 303, 120902. https://doi.org/https://doi.org/10.1016/j.apcatb.2021.120902.

(64) Luo, D.; Huang, Y.; Zhao, Y.; Fang, Y.; Li, Z.; Guo, Q.; Wei, Y.; Fan, L.; Wu, J. Visible-Light-Driven $HSr_2Nb_3O_{10}$/CdS Heterojunctions for High Hydrogen Evolution Activity. Int J Hydrogen Energy 2020, 45 (4), 2896–2908. https://doi.org/https://doi.org/10.1016/j.ijhydene.2019.11.193.

(65) Guigoz, V.; Balan, L.; Aboulaich, A.; Schneider, R.; Gries, T. Heterostructured Thin $LaFeO_3$/g-C_3N_4 Films for Efficient Photoelectrochemical Hydrogen Evolution. Int J Hydrogen Energy 2020, 45, 17468–17479. https://doi.org/10.1016/j.ijhydene.2020.04.267.

(66) Gong, J.; Lai, Y.; Lin, C. Electrochemically Multi-Anodized TiO_2 Nanotube Arrays for Enhancing Hydrogen Generation by Photoelectrocatalytic Water Splitting. Electrochim Acta 2010, 55, 4776–4782. https://doi.org/10.1016/j.electacta.2010.03.055.

(67) Zhou, C.; Zhao, Y.; Shang, L.; Shi, R.; Wu, L.-Z.; Tung, C.-H.; Zhang, T. Facile Synthesis of Ultrathin $SnNb_2O_6$ Nanosheets towards Improved Visible-Light Photocatalytic H_2-Production

Activity. Chemical Communications 2016, 52 (53), 8239–8242. https://doi.org/10.1039/C6CC03739A.

(68) Jafari, T.; Moharreri, E.; Amin, A. S.; Miao, R.; Song, W.; Suib, S. L. Photocatalytic Water Splitting—The Untamed Dream: A Review of Recent Advances. Molecules. 2016. https://doi.org/10.3390/molecules21070900.

(69) Miseki, Y.; Kato, H.; Kudo, A. Water Splitting into H_2 and O_2 over Niobate and Titanate Photocatalysts with (111) Plane-Type Layered Perovskite Structure. Energy & Environmental Science, 2009, 2. https://doi.org/10.1039/b818922f.

(70) Han, J.; Dai, F.; Liu, Y.; Zhao, R.; Wang, L.; Feng, S. Synthesis of CdSe/$SrTiO_3$ Nanocomposites with Enhanced Photocatalytic Hydrogen Production Activity. Appl Surf Sci 2018, 467. https://doi.org/10.1016/j.apsusc.2018.10.267.

(71) Khanal, V.; Ragsdale, W.; Gupta, S.; Subramanian, V. Insights into the Photoactivity of Iron Modified Bismuth Titanate (Fe_BTO) Nanoparticles. Catal Today 2017, 300. https://doi.org/10.1016/j.cattod.2017.07.017.

(72) Wang, L.; Ma, T.; Dai, S.; Ren, T.; Chang, Z.; Dou, L.; Mingkai, F.; Li, X. Experimental Study on the High Performance of Zr Doped $LaCoO_3$ for Solar Thermochemical CO Production. Chemical Engineering Journal 2020, 389, 124426. https://doi.org/10.1016/j.cej.2020.124426.

(73) Zhu, Z.; Wan, S.; Zhao, Y.; Gu, Y.; Wang, Y.; Qin, Y.; Zhang, Z.; Ge, X.; Zhong, Q.; Bu, Y. Recent Advances in Bismuth-Based Multimetal Oxide Photocatalysts for Hydrogen Production from Water Splitting: Competitiveness, Challenges, and Future Perspectives. Materials Reports: Energy 2021, 1 (2), 100019. https://doi.org/https://doi.org/10.1016/j.matre.2021.100019.

(74) Bhawna; Gupta, A.; Kumar, P.; Tyagi, A.; Kumar, R.; Kumar, A.; Singh, P.; Singh, R. P.; Kumar, V. Facile Synthesis of N-Doped SnO_2 Nanoparticles: A Cocatalyst-Free Promising Photocatalyst for Hydrogen Generation. ChemistrySelect 2020, 5 (26), 7775–7782. https://doi.org/10.1002/SLCT.202001301.

(75) Gogoi, D.; Namdeo, A.; Golder, A.; Peela, N. R. Ag-Doped TiO_2 Photocatalysts with Effective Charge Transfer for Highly Efficient Hydrogen Production through Water Splitting. Int J Hydrogen Energy 2019. https://doi.org/10.1016/j.ijhydene.2019.11.127.

(76) Reddy, A.; Kim, J. An Efficient G-C_3N_4-Decorated CdS-Nanoparticle-Doped Fe_3O_4 Hybrid Catalyst for an Enhanced H_2 Evolution through Photoelectrochemical Water Splitting. Appl Surf Sci 2020, 513, 145836. https://doi.org/10.1016/j.apsusc.2020.145836.

CHAPTER 2

Synthesis and characterization techniques

2.1 Synthetic approach for synthesis of perovskite materials

2.1.1. Hydrothermal synthesis

In 1792, British geologist Roderick Murchison firstly used the term “hydrothermal” and reported that it is the most beneficial technique for synthesis of nanoparticles with distinct morphologies[1].

It is the solution-based approach for synthesis of nanomaterials. The hydro/solvo thermal technique refers to a chemical process that is conducted within an enclosed stainless-steel autoclave. The process of crystal growth is supported in a precise apparatus referred to as autoclave, it is a Teflon lined stainless-steel pressure vessel. This vessel facilitates the infusion of a nutrient along with water[2]. The benefit of this technique is that the solvents with low boiling points such as water and ethanol can be used during the synthesis. When water is used during the synthesis as reaction medium the process is known as hydrothermal, on other hand if any solvent other than water is applied for the synthesis then the technique is called as solvothermal process.

Generally, this approach is applied for synthesis of those constitute materials which cannot be dissolved at standard conditions. The hydrothermal synthesis primarily entails two steps: crystal nucleation and subsequent growth of nanomaterials. Under ambient temperature and pressure conditions, an aqueous solution consisting of precursor and solvent put in stainless steel autoclave to facilitate the hydrothermal reaction. The chemical reaction among the precursors is accelerated under hydrothermal conditions, leading to enhanced hydrolysis and streamlined nucleation, ultimately resulting in the crystal growth of nanoparticles in aqueous solution.

The autoclave (made up of stainless steel and have teflon lining) is the primary constituent in hydrothermal synthesis and is widely preferred over glass and quartz autoclaves owing to its diverse features such as commendable resistance to corrosion, robustness under conditions of elevated pressure and temperature[3].

Hydrothermal synthesis has been employed effectively for preparation of various nanomaterials and it is a green method. The hydrothermal method is low cost and there is no need of additional solvents.

The hydrothermal technique has numerous benefits over other conventional and non-conventional approaches of synthesis. In preparation of perovskite complexes having fine powders and good purity, hydrothermal method is considered efficient because of following reasons: -

- Controlling particle size, shape and morphology by regulating reaction conditions such as temperature, pressure, solvent, pH of solution, precursors concentration etc.
- Homogeneous and uniform crystals with fine size can be produced by this method
- No requirements of expensive precursors or equipment's
- Moderate reaction conditions are required
- Low energy consumption
- Environmentally friendly and sustainable
- Surfactant free method

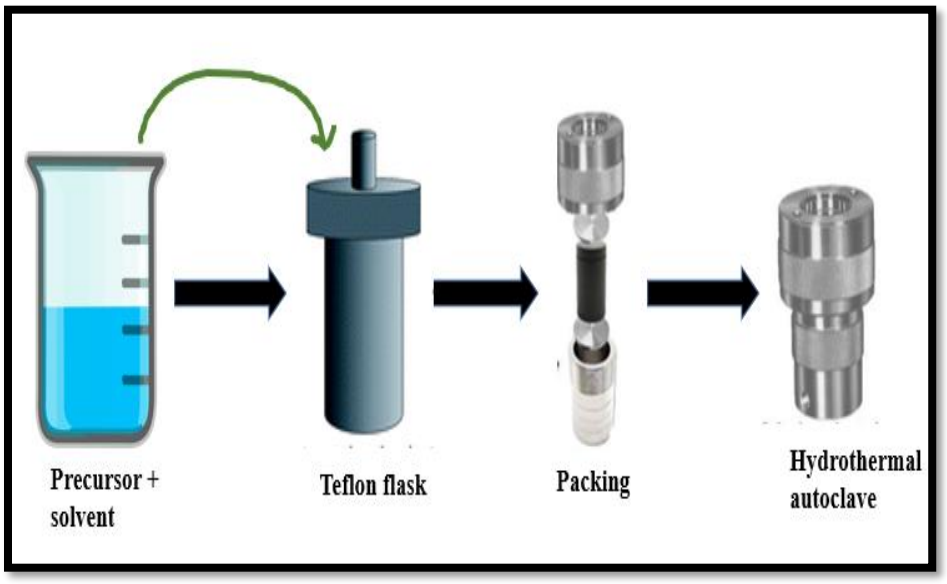

Fig 2.1 Hydrothermal synthesis scheme.

In this thesis, bismuth titanates ($Bi_4Ti_3O_{12}$), cadmium sulfide (CdS) and lead sulfide (PbS) nanoparticles have been produced by hydrothermal technique. A 100ml teflon lined autoclave made of stainless steel has been used for the synthesis of nanomaterials via hydrothermal approach.

2.1.2 Synthetic details

2.1.2.1 Preparation of titanium dioxide (TiO_2)

Titanium dioxide powder has been synthesized by chemical co-precipitation method[4].

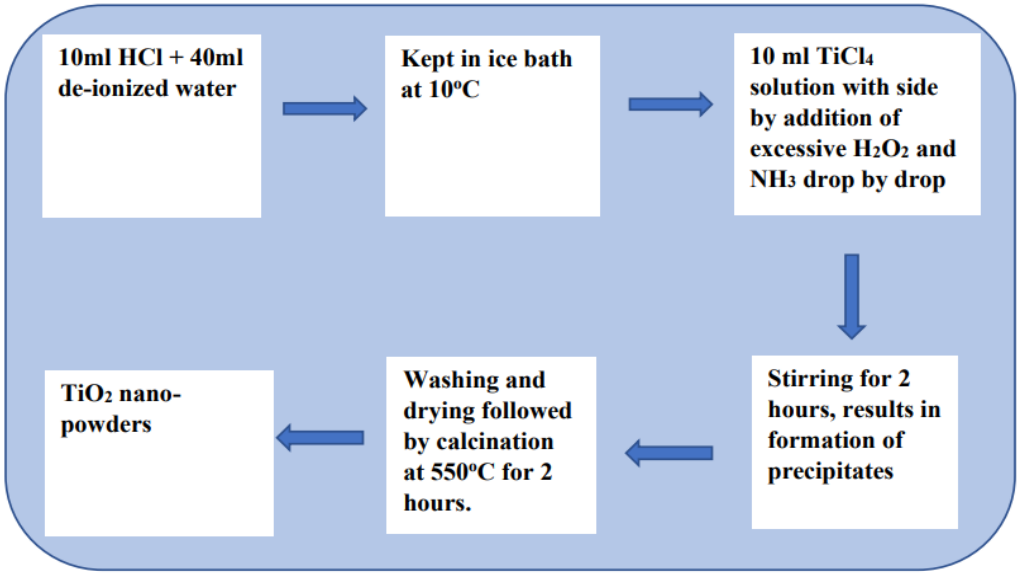

Fig 2.2 Synthesis procedure of titanium dioxide.

2.1.2.2 Synthesis of bismuth titanates ($Bi_4Ti_3O_{12}$)

The penta hydrated form of bismuth nitrate [$Bi(NO_3)_3 \cdot 5H_2O$] and TiO_2 (titanium dioxide) has been taken as the starting material having mole ratio of 3:1. Initially, 3M solution of bismuth nitrate pentahydrate was prepared in double deionized distilled water followed by preparation of 1M solution of TiO_2. The pure TiO_2 nanostructured materials were synthesized by using chemical coprecipitation method**.** Afterwards, the aforementioned prepared solutions were mixed while maintaining a constant stirring. Further, 2M solution of sodium hydroxide (NaOH), which acts a capping agent, was added very slowly in a dropwise manner with continuous stirring for half an hour until the pH approaches to 12. To counteract the early synthesis of bismuth titanate nanoparticles driven by NaOH solution, the above prepared solution was kept for 35 min. on ultrasonic water bath before being poured to stainless steel autoclave, and it was maintained at a filling proportion of 70%. The reaction mixture was heated in autoclave at 200°C for 8 hours and was allowed to cool at ambient temperature after completion of reaction. The resulting precipitates were washed twice with double deionized water and ethanol, separately. Finally, obtained powder was dried in oven at 100°C for 10 hours followed by grinding in pestle mortar for 1 hour. Finally, light orange-colored nanoparticles were obtained.

2.1.2.3 Synthesis of cadmium sulfide nanoparticles (CdS)

Cadmium sulphide nanoparticles have been synthesized by hydrothermal technique with thiourea as a source of sulphur and dehydrated cadmium chloride as a source of cadmium. 1M cadmium chloride solution was prepared in 100ml distilled water followed by dropwise addition of thiourea resulting in turbidity, on further addition of thiourea a transparent clear solution is obtained. The above solution was then put into a stainless-steel vessel lined with Teflon and subsequently exposed to a hydrothermal reaction at a temperature of 200ºC for a duration of 10 hours. Samples were allowed to cool at room temperature followed by washing with ethanol and distilled water many times to obtain final yellow-coloured precipitates of CdS.

2.1.2.4 Synthesis of lead sulfide nanoparticles (PbS)

Hydrothermal procedure has been implemented for synthesis of PbS nanoparticles by using lead chloride as a source of lead and for sulphur source thiourea was used. 1molar solution of lead chloride was prepared in 100ml distilled water further thiourea solution was added dropwise resulting in appearance of turbid solution, on supplementary addition of thiourea transparent a distinct solution was obtained with clarity. Consequently, dropwise addition of 1M sodium sulphide (Na_2S) solution was done with constant stirring until pH reaches to 8-9**.** Afterwards 30 minutes of continuous stirring, the above prepared solution was poured to autoclave having Teflon lining, and endured a hydrothermal reaction at 160ºC temperature for a time period of 8 hour. Afterwards, the autoclave was permitted to cool at ambient temperature conditions. The resulted nanoparticles were centrifuged and rinsed many times with ethanol and deionized water. The powder was dried in oven at 100ºC up to 4 hours. The black coloured precipitates were obtained.

2.1.2.5 Synthesis of CdS doped bismuth titanate nanoparticles

The pre-synthesized yellow coloured CdS nanoparticles (NPs) were mixed with above synthesized Bismuth titanates. The CdS NPs of appropriate mass percentage (0.1%, 0.3% and 0.6% w/w %) were mixed with Bismuth titanate perovskite (BTP) materials in pestle mortar by mechanical method and grind well for 4 hours so that CdS NPs incorporated in BTNPs. The observations about physical properties show that colour transformation takes place from light orange to yellowish appearance and the resulted powder was calcined at 600ºC resulting in improvement of crystallinity of sample and removes the excess moisture. Thereafter, the calcined samples were

characterized by XRD, FTIR and FESEM instrumentation for further detection, identification and purity of above said samples.

2.1.2.6 Synthesis of PbS doped bismuth titanate nanoparticles

The previously prepared bismuth titanates were mixed with black-coloured PbS nanoparticles. By using a pestle mortar to mechanically grind the NPs of various weight percentages (0.1%, 0.3% and 0.6% w/w %) and continued the process of grinding for 5 hours so that PbS NPs successfully absorbed in BTP lattice. The empirical evidence pertaining to physical properties indicates a noticeable alteration in colouration, progressing from a shade of pale orange to greenish shadow and obtained powder was subjected to calcination at 600ºC for a duration of 4 hours. Consequently, obtained nanoparticles were analyzed with XRD, FTIR, DRS-UV, XPS, EPR, HR-TEM and FESEM characterizations for further analysis and recognition of the phase and purity of aforementioned samples.

2.1.2.7 Synthesis of graphene oxide

Graphene oxide was synthesized by modified hummer's method. First of all, 60ml of sulphuric acid (95%) was taken in a beaker followed by addition of 1g of graphite powder resulting in appearance of black coloured solution. Then ice bath was setup, 2.5g of $KMNO_4$ was added very - very slowly by maintaing the temperature of solution at 0-5ºC. The subsequent solution was set aside on magnetic stirrer for 3 hours with ice bath (ice bath was removed after 20 minutes). After 3 hours of continuous stirring, 50mL water was added dropwise. After some time, the colour was changed to dark brownish followed by further addition of 100mL water instantly. Then, 2 mL of hydrogen peroxide (30wt%) was added instantly. Finally, filtration, washing with water and 10% HCl solution was done. The resultant powder was allowed to dry in oven for a time period of 4 hours at 100ºC.

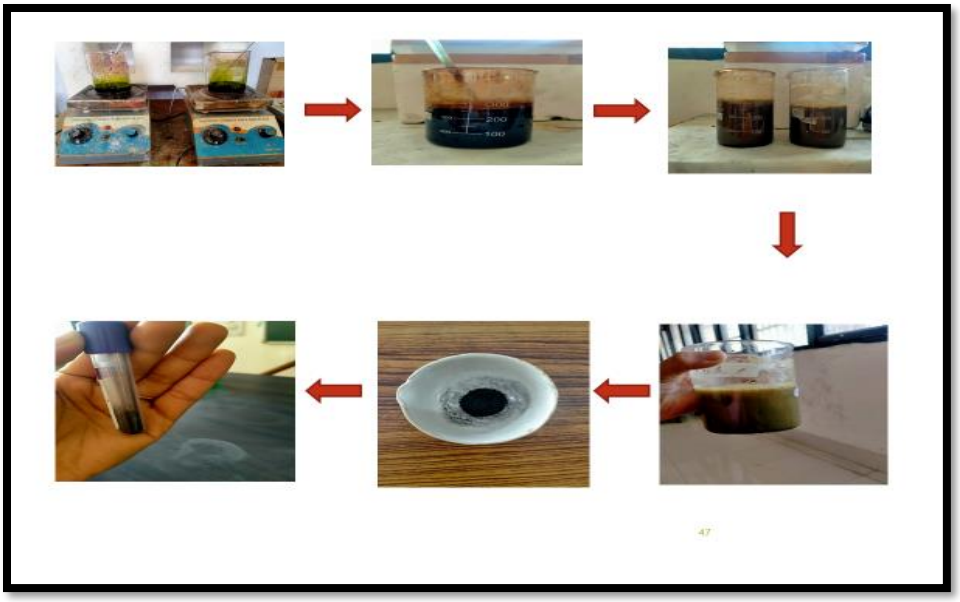

Fig 2.3 Schematic illustration for preparation of graphene oxide.

2.1.2.8 Synthesis of GO composite with CdS doped bismuth titanate nanoparticles

Specifically, 0.3 g of prepared 0.1%, 0.3% and0.6% CdS doped bismuth titanates were carefully mixed with 1 wt% of GO as synthesized by modified hummers method by mechanical method and ground well up to 2 hours in pestle mortar followed by calcination at 600^{o}C. The motivation behind the grinding of CdS/BT and GO is to incorporate the GO nanoparticles in CdS/BT. The resulted powder of CdS/BT and GO composite was employed to determine the influence of graphene oxide on hydrogen gas production efficiency by photocatalytic splitting of water.

2.1.2.9 Synthesis of GO composite with PbS doped bismuth titanate nanoparticles

To prepare the composite of PbS/BT with GO, 1 wt% of graphene oxide synthesized by modified Hummer's method, was mixed well with 0.3 g of 0.3% and 0.6% PbS doped bismuth titanates by mechanical method and ground well up to 2 hours in pestle mortar followed by calcination at 600^{o}C. Resulting in incorporation of GO into PbS/BT and further examined for GO effect on enhancement in photocatalytic efficiency for hydrogen production.

2.2 Characterization techniques

Prior to test the photocatalytic efficiency of synthesized sample to evolve hydrogen through splitting of water, various spectroscopic methods were employed to analyze the photocatalysts.

However, the materials which showed best results for hydrogen production were further analyzed by various sophisticated analytical techniques. In the present work, the frequently employed characterization techniques are XRD, FTIR, DRS-UV, FE-SEM, Gas chromatography having thermal conductivity detector (GC-TCD) and XPS, EPR, HR-TEM for deep understanding of photocatalysts about their morphological, structural features, oxidation states and distribution of unpaired electrons. Hence to further elucidate, the characterization techniques are essential and the following section gives a brief discussion of theoretical context and operational outline of these characterization techniques.

2.2.1 XRD

To study about crystallographic structure, identification of phase and lattice size, XRD is the most widely used non-destructive technique. Further, there is no requirement of sample preparation for analysis. Fig 2.4 depicts the basic representation of XRD technique**.**

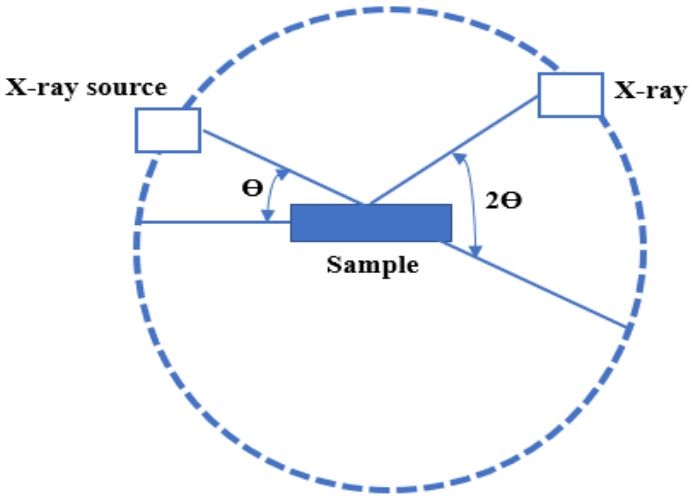

Fig 2.4 X-ray diffraction – an overview.

The XRD spectrum was recorded on Bruker D8 diffractometer and Cu Kα was used as a source of radiation having λ = 1.54056 Å. The sample was taken in powdered form. The sample follows Bragg's law, when X-rays strikes on it and interact with crystal lattices, producing constructive interference. In accordance with Bragg's law, the path length difference of reflected beam's is an integer multiple of wavelength of used x-rays[5]. Where,

$$n\lambda = 2d\sin\theta$$

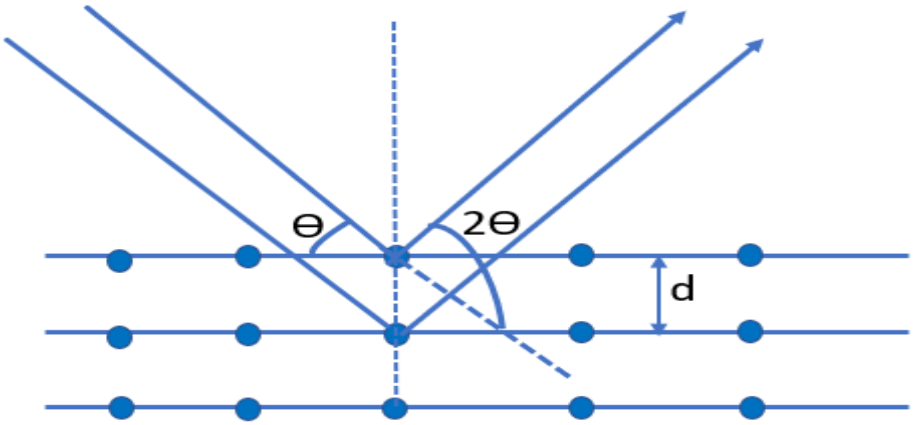

Fig 2.5 Schematic representation of Braggs Constructive diffraction.

Where, n = order of diffraction (integer)

d = the interplanar distance between consecutive parallel planes

λ = wavelength of X-rays

θ = glancing angle

To identify an unknown sample, examine the PXRD patterns produced by samples that have various atom arrangements in the crystal lattice. Debye Scherrer formula was utilized to calculate the size of crystallites:

$$D = 0.89\,\lambda/\beta\cos\theta$$

The diffraction pattern of samples was captured in the 2θ range of 20º to 80º. The acquired diffraction patterns are then compared to typical JCPDS patterns.

2.2.2 FTIR

To identify the functional groups, present and structural analysis of materials, they are exposed to infra-red radiations, absorption of radiations at characteristic frequencies takes place due to the vibration of chemical bonds at particular frequencies. The spectral range employed for scanning the samples was 4000-400 cm^{-1}. Fig 2.6 depicts the instrumentation of FTIR spectroscopy.

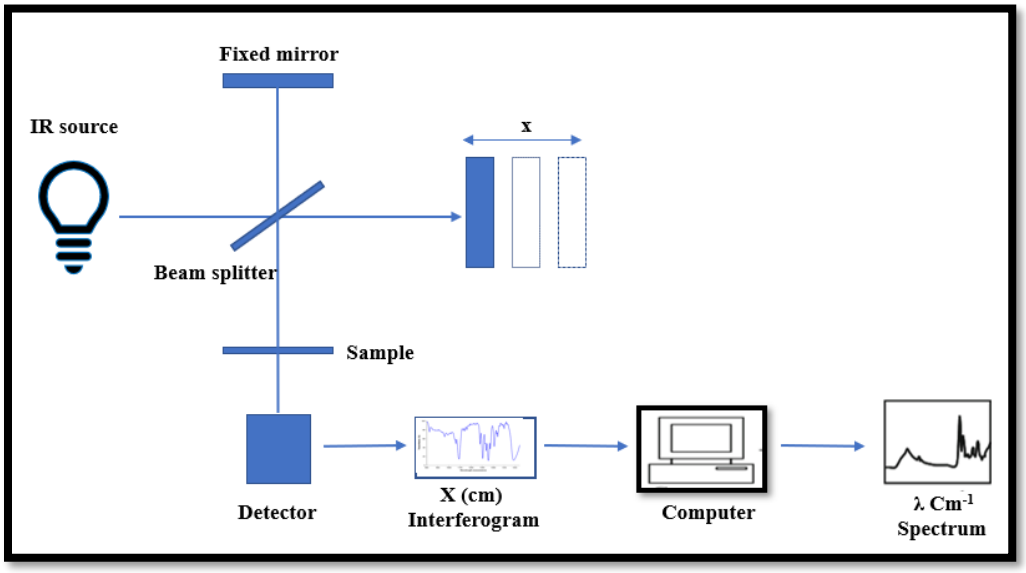

Fig 2.6 Instrumentation of FTIR spectroscopy.

The method reveals precise details regarding the molecular structures, rotational modes, chemical bonds, and mode of vibration that exist in the sample. This methodology serves as a distinctive identifier of the interatomic connections within the specimen. Given that any substance is an exclusive integration of particles, with no other compounds exhibiting precisely the similar composition and also known as finger print spectrum.

Below is the description of how FTIR works[6]:

I. Source: the beams generated by the black body source pass across the aperture and falls on the given sample.
II. Interferometer: Inside the interferometer, the encoded beam moves towards the material being studied.
III. The sample: The incident beam that comes from the interferometer impinges upon the samples, and the response of the samples varies depending on the frequency of the beam, whereby absorption, transmission, or reflection may occur.
IV. Detector: A detector is used for detection of beam that comes from the sample.
V. Reflection gratings: stray beams are avoided by this.
VI. Mirrors: For focusing and redirecting of IR radiations.

VII. The computer: Finally, the graph is displayed by decoding the signals by computer Fourier transform.

2.2.3 DRS-UV- Visible

The diffused reflection spectrum (DRS-UV) was assessed for the photocatalysts by means of a Perkin Elmer Lambda 900 spectrophotometer with in a range of 200-800nm. Basically, the spectrophotometer detects only the diffused reflected light by the specimen being studied. Reflection of light takes place from the sample when it is irradiated to UV-visible light of solar spectrum and UV-visible-DRS spectrophotometer detects this reflected light by photodetector and gives information in the form of spectrum. Upon irradiation by UV-vis light, electronic transitions take place resulting in photo-excitation of electrons from ground state (GS) to excited state (ES). Different types of electronic transitions take place like σ and π transitions, d and f electronic transitions and charge transfer transitions may occur. The absorption versus wavelength spectrum has been given by this analysis.

This spectrophotometer, gives information about structural features of sample and optical characteristics such as band gap. The band gap difference of the photocatalyst was resolved from Tauc plot by making use of absorption data.

$$(\alpha h\nu)^{1/n} = A\,(h\nu - E_g)$$

Where,

α = is the absorption coefficient

A = constant of proportionality

$h\nu$ = the energy of incident photons

E_g = band edge potential of material in eV

n = nature of electronic transitions taking place between VB and CB (n= 1/2 for direct transition while n= 2 for indirect band transitions)[7].

The energies of band gap were calculated by Tauc plots giving spectrum between $(\alpha h\nu)^{1/n}$ vs. $h\nu$.

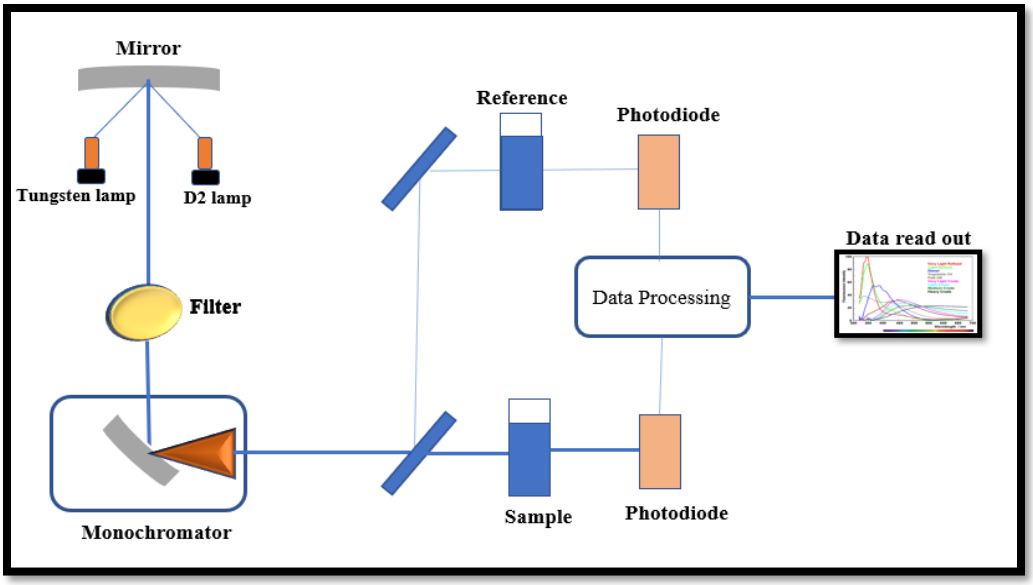

Fig 2.7 Working principle of UV-Visible spectrophotometer.

2.2.4 FESEM

FESEM (JEOL) working on an accelerating voltage of 20kV, was utilized to examine the morphologies and lattice arrangements of as-prepared nanomaterials. It is most extensively employed electron microscopy technique utilized for the analysis of the surface characteristics and morphological attributes of synthesized photocatalysts. In this technique, the topography of the specimen is scanned by highly energetic electron beam in a raster scan pattern.

A highly energetic electrons beam, ejected from electron gun passing through the monochromator and electromagnetic lenses is bombarded on the sample surface. These electron beam results in scanning of the surface of sample, interacting with the atoms lying on the surface, various phenomenon takes place such as reflection, scattering, ejections of atoms of surface and resulting in production of secondary electrons, photons, x-rays, backscattered electrons and auger electrons. The detectors detect the secondary electrons and transforms the amplified signals to various images providing morphological information[8].

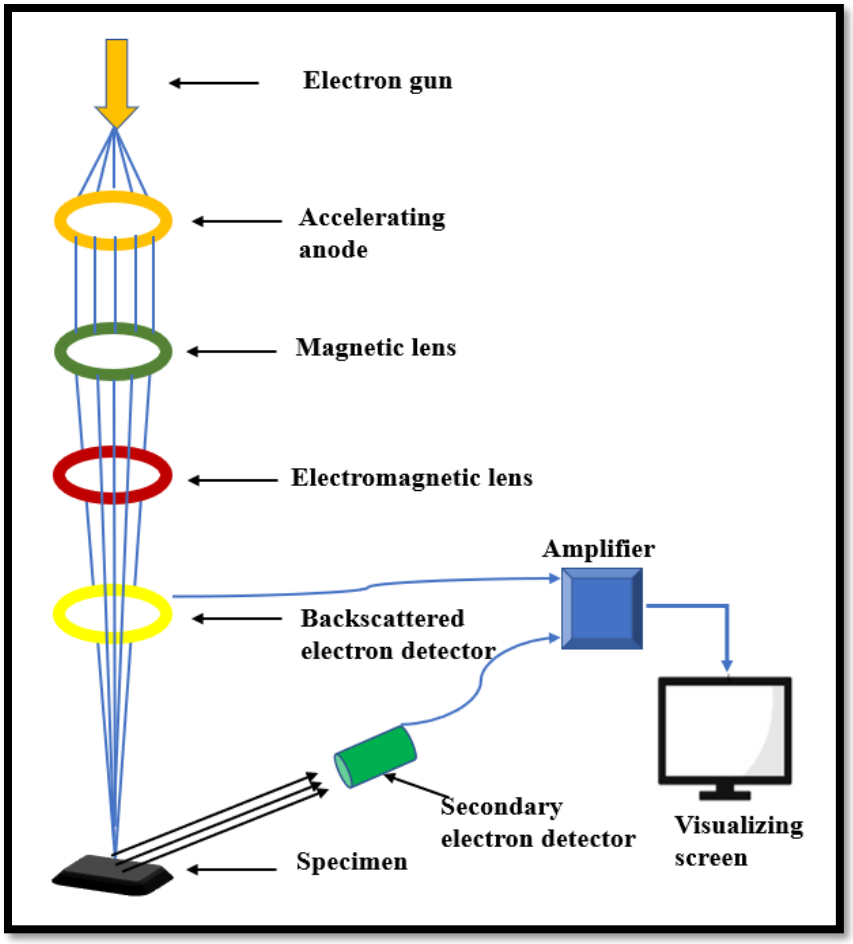

Fig 2.8 Schematic representation of FE-SEM working principle.

2.2.5 HR-TEM

The HR-TEM is a remarkable technique helpful in evaluation of the inner structure of crystals, particle size, and morphology of nanomaterials. In this work HRTEM pictures were recorded by JEOL (JEM 2100) plus electron microscope providing high quality images with good resolution and clarity.

Equivalent to a conventional microscope, the transmission electron microscope functions in the similar manner. In a conventional microscope, visible light concentrated on the object produces the images, however in a transmission electron microscope (TEM), electrons hitting on a fluorescence screen provide an image.

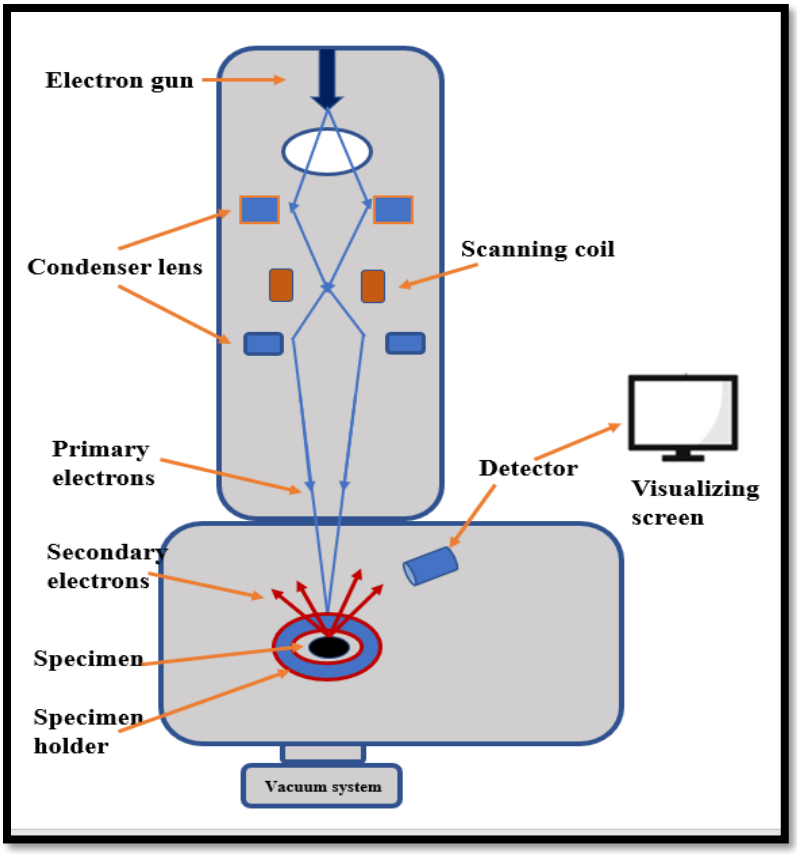

Fig 2.9 Block diagram for instrumentation of HR-TEM.

Highly energetic beams of electrons are used in this technique for bombarding a sample surface and deals with the secondary electrons transmitted by the sample. An electron gun was used in this analysis for ejection of electrons. The electron beam was ejected, accelerated followed by focusing on the sample by condenser lenses. Further, the secondary electrons were spotted by the detector and the picture was produced on the luminescence screen[9].

2.2.6 XPS

Electron Spectroscopy for Chemical Analysis (ESCA) is an additional acronym for XPS. Physical Electronics having Model- PHI 5000 Versa Probe III has been employed for surface assessment of the developed photocatalyst in the present study. It assists both qualitative and quantitative determination of the elements located on the surface of the sample. It delivers information about the oxidation states and chemical composition of elements presents in photocatalyst. Basically, XPS spectroscopy deals with the electrons of core shells hence determining the binding energy and chemical characteristics of inner electrons.

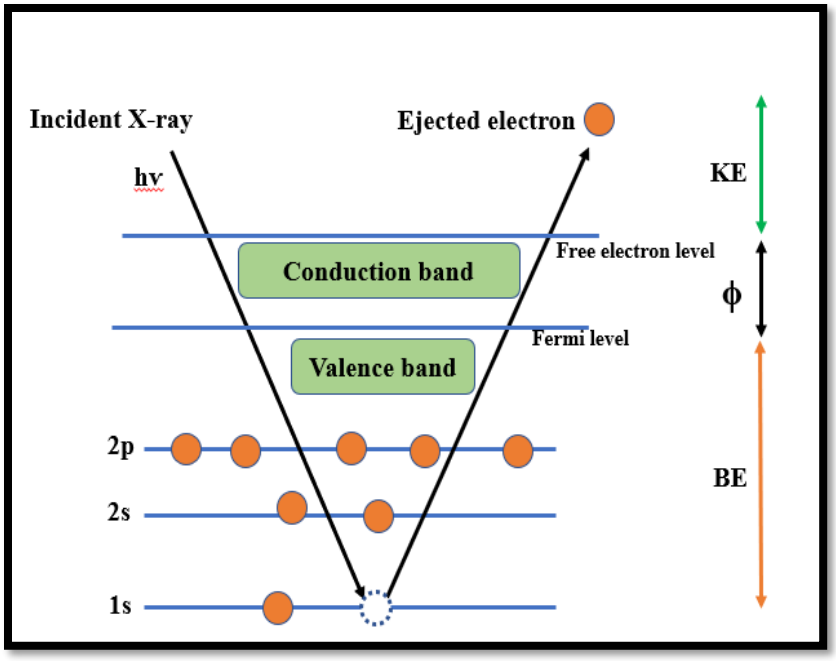

Fig 2.10 An overview of working principle of XPS.

The solid samples are bombarded with the X-rays (Al Kα or Mg Kα as a source) having specific energy and giving the spectrum as a plot between number of ejected electrons vs. their binding energy (in eV). This analysis is based on the photoelectric effect. When photons of specific energy strike the sample surface, core shell electrons were ejected and their kinetic energy (KE) was measured. The KE of ejected electrons depends on the intensity of incident X-rays additionally, also affected by binding energy of core shell electrons. Hence, by knowing about KE, binding energy of ejected electrons an also be calculated[10].

2.2.7 EPR

Paramagnetic electron resonance spectroscopy, commonly denoted as electron spin resonance (ESR), is a notable scientific tool employed for the scientific study of molecules that possess unpaired electrons. This technique harnesses microwave radiation to facilitate the analysis. When the chemical species with unpaired electrons (behaving as tiny magnets) are positioned in constant magnetic field, their magnetic axes partially align along the magnetic field. An electron paramagnetic resonance spectrum is obtained by measuring the absorbed radiation as a function of the changing variable when either the stationary field or microwave frequency are varied.

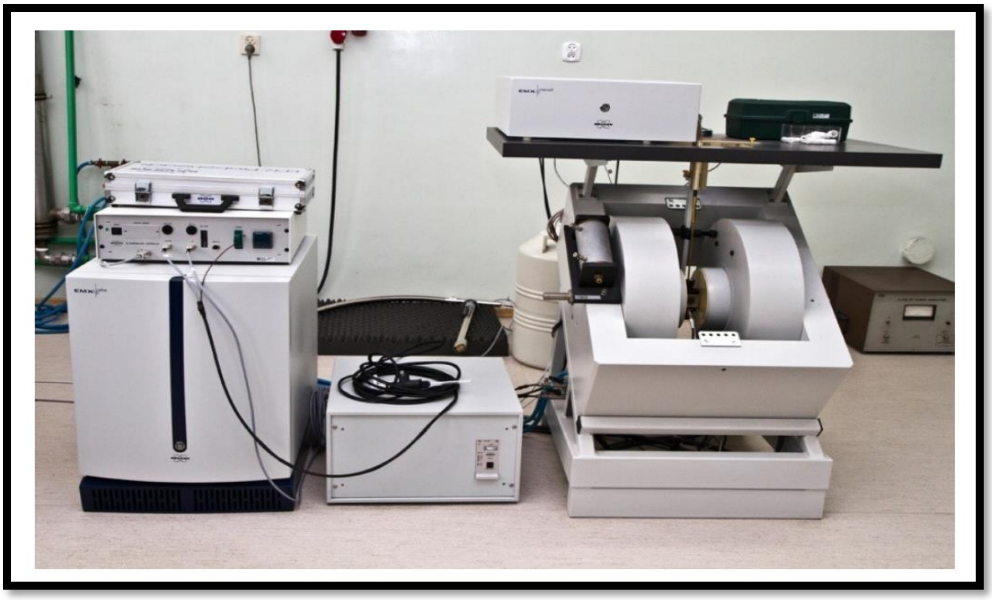

Fig 2.11 Instrumentation of electron paramagnetic resonance.

The spectrum commonly represented as a plot of the absorption of microwave energy against a stationary magnetic field that has been applied. The Lande splitting factor (g) values can also be obtained from EPR spectrum[11].

In this thesis work, EPR spectroscopy is done by using the BRUKER BIOSPIN, Model EMX micro A200-9.5/12/S/W.

2.2.8 GC-TCD

The gas chromatography is an effective method for separation and evaluation of gaseous components. Gas chromatography constitute the three basic fundamental components:

a) column (a stationary phase),
b) carrier gas (a mobile phase),
c) a detector.

Fig 2.12 demonstrates the components of GC apparatus. Firstly, the moving phase is permitted to run along the column followed by injection of sample in injection port through micro syringe.

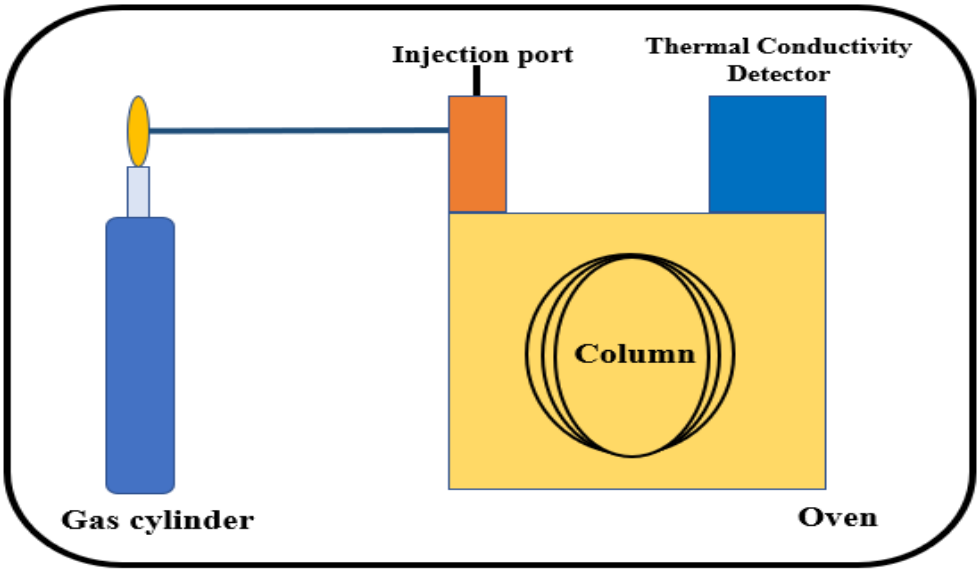

Fig 2.12 Components of gas chromatography.

During the process, the analyte sample is transported through the column, where it interacts with the column's wall or packing material, resulting in adsorption of the analyte molecules. The rate of flow of analyte constituents is determined by the molecules of stationary phase. Thereby, carrier gas plays an important role, He, N_2, H_2 and Ar are commonly used carrier gases. Although, the most commonly used carrier gas is Ar for detection of hydrogen gas, due to its superior thermal conductivity, as opposed to He or N_2 gas.

The most frequently used detectors in gas chromatography are thermal conductivity and flame ionization detector also known as TCD and FID respectively. However, for detection of gaseous components the most widely used is TCD detector[12].

In the present work, Gas chromatography has been used for detection and quantitative estimation of the amount of hydrogen gas evolution during photocatalytic splitting of water. A gas chromatograph with Ar as a carrier gas and equipped with TCD detector is used for analysis.

2.3 Photocatalytic splitting of water

Photocatalytic efficiency of the photocatalyst was assessed via splitting of water with the help of photoreactor. For this, external irradiation cell made up of quartz, linked to a gas-closed circulation system, was utilized for water splitting reaction. 0.01 g of the photocatalyst (in powdered form) was suspended in round bottom flask having 40ml of water and was placed on a magnetic stirrer.

Subsequently, a rubber septum was utilized to seal the reactor, and the mixture was subjected to sonication until accomplishing uniform dispersion of photocatalytic material. To ensure homogeneity, the resultant mixture was subjected to continuous stirring throughout the course of the experiment. The high-pressure Xenon lamp with cut of filter was used as the light source. N_2 gas was used for purging to remove the dissolved O_2 or any other gas after sealing the chamber. The aliquots were collected in air tight syringe after fixed intervals of time. The evolution of hydrogen gas was spotted by employing GC-TCD with N_2 as a carrier gas.

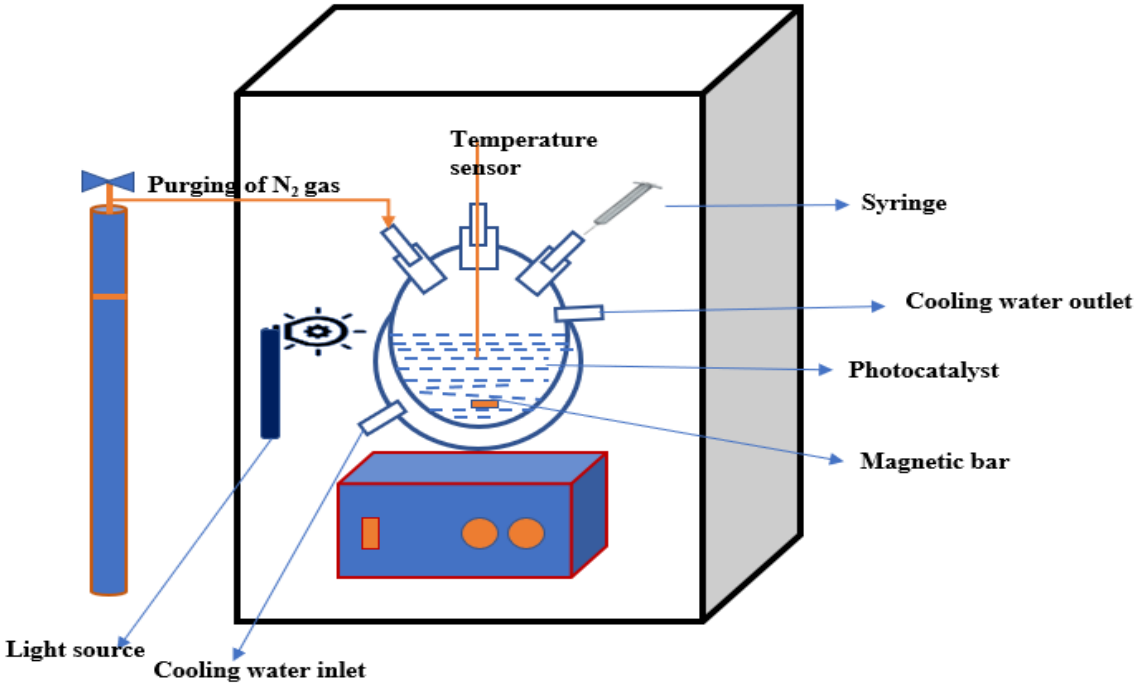

Fig 2.13 Illustration of photoreactor setup.

References:

(1) Hayashi, H.; Hakuta, Y. Hydrothermal Synthesis of Metal Oxide Nanoparticles in Supercritical Water. Materials (Basel). 2010, 3. https://doi.org/10.3390/ma3073794.

(2) Kumar, D. Hydrothermal Methods Of Nanoparticles : An Overview. 2019, 6 (1), 700–702.

(3) Gan, Y.; Jayatissa, A.; Yu, Z.; Chen, X.; Li, M. Hydrothermal Synthesis of Nanomaterials. J. Nanomater. 2020, 2020, 1–3. https://doi.org/10.1155/2020/8917013.

(4) Rathod, P. B.; Nemade, K. R.; Waghule, S. A. Study of Structure and Optical for Chemically Synthesized Titanium Dioxide Nanoparticles. Int. J. Chem. Phys. Sci. 2015, 4, 491–495.

(5) Bunaciu, A. A.; UdriŞTioiu, E.; Aboul-Enein, H. X-Ray Diffraction: Instrumentation and Applications. Crit. Rev. Anal. Chem. / CRC 2015, 45. https://doi.org/10.1080/10408347.2014.949616.

(6) Khan, S.; Khan, S.; Khan, L.; Farooq, A.; Akhtar, K.; Asiri, A. M. Fourier Transform Infrared Spectroscopy: Fundamentals and Application in Functional Groups and Nanomaterials Characterization. In Handbook of Materials Characterization; 2018; pp 317–344. https://doi.org/10.1007/978-3-319-92955-2_9.

(7) Jayakumar, S. Components, Principle and Applications of UV Vis-Spectophotometer; 2016. https://doi.org/10.13140/RG.2.1.1142.6805.

(8) Kim, Y.; Park, C. Principle of Field Emission-Scanning Electron Microscopy (FE-SEM) and Its Application to the Analysis of Carbon Nanostructures. Carbon Lett. 2001, 2.

(9) Hettler, S.; Dries, M.; Zeelen, J.; Oster, M.; Schröder, R.; Gerthsen, D. High-Resolution Transmission Electron Microscopy with an Electrostatic Zach Phase Plate. New J. Phys. 2016, 18, 53005. https://doi.org/10.1088/1367-2630/18/5/053005.

(10) Sudhanshu, R. X-ray Photoelectron Spectroscopy (XPS) Technology; 2020.

(11) Pan, Y.; Nilges, M. Electron Paramagnetic Resonance Spectroscopy: Basic Principles, Experimental Techniques and Applications to Earth and Planetary Sciences. Rev. Mineral. Geochemistry 2014, 78, 655–690. https://doi.org/10.2138/rmg.2014.78.16.

(12) Kaur, G.; Sharma, S. Gas Chromatography -A Brief Review. 2018.

CHAPTER 3

Synthesis and characterization of bismuth titanate perovskite materials for hydrogen production

3.1 Introduction

As environmental pollution by greenhouse gases and the energy crisis due to limited availability of fossil fuels strengthen, photocatalysis, a "green" approach, is significant in the utilization of solar energy for generation of renewable source of energy along with the degradation of pollutants released by industries. The industrial waste releases are significant organic pollutants (dyes) thereby affecting the aquatic life, human health and ecosystem. Waste water is the primary root of pollution, eutrophication, and disruption to marine organisms in ecosystem. TiO_2 has a number of benefits which makes it a highly effective photocatalyst, including thermal stability, affordability, nontoxicity, and significant photocatalytic activity. However, the use of TiO_2 photocatalyst's is constrained by its poor quantum efficiency and 3.2 eV of wide band gap energy[1]. Researchers have developed a variety of photocatalysts with improved efficiency for solar light absorption showing utilization of visible light. At present, a number of oxides like $BiVO_4$, $SrTiO_3$, and Bi_2WO_6 have been found to exhibit photocatalytic activity[2]. Recently, a major family of photocatalysts including bismuth-titanate based perovskite photocatalysts particularly $Bi_4Ti_3O_{12}$, $Bi_{20}TiO_{32}$, $Bi_2Ti_2O_7$ and Bi_2TiO_{20} have gained attention because of absorption of light in visible region. The valence band of bismuth-doped semiconducting materials, is composed of hybrid orbitals of the Bi 6s and 2p of oxygen atom, resulting in a lower bandgap, contrary to other metal oxides acting as semiconductors whose VB is typically consisting of the 2p orbital of oxygen atom. The valence band edge potential of Bismuth titanate is 1.12eV while the conduction band potential is -1.88eV which is more negative than the potential of redox couple $H+/H_2$ (0V Vs NHE) and O_2/H_2O (1.23eV Vs NHE)[3]. As a result, bismuth-based semiconductor materials have good visible light absorption. In last decade, several approaches have been developed by researchers to check the efficiency of bismuth titanates in presence of solar light. Krishnendu Das et. al. successfully synthesized CdS doped Bismuth titanates by hydrothermal method and further showing the hydrogen production rate of 1890µmol/g/h by water splitting reaction[4]. Similarly, hybrid phase Aurivillius type of $Bi_4Ti_3O_{12}$ and $Bi_2Ti_2O_7$ pyrochlore type bismuth titanates have been synthesized by Huihui G. et. al. adopting solid state method and studied the dye degradation of

Rhodamine[5]. From the above reports, it is undeniable that photocatalysts based on bismuth type semiconductors have grown in importance.

In this study, a low temperature assisted hydrothermal method have been adopted for synthesis of bismuth titanate perovskite nanomaterials and checked their efficiency for generation of hydrogen from splitting of water. Different sacrificial agents like methanol and TEOA were used to enhance the efficiency for water splitting.

3.2 Experimental section

3.2.1 Synthesis procedure of TiO_2:

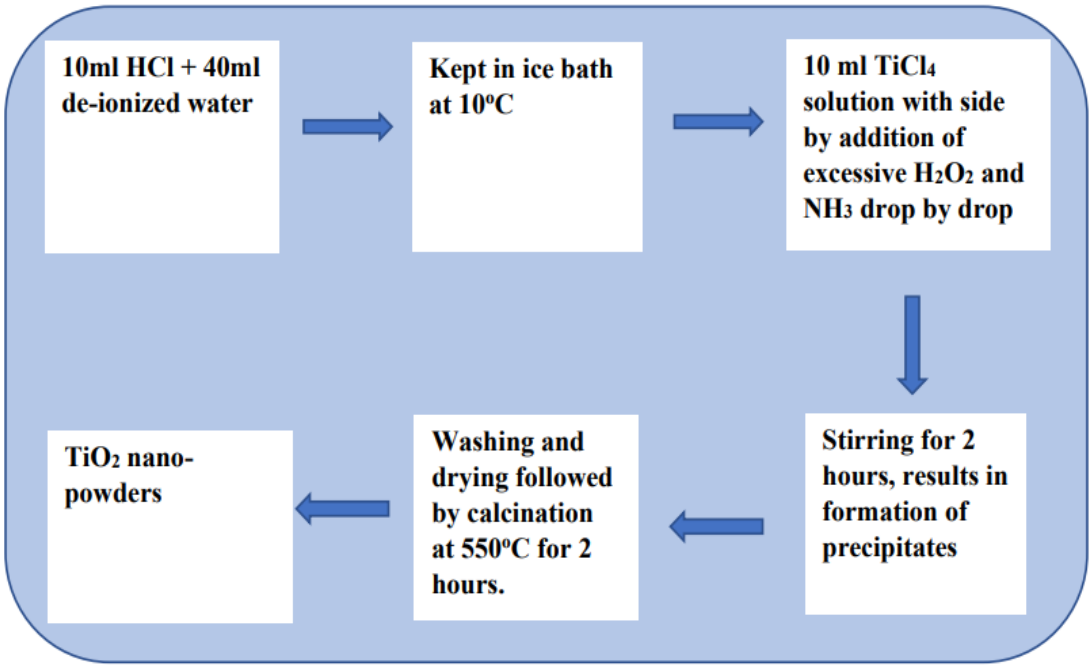

Fig 3.1 Flow chart for synthesis of titanium dioxide.

3.2.2 Preparation of bismuth titanate photocatalysts

The chemicals were of analytical grade and have been purchased from HIMEDIA chemicals. No further purification was needed before usage. The surfactant free pathway has been chosen for preparation of bismuth -based titanate nanomaterials. The penta hydrated form of bismuth nitrate [$Bi(NO_3)_3 \cdot 5H_2O$] and TiO_2 (titanium dioxide) has been taken as the starting material having mole ratio of 3:1. Initially, 3M solution of bismuth nitrate pentahydrate was prepared in double

deionized distilled water followed by preparation of 1M solution of TiO_2. The pure TiO_2 nanostructured materials were synthesized by using chemical co-precipitation method**.**

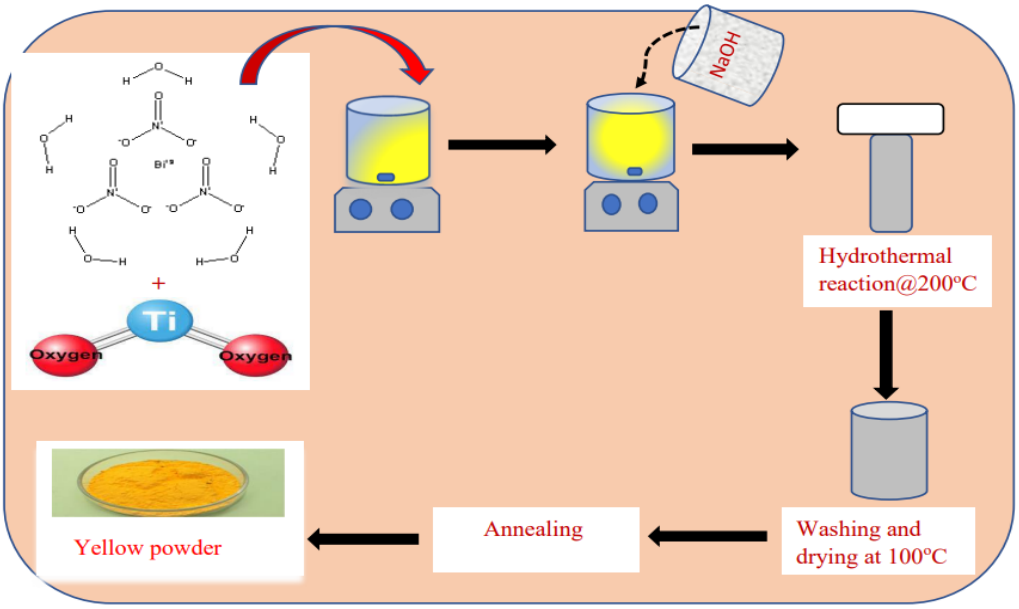

Fig 3.2. The steps for preparation of bismuth titanates.

After that the above prepared solutions were mixed with continuous stirring. Further, 2M solution of sodium hydroxide (NaOH), which acts a capping agent, was added very slowly in a dropwise manner with continuous stirring for half an hour until the pH approaches to 12. To counteract the early synthesis of bismuth titanate nanoparticles driven by NaOH solution, the above prepared solution was kept for 35 min. on ultrasonic water bath before being poured to stainless steel autoclave, and it was maintained at a filling proportion of 70%. The reaction mixture was heated in autoclave at 200ºC for 8 hours and was allowed to cool at ambient temperature after completion of reaction. The resulting precipitates were washed twice with double deionized water and ethanol, separately. Finally, obtained powder was dried in oven at 100ºC for 10 hours followed by grinding in pestle mortar for 1 hour. Finally, light orange-coloured nanoparticles were obtained.

3.3 Characterization of bismuth titanate photocatalysts

The structural properties of the obtained nanomaterials were analyzed by Bruker D8 Advance X-ray diffractometer having Cu Kα as a source of radiation, in 2θ range of 20-70º in step scan mode of 5s. The diffused reflectance spectroscopy (DRS- UV) was employed for the dry-pressed disk sample using a Perkin Elmer Lambda 900 spectrophotometer equipped with an integrating sphere

assembly, for calculation of band gap energy. The surface morphology was verified through FESEM (JEOL) or field emission scanning electron microscopy. The FTIR (Perkin Elmer) spectroscopy helps in the study of functional groups by scanning in 400cm^{-1} to 4000cm^{-1} range. The photocatalytic activity of the nanomaterials was observed with the help of photoreactor consisting of xenon lamp.

3.4 Photocatalytic activities test

The water splitting efficiency of synthesized nanoparticles has been analyzed by use of photoreactor consisting of two xenon lamps of 250 W each, were employed for light irradiation. A round bottom flask, having 0.10g photocatalyst in 100mL water (0.01mmol^{-1}), was kept on magnetic stirrer. Then, while being stirred magnetically, the solution was continuously exposed to light irradiation. The desired amount of suspension was taken at fixed intervals of time and was analyzed by GC-TCD.

3.5 Results and discussion

3.5.1 XRD spectrum

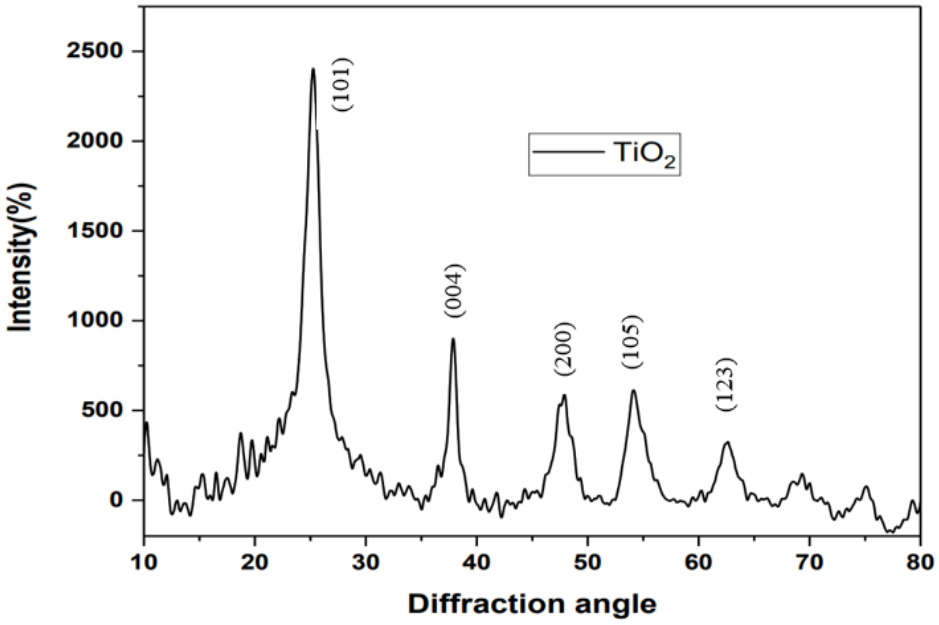

Fig. 3.3 XRD pattern of titanium dioxide.

The XRD pattern of TiO_2 nanoparticles has been depicted in Figure 3.3. According to the standard JCPDS card no. 21-1272, all diffraction peaks correspond to pure anatase phase[6]. No peaks were detected for brookite phase, rutile phase or any other impurities.

Figure 3.4 illustrates the XRD peaks of the hydrothermally synthesized BT spheres. The literature and diffraction pattern can be correlated with layered perovskite $Bi_4Ti_3O_{12}$[7]. From this pattern, there were no peaks of contaminants found. The high crystallinities of the BT samples are indicated by the strong and sharp peaks. The diffraction angle at 2θ - 30.2°, corresponding to (JCPDS Card no. 50-0300) and at 2θ - 21.8°, 32.8°, 39.7°, 47.2°, 51.8°, 57.2° can be indexed to orthorhombic bismuth titanate perovskite (JCPDS Card no. 35-0795). Additionally, by applying the scherrer formula to the XRD results for most intense peak at 2θ – 30.2°, the crystallite size is 30.20nm.

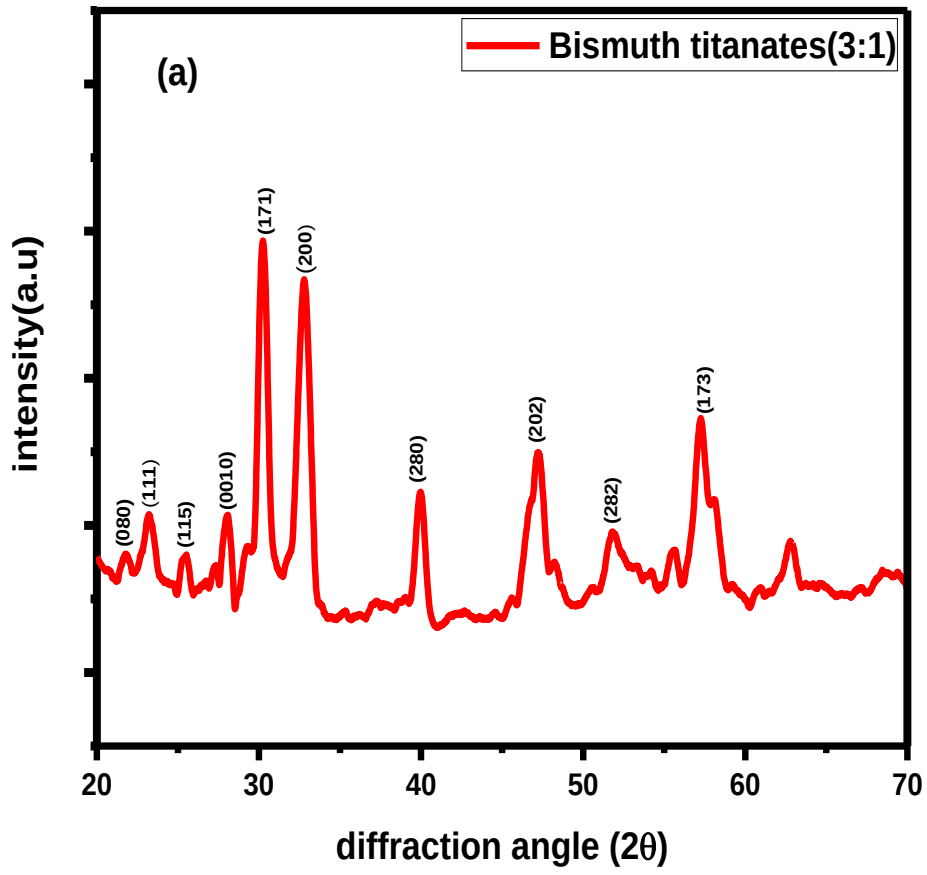

Fig 3.4 XRD spectrum of bismuth titanates.

3.5.2 FTIR

At room temperature, the FTIR spectral analysis was carried out in range of 400-4000cm^{-1}. The calcined BTP nanomaterials show only two predominant peaks at 546cm^{-1} and 818cm^{-1}. The sharp peak at 546cm^{-1} is characteristic of $Bi_4Ti_3O_{12}$[8]. The peak position at 818 cm^{-1} is attributed to Ti-O stretching vibration and also due to O-Ti-O stretching vibration of TiO_2.

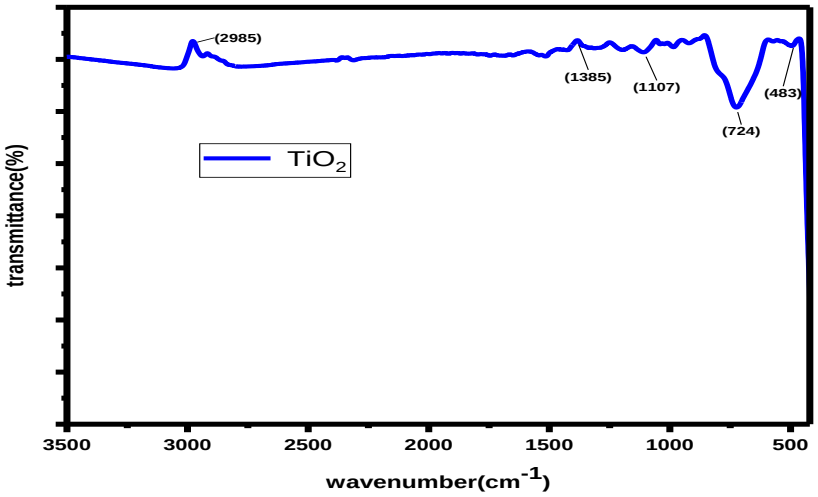

Fig 3.5 FTIR spectra of titanium dioxide.

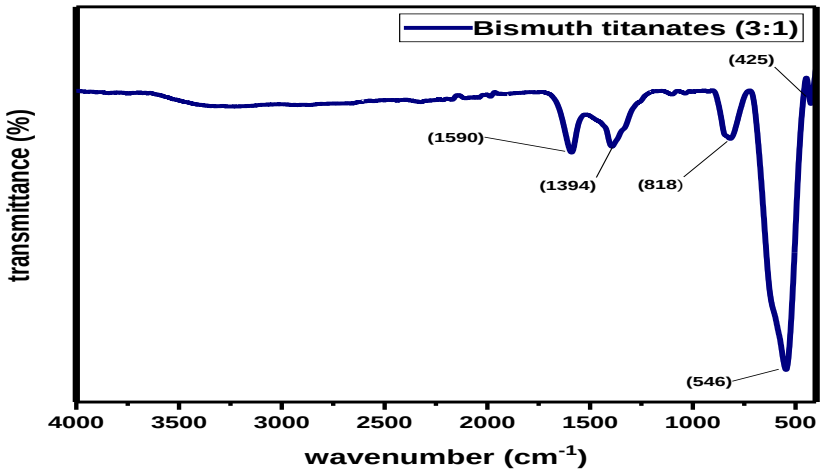

Fig 3.6 FTIR spectrum of bismuth titanates.

3.5.3 FESEM

Fig 3.7 reveals the formation of sheet like nanoparticles giving rise to resulting structure of nanosheets (having larger surface area giving rise to greater number of photocatalytic reactions) growing out from the microspheres. Bismuth titanates have mostly spherical morphology with agglomeration in the low resolution. The well packed morphology is a typical representation of layered bismuth titanates. Moreover, nanoparticles were found crispy in nature showing insertion of nanosheets in xy plane.

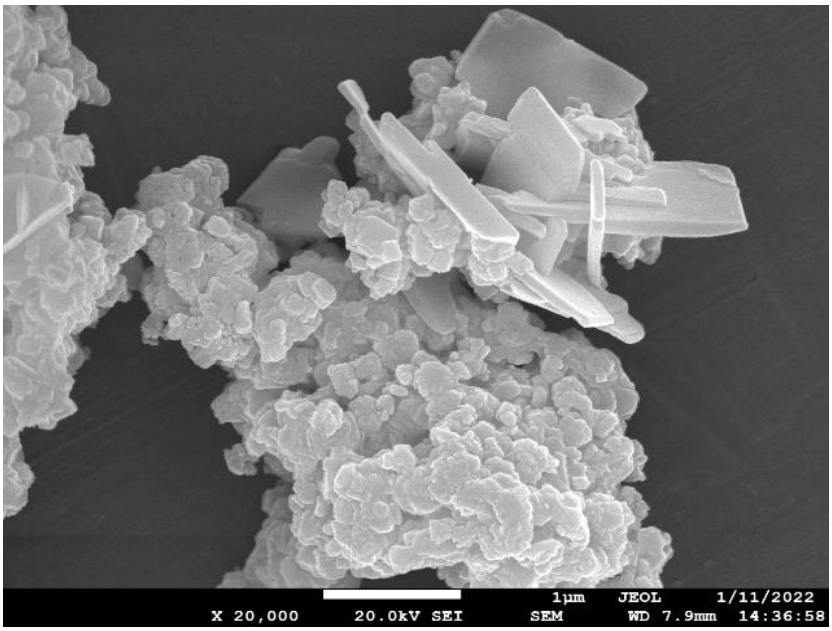

Fig 3.7 FESEM image of Bismuth titanates.

3.5.4 UV-visible spectra

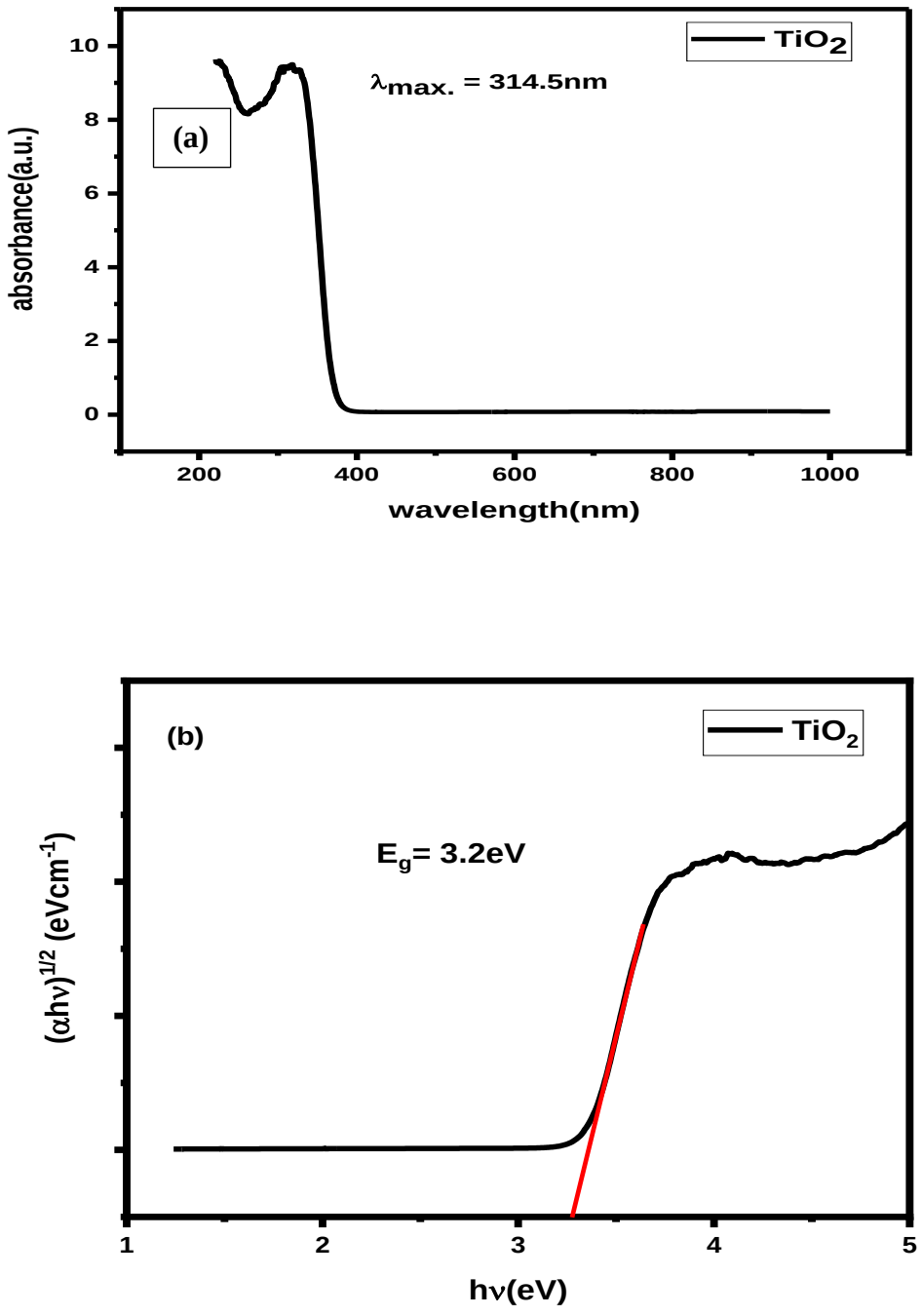

Fig 3.8 (a) UV absorbance of titanium dioxide (b) tauc plot of Tio_2.

Titanium dioxide absorbs ultraviolet light at 314.5 nm and showing the band gap of 3,2eV. The UV spectra of bismuth titanates shows the maximum absorption of light at 323.43 nm, indicating the absorption of ultraviolet light[9]. The band gap of 3.25eV has been calculated from the tauc plot indicating the absorption of light in ultraviolet region.

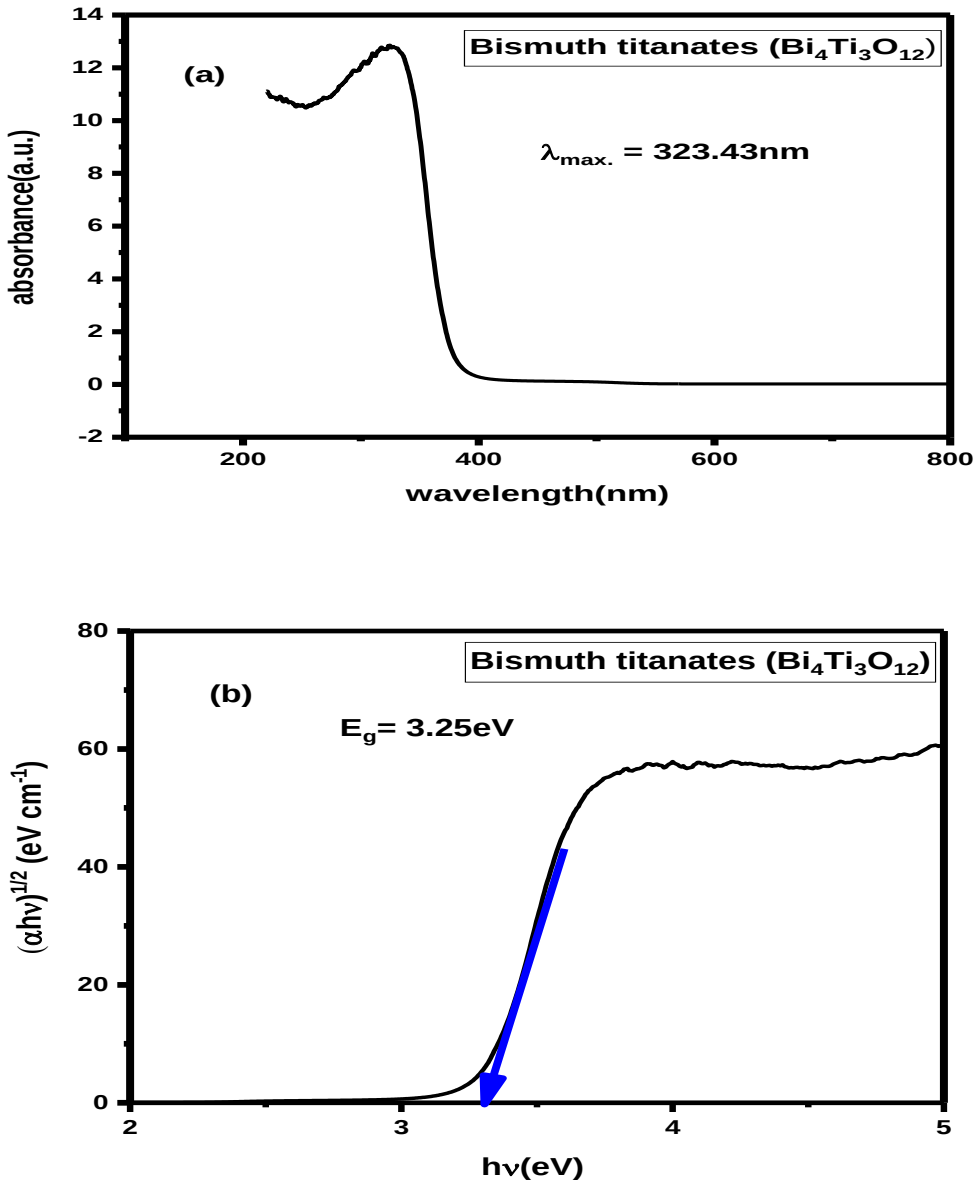

Fig 3.9 (a) UV-visible spectra for absorbance and (b) tauc plot for BT.

3.5.5 Experiment procedure of hydrogen production by bismuth titanates

The hydrogen generation efficiency of bismuth titanates synthesized by hydrothermal route was examined by splitting of water under light irradiation in photoreactor cell. In the experiment, 0.10g of photocatalyst was suspended in 100mL of H_2O taken in round bottom flask (RBF) under vigorous magnetic stirring(450rpm). When the light radiations from the Xe lamp (2 lamp of 250W each) have been allowed to fall on RBF the reaction starts leading to generation of electron-hole pairs. After 2 hours of continuous illumination the gas was collected in gas tight syringe and measured by GC-TCD with flow of helium and nitrogen as a carrier gas. After that, the experiment was performed by suspending TEOA and methanol respectively (acting as sacrificial agents), along with the photocatalyst in water and checked their hydrogen production efficiency as shown in fig 3.10.

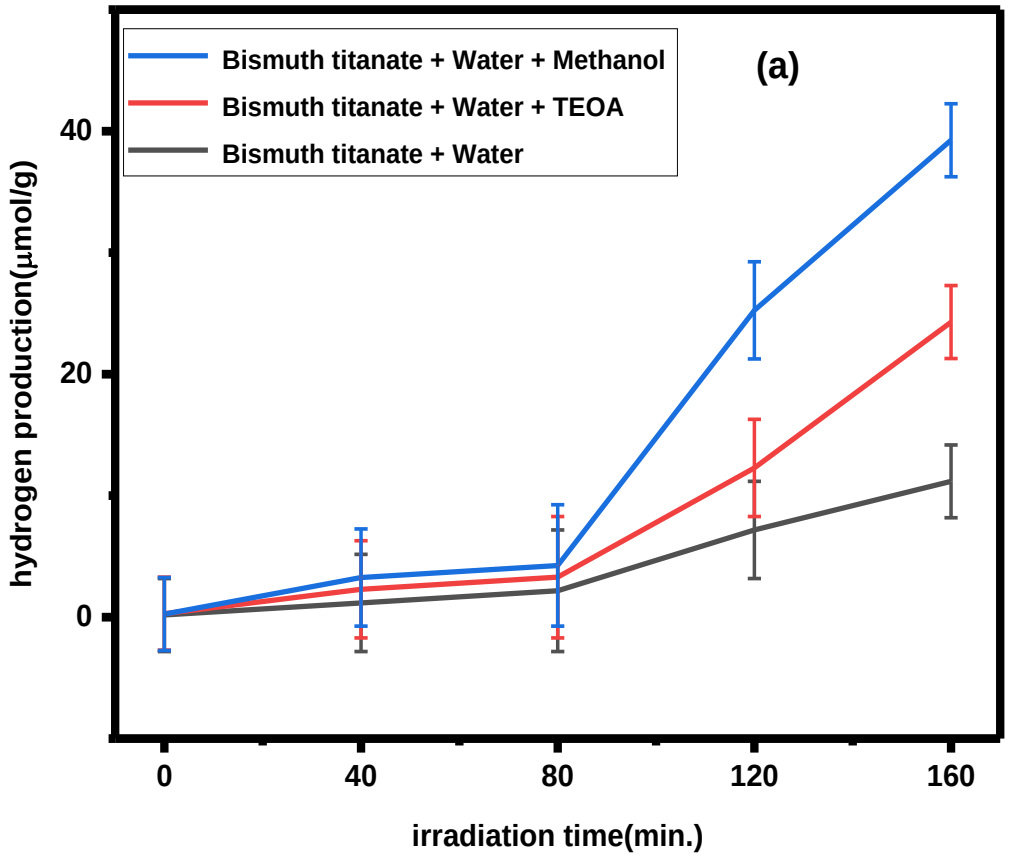

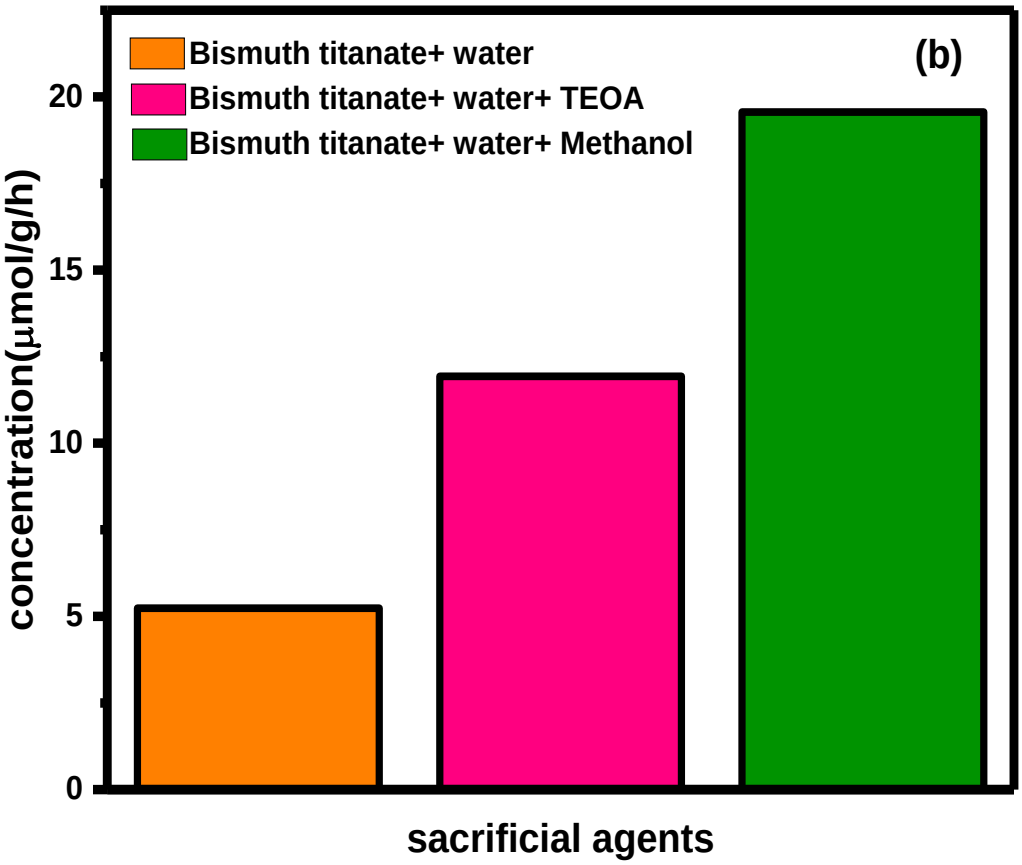

Fig 3.10 (a) Photocatalysis by bismuth titanates (b) Bar diagram showing hydrogen production efficiency of bismuth titanates with different sacrificial agents.

Initially, the reaction was carried out under solar irradiation by use of pure BT perovskite material and produced only 10.93µmol/g hydrogen. After that, triethanolamine (TEOA) and methanol were added as sacrificial agents to improve water splitting by reducing the recombination rate by capturing hole in valance band. The efficiency of hydrogen production was enhanced 24.17 µmol/g and 39.24 µmol/g with addition of TEOA and methanol respectively. The fig 3.10 (b) reveals that MeOH acts as better sacrificial agent in comparison to TEOA[10] because TEOA gets oxidized in aqueous solution[11].

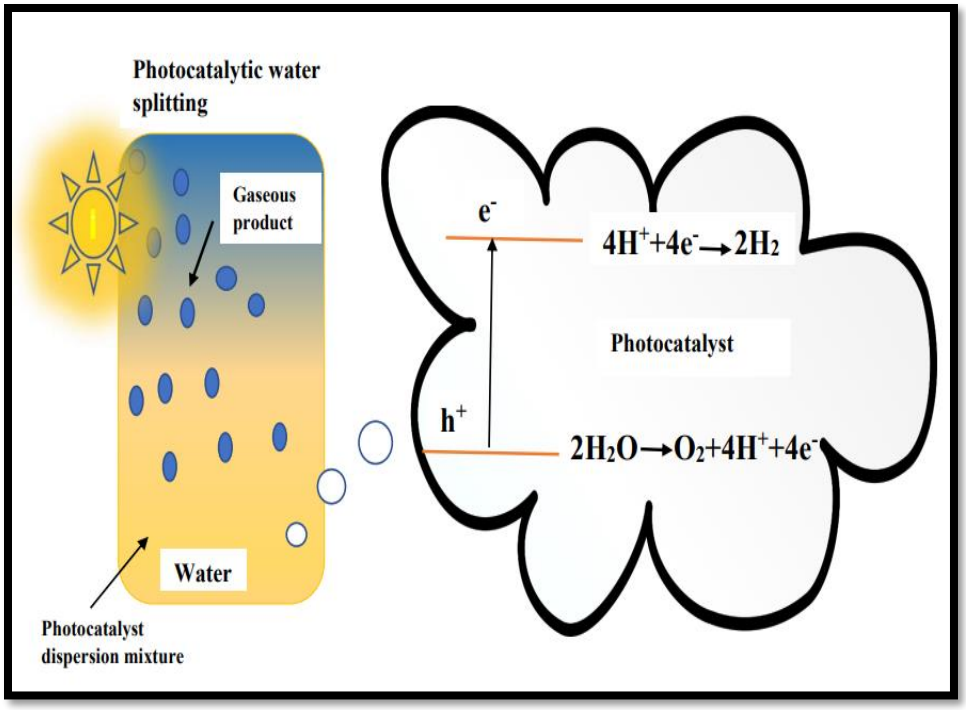

Fig 3.11 Mechanism of hydrogen production by splitting of water under sun light.

3.6 Conclusion

The above findings demonstrated synthesis of BT perovskite nanomaterials by a simple hydrothermal method and further, their use for water splitting reactions acting as photocatalysts resulting in generation of hydrogen under ultraviolet radiations. The identification and purification of samples were examined by XRD and FTIR technique. XRD study reveals that nanoparticles are orthorhombic in nature with crystallite size of 20.09nm and IR peak at 818cm^{-1} corresponds to O-Bi-O bond stretching vibration at 546cm^{-1} is for O-Ti-O stretching vibration of TiO_2. The maximum for hydrogen efficiency of 39.24 µmol/g was obtained in presence of a hole scavenger i.e. methanol. Thus, methanol was employed to promote the hydrogen production by suppressing the mixing of electron and hole pairs, functioning as a sacrificial agent. However, the hydrogen production efficiency is still low for $Bi_4Ti_3O_{12}$ nanostructured materials because of large optical band of 3.25 eV, it absorbs UV region and further can be improved by use of dopant materials such as CdS and PbS materials**.**

References

(1) Khan, M. M.; Adil, S. F.; Al-Mayouf, A. Metal Oxides as Photocatalysts. J. Saudi Chem. Soc. 2015, 19 (5), 462–464. https://doi.org/https://doi.org/10.1016/j.jscs.2015.04.003.

(2) Gan, Y.; Jayatissa, A.; Yu, Z.; Chen, X.; Li, M. Hydrothermal Synthesis of Nanomaterials. J. Nanomater. 2020, 2020, 1–3. https://doi.org/10.1155/2020/8917013.

(3) Hao, P.; Zhao, Z.; Tian, J.; Sang, Y.; Yu, G.; Liu, H.; Chen, S.; Zhou, W. Bismuth Titanate Nanobelts through a Low-Temperature Nanoscale Solid-State Reaction. Acta Mater. 2014, 62, 258–266. https://doi.org/10.1016/j.actamat.2013.10.006.

(4) Das, K.; Bariki, R.; Majhi, D.; Mishra, A.; Das, K. K.; Dhiman, R.; Mishra, B. G. Facile Synthesis and Application of CdS/$Bi_{20}TiO_{32}$/$Bi_4Ti_3O_{12}$ Ternary Heterostructure: A Synergistic Multi-Heterojunction Photocatalyst for Enhanced Endosulfan Degradation and Hydrogen Evolution Reaction. Appl. Catal. B Environ. 2022, 303, 120902. https://doi.org/https://doi.org/10.1016/j.apcatb.2021.120902.

(5) Gan, H.; Liu, J.; Zhang, H.; Qian, Y.; Jin, H.; Zhang, K. Enhanced Photocatalytic Removal of Hexavalent Chromium and Organic Dye from Aqueous Solution by Hybrid Bismuth Titanate $Bi_4Ti_3O_{12}$/$Bi_2Ti_2O_7$. Res. Chem. Intermed. 2018, 44. https://doi.org/10.1007/s11164-017-3218-7.

(6) Thirugnanasambandan, T.; Alagar, M. Titanium Dioxide (TiO_2) Nanoparticles XRD Analyses: An Insight. JOURNAL CI. 2013, http//arxiv.org/abs/1307.1091.

(7) Correya, A.; Nadeer, A.; Nampoori, V. P. N.; Mujeeb, A. The Effect of Polyethylene Glycol on the Formation of Bismuth Titanate Nanosheets and Its Effect on Optical Characteristics. J. Clust. Sci. 2022, 34. https://doi.org/10.1007/s10876-022-02290-x.

(8) Chen, D.; Jiao, X. Hydrothermal Synthesis and Characterization of $Bi_4Ti_3O_{12}$ Powders from Different Precursors. Mater. Res. Bull. 2001, 36 (1), 355–363. https://doi.org/https://doi.org/10.1016/S0025-5408(01)00513-X.

(9) Alkathy, M. S.; Zabotto, F. L.; Milton, F. P.; Eiras, J. A. Bandgap Tuning in Samarium-Modified Bismuth Titanate by Site Engineering Using Iron and Cobalt Co-Doping for Photovoltaic Application. J. Alloys Compd. 2022, 908, 164222. https://doi.org/https://doi.org/10.1016/j.jallcom.2022.164222.

(10) Kumaravel, V.; Imam, M. D.; Badreldin, A.; Chava, R. K.; Do, J. Y.; Kang, M.; Abdel-Wahab, A. Photocatalytic Hydrogen Production: Role of Sacrificial Reagents on the Activity of Oxide, Carbon, and Sulfide Catalysts. Catal. 2019, Vol. 9, Page 276 2019, 9 (3), 276. https://doi.org/10.3390/CATAL9030276.

(11) Zhang, T.; Lu, S. Sacrificial Agents for Photocatalytic Hydrogen Production: Effects, Cost, and Development. Chem Catal. 2022, 2 (7), 1502–1505. https://doi.org/https://doi.org/10.1016/j.checat.2022.06.023.

CHAPTER 4

Facile synthesis of CdS doped bismuth titanate perovskites: A cocatalyst-Free promising photocatalyst for hydrogen generation

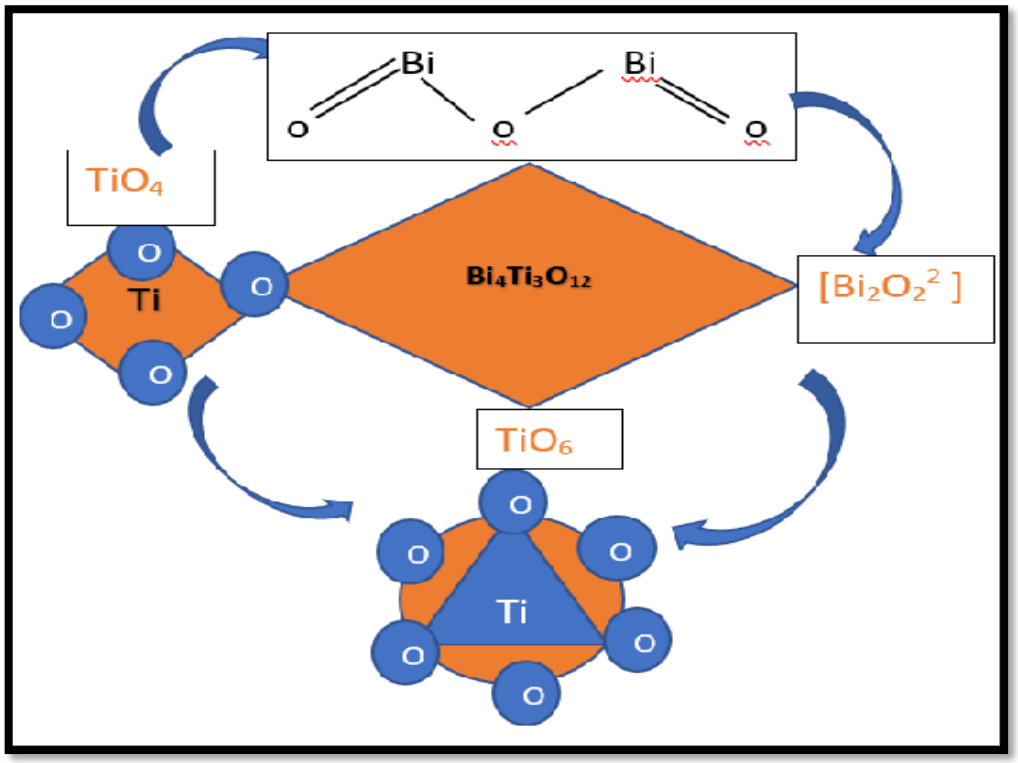

4.1 Introduction

In recent times, it has become very crucial to develop renewable energy sources to meet the requirement of growing energy demand because of increasing population and depletion in current sources of energy. Most of the energy that we use come from fossil fuels. But the amount of fossil fuels on earth are limited and also production of greenhouse gases on burning of fossil fuels. In developing countries, it has become a major challenge to produce some alternate source of energy to overcome the problem of energy crisis. Since the last three decades, the generation of renewable source of energy has got distinguished attention because the energy demands can be satisfied by use of solar energy which is enormously available. To replace or reduce the use of fossil fuels, several alternate energies have been developed, from them solar energy is accepted as an abundant, rich and sustainable clean energy source to meet current and future human energy needs[1].

From the same objectivity, the most discrete method is the use of solar energy for water splitting resulting in hydrogen generation as a renewable energy source. Solar energy has been regarded for conversion to chemical energy impersonating the natural photosynthesis to generate ideal and sustainable hydrogen fuel. A renewable and alternate energy source should be established to protect the environment. Hydrogen is the ideal fuel for the future due to its high energy density and low calorific value[2].

Various technologies like thermochemical, photobiological, photocatalytic and PEC water splitting can be used to generate H_2, only some of them be considered environment friendly. Recently, among various technologies of hydrogen production, the researchers have keen interest in photocatalytic water splitting using a photocatalyst in presence of sunlight. A number of photo-catalysts have been designed for hydrogen production from water under solar light irradiation. ZnSe, TiO_2, ZnO, WO_3 were considered efficient semiconductors for hydrogen production under solar light irradiation. However, the photocatalysts are facing the main challenges, having wide band gap energies (E_g> 3.0), rapid recombination of photo generated electrons and holes, low photocatalysis efficiency because of limited utilization of solar energy in UV region[3]. The major task is to design suitable photocatalyst which works under visible light and meet the requirements of tunable band gaps, good charge separation etc. Among a wide range of photocatalysts bismuth-based titanate perovskite materials have been considered to be the best materials which act as semiconductors for effective solar to hydrogen conversion efficiency, having a band gap of around 3.5eV acting as a photocatalyst in ultraviolet region.

Although considerable studies are present in the literature on the use of bismuth titanates and its composite materials for hydrogen production acting as photocatalyst. However, hydrogen efficiency is less due to wide band gap and its practical applicability has been limited due to less absorption of solar light and high electron holes recombination rates. Therefore, to use perovskites for photocatalytic splitting of water for hydrogen generation, its band gap should be altered by band gap engineering of material and doping is one of the most crucial methods for bandgap tailoring.

Bismuth titanate-based perovskite materials have found applications in various fields. Chao Zhou et. al. adapted hydrothermal method for synthesis of $Sr_2Ta_2O_7$ nanomaterials and checked their photocatalytic activity for hydrogen production [4]. Juan C. Pantoja et. al. synthesized Zinc titanates

by modified pechini method and checked their photocatalytic properties under solar light in presence of methanol and triethanolamine as sacrificial agents[5]. Similarly, the photocatalytic activity of $Bi@Bi_4Ti_3O_{12}$ nanosheets synthesized by hydrothermal route has been reported by Liang Bao et. al.[6]. Chen et al. proposed a sol-gel method for synthesis of crystalline $Bi_4Ti_3O_{12}$ nanosheets having average side lengths of ca. 100 and 150 nm [7]. Strontium titanate perovskite materials are the potential photocatalyst having a significant band gap of 3.3eV leads to a poor hydrogen production efficiency and this study was performed by Pushkal Sharma et. al. The minimal energy gap for light absorption can be decreased by replacing some metal ions by dopants resulting in generation of new energy levels close to valence band or conduction band. Jeferson et. al. revealed effect of different calcination temperatures on synthesis of $Bi_4Ti_3O_{12}$ spherical shaped nanomaterials having 3.2eV band gap estimated by Tauc plot. However, the as-synthesized $Bi_4Ti_3O_{12}$ nanoparticles possess a band gap of 3.2eV, indicating the less utilization of solar light [8]. Therefore, it has become crucial to synthesize $Bi_4Ti_3O_{12}$ nanomaterials of narrow band gap for more utilization of solar light in visible region.

In this work, bismuth titanate -based perovskite materials have been synthesized by low temperature assisted hydrothermal method. To increase the hydrogen production efficiency and to decrease the recombination of electrons and holes, different concentrations of cadmium sulfide (CdS) has been doped on BT surface by mechanical method resulting in reduction of band gap of BTNPs, which is due to hybridization of atomic orbitals of Ti (3d) and Cd (3d) orbitals.

Furthermore, the oxidation ability of holes in low level valence band have been increased and accordingly decreasing the ability of reduction of electrons in the conduction band resulting in enhanced photocatalytic reactions of electrons in conduction band and holes in valence band. These nanomaterials have been analyzed as an adequate photocatalyst for generation of hydrogen in presence of different sacrificial agents.

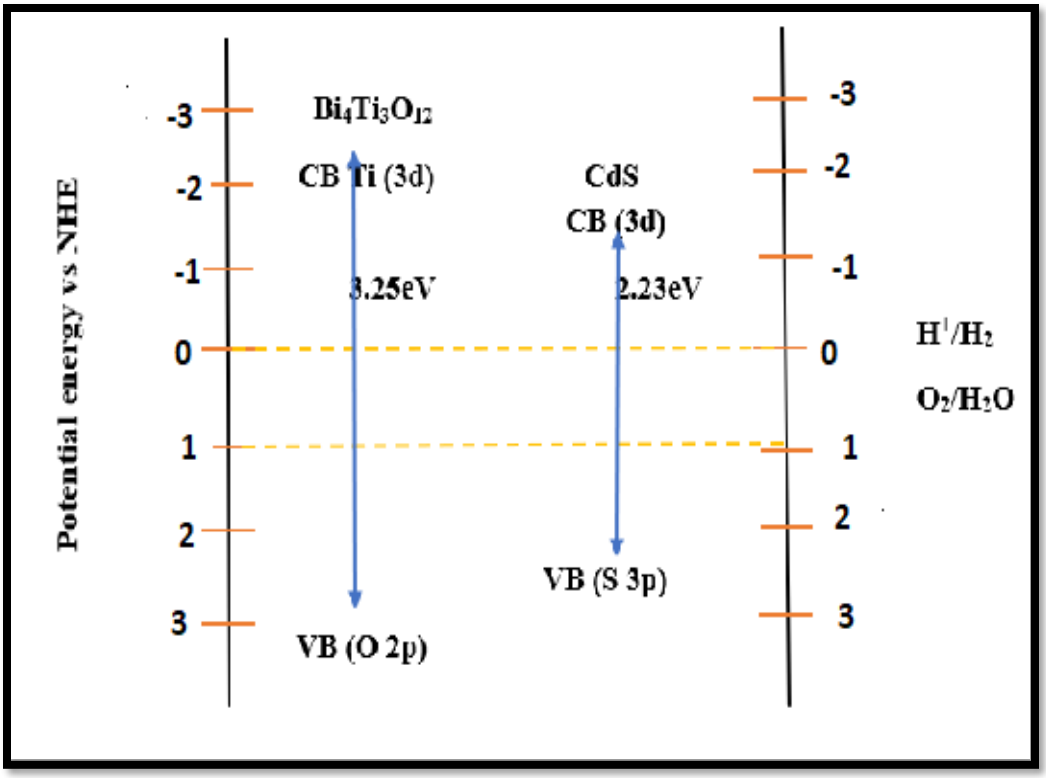

Fig 4.1 The band gap structure of $Bi_4Ti_3O_{12}$ and CdS dopant.

4.2. Experimental section

4.2.1 Materials

Analytical grade bismuth nitrate pentahydrate {$Bi(NO_3)_3$.$5H_2O$} and titanium dioxide {TiO_2 anatase} were used as a source of bismuth and titanium respectively and has been purchased from HIMEDIA. No further purification was done at laboratory scale. Double ionized water was used during the whole experiment.

4.2.2 Synthesis of bismuth titanate nanoparticles (BTNPs)

The 3M solution of bismuth nitrate pentahydrate was mixed with the 1M titanium dioxide acting as titanate source in 3:1 ratio and refluxing the solution with the help of magnetic stirrer with constant heating for 2 hours resulted in appearance of white transparent solution. Further, addition of 2M sodium hydroxide {NaOH} solution was done in a dropwise manner until the pH approaches to 13 until the formation of white precipitates. The above solution was kept on magnetic stirrer for 2hours in order to obtain the uniform size nanostructured materials. Then, the above mixture was transferred to the teflon lined stainless steel autoclave and heated to the

temperature of 150ºC up to 10 hours. The autoclave was allowed to cool at room temperature. The resulting powders were washed repeatably with deionized water and ethanol. Then the obtained powder was dried in an oven at 100ºC for 12hours followed by grinding well in pestle mortar for half an hour. The prepared nanoparticles have light orange colour appearance.

4.2.3 Synthesis of cadmium sulphide (CdS) nanoparticles

Cadmium sulphide nanoparticles have been synthesized by hydrothermal technique with thiourea as a source of sulphur and dehydrated cadmium chloride as a source of cadmium. 1M cadmium chloride solution was prepared in 100mL distilled water followed by dropwise addition of thiourea resulting in turbidity, on further addition of thiourea a transparent clear solution is obtained. The above solution was transferred to teflon lined stainless steel vessel and subjected to hydrothermal reaction at 200°C for 10 hours. Samples were allowed to cool at room temperature followed by washing with ethanol and distilled water many times to obtain final yellow-coloured precipitates of CdS.

4.2.4 Synthesis of CdS doped bismuth titanates

The pre-synthesized yellow coloured CdS NPs were mixed with above synthesized bismuth titanates. The CdS NPs of appropriate mass percentage (0.1%, 0.3% and 0.6% w/w %) were mixed with bismuth titanate perovskite materials in pestle mortar by mechanical method and grind well for 4 hours so that CdS NPs incorporated in BTP. The observations about physical properties show that colour transformation takes place from light orange to yellowish appearance and the resulted powder was calcined at 600ºC resulting in improvement of crystallinity of sample and removes the excess moisture. Thereafter, the calcined samples were characterized by XRD, FTIR and FESEM instrumentation for further detection, identification and purity of above said samples.

4.2.5 Characterization of the photocatalyst

The structural properties of the obtained materials were verified by monochromator Cu Kα radiation (45 kV, powder X-ray diffractometer Bruker D8 ADVANCE) in the 2θ range of 20º – 80º for a period of 5s in the step scan mode. The diffused reflection spectra (DRS-UV) was evaluated for the photocatalysts using a Perkin Elmer Lambda 900 spectrophotometer, for determination of band gap from Tauc plot. FESEM, or Field emission scanning electron microscopy (JEOL) was employed to analyze morphologies and lattice structures of as-

synthesized nanomaterials. The functional groups were detected by Fourier Transform Infrared Spectrometer (PERKIN ELEMER) by scanning in 400cm^{-1} – 4000cm^{-1}.

4.2.6 Photocatalytic reaction

A quartz external irradiation cell linked to a gas-closed circulation system was employed to conduct the photocatalytic gas evolution by water splitting. 0.01g of the photocatalyst powder was suspended in a round bottom flask kept on a magnetic stirrer, 40 mL of water was placed in the cell. The 300 W high-pressure Xenon lamp with cut off filter served as the source of light. The generation of hydrogen gas was detected by GC-TCD.

4.3. Results and Discussion

4.3.1 Powder X- ray diffraction

XRD was employed to characterize the synthesized powders. The sample was scanned in the 2θ range of 20º – 80º for a period of 5s in the step scan mode using Bruker D8 ADVANCE. Powder X-ray diffraction pattern of the BTP nanoparticles as-synthesized by hydrothermal route has been shown in Figure 4.2. In XRD investigation of the material, no significant impurity phase has been detected, revealing the purity of the phase. The polycrystalline nature of bismuth titanates can be seen from the diffraction pattern of obtained peaks. The perusal of graph shows that the sharp peaks obtained at 30.05º and 32.84º can be indexed to orthorhombic bismuth titanate perovskite and has been well matched with JCPDS Card no. 50-0300. All diffraction peaks can be indexed to layered perovskite $Bi_4Ti_3O_{12}$, which are consistent with the literature [9].

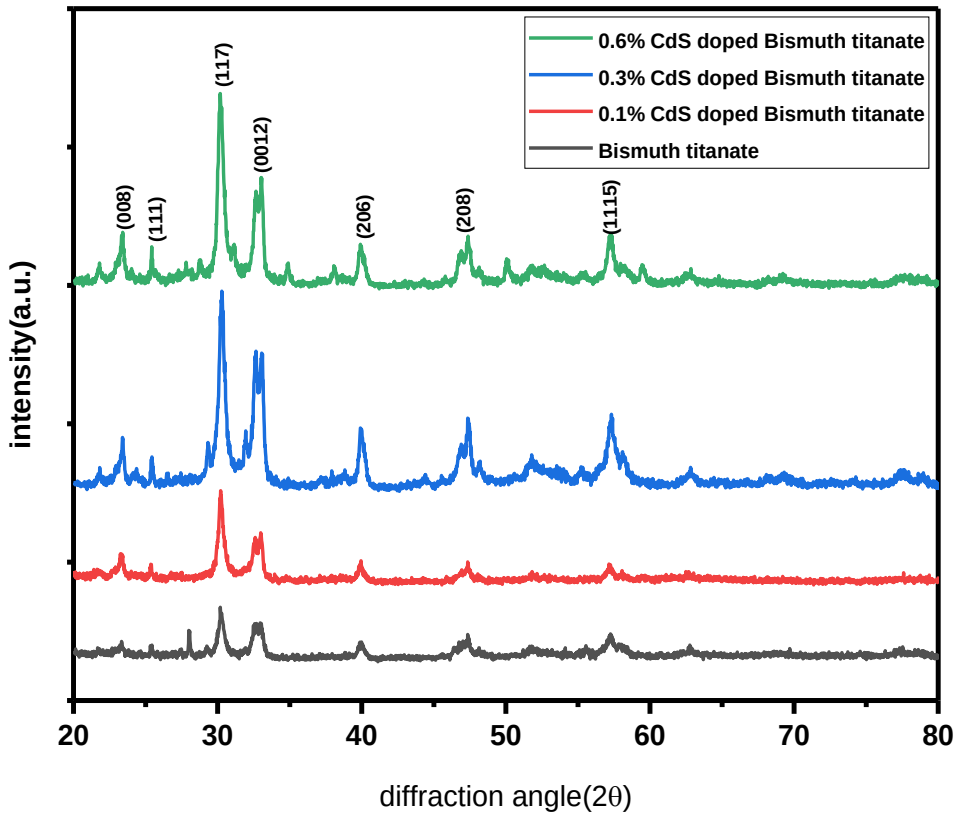

Fig 4.2 Comparative XRD graphs of CdS doped BTP.

The strong and sharp peaks indicate high crystallinities of the as-prepared BTP nanomaterials. It has been found that the resulted nanoparticles are orthorhombic in nature having space group Aba2. The cell parameters were found to be a= 32.83, b= 5.411, c= 5.448 (from MAUD software) and have been well matched with literature [10]. It has been observed that the crystallite size is strongly influenced by CdS dopant inserted into the lattice. The average crystallite size of Bismuth titanates is 30.20nm. Whenever the dopant (CdS) is introduced to the lattice sites of Bismuth titanate nanoparticles the crystallite size decreases, potentially due to deformation cause on by the dopant in the lattice. For 0.1%, 0.3% and 0.6% dopant concentration, the corresponding crystallite size is 30.05, 29.30 and 24.69nm respectively, as calculated by Debye Scherrer formula:

$D = K. \lambda / \beta. \cos \theta$

Where D is the particles crystallite size, K is the shape factor, λ is the wavelength of X-rays (1.5418Aº for Cu Kα), β is full width at half maximum (FWHM), θ is the detected peak angle in

degree. The intensity of peak from diffraction at [008], [117] and [0012] planes increase with increase in dopant concentration. The [117] crystalline plane shows the highest diffraction intensity. The perusal of XRD peak shows that on addition of dopant concentration CdS, the intensity of peak at 30.05º corresponding to [117] plane increases with increase in concentration of dopant from 0.1% to 0.3% and 0.6% dopant (CdS) concentration, illustrating the improved crystallinity. The contrast in variation of intensities in XRD graphs indicates the incorporation of Cd^{2+} ions in bismuth titanate perovskites. Furthermore, with addition of dopant concentration some additional peaks were detected at 22.9º ,26.2º, 38.7º corresponding to CdS[11]. It was noticed that with increase in dopant concentration crystallite size decreases.

Table 4.1. Crystallite size of BTP and CdS doped BTNPs.

Photocatalyst	**FWHM**	**Crystallite size**
Bismuth titanate (BT)	0.266	30.20nm
0.1% CdS doped BT	0.286	30.05nm
0.3% CdS doped BT	0.296	29.30nm
0.6% CdS doped BT	0.348	24.69nm

4.3.2 FTIR study

FTIR spectroscopy has been used to study the bonding properties of CdS doped BTNPs. The FTIR spectra was recorded at room temperature in the range of 400-4000cm^{-1}. The calcined BTP nanomaterials show only two predominant peaks at 546cm^{-1} and 818cm^{-1}. The sharp peak at 546cm^{-1} is characteristic of bismuth titanate($Bi_4Ti_3O_{12}$)[12]. The peak at 818 cm^{-1} is attributed to the Ti-O stretching vibration and peak at 425 cm^{-1} is due to O-Ti-O stretching vibration of TiO_2.

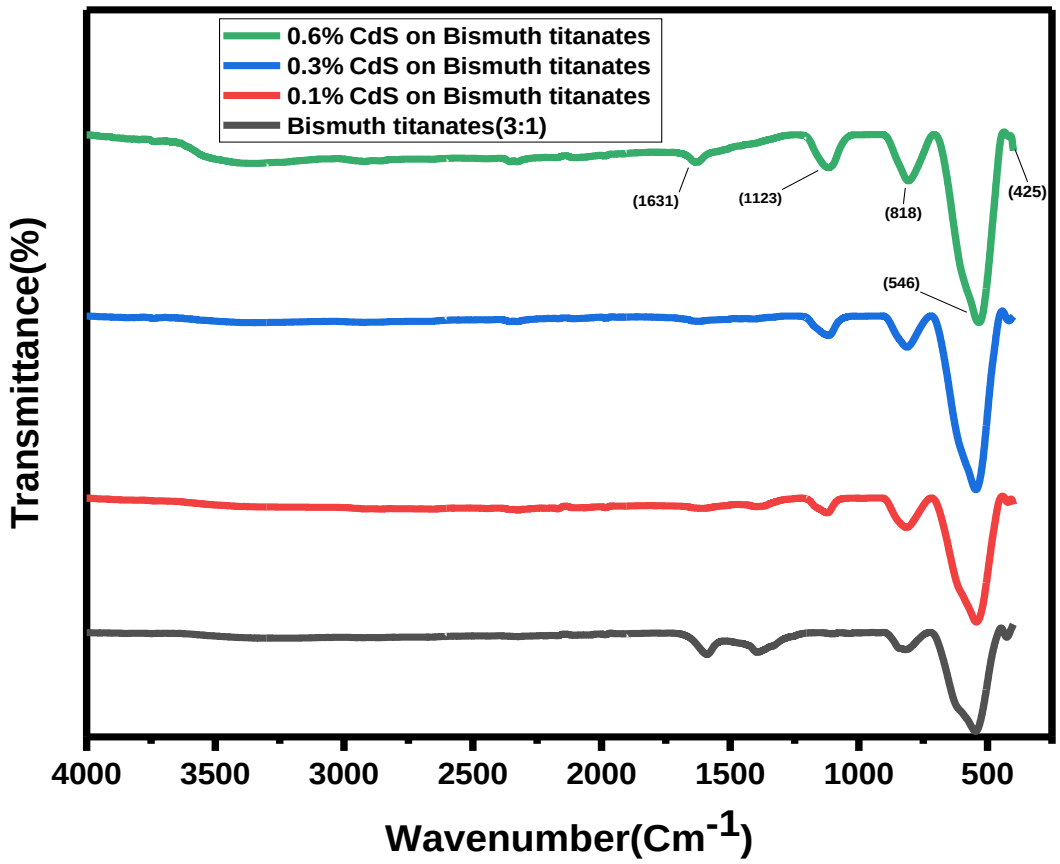

Fig 4.3. FTIR spectra of CdS doped bismuth titanates.

It is reported that the absorbance of peak at position 818cm^{-1} is increasing with increase in dopant concentration. Furthermore, a new absorption peak has been observed at 1123cm^{-1} and its absorbance increases with increase in dopant concentration. The FTIR spectra of dopants show peaks at 1123cm^{-1} and 815cm^{-1} indicating the incorporation of CdS in bismuth titanates.

4.3.3 UV- Visible spectroscopy

The UV-Visible spectrum of bismuth titanate perovskite materials has been shown in Figure 4.4. Bismuth titanate shows the bandgap of 3.25 eV indicates the absorption in UV region, which has been further decreased by doping of cadmium sulfide nanoparticles which might be due to generation of new band over valence band. As the doping concentration increases from 0.1% to 0.6% band gap reduced from 3.25eV to 3.05eV. 0.6% CdS doped BTNPs has shown the shift towards higher wavelength with a bandgap of 3.05 eV and was estimated from the tangent line in

the tauc plot $(\alpha h\nu)^{1/2}$ function against the photon energy, as shown in the fig 4.4 and matched well with the earlier report [13]. The extension of absorption has been reported as a result of CdS dopant. On CdS doping, some of the Cadmium(3d) orbitals of CdS gets hybridized with Ti (3d) orbitals of bismuth titanate lattice resulting in impurity levels below the conduction band hence shifted the absorption edge to lower energy[14].

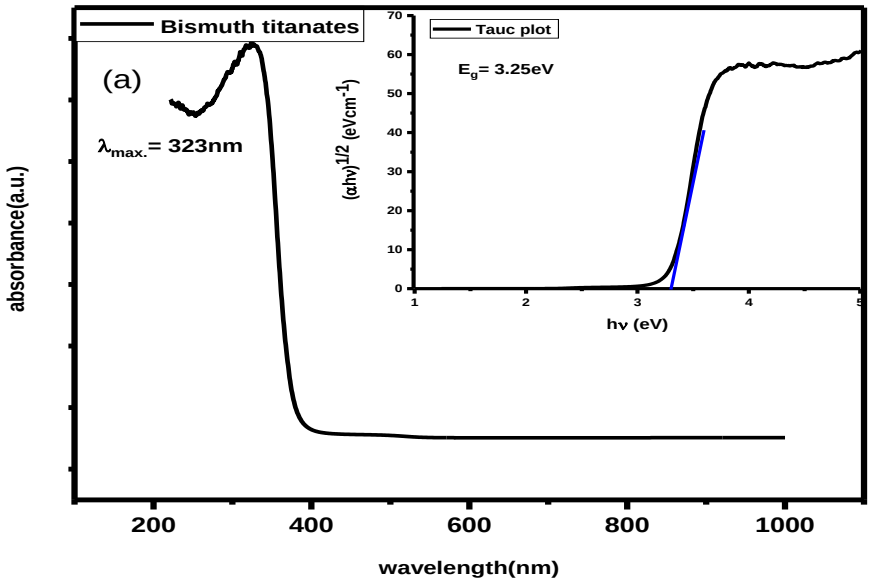

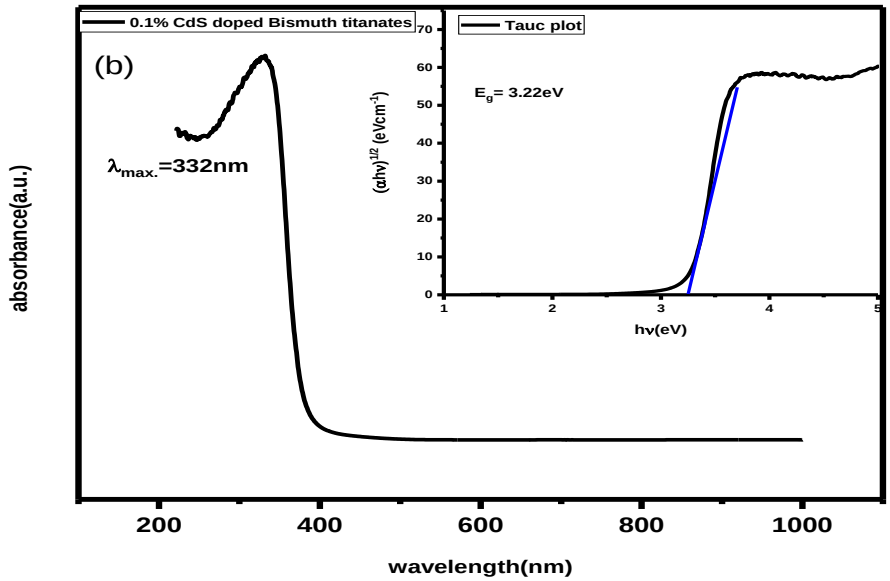

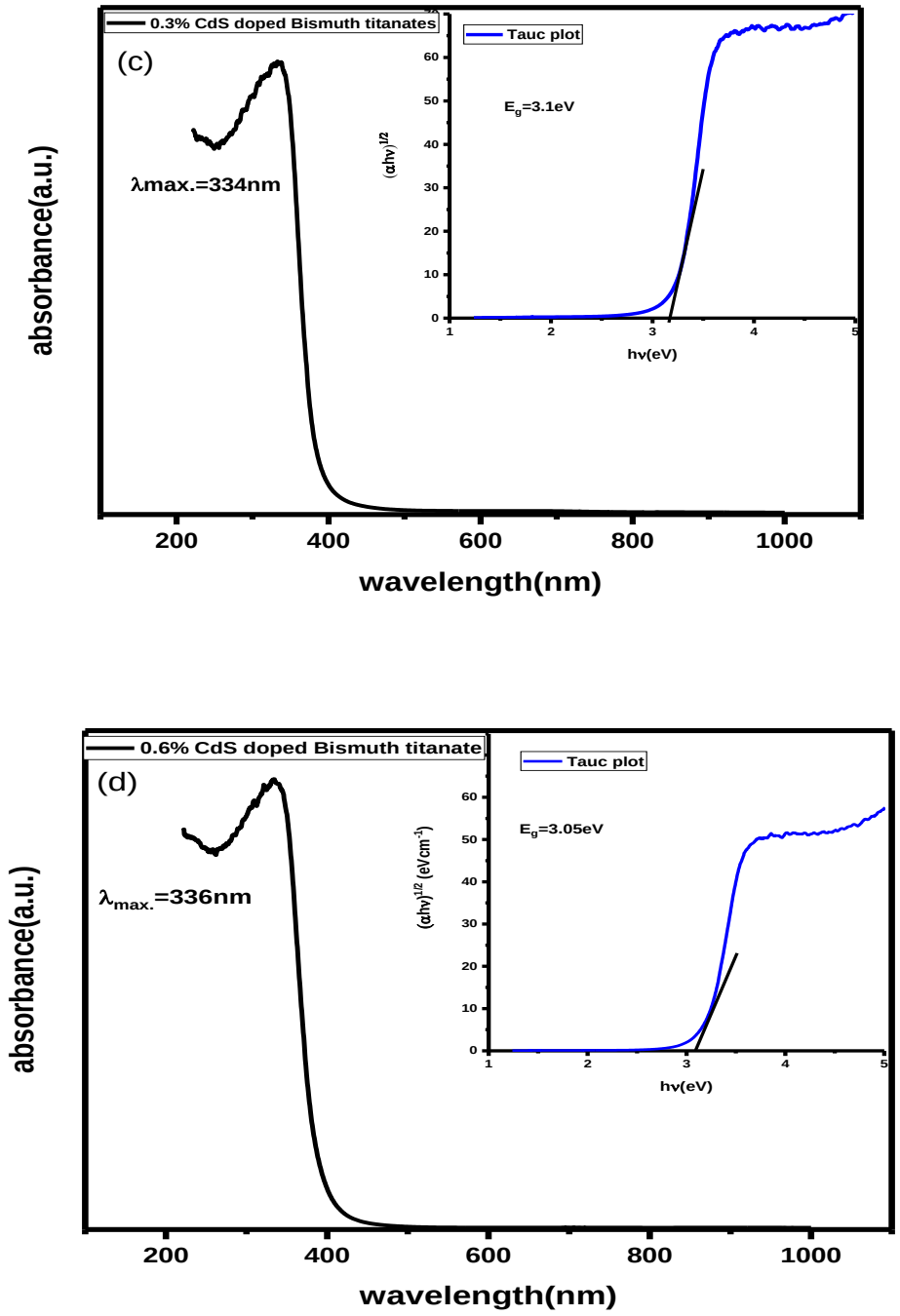

Fig. 4.4 (a) The band gap of bismuth titanates (b) band gap of 0.1% CdS doped BT (c) band gap of 0.3% CdS doped BT and (d) 0.6% CdS doped BT.

As can be seen from table, on increasing the dopant concentration band gap decreases due to extension of absorption to higher wavelength.

Table 4.2. Band gap of various photocatalyst calculated from tauc plot.

Photocatalyst	**λmax.**	**Band gap**
Bismuth titanate	323nm	3.25 Ev
0.1% CdS doped BT	332nm	3.22 eV
0.3% CdS doped BT	334nm	3.1 eV
0.6% CdS doped BT	336nm	3.05 eV

4.3.4 Morphological study

The crystalline size of CdS doped BTNPs, as analyzed by XRD data was further investigated by FESEM analysis. Field emission scanning electron microscopy analysis were performed on the plane surface and using the micrographs, which were captured under (X 30,000) magnification clearly reveals the formation of homogenously distributed spherical shaped nanoparticles. Furthermore, to confirm the doping of CdS and resulting in formation of nanosheets certifying the insertion of CdS along axis in BTNPs. At 0.6% CdS concentration nanorods formation can be detected clearly.

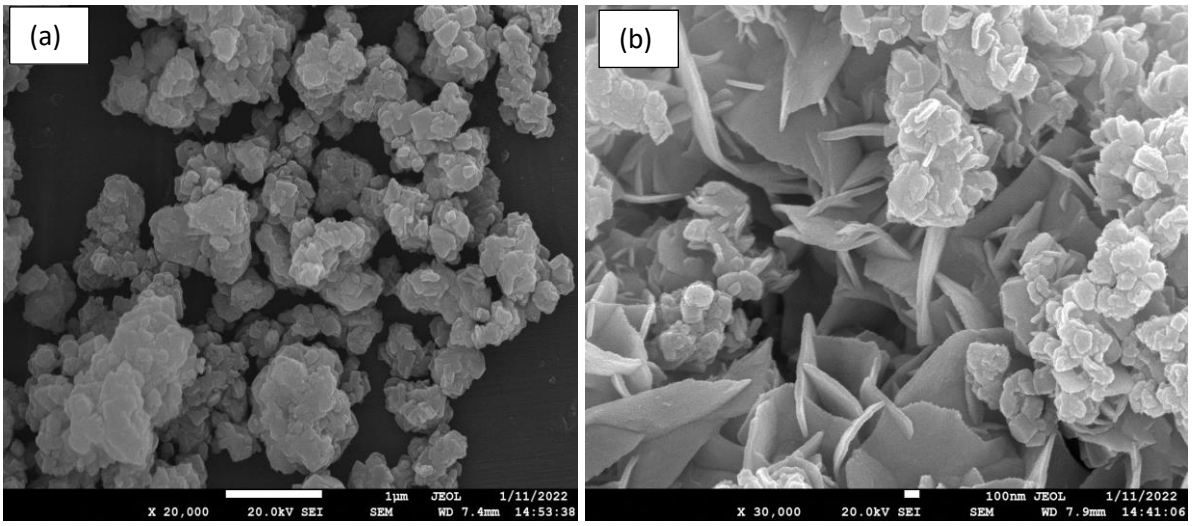

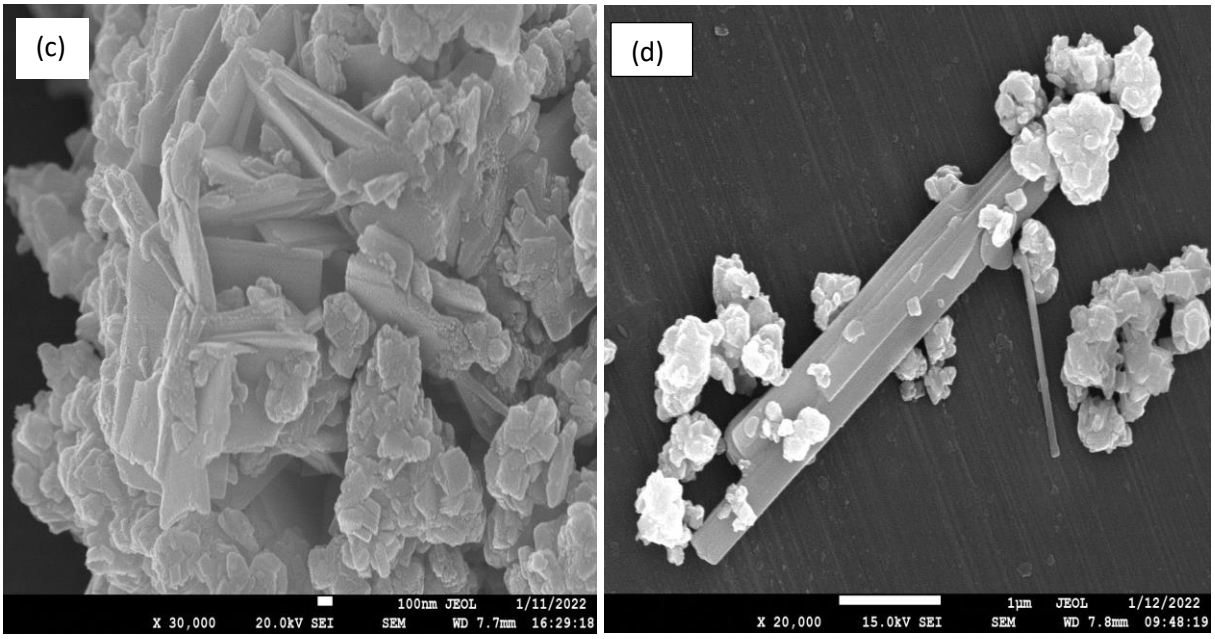

Fig.4.5 (a) FESEM images of BTNPS, (b) 0.1% CdS doped BT, (c) 0.3% CdS doped BT and (d) 0.6% CdS doped BT.

4.3.5 Photocatalytic hydrogen generation

Photocatalytic water splitting activity of bismuth titanate, 0.1%, 0.3% and 0.6% CdS doped bismuth titanate nanoparticles was performed in the presence of ethylenediaminetetraacetic acid (EDTA) acting as a sacrificial agent. Fig 4.6 depicts that in presence of EDTA, BTNPs shows the hydrogen production efficiency of only 11.61µmol/g which is very less which might be due to recombination of electrons and holes and absorption of light in ultraviolet region because of wide band gap of 3.25 eV. In hydrogen production the band gap plays a vital role, further the band gap has been reduced by doping of CdS on BTNPs resulting in mixing of atomic orbitals. A new band level has been observed below the conduction band minimum facilitating easy migration of electrons on light irradiation to conduction band reducing H^+ ions to H_2.

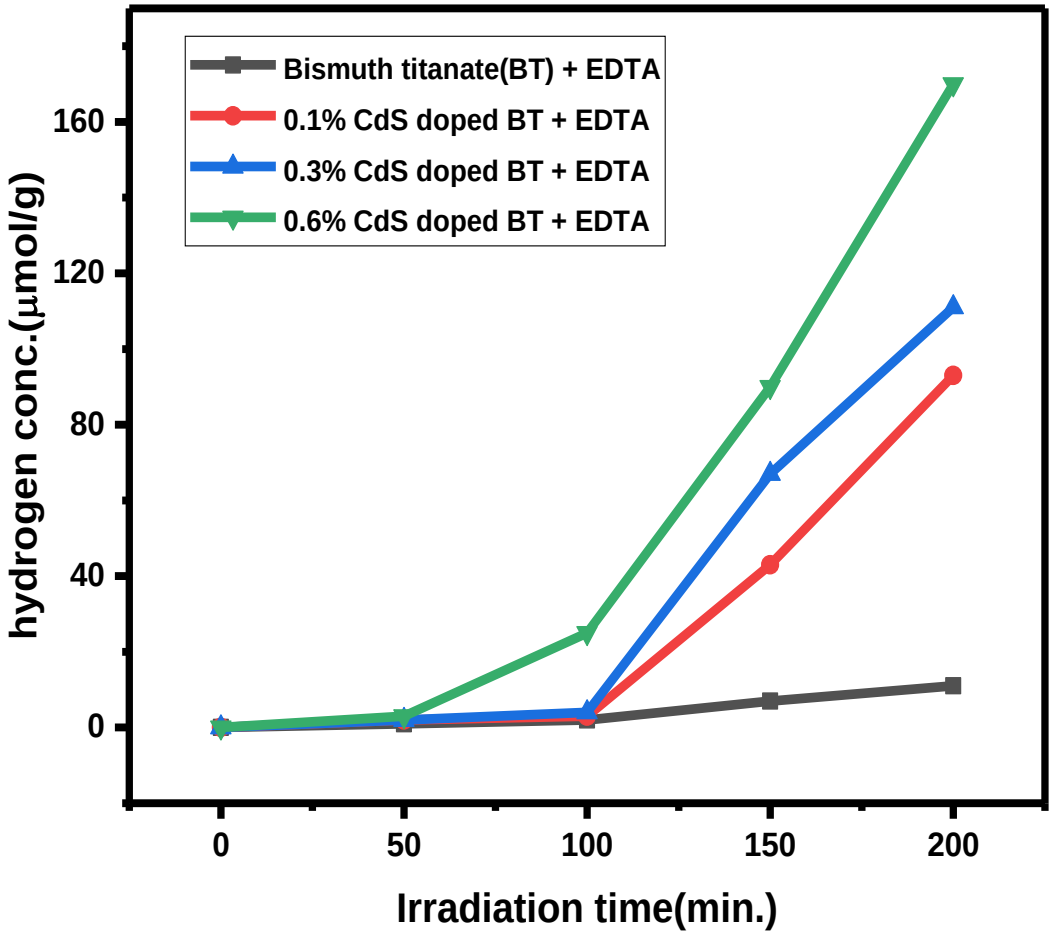

Fig 4.6. Photocatalytic water splitting by BTNPs and CdS doped BT in presence of EDTA.

The experiment was performed in presence of different sacrificial agents (fig 4.7) to deal with the phenomenon of recombination of electron-hole pairs on photoirradiation. MeOH > EDTA >TEOA is the decreasing order for hydrogen evolution utilizing 0.6% CdS doped BTNPs.

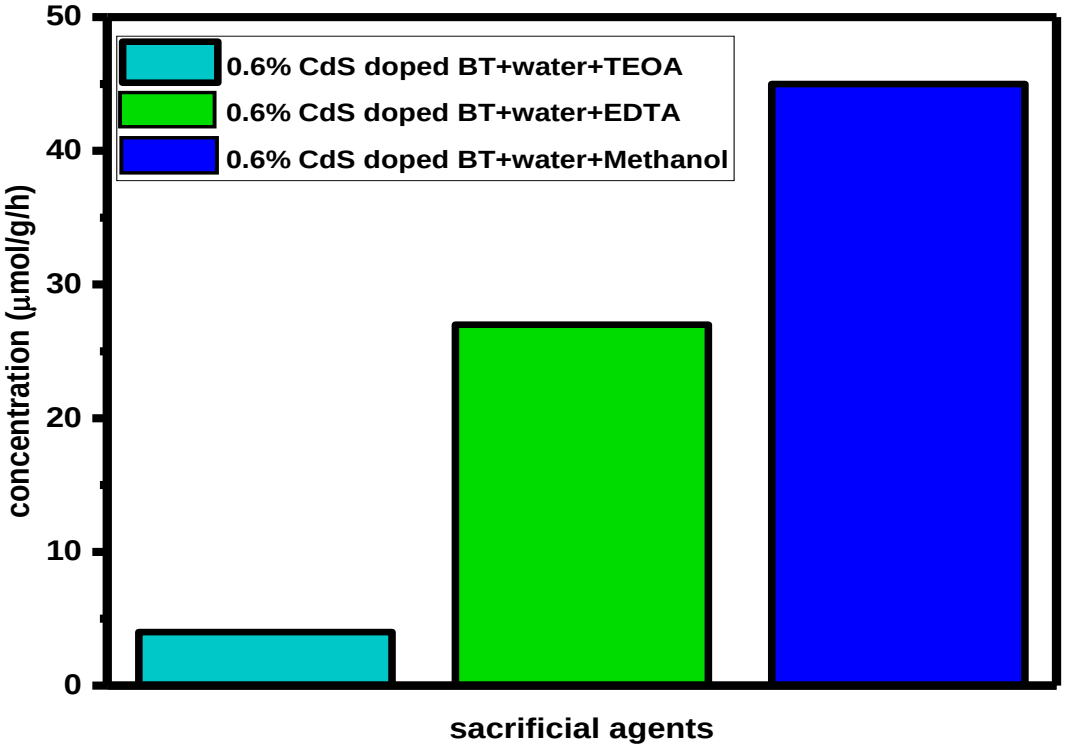

Fig 4.7. Bar diagram shows photocatalytic H_2 generation by 0.6% CdS doped BTNPs.

From the photocatalytic splitting experiments, the maximum amount of hydrogen evolved using 0.6% CdS doped Bismuth titanate is observed with MeOH (171 µmol/g) as sacrificial agents. The CdS doping results in generation of a new band below the minimum of conduction band by mixing of atomic orbitals of Cd (3d) with that of Ti (3d). MeOH appears to slow down the process of electron-hole recombination by snatching holes from the doped valence band of BTNPs. As a result, methanol reduces OH radicals, thus enhancing hydrogen evolution rate and acting as a hole scavenger [15]. It has been observed that CdS doping increases the charge carriers by shift in band position and affects the oxidation/reduction abilities of the photogenerated electrons and holes, which significantly results in the enhancement of photocatalytic reactions. It was discovered that the rate of hydrogen evolution was minimum with TEOA which might be due to very sensitive nature of TEOA undergoing oxidation in aqueous solution[16]. In presence of EDTA hydrogen efficiency is less which might be due to utilization of EDTA during the photocatalytic activity[17].

4.4 Mechanistic aspects

The fundamental characteristics of the photocatalytic activity of CdS doped bismuth titanates based on the above results and literature review, for the water splitting reaction, has been represented as pictorial elucidation in fig 4.8. When the radiations of energy greater than the band gap energy falls on the photocatalysts, leading to migration of electrons from VB to CB and leaving the holes in VB. The electrons at conduction band facilitates the reduction of H^+ ions to hydrogen gas and oxidation of water takes place in VB resulting in generation of oxygen gas.

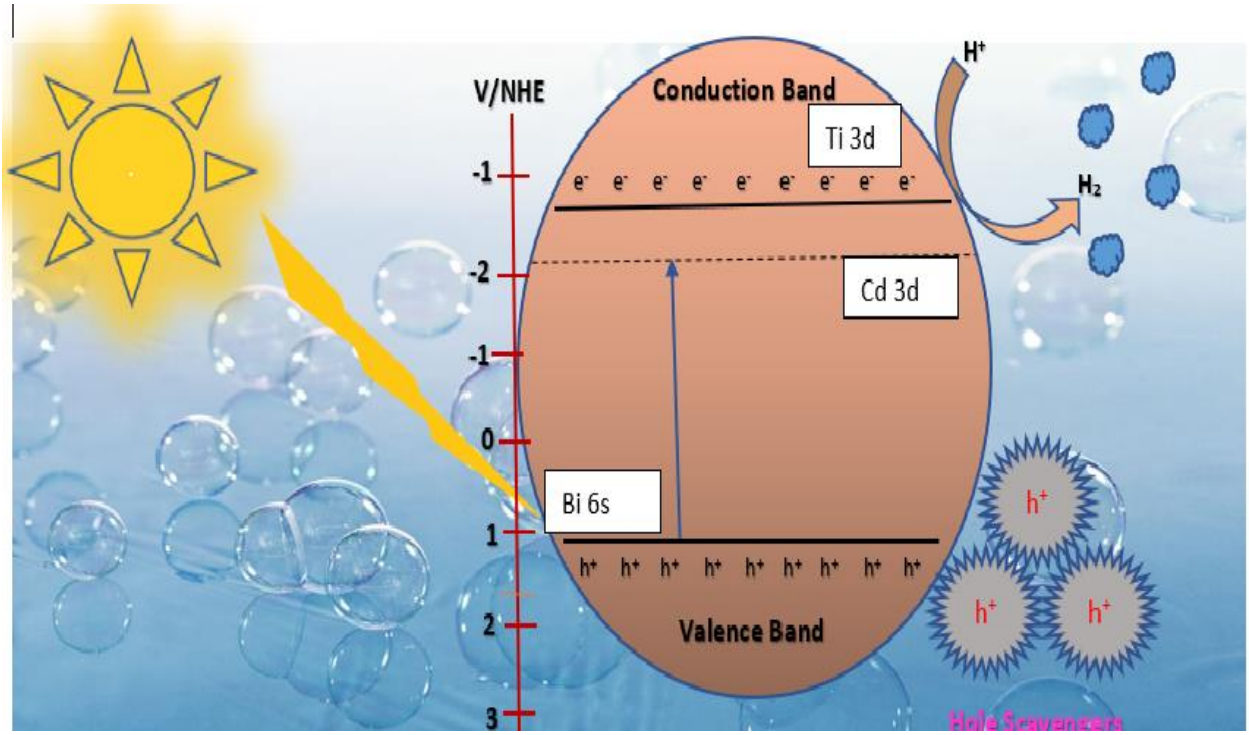

Fig 4.8 Proposed mechanism for hydrogen generation by CdS doped bismuth titanates.

The sacrificial reagents such as methanol, EDTA and TEOA provides electrons resulting in prevention of electron-hole recombination[18]. The enhanced photocatalytic activity for the 0.6% CdS doped BT should be due to lower band gap of 3.05eV as calculated from UV-DRS studies and nanosized particles. There is mixing of atomic orbitals of Ti and Cd resulting in generation of low-level conduction band which helps in easy and fast movement of electrons from VB to CB and also the smaller particles have high surface area resulting in enhanced photocatalytic activity by more absorption of light.

4.5 Conclusion

In current study, the water splitting activity of CdS doped bismuth titanates have been confirmed which also reveals a simple hydrothermal approach for producing bismuth titanate nanomaterials. The XRD analysis confirms the crystalline nature of as-synthesized nanoparticles having crystallite size of 30.20nm and the peak position at 30.05º having plane (117) confirms the orthorhombic nature of BTNPs. UV-visible spectroscopy revealed the minimum band gap of 3.05eV for 0.6% CdS doped bismuth titanates as calculated from tauc plot. The peak at 546cm^{-1} approves the presence of $Bi_4Ti_3O_{12}$ as analyzed from FTIR study. Ti-O stretching vibration was confirmed by FTIR spectroscopy over peak at 818 cm^{-1} and peak position at 425 cm^{-1} is accredited to O-Ti-O stretching vibration of TiO_2. FESEM analysis confirms the spherical shape of bismuth titanate nanoparticles further, CdS doped BTNPs shows the rod-shaped morphology. The highest hydrogen production efficiency of 171µmol/g was detected with 0.6% CdS doped BTNPs. The photocatalytic splitting of water was carried out with several scavengers (TEOA, EDTA, and MeOH), further it was discovered that the hydrogen production was highest with methanol acting as a hole scavenger. Higher photocatalytic efficiency is ascribed to generation of new band below CB facilitating the easy transfer of electrons from VB. Consequently, the findings demonstrates that CdS doped BTNPs nanoparticles encourage optical absorption for photocatalytic reactions and that employing methanol as a hole scavenger minimizes the recombination of electron-hole couples. These findings potentially provide new possibilities for using CdS as a dopant to serve as a good photocatalyst for the production of H_2.

References

(1) Lokhande, P. E.; Chavan, U. S. Conventional Chemical Precipitation Route to Anchoring $Ni(OH)_2$ for Improving Flame Retardancy of PVA. Mater. Today Proc. 2018, 5 (8, Part 3), 16352–16357. https://doi.org/https://doi.org/10.1016/j.matpr.2018.05.131.

(2) Lokhande, P. E.; Kulkarni, S.; Chakrabarti, S.; Pathan, H. M.; Sindhu, M.; Kumar, D.; Singh, J.; Kumar, A.; Kumar Mishra, Y.; Toncu, D.-C.; Syväjärvi, M.; Sharma, A.; Tiwari, A. The Progress and Roadmap of Metal–Organic Frameworks for High-Performance Supercapacitors. Coord. Chem. Rev. 2022, 473, 214771. https://doi.org/https://doi.org/10.1016/j.ccr.2022.214771.

(3) Rafique, M.; Hajra, S.; Irshad, M.; Usman, M.; Imran, M.; Assiri, M. A.; Ashraf, W. M. Hydrogen Production Using TiO_2-Based Photocatalysts: A Comprehensive Review. ACS Omega 2023, 8 (29), 25640–25648. https://doi.org/10.1021/acsomega.3c00963.

(4) Zhou, C.; Chen, G.; Li, Y.; Zhang, H.; Pei, J. Photocatalytic Activities of Sr 2Ta 2O 7

Nanosheets Synthesized by a Hydrothermal Method. Int. J. Hydrog. Energy 2009, 34, 2113–2120. https://doi.org/10.1016/j.ijhydene.2008.12.074.

(5) Pantoja-Espinoza, J. C.; Domínguez-Arvizu, J. L.; Jiménez-Miramontes, J. A.; Hernández-Majalca, B. C.; Meléndez-Zaragoza, M. J.; Salinas-Gutiérrez, J. M.; Herrera-Pérez, G. M.; Collins-Martínez, V. H.; López-Ortiz, A. Comparative Study of $Zn_2Ti_3O_8$ and $ZnTiO_3$ Photocatalytic Properties for Hydrogen Production. Catalysts. 2020. https://doi.org/10.3390/catal10121372.

(6) Bao, L.; Bao, Q.; Jiang, W.; Xu, G. Hydrothermal Synthesis of $Bi@Bi_4Ti_3O_{12}$ Nanosheets with Enhanced Visible-Light Photocatalytic Activity. CrystEngComm 2020, 22 (38), 6316–6321. https://doi.org/10.1039/D0CE00994F.

(7) Chen, Z.; He, X. Low-Temperature Preparation of Nanoplated Bismuth Titanate Microspheres by a Sol–Gel-Hydrothermal Method. J. Alloys Compd. 2010, 497 (1–2), 312–315. https://doi.org/10.1016/J.JALLCOM.2010.03.053.

(8) Dias, J.; de Oliveira, J.; Renda, C.; Morelli, M. Production of Nanometric $Bi_4Ti_3O_{12}$ Powders: From Synthesis to Optical and Dielectric Properties. Mater. Res. 2018, 21. https://doi.org/10.1590/1980-5373-mr-2018-0118.

(9) Lin, X.; Lv, P.; Guan, Q.; Li, H.; Zhai, H.; Liu, C. Bismuth Titanate Microspheres: Directed Synthesis and Their Visible Light Photocatalytic Activity. Appl. Surf. Sci. 2012, 258 (18), 7146–7153. https://doi.org/10.1016/J.APSUSC.2012.04.019.

(10) Ramana, E. V.; Prasad, N. V; Tobaldi, D. M.; Zavašnik, J.; Singh, M. K.; Hortigüela, M. J.; Seabra, M. P.; Prasad, G.; Valente, M. A. Effect of Samarium and Vanadium Co-Doping on Structure, Ferroelectric and Photocatalytic Properties of Bismuth Titanate. RSC Adv. 2017, 7 (16), 9680–9692. https://doi.org/10.1039/C7RA00021A.

(11) Al-Mamoori, M. H. K.; Mahdi, D. K.; AlShrefi, S. M. Synthesis and Spectroscopic Study of CdS Nanoparticles Using Hydrothermal Method. AIP Conf. Proc. 2018, 1968 (1). https://doi.org/10.1063/1.5039198/727224.

(12) Meenakshi, P.; Selvaraj, M. Bismuth Titanate as an Infrared Reflective Pigment for Cool Roof Coating. Sol. Energy Mater. Sol. Cells 2018, 174, 530–537. https://doi.org/10.1016/j.solmat.2017.09.048.

(13) Saai Harini, R.; Easwaramoorthy, D.; Sai Muthukumar, V.; Gowrishankar, R.; Anandan, S. Bandgap Engineered (Tin & Carbon Co-Doped) Bismuth Titanate Nanowires for Improved Visible-Light Assisted Photocatalytic Application. Environ. Nanotechnology, Monit. Manag. 2019, 12, 100228. https://doi.org/https://doi.org/10.1016/j.enmm.2019.100228.

(14) Hou, J.; Wang, Z.; Jiao, S.; Zhu, H. 3D $Bi_{12}TiO_{20}/TiO_2$ Hierarchical Heterostructure: Synthesis and Enhanced Visible-Light Photocatalytic Activities. J. Hazard. Mater. 2011, 192 (3), 1772–1779. https://doi.org/10.1016/J.JHAZMAT.2011.07.013.

(15) Kumar, V.; Bhawna; Yadav, S. K.; Gupta, A.; Dwivedi, B.; Kumar, A.; Singh, P.; Deori, K. Facile Synthesis of Ce–Doped SnO_2 Nanoparticles: A Promising Photocatalyst for Hydrogen Evolution and Dyes Degradation. ChemistrySelect 2019, 4 (13), 3722–3729. https://doi.org/10.1002/SLCT.201900032.

(16) Abinaya, K.; Karthikaikumar, S.; Sudha, K.; Sundharamurthi, S.; Elangovan, A.; Kalimuthu, P. Synergistic Effect of 9-(Pyrrolidin-1-Yl)Perylene-3,4-Dicarboximide

Functionalization of Amino Graphene on Photocatalytic Hydrogen Generation. Sol. Energy Mater. 2018, 185, 431–438. https://doi.org/https://doi.org/10.1016/j.solmat.2018.05.045.

(17) Galińska, A.; Walendziewski, J. Photocatalytic Water Splitting over Pt−TiO_2 in the Presence of Sacrificial Reagents. Energy & Fuels 2005, 19. https://doi.org/10.1021/ef0400619.

(18) Mamiyev, Z.; Balayeva, N. Metal Sulfide Photocatalysts for Hydrogen Generation: A Review of Recent Advances. Catalysts 2022, 12, 1316. https://doi.org/10.3390/catal12111316.

Chapter 5

Hydrothermally synthesized PbS doped bismuth titanate perovskites as highly efficient photocatalyst for hydrogen production

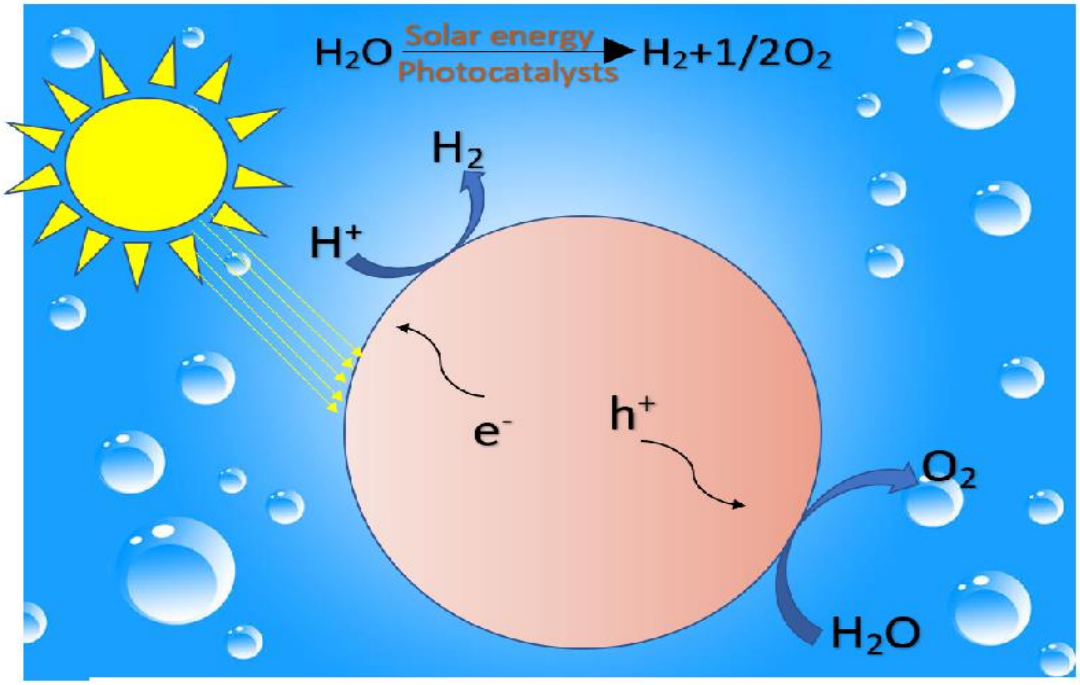

5.1 Introduction

Environmental destruction and energy challenges are intensifying as a consequence of contemporary humankinds' rapid growth and enormous fossil fuel consumption. As a result, both environmental sustainability and energy use are considered valuable in our universe. Too far, fossil fuels have accounted for nearly 89% of worlds energy usage. Consequently, the worldwide energy requirement is growing much faster than the capacity and availability of fossils fuels owing to a crisis of energy. More notably, the worlds escalating use of fossils fuel has a tremendous negative effect on the environment. These both factors together represent a noteworthy threat to the advancement of human beings.

Accordingly, the global emphasis is on the advancement of alternative sources of renewable energy. Afterwards the discovery of Fujishima and Honda, interest was drawn to photocatalytic hydrogen generation[1].

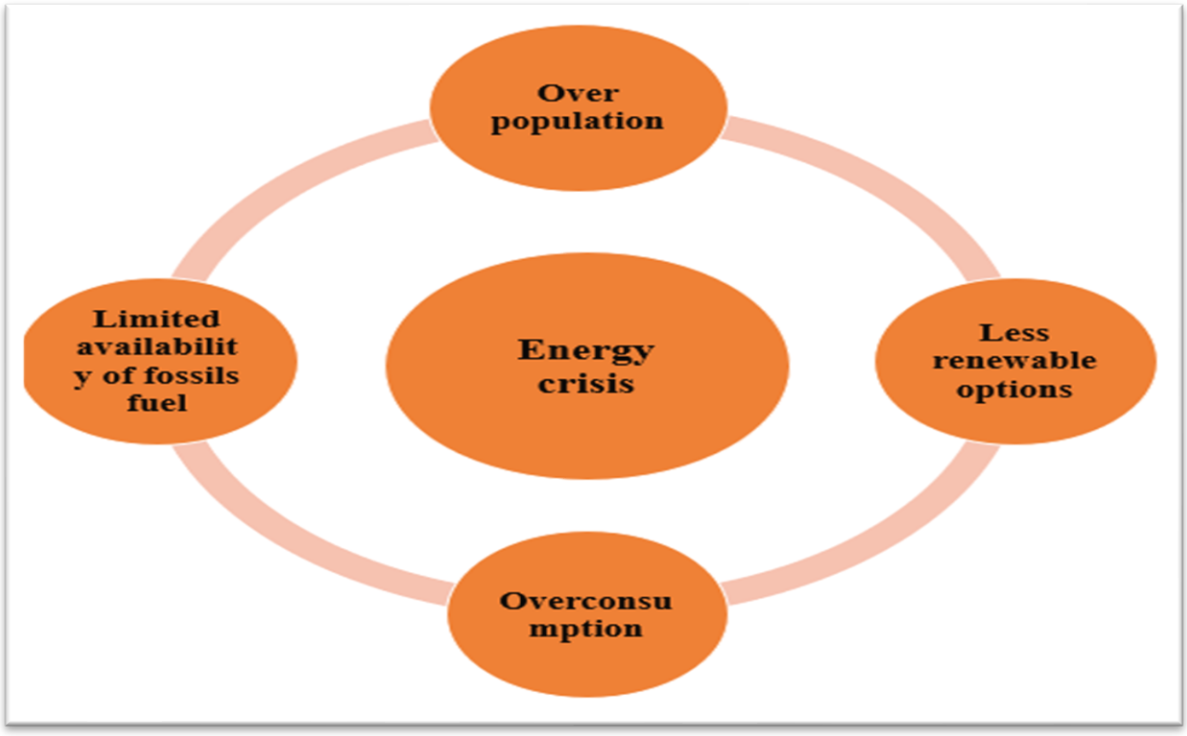

Fig 5.1 The factors causing energy crisis.

Among the variety of sources, sustainable production of hydrogen in presence of solar light provides a viable way to address the future energy demands. Which directly produces the chemical energy by use of solar light in presence of semiconductor having photocatalytic properties[2]. For hydrogen generation via photocatalysis, synthesis of effective and suitable photocatalysts has risen tremendously over the years[3].

Among various photocatalysts perovskite materials are indeed a profound and extensive class of emerging nanostructured materials that have attracted significant attention[4]. The researchers have proposed the importance of perovskites in different fields like hydrogen generation by water splitting, in fuel cells, gas sensors, glucose sensors, batteries and in solar cells[5]. Due to their outstanding optoelectronic, magnetic, ferroelectric and good thermal stability characteristics, perovskites materials are recognized as intriguing photocatalysts for an extensive array of photocatalytic applications[6].

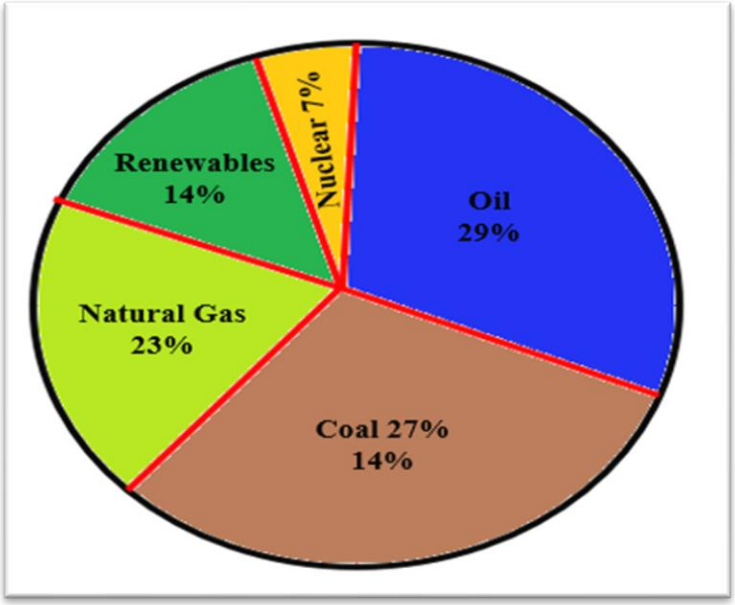

Fig 5.2 World energy consumption with energy source.

These characteristics are anticipated to improve their relatively photocatalytic activity.

The formula of perovskites is ABO_3 where A and B are cations of transition metals and alkali or alkaline earth metals respectively. These cations can be replaced by some other cations of similar radii thus generating a large number of perovskites having similar structures. A number of perovskite materials have been synthesized including $SrTiO_3$, $BaTiO_3$, $BiTiO_3$, $Bi_4Ti_3O_{12}$, $Bi_{20}TiO_{20}$, $KTaO_3$, $NaTaO_3$, $KNbO_3$, and $NaNbO_3$ for photocatalytic applications and were reported to have a significant impact of preparation method and morphologies on their photocatalytic efficiency[7].

Over the last three decades, several literature studies have evaluated the basic aspects of perovskite materials in photocatalytic applications for hydrogen production. A variety of titanate-based perovskites were investigated by Adnan et al.[8]. In 2019 Phoon et. al. worked on $SrTiO_3$ based photocatalyst for H_2 generation by adopting polymerized complex and solid-state method for synthesis of photocatalysts. The 1300 $\mu molg^{-1}h^{-1}$ was the calculated hydrogen production efficiency in presence of methanol[9].

Similarly, Morteza Kolaei et. al. produced Sodium titanate photocatalysts by hydrothermal method and noticed the effect of titanium dioxide (TiO_2) and sodium hydroxide concentration (NaOH) in

enhancement of photoelectrochemical splitting of water. Further the photocurrent density was found to enhanced for $Ti/TiO_2/Na_2Ti_3O_7$ photoanode[10]. Another noteworthy investigation was done by Shinde et. al. $Pt/NaFeTiO_4$ photocatalyst showing 445.4 $\mu molg^{-1}h^{-1}$ hydrogen yield in presence of 25 vol% of methanol[11].

It is noteworthy that hydrogen generation is most crucial for future development. Though TiO_2 is a reliable, affordable, and effective photocatalyst for producing hydrogen from water but it is only active in UV light, which contributes to just 3-5% of solar energy[12]. Lead sulphide is the another frequently researched visible light active photocatalyst having bandgap 2.4 eV.

Presently to develop visible light active photocatalyst, numerous modifications and band engineering techniques have been applied, since solar radiation comprises around 40% visible light and only 3-5% UV radiation[13].

In this study, the H_2 production efficiency of PbS doped bismuth titanate photocatalysts, synthesized by hydrothermal method, has been evaluated by photocatalytic experiment. The $PbS/Bi_4Ti_3O_{12}$ shows the reduction in band gap to 2.7 eV due to generation of new band over valence band. The effect of different sacrificial agents on photocatalytic efficiency was studied and compared the efficiency of 0.6% PbS doped BTNPs in presence of TEOA, EDTA and methanol.

5.2 Experimental details

5.2.1 Materials

The pentahydrated form of bismuth nitrate $\{Bi(NO_3)_3 .5H_2O\}$, titanium dioxide $\{TiO_2$ anatase$\}$, lead chloride and thiourea were purchased from HIMEDIA laboratories. All the chemicals were of AR grade and has been used without any further purification at laboratory scale. The whole synthesis was performed by taking Double deionized water.

5.2.2 Preparation of bismuth titanate nanoparticles (BTNPs)

For synthesis of bismuth titanate nanoparticles, bismuth nitrate $(Bi\ (NO_3)_3.5H_2O)$ and titanium dioxide were selected as the precursors. Firstly, 3 molar solution of bismuth nitrate was prepared followed by dropwise addition of 1M titanium dioxide solution with constant stirring of 2 hours on magnetic stirrer at 4000rpm and a white-coloured transparent solution was obtained. Further, dropwise addition of 2M solution of sodium hydroxide (NaOH) was done to the above prepared

mixture until the pH approaches 12.5 resulting in appearance of white precipitates. Finally, above solution mixture was poured into the autoclave made up of stainless steel with teflon lining and heated the mixture at 150ºC for 10 hours. At ambient temperature conditions, the autoclave was allowed to cool. The obtained powder was rinsed repeatably with deionized water and ethanol. Then, the powder was dried in an oven at 100ºC for 12 hours, before being thoroughly ground in a pestle and mortar for 30 minutes. The resulted nanoparticles have a faint orange colour tint.

5.2.3 Preparation of lead sulphide (PbS) nanoparticles

Hydrothermal technique has been adopted for preparation of PbS nanoparticles by using lead chloride as a source of lead and for sulphur source thiourea was used. 1molar solution of lead chloride was prepared in 100mL distilled water further thiourea solution was added dropwise resulting in appearance of turbidity, on subsequent injection of thiourea transparent solution was obtained. Consequently, dropwise addition of 1M sodium sulphide (Na_2S) solution was done with constant stirring until pH reaches to 8-9. After continuous stirring for 30 min. the aforementioned solution mixture was transferred to stainless steel autoclave with teflon coating and heated at 160°C for 8 hours to undergo hydrothermal reaction. Thereafter, the autoclave was allowed to cool down at ambient temperature conditions. The produced nanoparticles were centrifuged and rinsed many times with ethanol and distilled water (H_2O). The resulted powder was dried in oven at 100ºC upto 4 hours. The black coloured precipitates were obtained.

5.2.4 Preparation of PbS doped bismuth titanates

The previously synthesized bismuth titanates were mixed with black coloured PbS nanoparticles. By using a pestle mortar to mechanically grind the NPs of various mass percentage (0.1%, 0.3% and 0.6% w/w %) and continued the process of grinding for 5 hours so that PbS NPs successfully absorbed in BTP lattice. The empirical evidence pertaining to physical properties indicates a noticeable alteration in coloration, progressing from a shade of pale orange to greenish shadow and obtained powder was subjected to calcination at 600ºC for a duration of 4 hours. Consequently, obtained nanoparticles were analyzed with XRD, FTIR, DRS-UV, XPS, EPR, HR-TEM and FESEM characterizations for further detection, recognition of phase and purity of aforementioned samples.

5.2.5 Photocatalysts Characterization

The crystallinity of the resulted nanomaterials was analyzed by using powder XRD (X-ray diffractometer Bruker D8 ADVANCE) equipped with monochromator having Cu Kα radiation (45 kV) and the scanning of samples was operated in the 2θ range of $20^o – 80^o$ for a duration of 5s. The absorbance spectra were assessed by utilizing the Perkin Elmer Lambda 900 diffused reflection spectrophotometer (DRS-UV) and band gap was detected from tauc plot. The morphologies and lattice structures of as-prepared materials was detected by FESEM (Field emission scanning electron microscopy, JEOL). The detection of functional groups was done by scanning the samples in $400cm^{-1} – 4000cm^{-1}$ range with the help of FTIR instrument (PERKIN ELEMER). FESEM and HR-TEM techniques were used for surface analysis.

5.2.6 Photocatalytic reaction

The photocatalytic reactor has been employed to carry out the photocatalytic reaction for hydrogen production by water splitting. The photoreactor was enclosed in a rectangular box having light source, magnetic stirrer and a gas collector. A round bottom flask of 100mL capacity was used for the reaction. The 0.1g of photocatalyst was suspended in 40mL water followed by addition of different sacrificial agents. During the whole experiment the solution was continuously agitated on magnetic stirrer so that the photocatalyst was evenly distributed. The solution was illuminated with 250W xenon lamp with 420λ cutoff filter. At fixed interval of every 50 min. the gas collector was removed from the setup and GC-TCD was employed to analyze the efficiency of photocatalyst for hydrogen generation.

5.3 Results and Discussion

5.3.1 Powder XRD

X-ray diffraction analysis was performed to determine the structural properties of synthesized samples. The nanomaterials endured scanning in the angular range of $20^o – 80^o$ (2θ) for a period of 5s using Bruker D8 ADVANCE. Figure 5.3 illustrates the XRD pattern of the BTP nanoparticles, which were developed by employing the hydrothermal approach. The XRD investigation reveals that, no significant impurity phase exists, indicating the purity of the phase. The diffraction pattern of acquired peaks provides confirmation of the polycrystalline characteristics of bismuth titanat

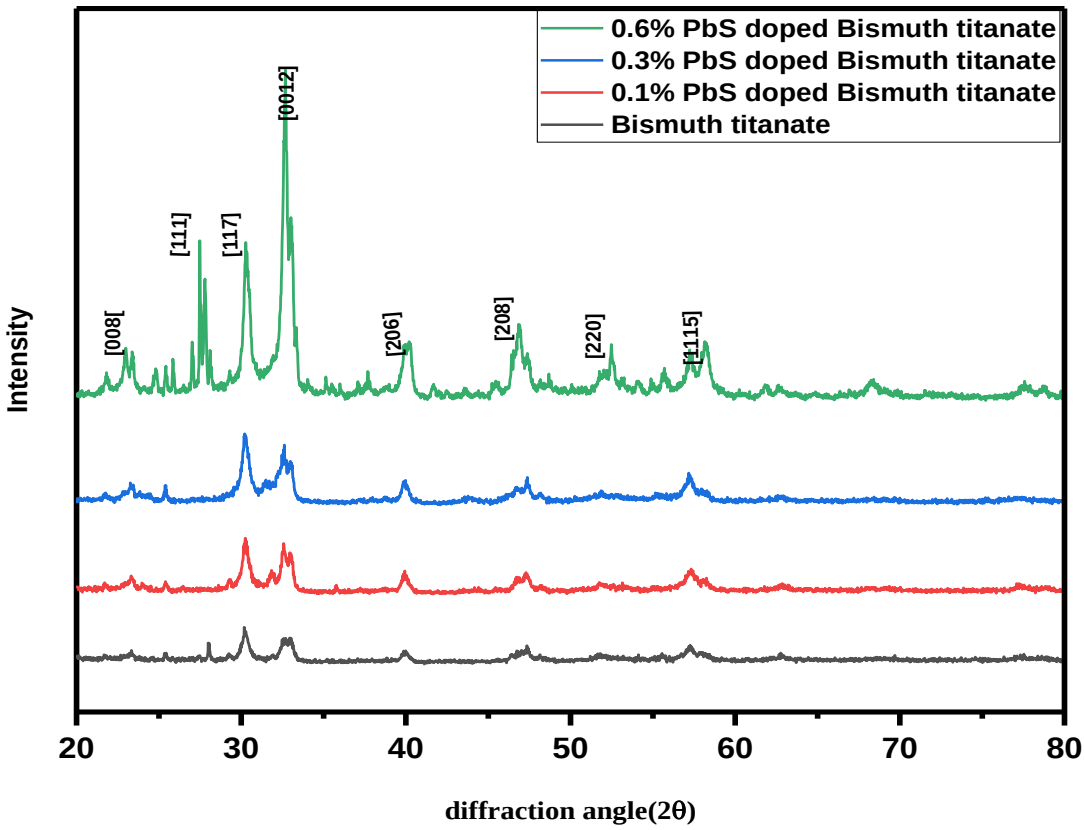

Fig 5.3 Comparative XRD graphs of PbS doped BTP.

The evaluation of graph shows that the sharp peaks observed at 30.05º and 32.84º can be attributed to orthorhombic bismuth titanate perovskite and exhibits a significant correlation with JCPDS Card no. 50-0300. The diffraction peaks detected in the sample can be effectively attributed to the layered bismuth titanate perovskite structure ($Bi_4Ti_3O_{12}$), which are consistent with the current reservoir of academic research[14]. The presence of prominent and well-defined peaks suggests high degree of crystallinity of the as-prepared BTP nanomaterials.

The peak position at 2θ of 28◦, 30◦ and 32◦, are the strongest peak corresponding to (1 1 1), (1 1 7) and (0 0 1 2) hkl planes respectively. The Rietveld analysis was done to check the crystal structure, which confirms the existence of orthorhombic phase of bismuth titanates ($Bi_4Ti_3O_{12}$).

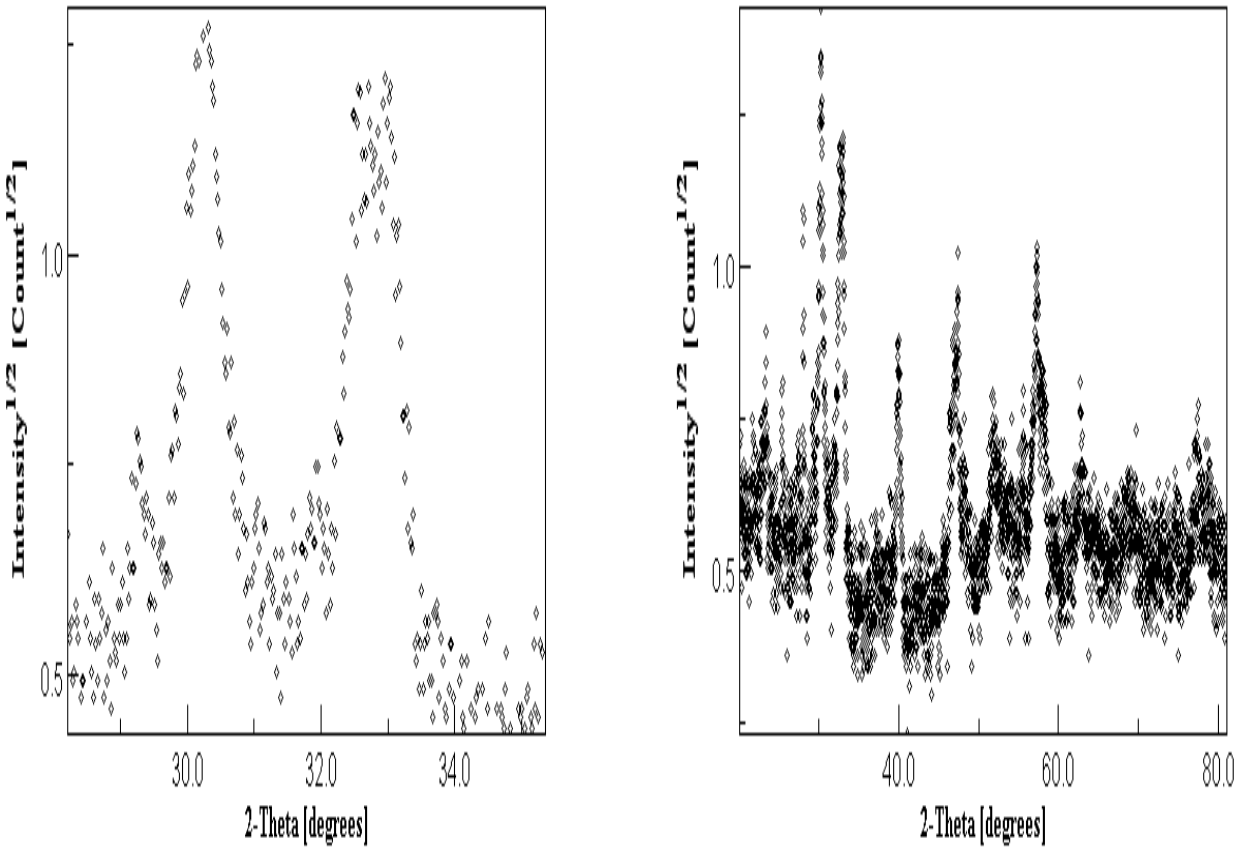

Fig 5.4 Rietveld refinement of bismuth titanates XRD.

Fig 5.4 shows the results of Rietveld refinement of bismuth titanates which are in well agreement with the experimental data. The Rietveld agreement factors including lattice parameters has been depicted in Table 5.1 While the refined atomic positions have been listed in table 5.3. The Rwp (R-weighted pattern), the standard of degree of calculated and measured values is equal to 11.12% i.e. very small, the S (goodness of fit) is equal to 2.76, demonstrating that fitting is excellent in Rietveld analysis.

The nanoparticles synthesized via hydrothermal approach exhibits an orthorhombic crystal structure characterized by the Aba2 space group. The cell parameters were determined to be having a= 32.83, b= 5.411, c= 5.448 calculated from MAUD software and these values closely align with those reported in the literature[15].

Table 5.1 Unit cell parameters, Unit cell volume and Rietveld agreement factors for bismuth titanates.

Crystallographic system	Orthorhombic
Space group	Aba2
a(Å)	32.83
b(Å)	5.411
c(Å)	5.448
Unit cell volume ($Å^3$)	967.79
R_{wp}	11.12
R_{wnp}	20.05
R_b	9.05
S	2.76

It has been noticed that the PbS dopant incorporated into the lattice of BTNPs greatly influence the crystallite size. For 0.1%, 0.3% and 0.6% dopant concentration, the crystallite size is 26.44, 19.98 and 18.24nm respectively and was calculated by applying Debye Scherrer formula:

$D = K. \lambda / \beta. \text{Cos } \theta$

Where D denotes the crystallite size of particles, K represents the shape factor, X-ray's wavelength is λ (1.5418Aº for Cu Kα), FWHM (full width at half maximum) is represented by β, the detected peak angle is expressed in degree (θ).

The average crystallite size of bismuth titanates is 30.20nm which further reduces on addition of dopant in lattice sites of BTNPs which might be due to the distortion caused by dopant in lattice. The distortion in lattice is due to the difference in radius of dopant and replaced element.

Table 5.2 Demonstrates the crystallite size of BTP and PbS doped BTNPs.

Photocatalyst	**FWHM**	**Crystallite size**
Bismuth titanate (BT)	0.266	30.20nm
0.1% PbS doped BT	0.327	26.44nm
0.3% PbS doped BT	0.430	19.98nm
0.6% PbS doped BT	0.471	18.24nm

Table 5.3 Atomic coordinated occupancies of bismuth titanates.

Atom	**X**	**Y**	**Z**	**Occupancy**
Ti_2	0.3714	0.999	0.0533	1
Bi_1	0.0688	0.9978	0	1
O_4	0.3185	0.926	0.96	1
Bi_2	0.21135	0.0199	0.9991	1
Ti_1	0.5	0	0.0452	1
O_2	0.2507	0.252	0.264	1
O_3	0.4404	0.975	0.073	1
O_1	0.9967	0.222	0.207	1
O_6	0.869	0.2	0.159	1
O_5	0.1215	0.285	0.294	1

The analysis of X-ray diffraction (XRD) peak reveals that on inclusion of dopant concentration PbS, it leads to augmentation in the intensity of peaks at 30.05º as the dopant concentration increases from 0.1% to 0.3% and abnormally increase with 0.6% dopant concentration. The inconsistence in the variation of intensities among the various X-ray diffraction (XRD) graphs suggests the existence of Pb^{2+} ions within bismuth titanate perovskite structures. Moreover, some

additional peaks were detected with addition of dopant concentration at 22.9^{o} ,26.2^{o}, 38.7^{o} corresponding to PbS. It has been discovered that with increase in dopant concentration there is a decrease in crystallite size.

$Bi_4Ti_3O_{12}$ can be represented as a regular stacking of fluorite like $[Bi_2O_2]^{+2}$ slabs and describing the Aurivillius structure family, four OH atoms form the apexes of perovskite blocks. The Bi^{+3} cation shows high polarizability and stereochemical activity due to presence of lone pair of electrons in $6s^2$, having the electronic configuration of [Xe] $4f^{14}5d^{10}6s^2$. In above structure Bi (I) shows 12 co-ordination number.

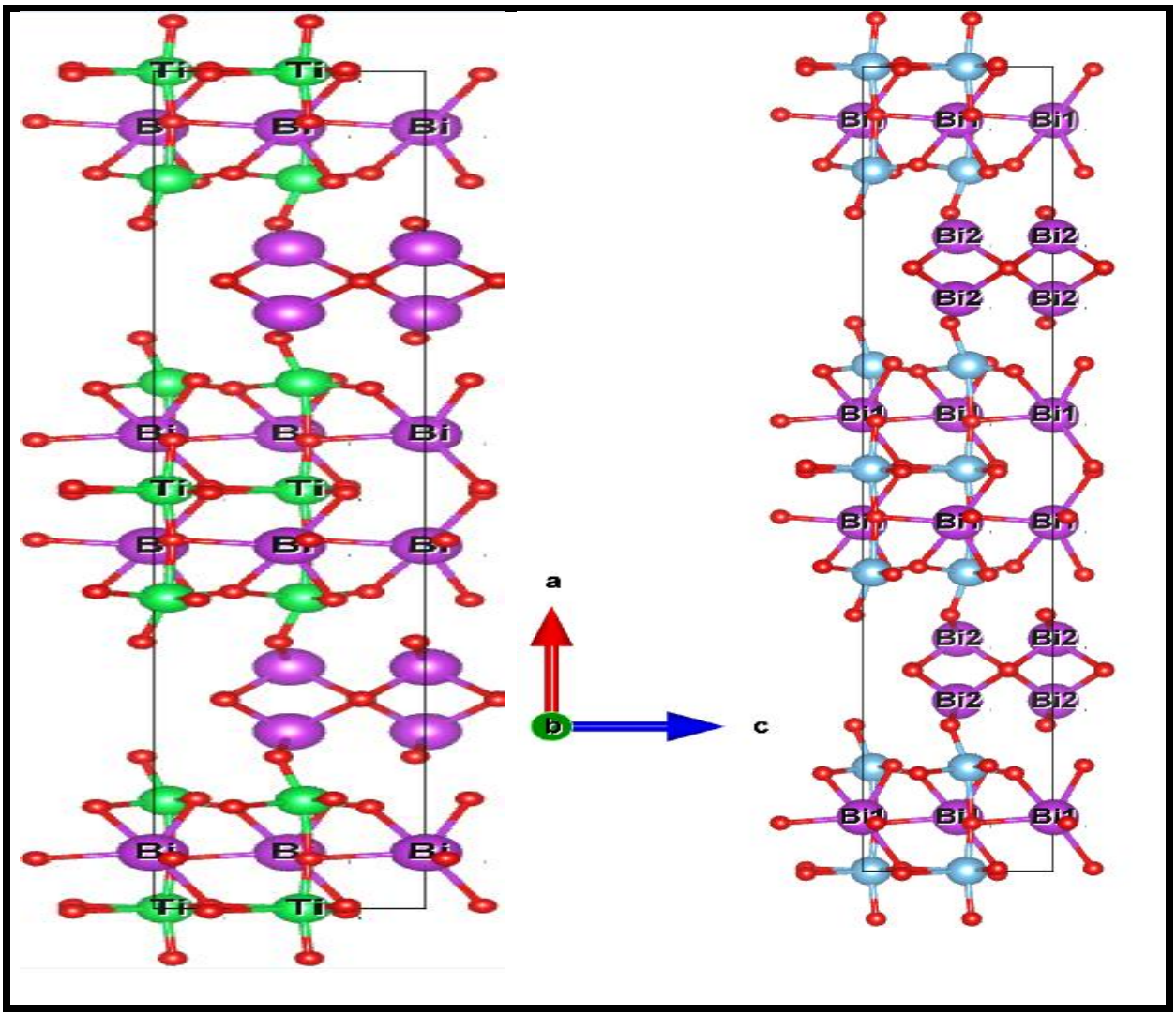

Fig 5.5 Crystal structure of $Bi_4Ti_3O_{12}$ drawn using VESTA.

Table 5.4 Radii of atoms of bismuth titanates calculated from VESTA.

Atom	Radii
Bi	1.82
Ti	1.47
O	0.74

5.3.2 FTIR study

The distinct peak observed at wavenumber of 540cm^{-1} exhibits the characteristic properties of $Bi_4Ti_3O_{12}$. The increase in concentration of dopant leads to an increase in absorbance of the peak located at position 830 cm^{-1}. Additionally, a novel absorption peak has detected at wavenumber of 1116cm^{-1} and its absorbance indicates a positive correlation with the concentration of dopant concentration.

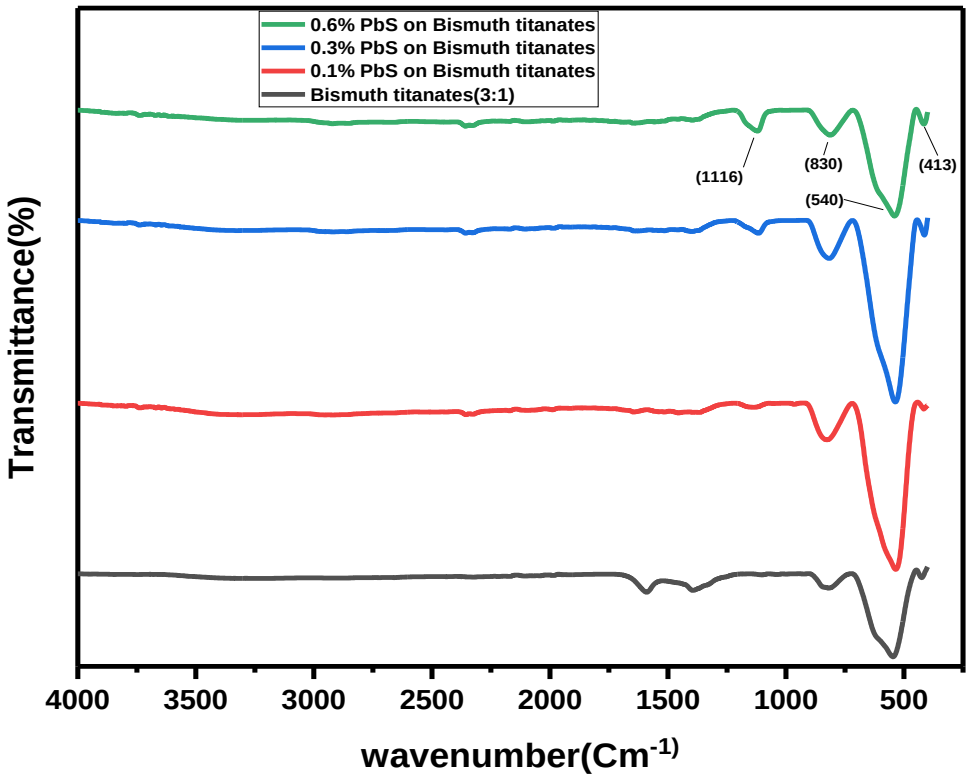

Fig 5.6 FTIR spectrum of PbS doped Bismuth titanates.

The FTIR spectrum of dopants (PbS) shows peaks at wavenumber of 1116cm^{-1} and 830cm^{-1} signifying the incorporation of lead sulfide (PbS) within bismuth titanate lattice.

5.3.3 DRS-UV Visible spectroscopy

Figure 5.8 illustrates the UV spectrum of bismuth titanate nanostructures. Bismuth titanate exhibits the bandgap of 3.25 eV illustrating the absorption in ultraviolet (UV) region and has been further reduced by doping of Lead sulfide nanoparticles. This decrease in absorption has been attributed due to generation of new band just above the valence band. As the concentration of dopant increases from 0.1% to 0.6% band gap diminished from 3.25eV to 2.76eV. The incorporation of 0.6% PbS into BTNPs resulted in a noticeable shift towards longer wavelength. The band gap of 0.6% PbS doped BTNPs was determined to be 2.76 eV and was calculated by the tangent line from the Tauc plot (αhν)1/2 function against the photon energy. The findings have been matched well with the previous report[16]. The trend of enhanced absorption has been documented as a consequence of incorporation of PbS dopant.

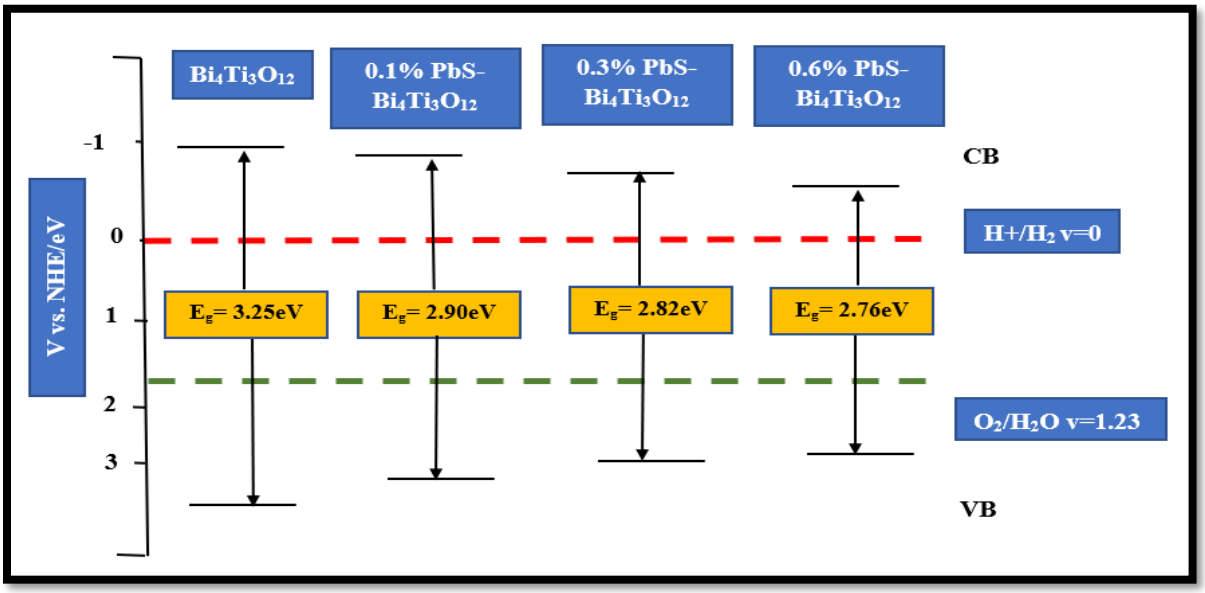

Fig 5.7 Band positions of bismuth titanate and PbS doped BT.

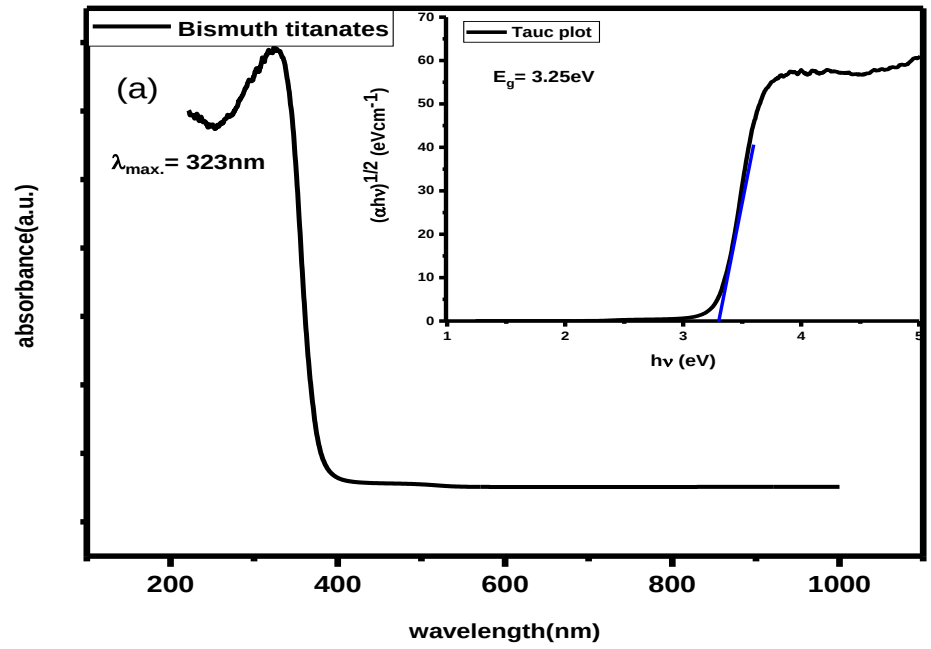
Bismuth titanates
(a)
λmax.= 323nm
absorbance(a.u.)
wavelength(nm)
Tauc plot
Eg= 3.25eV
(αhν)1/2 (eVcm-1)
hν (eV)

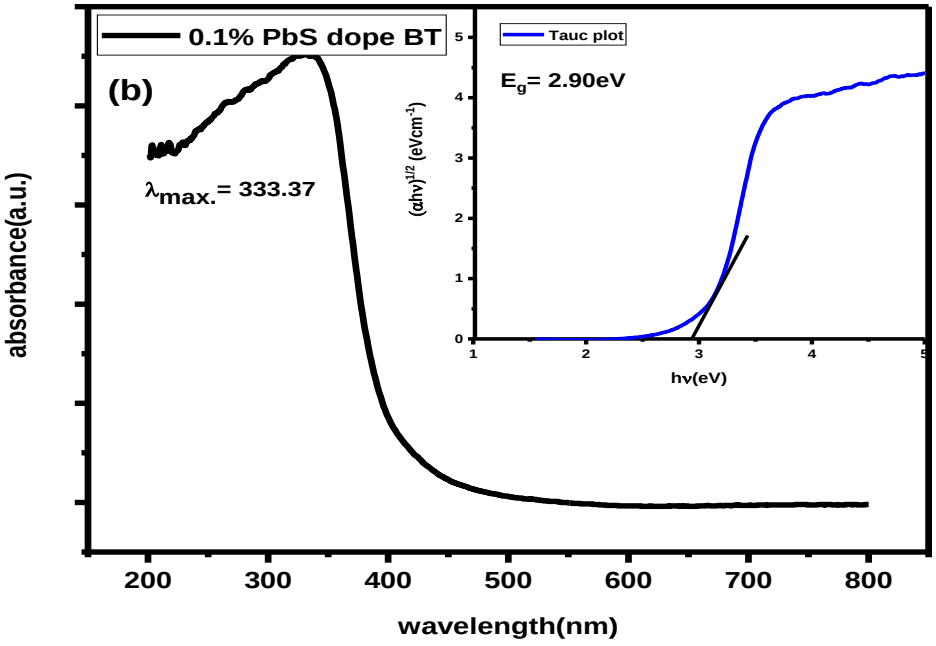
0.1% PbS dope BT
(b)
λmax.= 333.37
absorbance(a.u.)
wavelength(nm)
Tauc plot
Eg= 2.90eV
(αhν)1/2 (eVcm-1)
hν(eV)

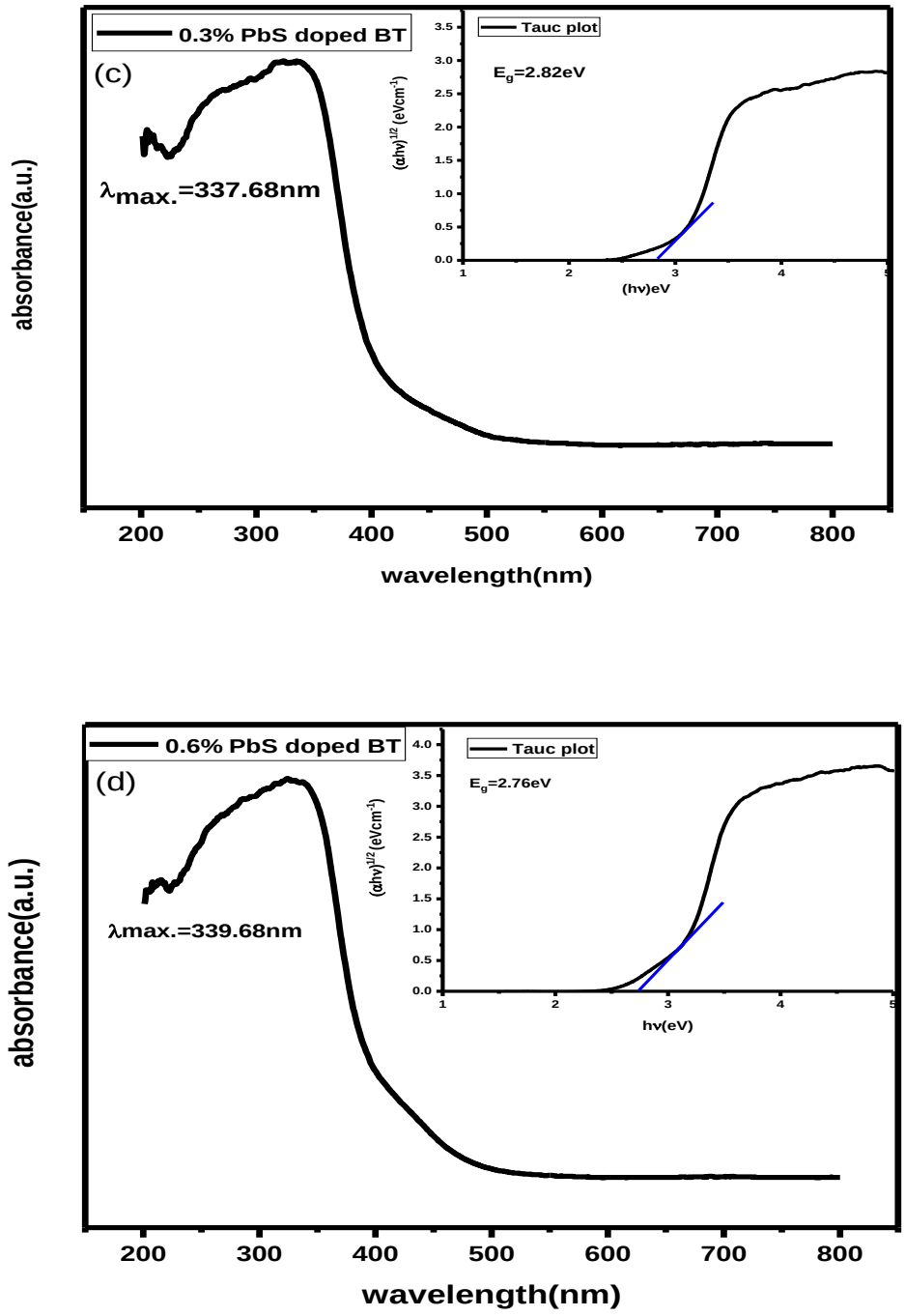

Fig. 5.8 (a) Illustrates the band gap of bismuth titanates (b) band gap of 0.1% PbS doped BT (c) band gap of 0.3% PbS doped BT and (d) 0.6% PbS doped BT.

On PbS insertion, certain lead(3d) orbitals of lead sulfide (PbS) gets hybridized with Ti (3d) orbitals present in the bismuth titanate lattice, resulting in formation of impurity levels positioned

below the conduction band, consequently causing a shift in absorption edge towards lower energy levels. The observed trend in the table indicates that an increase in dopant concentration leads to a decrease in the band gap, primarily attributed to the expansion of absorption towards longer wavelengths.

Table 5.5 Band gap of PbS doped photocatalyst.

Photocatalyst	**λmax.**	**Band gap**
Bismuth titanate	323nm	3.25 eV
0.1% PbS doped BT	333nm	2.90 eV
0.3% PbS doped BT	337nm	2.82 eV
0.6% PbS doped BT	339nm	2.76 eV

5.3.4 XPS

The bonding states of bismuth titanates were analyzed by using XPS instrument. Fig 5.9 Indicates that each of the peak on XPS scan spectrum could be assigned to the Bi, Ti, O and C core levels. The prominence of the carbon peak is accountable because of the carbon tape utilized for the XPS measurement. The high resolution XPS spectrum of Bi, Ti and O has been shown in fig 5.9 (b), (c) and (d) respectively and their Gaussian resolved results. The fig 5.9 (b) shows Gaussian-resolved result for Bi 4f spectrum displaying two peaks assigned to Bi $4f_{7/2}$ and Bi $4f_{5/2}$ centered at 158.80 and 164.15 eV respectively.

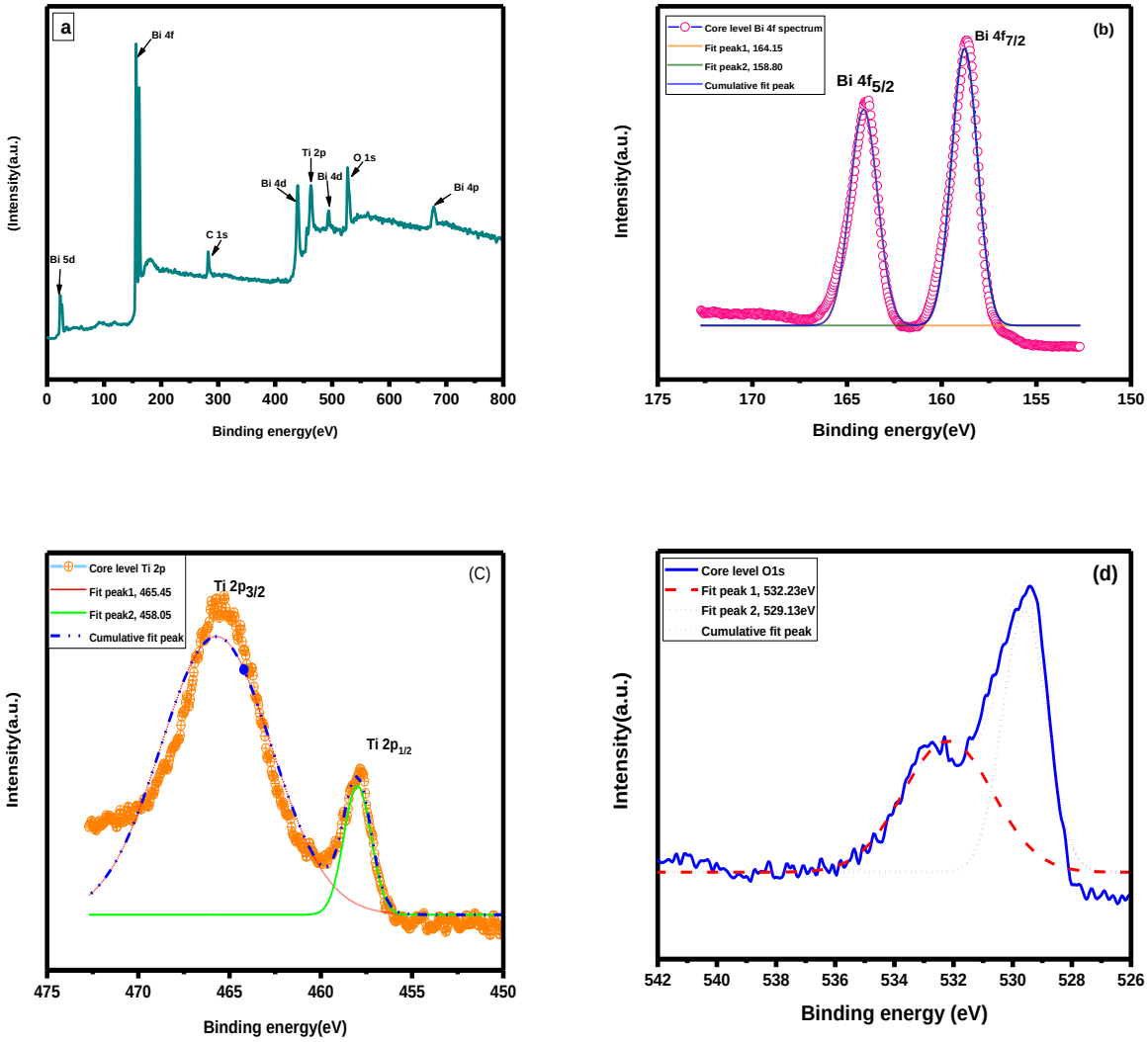

Fig 5.9 (a) Full length XPS spectrum of bismuth titanate, high resolution spectra of (b) Bi 4f (c) Ti 2p and (d) O 1s.

The gaussian resolved result for Ti as according to fig 5.9 (c) shows two major peaks at 458.05 and 465.45 eV, could be assigned to Ti $2p_{1/2}$ and Ti $2p_{3/2}$ respectively and are in accordance with the pure TiO_2. From fig 5.9 (d) wide and asymmetric high resolution XPS spectrum of O 1s can be seen indicating the existence of more than one chemical state of oxygen species. Two oxygen species i.e. the lattice oxygen from Ti-O bond at contributes in the deconvolution of oxygen spectrum with binding energy of 529.13eV and oxygen adsorbed on surface withy -OH group showing higher binding energy of 532.23eV.

5.3.5 EPR spectroscopy

The room temperature EPR spectroscopy was employed to analyze the oxygen vacancies of Bismuth titanates. To characterize the oxygen defects EPR is the most immediate and sensitive technique. The pristine bismuth titanates show the g factor at 2.09 indicating the presence of oxygen vacancies while, the g factor for 0.6% PbS doped bismuth titanates was found to be at 2.12, indicating the increase in oxygen vacancies.

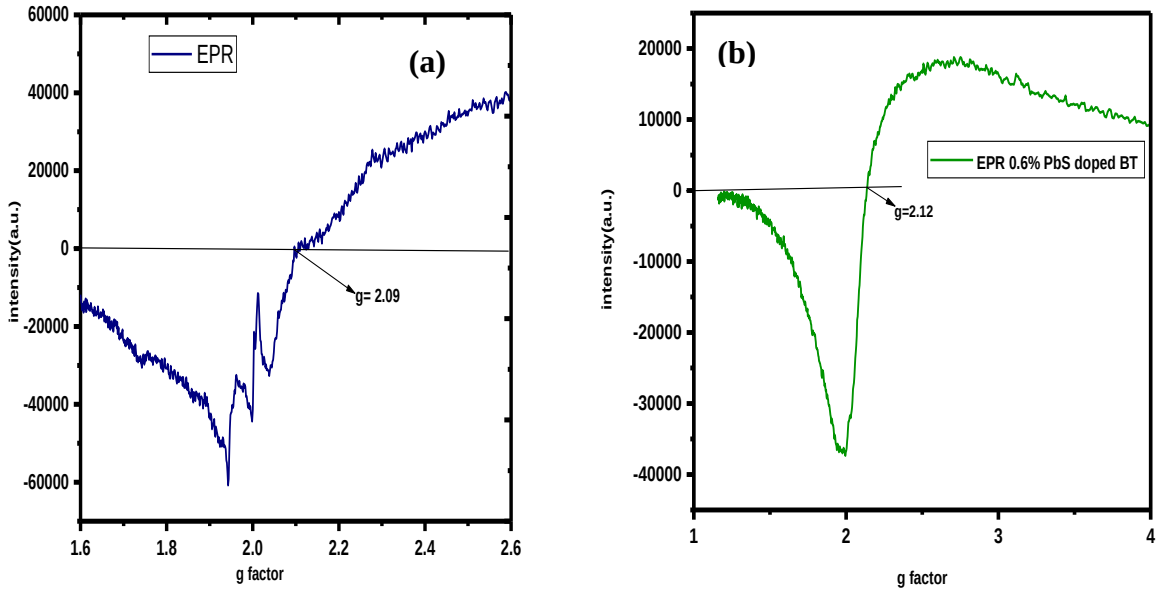

Fig 5.10 (a) EPR spectrum of Bismuth titanates and (b) 0.6% PbS doped BT.

5.3.6 Morphological study

5.3.6.1 FESEM

Using FESEM analysis, the surface morphology of the synthesized samples was evaluated. As shown in Fig.5.11 (a) spherical shape of bismuth titanate nanoparticles can be easily noticed and are homogeneously distributed. The analysis was performed on the plane surface and the evaluation was carried out by utilizing the micrographs, all of which were recorded at (X 30,000) magnification. From fig 5.11 (b), (c) and (d) PbS insertion into bismuth titanate can be easily detected by appearance of rod-shaped structures along the axis.

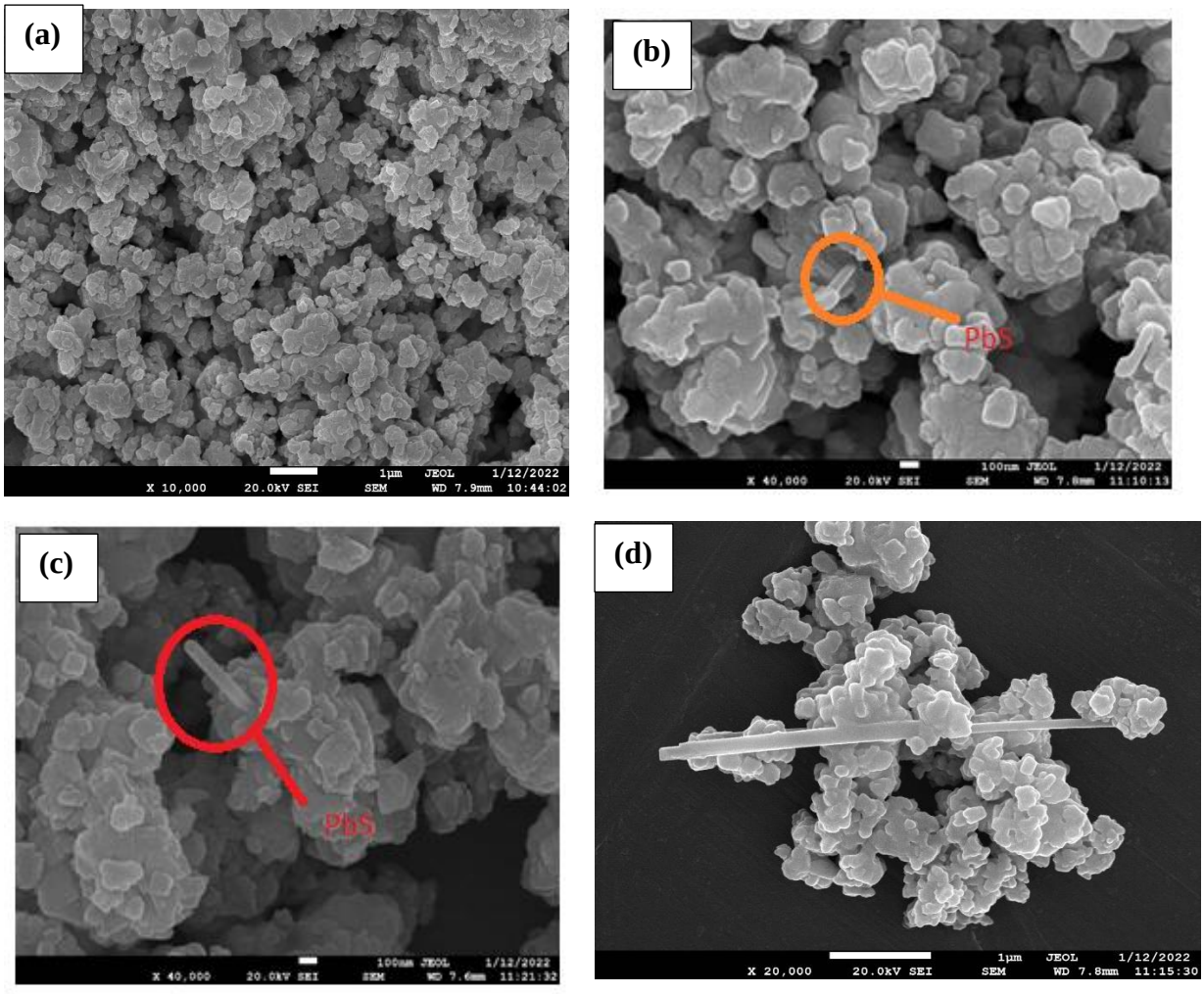

Fig 5.11 (a) FESEM image of BTNPS, (b) 0.1% PbS doped BT, (c) 0.3% PbS doped BT and (d) 0.6% PbS doped BT.

5.3.6.2 HR-TEM

The TEM images in fig 5.12 (A) and (B) depicts the morphology of bismuth titanate nanostructure indicating rectangular sheet like nanostructures having thickness in nanometer range. The sample thickness increases with addition of PbS dopant and the lateral dimensions are determined to be about 100 to 200nm. Due to practical constraints, nanosheets thickness could not be evaluated by TEM.

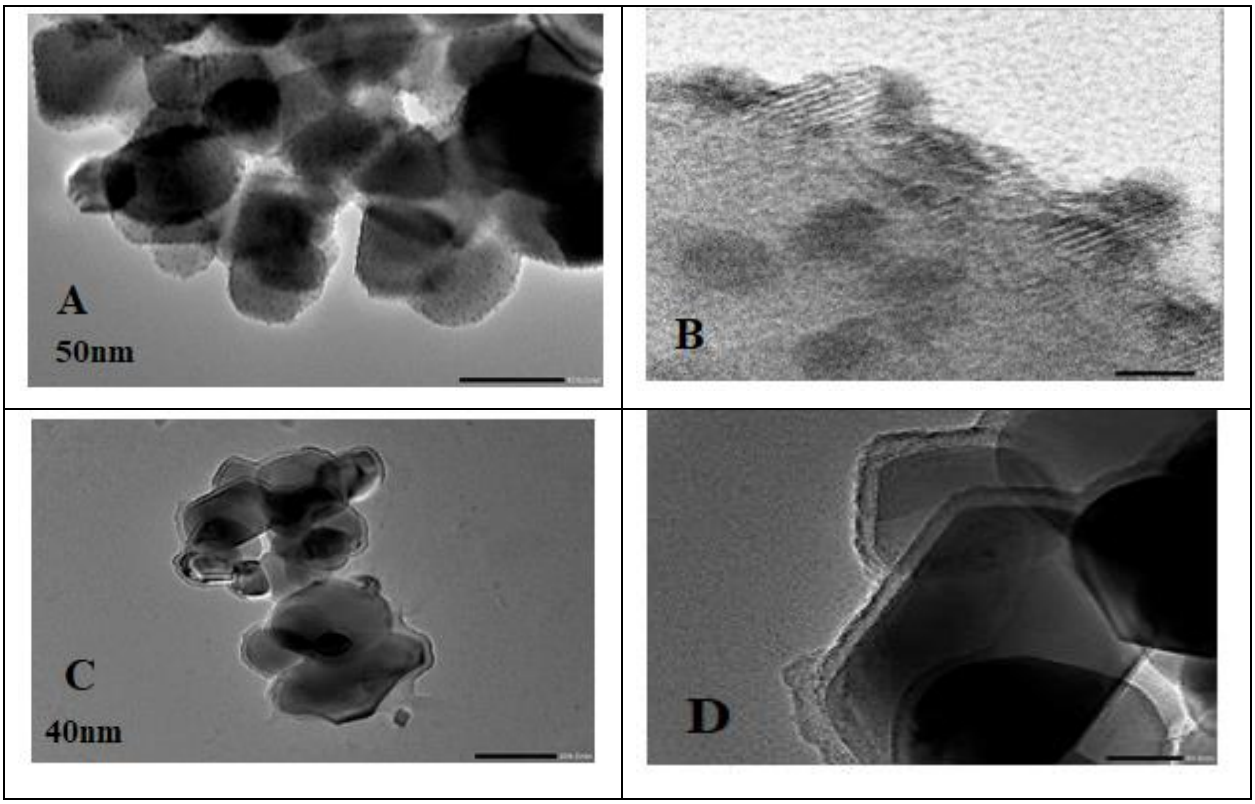

Fig 5.12 (A) and (B) Bismuth titanates and (C), (D) 0.6% PbS doped Bismuth titanate.

5.3.7 Photocatalytic activity

Pure bismuth titanate (BT), 0.1%, 0.3% and 0.6% PbS doped BT nanoparticles were employed as photocatalysts for splitting of water producing hydrogen gas. The reaction was carried out in presence of ethylenediaminetetracetate (EDTA) which acts as sacrificial agent. The BTNPs shows only 11.78μmol/g hydrogen production efficiency which is not so high and the reason behind that is the high recombination rates of electrons (e^-) and holes (h^+). The band gap also plays crucial role and due to broad band gap value of 3.25 eV, BTNPs also shows less hydrogen efficiency showing light absorption in UV region.

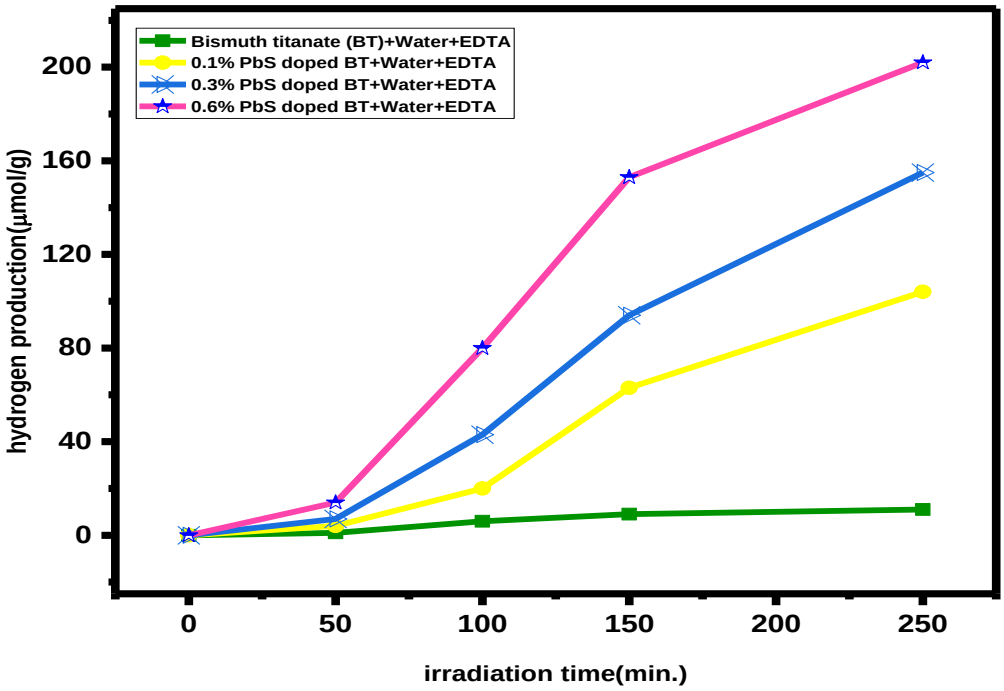

Fig 5.13. Photocatalytic splitting of water by bismuth titanate nanoparticles and PbS doped BT in presence of EDTA.

Table 5.6 Represents hydrogen evolution rates of different photocatalysts.

Photocatalyst	**Sacrificial agent**	**Reaction condition**	**Light source**	**H_2 evolution**
Bismuth titanate (BT)	EDTA	0.1g of powder in 40ml water	250W Xe lamp	11.78µmol/g
0.1% PbS doped BT	EDTA	0.1g of powder in 40ml water	250W Xe lamp	103.29µmol/g
0.3% PbS doped BT	EDTA	0.1g of powder in 40ml water	250W Xe lamp	154.37µmol/g
0.6% PbS doped BT	EDTA	0.1g of powder in 40ml water	250W Xe lamp	202.43µmol/g

Moreover, the band gap was narrowed by insertion of different amounts of 0.1%, 0.3% and 0.6% of PbS into BTNPs. The generation of new valence band (VB) above the VB maximum results in reduction of band gap thus, facilitating easy transfer of electrons to conduction band (CB) results in reduction of H^+ ions to H_2.

From fig 5.13, it can be seen that 0.6% PbS doped BTNPs showed the maximum hydrogen generation efficiency of 202.43 µmol/g which is very high in comparison to bare bismuth titanates. To resolve the phenomenon of electron-hole pair recombination upon photoirradiation, the reaction of 0.6% PbS doped BT was carried out in the presence of several hole scavengers (sacrificial agents). The descending order for H_2 production (fig 5.14) using 0.6% PbS doped BTNPs is MeOH > EDTA > TEOA.

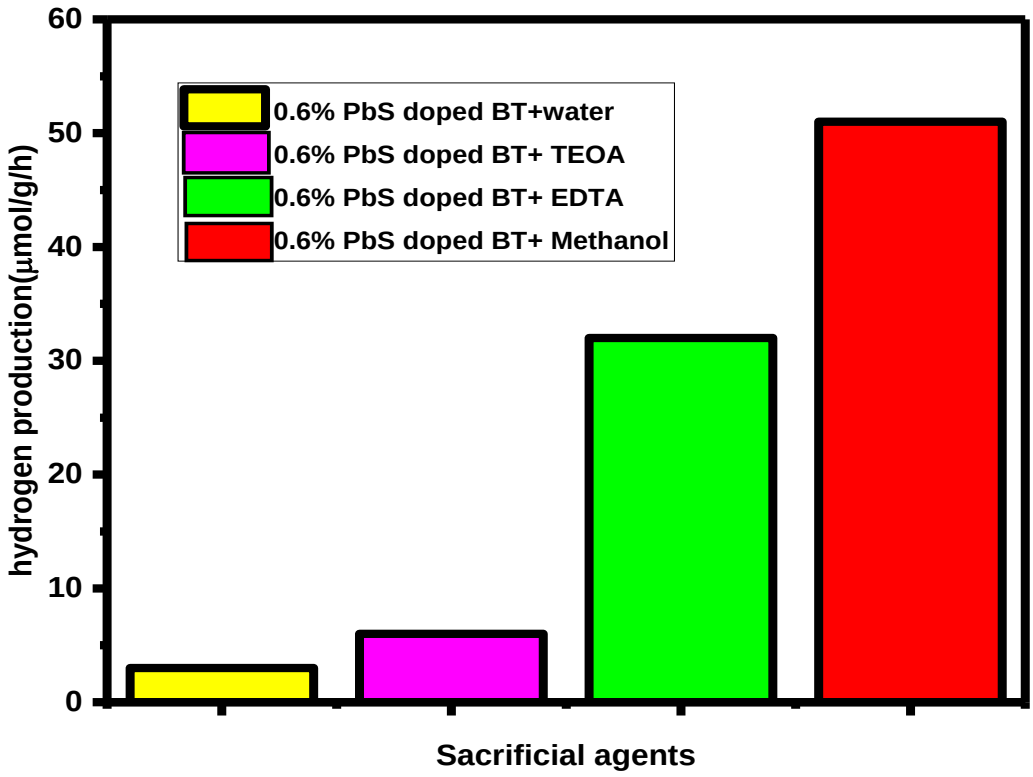

Fig 5.14 Bar diagram depicting photocatalytic H_2 generation of 0.6% PbS doped bismuth titanate nanoparticles (BTNPs).

The generation of new valence band occurs above the maximum of valence band position and thus reducing the band gap between VB and CB thereby easily facilitating electrons to CB[17]. It was detected that PbS doping leads to an increase in the charge carriers by means of a shift in band position. Additionally, influencing the oxidation and reduction abilities of the photogenerated electrons and holes, ultimately resulting in the notable improvement of photocatalytic reactions. The investigation revealed that the rate of hydrogen evolution was found to be minimum with triethanolamine (TEOA) which is potentially attributed to sensitive nature of TEOA to undergo oxidation in an aqueous solution[18]. The presence of EDTA leads to a decrease in hydrogen production efficiency which might be due to the consumption of EDTA during the process of photocatalysis. Methanol (MeOH) exhibits the ability to slow down the process of electron-hole recombination by capturing holes from the doped valence band of bismuth titanate nanoparticles. Consequently, the presence of methanol results in reduction of OH radicals thereby leading to increase in hydrogen evolution rate and serving as a hole scavenger[19].

5.4 Mechanistic aspects

The pictorial representation for water splitting reaction by PbS doped BT has been shown in fig 5.15 Migration of electrons takes place, when photons with energy exceeding the band gap energy impinges upon the photocatalysts, from low lying valence band to conduction band thereby, holes (h^+) remained in the valence band. The H^+ ions are reduced by electrons at conduction band resulting in production of hydrogen gas meanwhile in VB water oxidizes, leading to evolution of oxygen gas. The electron-hole recombination is diminished by sacrificial reagents such as methanol, EDTA and TEOA. In the methanol + water + photocatalyst mixture, photogenerated holes are captured by methanol[20] and production of formaldehyde during hole oxidation thereby, reducing the recombination of electron hole pairs. In the meantime, hydrogen gas is produced by reaction of two protons (synthesized during methanol oxidation) with the generated electrons produced by absorption of light by bismuth titanates.

$$\mathbf{Bi_4Ti_3O_{12}\ h\nu \rightarrow h^+ + e^-}$$

$$\mathbf{CH_3OH + 2h^+ \rightarrow HCHO + 2[H]^+}$$

$$\mathbf{2[H]^+ + 2e^- \rightarrow H_2(g)}$$

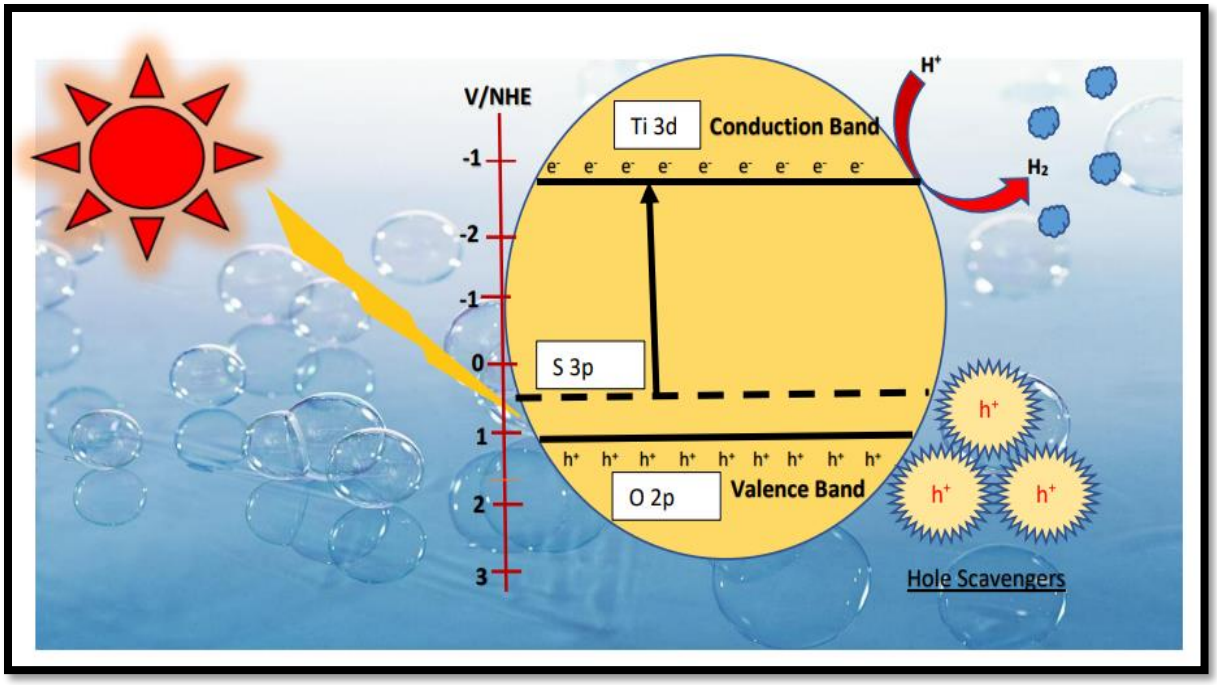

Fig 5.15 Proposed theoretical mechanism of hydrogen production by PbS doped bismuth titanates.

Formaldehyde will be further oxidized to formic acid and releasing hydrogen gas by combination of produced protons with photogenerated electrons.

$$HCHO + 2h^+ + H_2O \rightarrow HCOOH + 2[H]^+$$

$$2[H]^+ + 2e^- \rightarrow H_2(g)$$

Further, the formic dissociates into carbon dioxide along with production of two protons, consequently producing hydrogen gas.

$$HCOOH + 2h^+ \rightarrow CO_2(g) + 2[H]^+$$

$$2[H]^+ + 2e^- \rightarrow H_2(g)$$

The overall photocatalytic hydrogen production reaction is summarized below:

$$CH_3OH + H_2O \xrightarrow{hv,\ Bi4Ti3O12} CO_2(g) + 3H_2\ (g)$$

The improvement in photocatalytic efficiency for 0.6% PbS doped BT attributed to the lower value band gap of 2.76eV as derived from UV-DRS studies and nanosized particles also plays a

crucial role. The mixing of atomic orbitals of O (2p) and S (3p) subsequent in formation of high-level valence band which facilitates the easy and rapid movement of electrons from VB to CB and also the smaller particles exhibit the high surface area leading to enhancement in photocatalytic activity through improved light absorption[21].

5.5 Conclusion

In summary, a simple hydrothermal approach has been adapted to fabricate $Bi_4Ti_3O_{12}$ photocatalysts with oxygen vacancies. The 0.6% PbS doped orthorhombic bismuth titanate perovskites shows enhanced photocatalytic activity as compared to pristine BT in presence of EDTA, While the best sacrificial agent was found to be methanol which serves as a hole scavenger. The improved photocatalytic efficiency is accredited to generation of novel band over VB enabling the efficient transfer of electrons from VB to CB, and the inclusion of methanol as a hole scavenging agent. The hydrogen production rate of BT is 11.78μmol/g in presence of EDTA while this rate reaches up to 202.43μmol/g for 0.6% PbS doped BT which is many times high in comparison to bare BT. The superior photoactivity is because of the improved separation potential of photo-generated electron-hole pairs, which emerge from the valence band expansion (generation of new band over VB maximum due to doping). UV- visible spectroscopy reveals the band gap of 2.76eV for 0.6% PbS doped BT as calculated form tauc plot indicating the reduction in band gap (BT band gap 3.25eV) results in enhancement of water splitting activity.

References

(1) Amika; Sharma, R.; Sharma, A.; Chandrani, A.; Singh, J.; Kumar, D. Role of Titanate-Based Perovskites in Solar Water Splitting: An Overview. J. Phys. Conf. Ser. 2022, 2267 (1), 012016. https://doi.org/10.1088/1742-6596/2267/1/012016.

(2) Lokhande, P. E.; Kulkarni, S.; Chakrabarti, S.; Pathan, H. M.; Sindhu, M.; Kumar, D.; Singh, J.; Kumar, A.; Kumar Mishra, Y.; Toncu, D.-C.; Syväjärvi, M.; Sharma, A.; Tiwari, A. The Progress and Roadmap of Metal–Organic Frameworks for High-Performance Supercapacitors. Coord. Chem. Rev. 2022, 473, 214771. https://doi.org/https://doi.org/10.1016/j.ccr.2022.214771.

(3) Perović, K.; dela Rosa, F. M.; Kovačić, M.; Kušić, H.; Štangar, U. L.; Fresno, F.; Dionysiou, D. D.; Loncaric Bozic, A. Recent Achievements in Development of TiO_2-Based Composite Photocatalytic Materials for Solar Driven Water Purification and Water Splitting. Materials. 2020. https://doi.org/10.3390/ma13061338.

(4) Landman, A.; Dotan, H.; Shter, G. E.; Wullenkord, M.; Houaijia, A.; Maljusch, A.; Grader,

G. S.; Rothschild, A. Photoelectrochemical Water Splitting in Separate Oxygen and Hydrogen Cells. Nat. Mater. 2017 166 2017, 16 (6), 646–651. https://doi.org/10.1038/nmat4876.

(5) Jian, J.; Jiang, G.; van de Krol, R.; Wei, B.; Wang, H. Recent Advances in Rational Engineering of Multinary Semiconductors for Photoelectrochemical Hydrogen Generation. Nano Ene 2018, 51, 457–480. https://doi.org/https://doi.org/10.1016/j.nanoen.2018.06.074.

(6) Acar, C.; Dincer, I.; Naterer, G. F. Review of Photocatalytic Water-Splitting Methods for Sustainable Hydrogen Production. Int. J. Energy Res. 2016, 40 (11), 1449–1473. https://doi.org/10.1002/ER.3549.

(7) Hisatomi, T.; Domen, K. Reaction Systems for Solar Hydrogen Production via Water Splitting with Particulate Semiconductor Photocatalysts. Nat. Catal. 2019, 2 (5), 387–399. https://doi.org/10.1038/S41929-019-0242-6.

(8) Adnan, M.; Arifin, K.; Jeffery Minggu, L.; Kassim, M. Titanate-Based Perovskites for Photochemical and Photoelectrochemical Water Splitting Applications: A Review. Int. J. Hydrogen Energy 2018, 43. https://doi.org/10.1016/j.ijhydene.2018.10.173.

(9) Phoon, B. L.; Lai, C. W.; Juan, J. C.; Show, P. L.; Pan, G. T. Recent Developments of Strontium Titanate for Photocatalytic Water Splitting Application. Int. J. Hydrogen Energy 2019, 44 (28), 14316–14340. https://doi.org/10.1016/J.IJHYDENE.2019.01.166.

(10) Lin, X.; Guan, Q. F.; Li, H. B.; Liu, Y.; Zou, G. T. Preparation and Characterization of Dense Lanthanum-Doped Bismuth Titanate Ceramics. Sci. China Physics, Mech. Astron. 2012, 55 (1), 33–39. https://doi.org/10.1007/S11433-011-4574-8.

(11) Shinde, D. S.; Bhange, P. D.; Arbuj, S. S.; Kim, J. Y.; Bae, J. H.; Nam, K. W.; Tayade, S. N.; Bhange, D. S. NaFeTiO4: A Novel Visible Light Active Photocatalyst for Water Splitting and Environmental Remediation. Int. J. Hydrogen Energy 2020, 45 (15), 8605–8617. https://doi.org/10.1016/J.IJHYDENE.2020.01.083.

(12) Pantoja-Espinoza, J. C.; Domínguez-Arvizu, J. L.; Jiménez-Miramontes, J. A.; Hernández-Majalca, B. C.; Meléndez-Zaragoza, M. J.; Salinas-Gutiérrez, J. M.; Herrera-Pérez, G. M.; Collins-Martínez, V. H.; López-Ortiz, A. Comparative Study of $Zn_2Ti_3O_8$ and $ZnTiO_3$ Photocatalytic Properties for Hydrogen Production. Catalysts. 2020. https://doi.org/10.3390/catal10121372.

(13) Bao, L.; Bao, Q.; Jiang, W.; Xu, G. Hydrothermal Synthesis of $Bi@Bi_4Ti_3O_{12}$ Nanosheets with Enhanced Visible-Light Photocatalytic Activity. CrystEngComm 2020, 22 (38), 6316–6321. https://doi.org/10.1039/D0CE00994F.

(14) Chen, Z.; He, X. Low-Temperature Preparation of Nanoplated Bismuth Titanate Microspheres by a Sol–Gel-Hydrothermal Method. J. Alloys Compd. 2010, 497 (1–2), 312–315. https://doi.org/10.1016/J.JALLCOM.2010.03.053.

(15) Pushkal Sharmaa, Cheng-Ting Leeb, Jeffrey Chi-Sheng Wub, a. Sunlight- Driven Photocatalytic Hydrogen Production from Water Using Metal-Doped Strontium Titanate Perovskite Pushkal Sharma. 1994.

(16) Dias, J.; de Oliveira, J.; Renda, C.; Morelli, M. Production of Nanometric $Bi_4Ti_3O_{12}$

Powders: From Synthesis to Optical and Dielectric Properties. Mater. Res. 2018, 21. https://doi.org/10.1590/1980-5373-mr-2018-0118.

(17) Kumar, V.; Bhawna; Yadav, S. K.; Gupta, A.; Dwivedi, B.; Kumar, A.; Singh, P.; Deori, K. Facile Synthesis of Ce–Doped SnO2 Nanoparticles: A Promising Photocatalyst for Hydrogen Evolution and Dyes Degradation. ChemistrySelect 2019, 4 (13), 3722–3729. https://doi.org/10.1002/SLCT.201900032.

(18) Bhawna; Gupta, A.; Kumar, P.; Tyagi, A.; Kumar, R.; Kumar, A.; Singh, P.; Singh, R. P.; Kumar, V. Facile Synthesis of N-Doped SnO_2 Nanoparticles: A Cocatalyst-Free Promising Photocatalyst for Hydrogen Generation. ChemistrySelect 2020, 5 (26), 7775–7782. https://doi.org/10.1002/SLCT.202001301.

(19) Jin, Z.; Yang, H. Exploration of Zr–Metal–Organic Framework as Efficient Photocatalyst for Hydrogen Production. Nanoscale Res. Lett. 2017, 12 (1), 539. https://doi.org/10.1186/s11671-017-2311-6.

(20) Zhao, J.; Shi, R.; Li, Z.; Zhou, C.; Zhang, T. How to Make Use of Methanol in Green Catalytic Hydrogen Production. Nano Sel. 2020, 1 (1), 12–29. https://doi.org/10.1002/nano.202000010.

(21) Kumar, S.; Bhawna; Gupta, A.; Kumar, R.; Bharti, A.; Kumar, A.; Kumar, V. New Insights into Cu/Cu_2O/CuO Nanocomposite Heterojunction Facilitating Photocatalytic Generation of Green Fuel and Detoxification of Organic Pollutants. J. Phys. Chem. C 2023, 127 (15), 7095–7106. https://doi.org/10.1021/acs.jpcc.2c08094.

CHAPTER 6

Synthesis of composite of GO with 0.6%CdS and 0.6 % PbS doped BT to check their photocatalytic efficiency for hydrogen production.

6.1 Introduction

Over the recent years, there has been a significant worldwide development regarding the quest for sustainable and extremely efficient forms of alternative energy to substitute the inadequate fossil fuels. For given context, photocatalytic means of water splitting have been the subject of considerable attention from researchers in recent times due to their significant involvement in diverse energy conversion, notably hydrogen production. Therefore, hydrogen as an energy source, is a potential alternative to fossil fuels, mainly due to the limited availability and environmentally polluting characteristics of the latter. In this perspective, energy generation by use of renewable sources, particularly by means of photoinduced electron transfer processes has emerged as a significant field of scientific investigation[1].

Photocatalytic water splitting is a noteworthy phenomenon involving the water splitting into its primary constituents which are hydrogen and oxygen and this process is initiated by the utilization of photogenerated electrons obtained from the photocatalyst. This detailed interaction of light-driven processes establishes the stage for the incredible phenomenon of water splitting. In the context of photocatalysis, the task of achieving entirely separation of electron-hole pairs provides a considerable challenge when juxtaposed with their propensity for recombination.

Some of the most prevalent and effective photocatalysts are TiO_2, Pt-TiO_2, CdSe, $PbTiO_3$, $CdTiO_3$, SnO_2, MoS_2 and perovskite materials and are demonstrated the most efficient. While titanate perovskites are easily accessible compared to metal chalcogenides it is noteworthy that bismuth-based perovskites materials with good absorbance have attained a significant attention having easy charge separation. Although in the field of photocatalysis, the goal of obtaining entirely disentanglement of electron-hole pairs presents a considerable challenge when contrasted with the tendency of recombination[2]. Therefore, to enhance the transport rate of electrons perovskite nanomaterials has been used and to remove the holes, the experiment was performed in presence of scavengers. To encourage the charge departure and to successfully create the active sites, on

photocatalysts surface, various co-catalysts like platinum (Pt), Rhodium (Rh) and ruthenium (Ru) metals are usually loaded. Nevertheless, all these noble metals expensive and not readily available[3].

Graphene shows a significant surface area of 2630 m^2/g and carbon atoms (sp^2 bonded) are arranged in a single layer with π-conjugation structure thereby exhibiting a exceptional electronic mobility of 200,000 $cm^2/V/s$. The valence band possess bonding π while that of conduction band have antibonding π* orbitals and demonstrates interaction on the Brillouin zone corners thereby, categorizing it as semiconductor with zero band gap. The proximity of carbon atoms in graphene results in a significant overlap of electronic bands and the electronic properties can be reformed by incorporating new functionalities. For illustration, the electronic characteristics can be manipulated by introduction of oxygen (O_2) atoms which acts like a covering agent. Thereby, removing the equivalency between two carbon sublattices and forming the C-O bond which results in the alteration of original orbital structure. Oxygen has higher electronegativity in comparison to carbon atoms consequently making the p-doped GO material.

Graphene oxide (GO) acts as an intermediary state bridging the gap between graphene and graphite. The synthesis of GO can be accomplished using Modified Hummers' method which is a scalable technique that involves chemical oxidation to scale-off graphite[4].

In previous chapters, bismuth titanates and their CdS, PbS doped samples of different (0.1%, 0.3% and 0.6%) wt. % for water splitting reactions have been discussed and also checked their hydrogen production efficiency under light irradiation. It was noticed that 0.6 % CdS and 0.6% PbS doped samples showed maximum hydrogen production amount of 171 μmol/g and 202.43μmol/g efficiency correspondingly. Interestingly, it was detected that, samples with narrow band gap potential have slow rates of recombination of electron and hole couples thereby, increasing hydrogen evolution. While the efficiency is still low, which can be further improved by incorporation of graphene oxide into the sample.

Bismuth titanates and its CdS, PbS doped samples have been studied having overall good stability and non-toxicity. Incorporating the graphene oxide nanomaterials into CdS and PbS doped BT samples have distinct advantages in suppression of charge recombination. Moreover, the unpaired electrons (that are π electrons) of GO are particularly effective in bond formation with surface Bi atoms and enhances the light absorption of CdS/BT, PbS/BT samples. In this chapter, GO-CdS/BT

and GO-PbS/BT composites have been demonstrated to effectively utilizing photon energy for breakdown of water.

6.2 Experimental details

6.2.1 Synthesis of Graphene oxide by modified hummers process

Graphene oxide was produced by means of modified hummer's scheme as has been depicted in fig 6.1. First of all, 50ml of sulphuric acid was taken in a beaker followed by addition of graphite powder (2g) resulting in appearance of black coloured solution. Then ice bath was setup, known amount of $KMNO_4$ (6g) was added very - very slowly by maintaing the temperature of solution less than 20^oC. The subsequent solution was placed on magnetic stirrer up-to 3 hours with ice bath (ice bath was removed after 20 min.). After 3 h of continuous stirring 100mL water was added dropwise. After some time, the colour was changed to dark brownish followed by instant addition of 200mL water. Then, 10mL of hydrogen peroxide was added instantly. Finally, filtration, washing with water in addition to 10% Hcl solution. The obtained powder was dried in Oven for 4 hours at 100^oC.

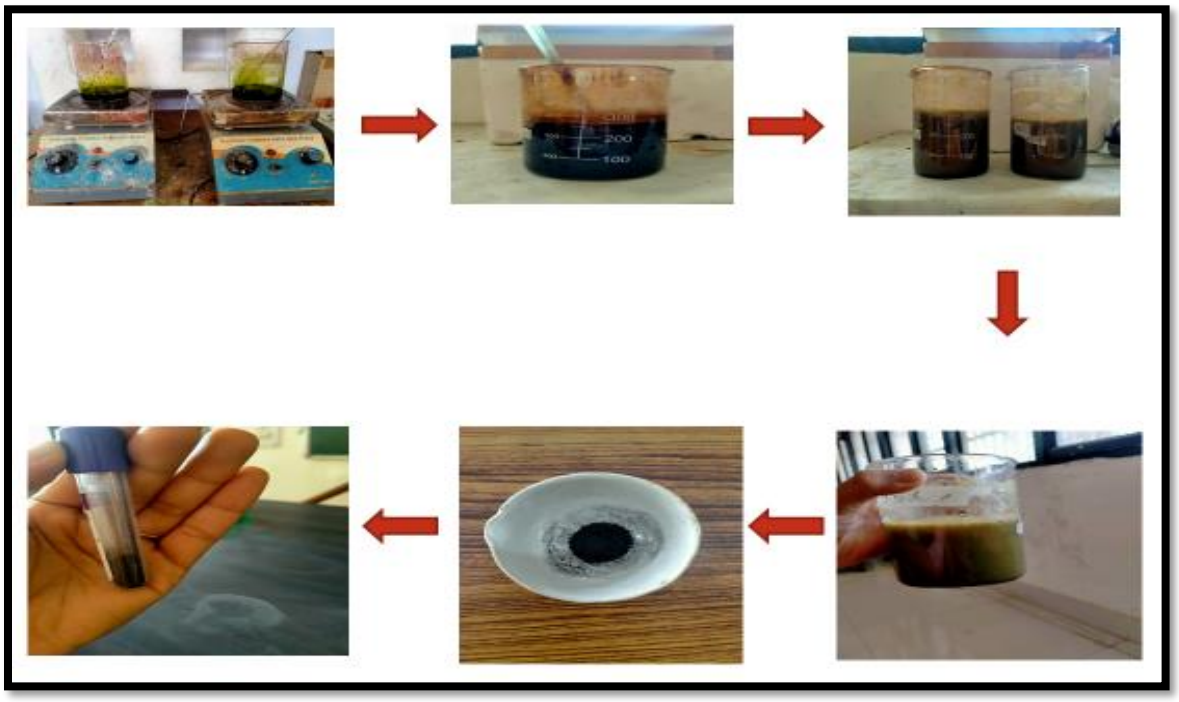

Fig 6.1 Block diagram depicting the schematic production of graphene oxide.

6.2.2 Synthesis of GO composite with CdS and PbS doped bismuth titanates

The 0.02g of graphene oxide synthesized by modified hummer's method was mixed well with 0.6% CdS doped and 0.6% PbS doped bismuth titanates by mechanical method and grind well up to 2 hours in pestle mortar followed by calcination at 600^{o}C. Resulting in incorporation of GO into CdS/BT and PbS/BT.

6.3 Results and Discussion

6.3.1 XRD spectrum

The XRD spectrum attained for as-prepared GO nanoparticles, by modified hummer's method has been depicted in Figure 6.2. It confirms the diffraction peak at $2\theta=10^{0}$, which is owing to oxidation of graphite. It shows that the product has been entirely oxidized afterwards the chemical oxidation[5].

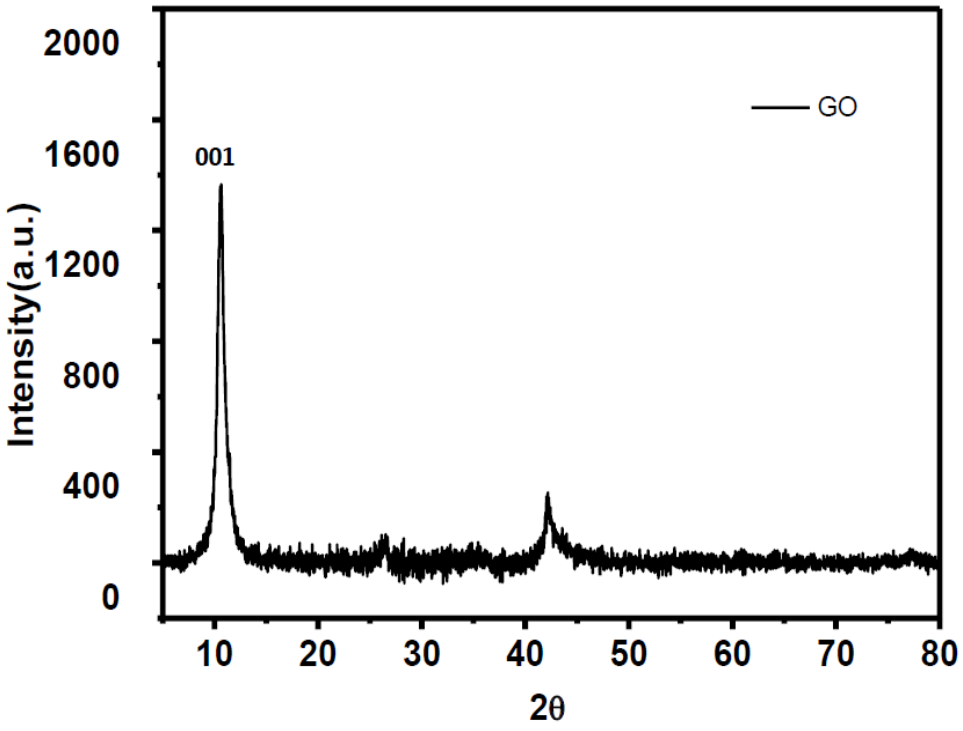

Fig 6.2 Depicts the XRD pattern of graphene oxide.

XRD pattern of GO composite with 0.6%CdS and 0.6%PbS doped BT samples have been depicted in fig 6.3 (a) and (b) correspondingly. The new peaks have been noticed as compared to 0.6% CdS and PbS doped BT samples. The peak at 34.69^0 altered from 32.56^0 after insertion of graphene oxide. Various new peaks (37.69^0, 40.41^0, 43.41^0, 49.79^0, 62.39^0) were noticed indicating the incorporation of graphene oxide into CdS/BT and PbS/BT samples.

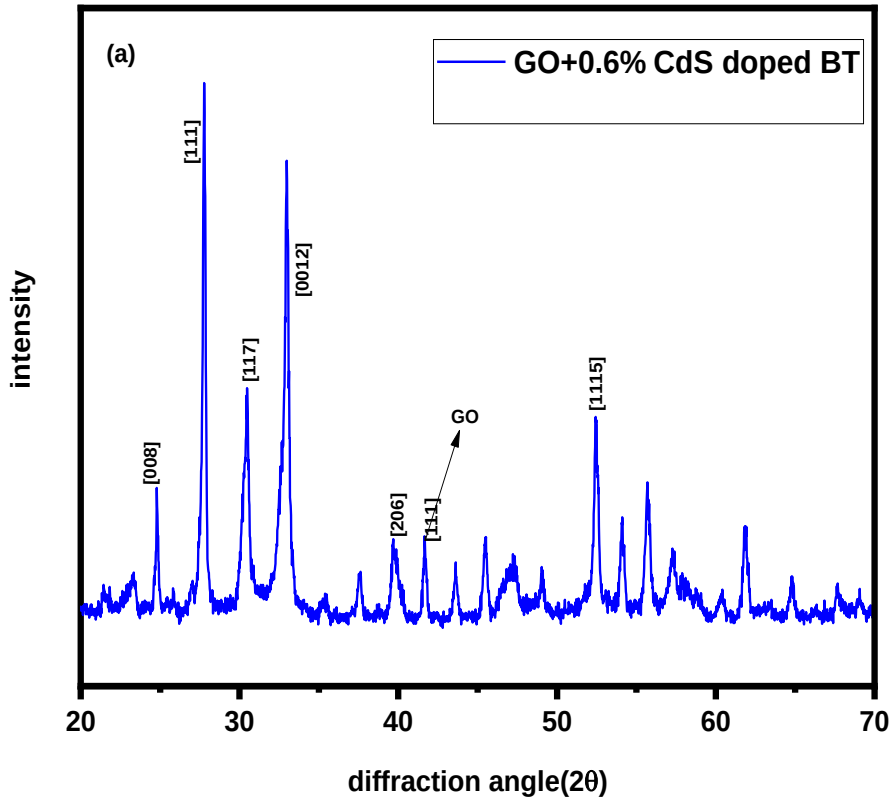

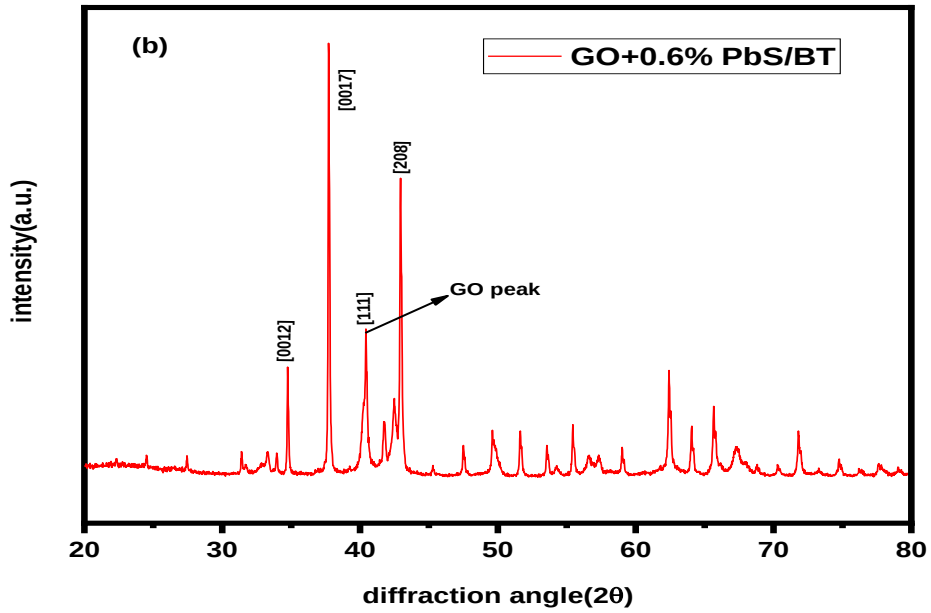

Fig 6.3 (a) XRD pattern of GO composite with 0.6% CdS doped BT and (b) represents XRD spectrum of composite of GO with 0.6% PbS doped BT.

The shift in peak positions of XRD spectrum of GO substituted composites reveals the successful addition of GO into CdS/BT and PbS/BT samples. Although, there is no change in the crystalline structure after incorporation of GO, however, there is a slight shift in the intensity and 2θ position and this shifting is because of delamination of GO layers[6].

6.3.2 FTIR

The spectrum for GO shows a extensive peak at 3140 cm^{-1} consistent to O-H stretching of water molecules absorbed onto the GO. The presence of absorption peak on 1616 cm^{-1} can be accredited to aromatic C=C stretching vibration.

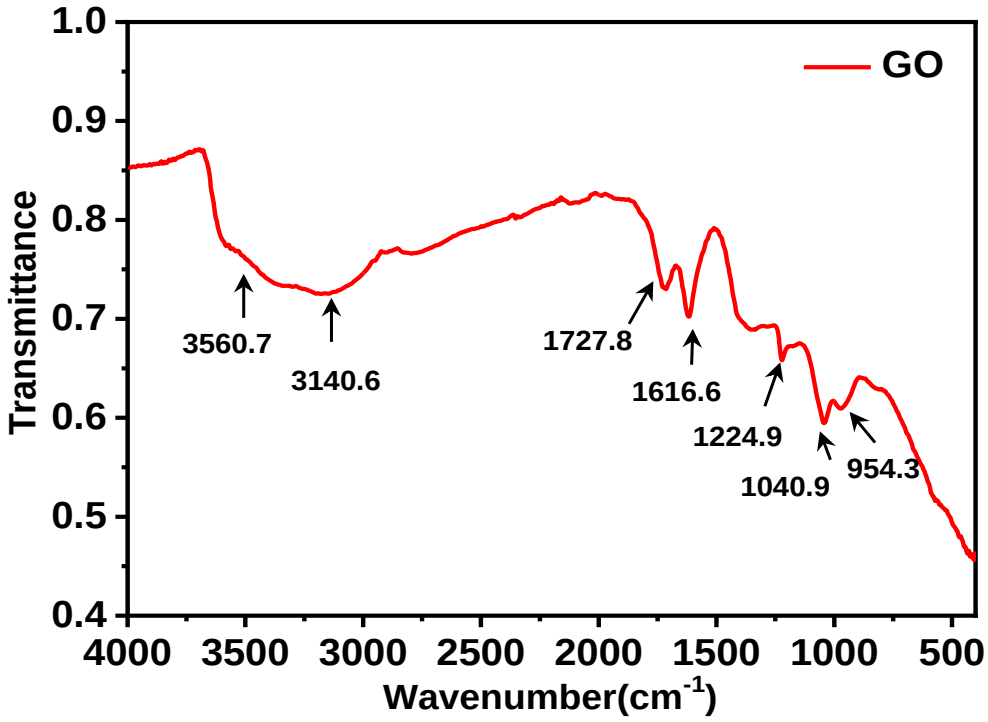

Fig 6.4 The FTIR spectrum of GO.

The peak at 1040 cm^{-1} agrees to alkoxy C-O stretching vibration. The presence of oxygen-containing functional group reveals that the graphite has been successfully oxidized into GO.

Fig 6.5 (a) and (b) demonstrates the FTIR spectrum of GO+ 0.6%CdS and 0.6%PbS composite respectively. In fig 6.5 (a) the sharp peak at 587cm^{-1} is attributed to the bismuth titanate while the peak at 818 cm^{-1} is owing to Ti-O stretching vibration. Furthermore, the spectrum shows the peak at 1040cm^{-1} and at 1727 cm^{-1} is due to insertion of graphene oxide into the CdS/BT sample.

Further, as can be perceived from fig 6.5 (b), the peak position at 587cm^{-1} is accredited to bismuth titanate nanostructures. The peak position at 1616cm^{-1} and 954cm^{-1} indicates the incorporation of graphene oxide into PbS/BT sample.

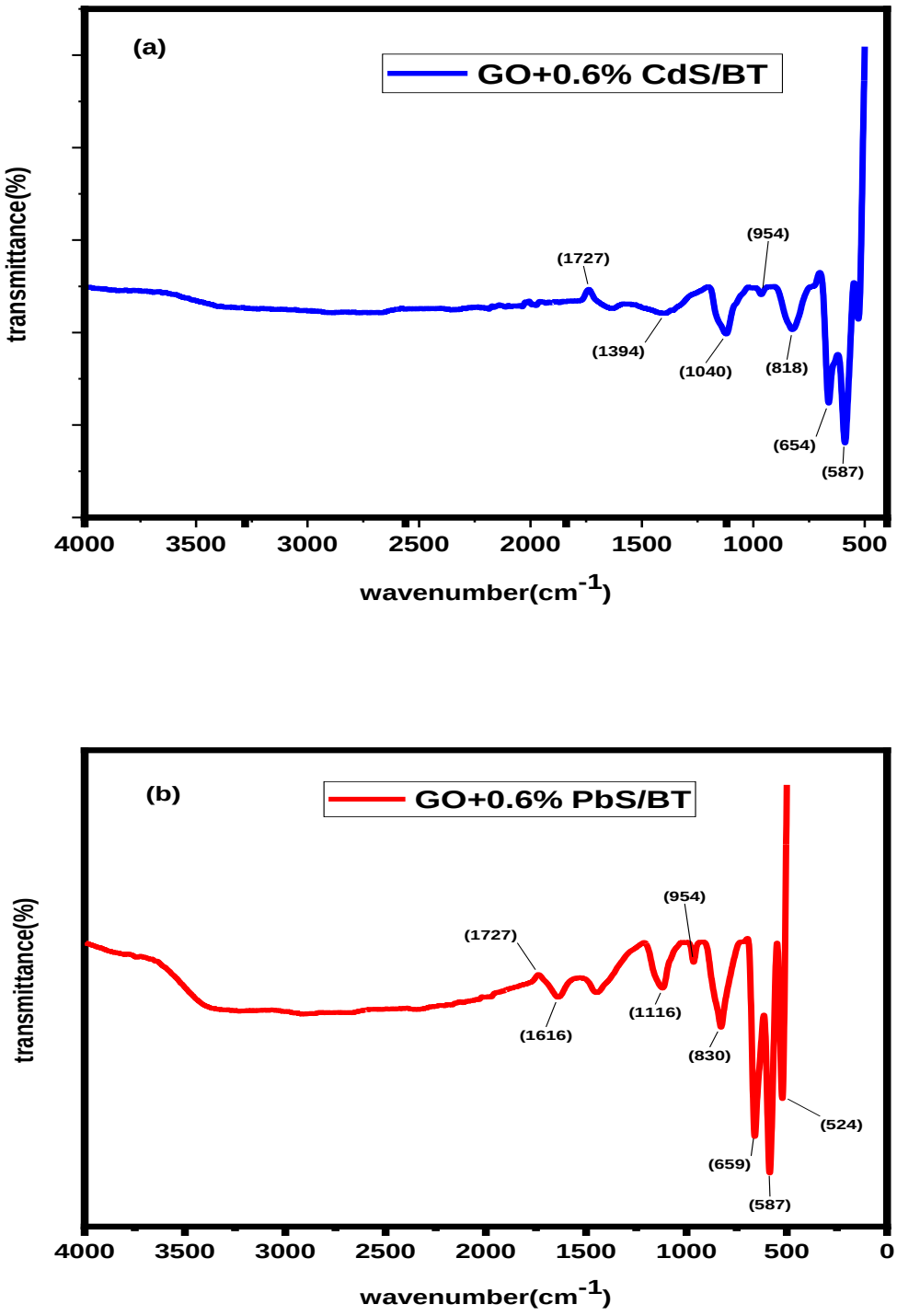

Fig 6.5 (a) FTIR spectra of GO+ 0.6%CdS doped BT (b) FTIR spectra of GO+ 0.6%PbS doped BT.

6.3.3 UV-visible spectroscopy

UV absorbance spectra of GO composite with 0.6% CdS doped BT has been depicted in figure 6.6. The graph shows the absorbance at 349nm for graphene Oxide composite with 0.6% CdS doped BT while GO composite with 0.6% PbS doped BT absorbs UV light at 356nm indicating the narrow band gap due to shift in absorbance wavelength.

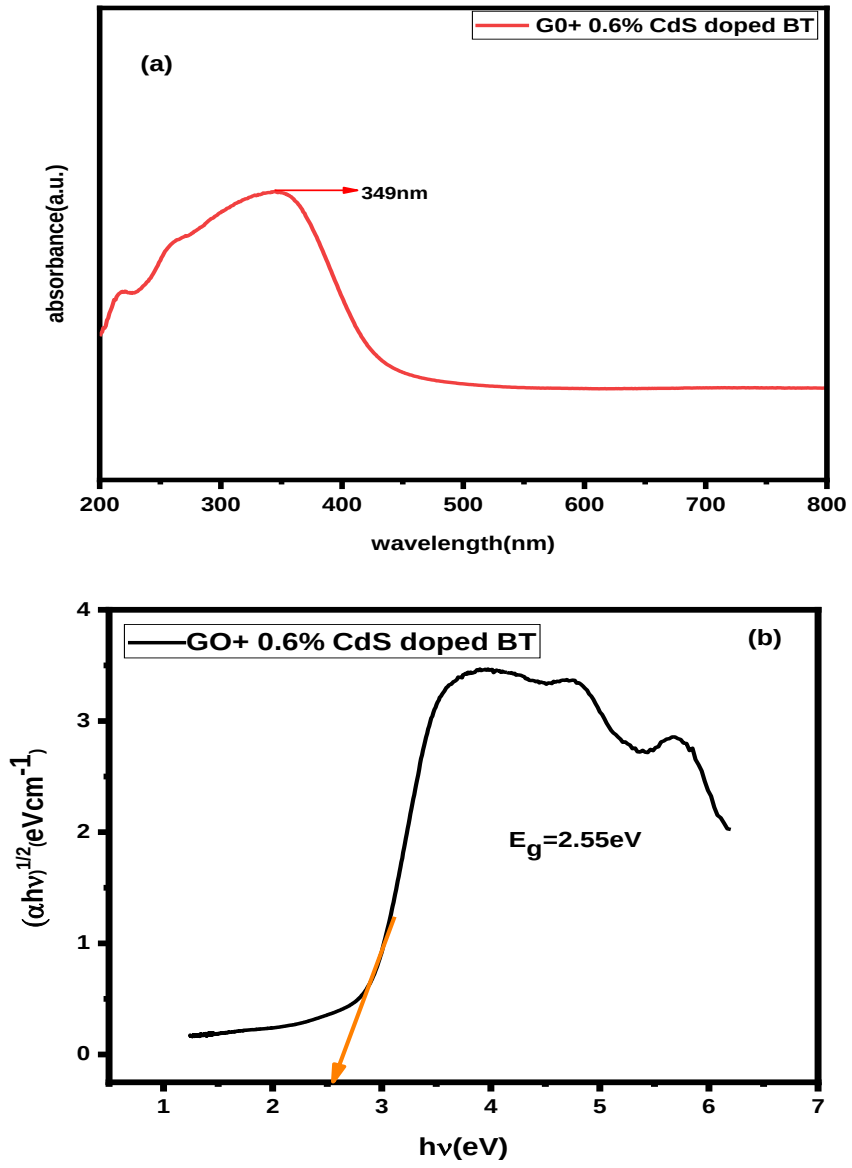

Fig 6.6 (a) UV absorbance spectra and (b) Tauc plot of GO composite with 0.6 % CdS doped BT.

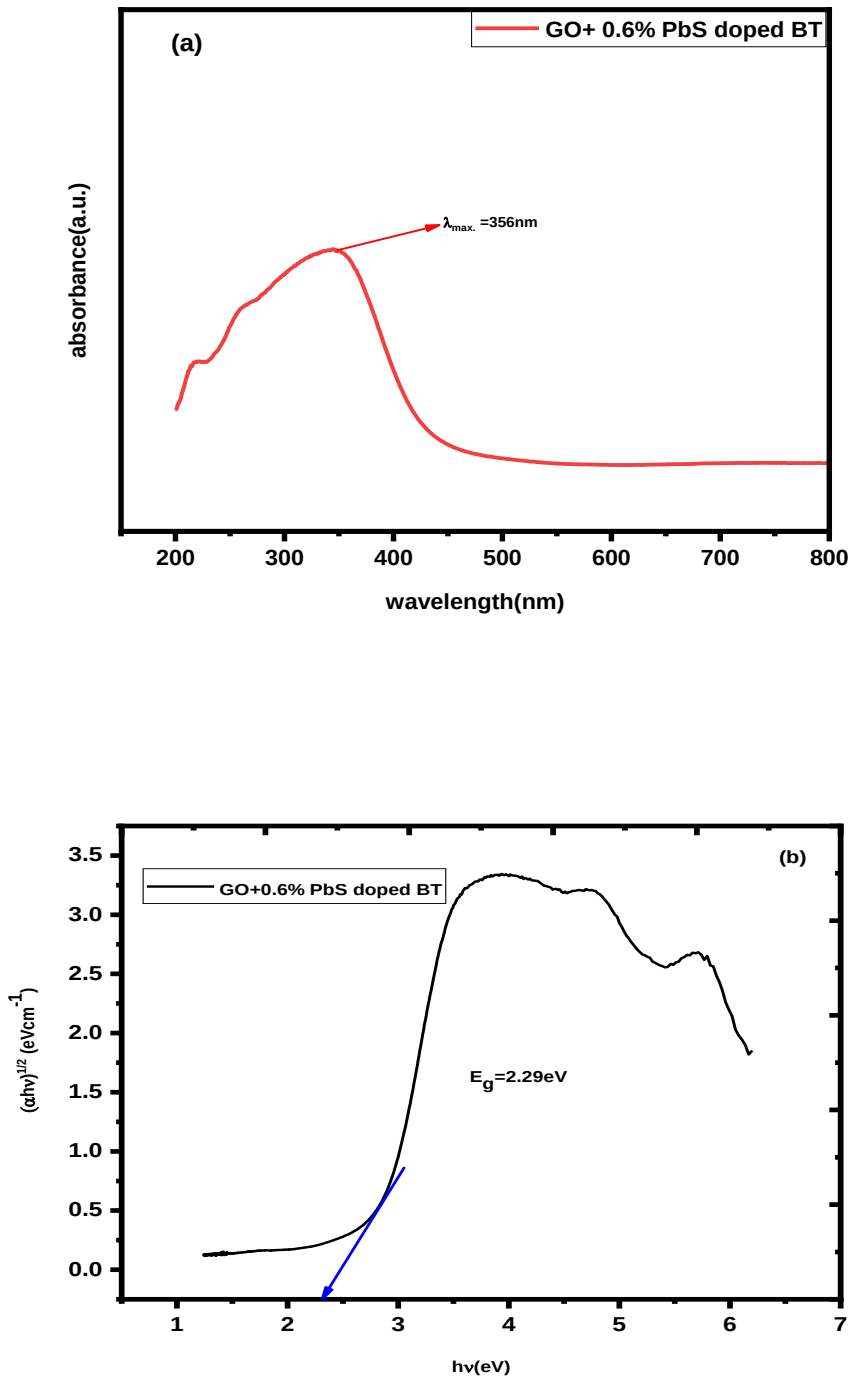

Fig 6.7 (a) UV absorbance spectra and (b) tauc plot of GO composite with 0.6 %PbS doped BT.

The calculated band of 2.55eV has been observed from tauc plot for graphene Oxide composite with 0.6% CdS doped Bismuth titanate. While, the band gap of 2.29eV has been depicted for graphene Oxide composite with 0.6% PbS doped bismuth titanate. Indicating the narrowing of band gap.

Table 6.1 Band gap of graphene oxide composites with absorbance.

Photocatalyst	**λmax.**	**Band gap**
GO + 0.6% CdS doped BT	349nm	2.55 eV
GO + 0.6% PbS doped BT	356nm	2.29 eV

6.3.4 FESEM

The insertion of graphene oxide into 0.6%CdS and 0.6% PbS doped BT samples were additionally confirmed by performing the FESEM analysis. The images were captured under X= 50000 and 25000 magnifications clearly reveal the presence of homogeneously distributed GO nanoparticles into the spherical shaped CdS/BT and PbS/BT samples.

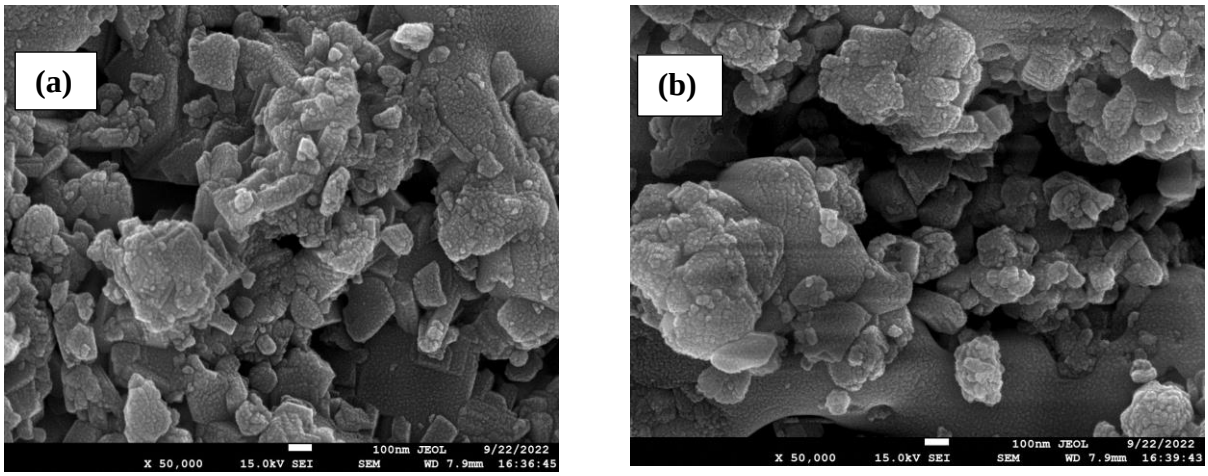

Fig 6.8 (a) Picture of GO composite with 0.6 %CdS doped BT (b) Image of GO composite with 0.6 %PbS doped BT.

6.3.5 HR-TEM

To know more about the structural features of the synthesized nanocomposites, some of them were analyzed by employing HRTEM. The picture depicts that graphene oxide is evenly distributed throughout the nanoparticles implementing almost whole image.

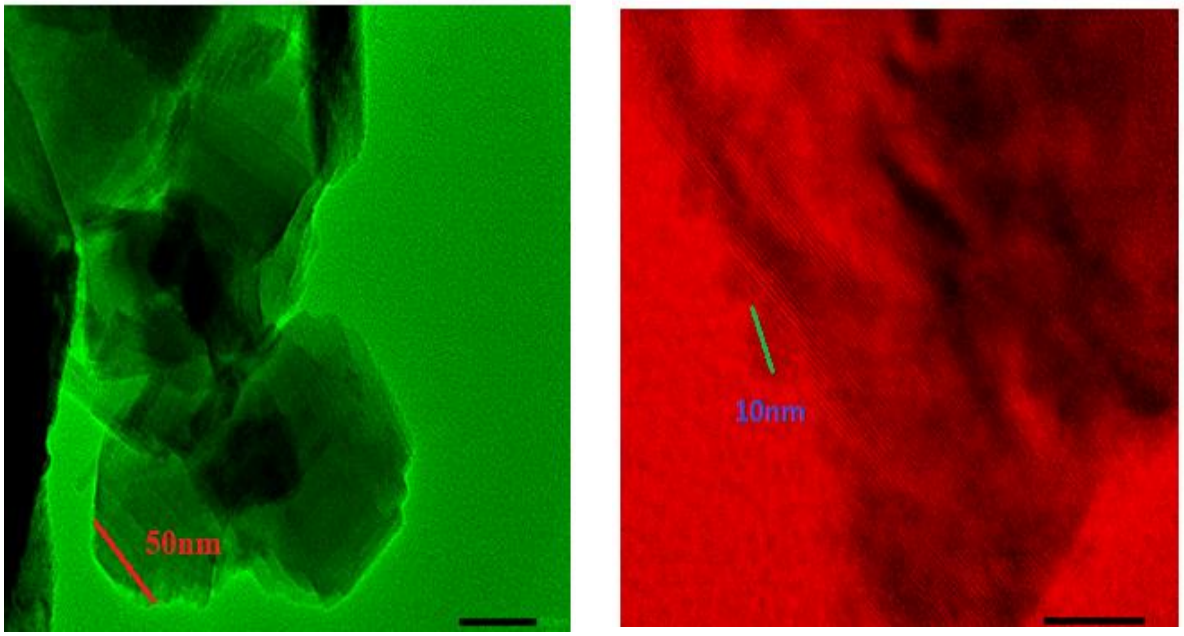

Fig 6.9 HR-TEM image of GO+0.6%PbS doped BT.

6.3.6 Photocatalytic activities test

The photocatalytic proficiency of GO composites with 0.6% CdS and 0.6%PbS doped BT samples was analyzed by water splitting reactions in photoreactor cell under illumination of light. In the experiment, 40ml of H_2O was taken in round bottom flask (RBF), addition of 0.10g of photocatalyst under vigorous stirring on magnetic stirrer at a rate of 450rpm. The light radiations were allowed to fall on RBK using Xe lamp (2 lamp of 250W each) as a source of light, the reaction starts leading to splitting of water and formation of electron-hole pairs takes place. After 50 minutes of illumination, the gas was collected in gas tight syringe and detected by GC-TCD with flow of Helium and Nitrogen as a carrier gas. Similarly, the amount of gas collected was analyzed after every 50 minutes of illumination and checked the amount of gas produced by GC-TCD.

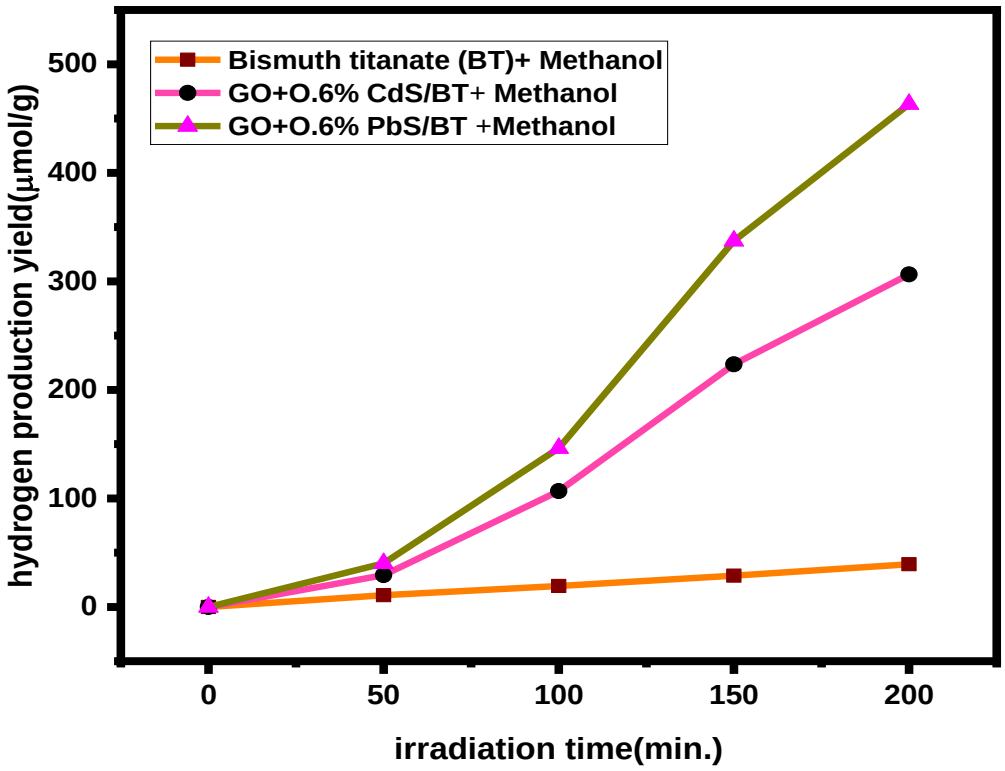

Fig 6.10. Comparative photocatalytic activity of various BT samples.

Photocatalytic water splitting activity of BT, GO composite with 0.6% CdS/BT and GO composite of 0.6% PbS/BT nanoparticles, was performed in the proximity of methanol (MeOH) as a hole emulsifying agent. The declining order of hydrogen evolution using methanol is GO+0.6% PbS/BT > GO+0.6% CdS doped BT > bismuth titanate. MeOH appears to inhibit the process of electron-hole reassimilation by catching holes in valence band of doped bismuth titanate. Henceforth, methanol behaves as a hole scrounger by diminishing OH radicals, thus improving rate of hydrogen gas evolution. Pristine BT show only 39.24µmol/g of hydrogen in 200 minutes, while GO composite of 0.6%CdS/BT leads to excellent hydrogen evolution of 306.38µmol/g, because of its narrower band potential (2.55eV), which is much high than BT and O.6%CdS doped BT. Further, GO+ 0.6%PbS /BT sample depicts the highest hydrogen yield of 438.21µmol/g. Showing that GO acts as a superior material for efficiently improving the yield of hydrogen attributed to its nature of electron and its ability to store the separated electrons sink as has been shown if fig 6.11.

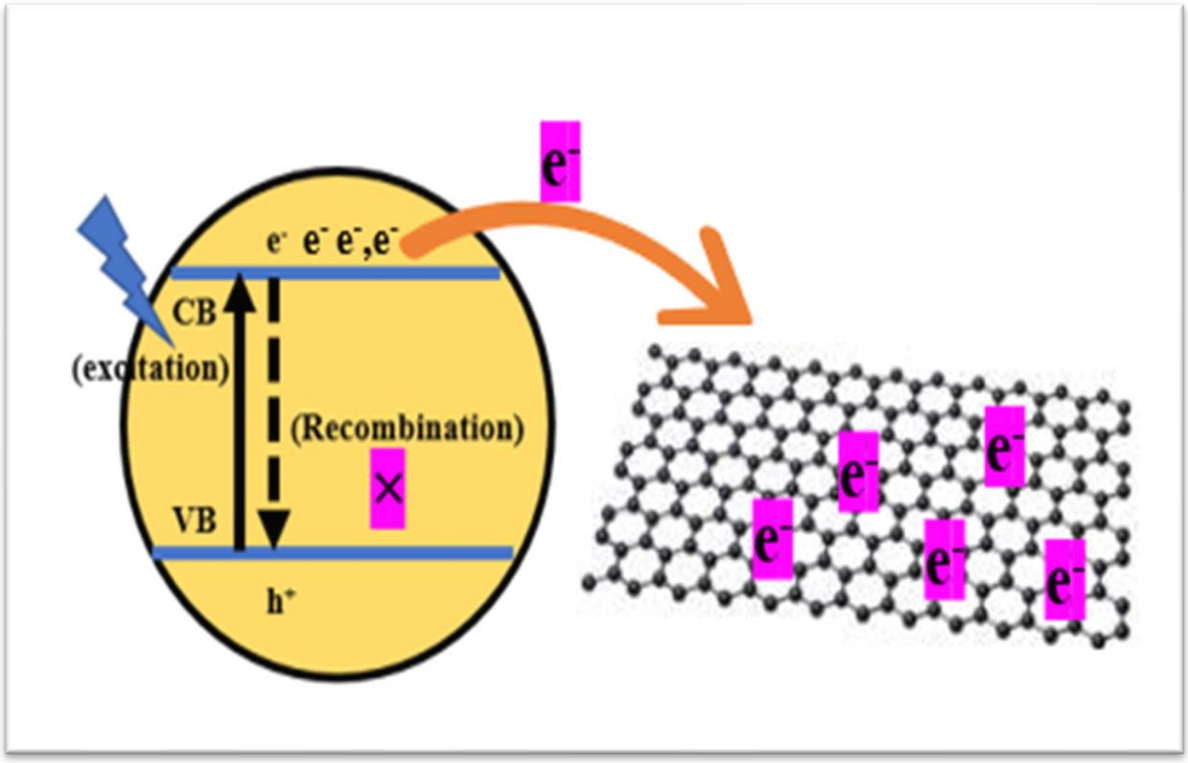

Fig 6.11 Diagram depicting electron trapping by GO.

Table 6.2 Hydrogen production yield of various photocatalyst along with reaction conditions.

Photocatalyst	**Sacrificial agent**	**Hydrogen evolution**	**Source of light**
Bismuth titanate	Methanol	39.21μmol/g/h	Xe lamp
GO+0.6%CdS doped BT	Methanol	306.38μmol/g/h	Xe lamp
GO+0.6%PbS doped BT	Methanol	463.21μmol/g/h	Xe lamp

6.4 Conclusion

In conclusion, this chapter demonstrates the photocatalytic efficiency of composite GO+0.6% CdS/BT and GO+0.6%PbS/BT revealing as a superior photocatalyst than CdS/BT and PbS/BT samples. GO which was produced by Modified Hammers process, was successfully incorporated

into the 0.6%CdS/BT and 0.6%PbS/BT nanomaterials by means of mechanical method. Furthermore, the narrow band gap (2.55eV) of GO+ 0.6%CdS/BT samples enhance the light consumption in visible region which induce generation of promising hydrogen gas. As a consequence, we have revealed a superior rate of hydrogen gas evolution 306.38μmol/g without the usage of any costly metal co-catalyst like Platinum (Pt), palladium (Pd) or Gold (Au) etc. Nevertheless, excellent rate of hydrogen production (438.21μmol/g/h) was observed for GO+ 0.6%PbS/BT in presence of methanol and a co-catalyst free environment.

References

(1) Devaraji, P.; Jo, W.-K. Two-Dimensional Mixed Phase Leaf-$Ti_{1-X}Cu_xO_2$ Sheets Synthesized Based on a Natural Leaf Template for Increased Photocatalytic H_2 Evolution. ChemCatChem 2018, 10 (17), 3813–3823. https://doi.org/https://doi.org/10.1002/cctc.201800814.

(2) Kumar, S.; Kumar, A.; Rao, V.; Kumar, A.; Muthukonda Venkatakrishnan, S.; Krishnan, V. Defect-Rich MoS_2 Ultrathin Nanosheets-Coated Nitrogen-Doped ZnO Nanorod Heterostructures: An Insight into in-Situ-Generated ZnS for Enhanced Photocatalytic Hydrogen Evolution. ACS Appl. Energy Mater. 2019, 2. https://doi.org/10.1021/acsaem.9b00790.

(3) Dholam, R.; Patel, N.; Santini, A.; Miotello, A. Efficient Indium Tin Oxide/Cr-Doped-TiO_2 Multilayer Thin Films for H_2 Production by Photocatalytic Water-Splitting. Int. J. Hydrogen Energy. 2010, 35 (18), 9581–9590. https://doi.org/https://doi.org/10.1016/j.ijhydene.2010.06.097.

(4) Yeh, T.-F.; Cihlář, J.; Chang, C.-Y.; Cheng, C.; Teng, H. Roles of Graphene Oxide in Photocatalytic Water Splitting. Mater. Today 2013, 16 (3), 78–84. https://doi.org/https://doi.org/10.1016/j.mattod.2013.03.006.

(5) Durairaj, S.; Kalimuthu, V.; Srinivasan, M.; Ramasamy, P. Graphene Oxide Reinforced Bismuth Titanate for Photocatalytic Degradation of Azo Dye (DB15) Prepared by Hydrothermal Method. Ceram. Int. 2021, 47. https://doi.org/10.1016/j.ceramint.2021.05.238.

(6) Abdollahi, R.; Taghizadeh, M. T.; Savani, S. Thermal and Mechanical Properties of Graphene Oxide Nanocomposite Hydrogel Based on Poly (Acrylic Acid) Grafted onto Amylose. Polym. Degrad. Stab. 2018, 147, 151–158. https://doi.org/https://doi.org/10.1016/j.polymdegradstab.2017.11.022.

Chapter 7

Conclusion

Photocatalytic splitting of water is an encouraging technique and ecologically friendly method to generate hydrogen. To efficiently synthesize the hydrogen, the presence of suitable photocatalysts along with solar radiations or light source is essential. The produced hydrogen can be regarded as: an energy carrier, can be stockpiled and utilized for generation of electricity, can also be used as a fuel exhibiting zero emissions of carbon.

The key objective of this research work is to conquer the prevailing energy and ecological challenges by employing photocatalytic technique. Although, several challenges encountered during the photocatalytic reactions, with the objective of enhancing the hydrogen generation efficiency for energy related applications. These challenges include the: (a) reducing the band gap of photocatalytic materials (b) to minimize the reassimilation of charges (c) to synthesize the photocatalyst that can work in visible light or to activate the produced semiconductor in visible region.

So as, to accomplish the above challenges, the titanate-based perovskite photocatalytic materials were synthesized and analyzed in the photoreactor set up. The intention of this evaluation was to produce hydrogen gas through water splitting in occurrence of scavengers like EDTA, TEOA and methanol.

7.1 Summary

The primary investigations and conclusions of thesis can be concisely outlined as:

- The Bismuth titanate photocatalytic material was synthesized adopting hydrothermal technique. The as prepared nanomaterials were characterized by employing XRD, XPS FTIR, EPR, FESEM and DRS-UV technique. The band gap of 3.25eV was deduced from UV-visible spectroscopic technique and checked the hydrogen production efficiency in photoreactor set up in presence of EDTA and methanol as a scavenger.

- Two doped samples of BT were prepared to enhance the photocatalytic efficiency.

- Different wt.% (0.1%, 0.3% and 0.6%) of CdS nanomaterials synthesized via hydrothermal method were mixed in BT samples by mechanical method. The doped samples were further examined by XRD, FTIR, FESEM and DRS-UV spectroscopic analysis. It was noticed that with increase in doping concentration, reduction in band gap occurs and also drop in crystallite size takes place, which assists in enhancing the light absorption in visible region. Further, hydrogen yield was noticed by photocatalytic reaction and found that 0.6%CdS/BT samples showed the highest hydrogen gas generation.

- PbS nanomaterials were incorporated in BT samples in various concentration of wt% by 0.1%, 0.3% and 0.6% and mechanical method was adapted for doping. The doped samples were checked for hydrogen formation in PC reactor set-up with addition of EDTA, TEOA and methanol (sacrificial agents). It was noticed that 0.6%PbS doped BT nanomaterials exhibits the maximum hydrogen production yield in proximity of methanol.

- To further enhance the yield of hydrogen gas, 0.6%CdS/BT and 0.6%PbS/BT samples were further corroborated with graphene oxide synthesized via Modified Hammers method. Prepared composites show reduced band gap and the photocatalytic efficiency was examined for GO composites in presence of methanol.

- Photocatalytic production of hydrogen with GO+0.6%PbS/BT composites displayed a highest rate with methanol as a scavenger.

Table 7.1 Comparison of band gap of synthesized photocatalysts.

Photocatalyst	**Band Gap**	**Photocatalyst**	**Band Gap**
Bismuth titanate	3.25eV		
0.1% CdS doped BT	3.22eV		
0.3% CdS doped BT	3.1eV		
0.6% CdS doped BT	3.05eV	GO+0.6% CdS doped BT	2.55eV
0.1% PbS doped BT	2.90eV		
0.3% PbS doped BT	2.82eV		
0.6% PbS doped BT	2.76eV	GO+0.6% PbS doped BT	2.29eV

Table 7.2 The hydrogen gas efficiency of various photocatalysts with reaction conditions.

Photocatalyst	**Sacrificial agent**	**Source of light**	**Hydrogen yield**
Bismuth titanate	Methanol	500 W Xe lamp	39.24 µmol/g
0.1%CdS doped BT	EDTA	500 W Xe lamp	90.86 µmol/g
0.3%CdS doped BT	EDTA	500 W Xe lamp	110.54 µmol/g
0.6%CdS doped BT	EDTA	500 W Xe lamp	171 µmol/g
0.1%PbS doped BT	EDTA	250 W Xe lamp	103.29µmol/g
0.3%PbS doped BT	EDTA	250 W Xe lamp	154.37 µmol/g
0.6%PbS doped BT	EDTA	250 W Xe lamp	202.43 µmol/g
GO+ 0.6%CdS doped BT	Methanol	500 W Xe lamp	306.38 µmol/g
GO+ 0.6%PbS doped BT	Methanol	500 W Xe lamp	463.21 µmol/g

7.2 Future scope

With relevance to the noteworthy findings of this research work, various activities have been projected for subsequent consideration in near future:

- To prepare more samples (higher concentration then 0.6 wt%) of CdS and PbS doped bismuth titanate nanomaterials to evaluate their photocatalytic efficiency.
- To develop the more efficient photocatalysts with different loading concentrations of graphene oxide on CdS doped BT and PbS doped BT nanomaterials.
- To investigate the impact of dosage of various sacrificial agents on photocatalysis.

List of Publications

1. Amika, Rajesh Sharma, Ajit Sharma, Ankush Chandrani, Jashanpreet Singh and Deepak Kumar, "Role of titanate-based perovskites in solar water splitting: An overview" Journal of Physics: Conference Series 2267 (2022) 012016, doi:10.1088/1742-6596/2267/1/012016.
2. Amika Gahlawat, Monika Sindhu, Ajit Sharma, Karan Singh Maan, Prabal Pratap Singh, Radhamanohar Aepuru, Deepak Kumar, "Synthesis and characterization of Bismuth titanate perovskite materials for hydrogen production" Materials Letters vol. 342, (2023), 134316. https://doi.org/10.1016/j.matlet.2023.134316.
3. Amika, Monika Sindhu, Ajit Sharma, Karan Singh Maan, Prabal Pratap Singh, Shubham Ladiya, Deepak Kumar, Rajesh Sharma, Pardeep Dahiya, "Facile Synthesis of CdS Doped Bismuth Titanate Perovskites: A Cocatalyst Free Promising Photocatalyst for Hydrogen Generation" Chemistry Africa (2023), https://doi.org/10.1007/s42250-023-00679-3.
4. Monika Sindhu, Ajit Sharma, Vijaykumar Patel, Amika Gahlawat, Prabal Pratap Singh, Karan Singh Maan, Deepak Kumar, Van-Huy Nguyen, "Characteristic studies of Ta_3N_5/BSC@PANI nanocomposites for hydrogen production via water-splitting under visible light irradiation" Chemical Engineering Research and Design Vol. 197, 2023, 572-580. https://doi.org/10.1016/j.cherd.2023.07.050.
5. Amika, Deepak Kumar, Rajesh Sharma, Monika Sindhu, "Structural and Morphological Properties of Bismuth Oxide Nanostructured Materials" ICMET AIP Conference proceedings.

List of Conferences attended

1. Participation in International Conference on Scientific Developments in the Current Era (ICSDCE-2021) Panipat, Haryana.
2. Poster presentation on “Role of titanate-based perovskites in solar water splitting: An overview” (RAFAS 2021), LPU Punjab.
3. Poster presentation on “Nanotechnology emerging field for future energy generation: An Overview” (E-ICRACS 21), LNMU, Darbhanga Bihar.
4. Poster presentation on “To investigate the structural and morphological properties of Bismuth Oxide nanostructured materials” (ICRABAS-2021), BMU, Rohtak Haryana.
5. Presented paper on Structural and Morphological Properties of Bismuth Oxide Nanostructured Materials in the International Conference on Materials for Emerging Technologies (ICMET-21) LPU, Punjab
6. Has attended successfully a three days’ workshop on “Thesis Writing” from 27th May, 2022 to 29th May, 2022 organized by Nuhianwali Education Society.
7. Presented paper “Synthesis and characterization of Graphene Oxide by Modified Hammers method” in ‘ICNTCR-2022’ organized by S.U.S Govt College Matak Majri Karnal.
8. Presented paper entitled “Synthesis and characterization of Cadmium Sulphide nanoparticles” in ADCAS-2023 organized by DCRUST-Murthal.